July 2016

Simulating the Hydrodynamics of Offshore Floating Wind Turbine Platforms in a Finite Volume Framework

Maija Benitz
University of Massachusetts - Amherst

SIMULATING THE HYDRODYNAMICS OF OFFSHORE FLOATING WIND TURBINE PLATFORMS IN A FINITE VOLUME FRAMEWORK

A Dissertation Presented

by

MAIJA A. BENITZ

Submitted to the Graduate School of the
University of Massachusetts Amherst in partial fulfillment
of the requirements for the degree of

DOCTOR OF PHILOSOPHY

May 2016

Mechanical and Industrial Engineering

SIMULATING THE HYDRODYNAMICS OF OFFSHORE FLOATING WIND TURBINE PLATFORMS IN A FINITE VOLUME FRAMEWORK

A Dissertation Presented

by

MAIJA A. BENITZ

Approved as to style and content by:

_____

David P. Schmidt, Co-chair

_____

Matthew A. Lackner, Co-chair

_____

Sanjay R. Arwade, Member

_____

Sundar Krishnamurty, Department Chair
Mechanical and Industrial Engineering

ACKNOWLEDGMENTS

ABSTRACT

SIMULATING THE HYDRODYNAMICS OF OFFSHORE FLOATING WIND TURBINE PLATFORMS IN A FINITE VOLUME FRAMEWORK

MAY 2016

MAIJA A. BENITZ

B.A., COLORADO COLLEGE

M.S.M.E., UNIVERSITY OF MASSACHUSETTS AMHERST

Ph.D., UNIVERSITY OF MASSACHUSETTS AMHERST

Directed by: Professor David P. Schmidt and Professor Matthew A. Lackner

There is great potential for the growth of wind energy in offshore locations where the structures are exposed to a variety of loading from waves, current and wind. A variety of computer-aided engineering (CAE) tools, based largely on engineering models employing potential-flow theory and/or Morison's equation, are currently being used to evaluate hydrodynamic loading on floating offshore wind turbine platforms. While these models are computationally inexpensive, they include many assumptions and approximations. Alternatively, high-fidelity computational fluid dynamics models contain almost no assumptions, but at the cost of high computational expense. In this work, CFD simulations provide detailed insight into the complex fluid flow that has not been captured experimentally, nor can be attained with reduced-order models.

This work includes a thorough validation of the various CFD toolboxes necessary for simulating offshore floating wind turbine platforms in the ocean environment, from numerical wave propagation to fluid-structure interactions. The fundamental physics of flow around complex structures is examined through various studies to better understand the effects of a fluid interface, truncated ends, structure size, multi-member arrangements and environmental conditions. These factors are explored in terms of drag, lift and frequency of the loads. Additionally, motion of structures in free decay tests and waves are investigated. The work provides insight into the complex fluid flow around floating offshore structures of small draft in a variety of environmental conditions. CFD simulations are used to assess assumptions and approximations of reduced-order engineering models, and explain why, and in which conditions, these models perform inaccurately. Finally, the work provides suggestions for improvements to engineering tools often used for hydrodynamics modeling of floating offshore wind turbines.

TABLE OF CONTENTS

LIST OF TABLES

LIST OF FIGURES

INTRODUCTION

Large-scale offshore wind energy has become a reality in Europe over the past decade, with continued development on the horizon in Europe, as well as Asia and the United States. While the vast majority of offshore wind energy development utilizes fixed bottom support structures, floating offshore wind turbines show great potential for harnessing the wind resource far from shore, where the wind resource is greater and concerns about visibility are reduced [151] [152]. However, in both near shore, shallow water applications, and especially in deeper waters farther from shore, technical and economic feasibility challenges must be overcome. Understanding the fundamental hydrodynamic forces in the offshore environment, and in particular the added challenges of operating floating platforms in the ocean environment, is crucial to the success of future projects. Not only are floating platforms subject to loading from ocean waves, but also increased motion due to the wave-body interactions.

Research Motivation

Hydrodynamic loads on floating offshore wind turbine platforms are often predicted with computer-aided engineering tools. There are a variety of computer-aided engineering (CAE) tools, which are based largely on potential-flow theory and/or Morison's equation. These CAE tools include a variety of assumptions and approximations, resulting in a low computational cost allowing for an iterative, rapid design process. These reduced order modeling assumptions require assessment. Verification and validation of CAE tools is necessary for building confidence in the accuracy of the models, and furthermore, identification of opportunities for model improvements is needed.

Experimental measurements of model-scale floating wind turbine platforms are available for verification and validation of the design tools. However, the tests omit measurements of hydrodynamic forces. Furthermore, these experimental load cases do not include full scale tests, nor extreme conditions such as breaking waves.

The assumptions and approximations of CAE tools, along with the gaps in experimental measurements, creates a clear need for supplemental and more detailed hydrodynamic data. Consequently, this thesis fill these voids by simulating hydrodynamic loads with computational fluid dynamics (CFD). This thesis work provides high-fidelity hydrodynamic predictions that provide a better understanding of the fundamental physics of the problem, and which may be used to assess the accuracy of CAE tools, and supplement the existing tank test data.

Research Goals

The goal of this thesis is to describe the underlying physics of the flow around complex geometries with representative traits of offshore floating wind turbine platforms, including surface-piercing members of limited draft. This dissertation aims to produce high-fidelity simulations of hydrodynamic loads on offshore structures, which are used to assess reduced-order models, and suggest model improvements, as well as supplement experimental data. Furthermore, the work seeks to provide an improved understanding of the effects of geometric and environmental factors on the flow behavior, loading and motion of floating bodies. CFD is used to assess the ramifications of the various assumptions and approximations of CAE tools, with the goal of identifying reasons for shortcomings in CAE tool predictions, and suggesting improvements to existing design tools.

Summary of Research Activities

To achieve the research goals outlined above, a variety of studies are performed with CFD, beginning with a thorough set of validation exercises, chosen to build confidence in the capability and accuracy of the CFD methodologies. Validation exercises include simulations of regular and irregular wave propagation, load predictions on stationary bodies as well as fluid-structure interactions which include loading and motion. In all of these exercises, CFD predictions are validated against experimental measurements. These validation exercises provide confidence in the CFD model which is employed in the remainder of the work.

Next, flow around complex geometries, and the resulting loads on the structure, are investigated. The effects of surface-piercing members, free ends and various angles of inclination are explored through high-fidelity CFD simulations. Predicted loads are considered, both in magnitude and frequency content. The effects of these geometrical complexities impact the loading behavior for offshore engineering, including floating wind turbine platforms, which have shallow draft, slanted members and pierce a free-surface.

The study of flow around complex geometries is extended to investigate a stationary semisubmersible wind turbine platform in steady current conditions. The CFD results are compared against HydroDyn, a computer-aided engineering tool for predicting hydrodynamic loads on wind turbine platforms. Discrepancies between the code predictions are explained through high-fidelity flow field visualizations of the complex flow physics and detailed load predictions from CFD. This work provides a better understanding of the shortcomings of the CAE tool, and suggests more careful selection of drag coefficients for inputs to reduced order models. CFD simulations of the stationary semisubmersible in waves are also performed, and better agreement with results from HydroDyn is found, when radiation/diffraction dominate.

Finally, fluid-structure interactions (FSI) are simulated with CFD, where the structure moves due to fluid forces without prescribing motion. The semisubmersible platform is simulated in free decay tests as well as waves. The motion predictions from CFD are compared to experimental tank tests. Poor agreement was found when a loosely-coupled FSI method was employed. A more tightly-coupled FSI performed more accuarately for smaller test cases, and will be used for future simulations of the semisubmersible in free decay and wave simulations.

Statement of Contributions

This work provides a better understanding of the fundamental physics of flow around complex geometries in various flow conditions, which had not been previously examined. The high-fidelity CFD simulations performed in this dissertation assist in the verification of FAST, which was previously only verified and validated for land-based wind turbines. The contributions of this thesis are briefly summarized here.

Simulations of surface-piercing cylinders with free ends were simulated over a range of aspect ratios that had not been previously investigated. Additionally, this work included experimental measurements in the exact same flow conditions and cylinder dimensions as the numerical work, which also had not been done before. The predicted loads showed a dependency on the presence of the free surface, the free end and the length of the cylinder. This results of this part of the thesis suggest that selection of drag coefficients for input to CAE tools be carefully selected based on these geometric factors, and that coefficients be applied sectionally.

A stationary semisubmersible was simulated in various steady currents, and the previously held practice of selecting drag coefficients for CAE tools based on infinitely-long, fully-submerged cylinders was found to be inappropriate. The CFD simulations in this thesis used high-fidelity flow field visualizations to explain the fundamental flow around the complex geometry of the semisubmersible, and why predicted drag

coefficients vary greatly from what was previously expected. This work suggests that CFD be used to determine drag coefficients of complex geometries in order to achieve more accurate results from coefficient-based CAE tools.

The hydrodynamics module of FAST was verified for wave modeling, through code-to-code comparison of hydrodynamic load predictions from CFD and HydroDyn. While FAST had been previously verified and validated for land-based turbines, this work presents new verification work for offshore scenarios. The work in this thesis found good agreement between codes, indicating that the potential flow based solution in HydroDyn produces accurate load predictions in regular waves.

For the first time, simulations of slanted cylinders (matching the pitch angle of the cross braces of the semisubmersible) in varying yaw orientations were conducted. It was found that the orientation of the cylinder relative to the flow direction impacted the flow behavior and loading on the cylinder. Furthermore, it was observed that the drag was altered near the free-surface and bottom end. This work also suggests careful selection of drag coefficients, where now the effects of body orientation must be included.

Finally, this dissertation presents 6 DoF CFD simulations of the semisubmersible. Before now, 6 DoF simulations of the structure using the opensource CFD toolbox OpenFOAM have not included mooring lines, nor comparisons against experimental tank test data. The work in this thesis provide the first steps towards the unique three-way comparison of CFD predictions, CAE tool results and experimental tank test measurements of the semisubmersible. Further simulations of the semisubmersible in free-decay tests and regular waves will be carried out to supplement tank test data which omitted loads.

While much of this thesis focuses on the semisubmersible platform, the findings are extendable to other offshore structures and applications such that the impact of this work is great.

Thesis Outline

The dissertation begins with four chapters of background, setting the stage for hydrodynamic predictions from CFD and the comparison against other models and experimental data. The background chapters include a basic overview of water wave theory, ocean physics and wave-body interactions, and culminates in a discussion of finite volume methods with a review of the limited previous CFD research on offshore wind turbine platforms.

Validation of the CFD model is presented in Chapter 5, providing the necessary confidence to perform the work in the remaining chapters of the thesis. Loads on truncated, surface-piercing cylinders are investigated in Chapter 6, both with CFD and experimental water tunnel tests. A semisubmersible platform for floating offshore wind turbines is simulated in steady current and wave conditions, in Chapter 7 and 8, respectively. Loads on slanted cylinders in various orientations, representative of the cross-braces of the semisubmersible, are simulated and discussed in Chapter 9. Finally, the semisubmersible platform is revisited in Chapter 10, this time introducing 6 degree-of-freedom motion of the body in free-decay tests and regular wave conditions.

The dissertation concludes with a summary of the work, including the new contributions to knowledge, and direction of the future work.

CHAPTER 1

WATER WAVE THEORY

A basic understanding of wave modeling is the first component necessary for simulating the interaction of rigid bodies in the ocean. Before delving into ocean wave theory, a more fundamental treatment of basic water wave theory is given in this chapter. Both linear and non-linear wave theories are discussed here. This chapter concludes with a brief discussion of the regions of applicability for various wave theories. The discussion here is synthesized from more detailed texts on water wave theory and ocean dynamics, including work by Apel [11], Mei [137], Sarpkaya [201], Phillips [178], Lamb [118], Stoker [219], Whitham [252] and Crapper [33].

Waves vary over a wide range of spatial and temporal domains. In describing ocean waves, there are variety of physical mechanisms which act as restoring forces. These are categorized in Table 1. This work focuses largely on wind waves and swell, which are the primary waves types that affect the motion and loading on floating platforms of offshore wind turbines. These waves are referred to as surface gravity waves, or sometimes just surface waves. As a starting point, the basic equations of fluid motion are reviewed, followed by simplifications for irrotational and inviscid flows. Boundary conditions for interfacial and rigid impermeable boundaries are covered. Linearized equations for infinitesimal waves are derived, followed by a discussion of non-linear wave theories.

Table 1.1. Wave type classification table. Adapted from Mei. [137]

Wave Type	Physical Mechanism	Typical Period	Region of Activity
Sound	Compressibility	$10^{-2} - 10^{-5}$s	Ocean interior
Capillary ripples	Surface tension	$< 10^{-1}$s	Air-water interface
Wind waves and swell	Gravity	$1 - 25$s	
Tsunami	Gravity	10 min - 2 h	
Internal waves	Gravity and density stratification	2 min - 10 h	Layer of sharp density change
Storm surges	Gravity and Earth rotation	1 - 10 h	Near coastline
Tides	Gravity and Earth rotation	12 - 24 h	Entire ocean layer
Planetary waves	Gravity, Earth rotation and variation of latitude or ocean depth	$O(100days)$	

1.1 Fundamental Equations

Water density varies little over time and space in gravity wave problems, such that we can describe the motion of the fluid with the incompressible Navier-Stokes equations. First, mass conservation for incompressible flow is given by,

$$\nabla \cdot \mathbf{u} = 0 \tag{1.1}$$

The conservation of momentum is expressed as,

$$(\frac{\partial}{\partial t} + \mathbf{u} \cdot \nabla)\mathbf{u} = -\nabla(\frac{p}{\rho} + gz) + \nu\nabla^2\mathbf{u} \tag{1.2}$$

where $\mathbf{u}$ is the velocity vector in the x, y and z directions, p is pressure, ρ is the density, g is gravity, z upwards in is the vertical direction and ν is the viscosity.

Vorticity is defined as the curl of velocity ($\Omega = \nabla \times \mathbf{u}$). Taking the curl of the momentum equation results in an expression describing the evolution of the vorticity, shown below.

$$\left(\frac{\partial}{\partial t} + \mathbf{u} \cdot \nabla\right)\Omega = \Omega \cdot \nabla\mathbf{u} + \nu\nabla^2\Omega \tag{1.3}$$

In water, the viscosity is small, so a good approximation of the evolution of vorticity is given by,

$$\left(\frac{\partial}{\partial t} + \mathbf{u} \cdot \nabla\right)\Omega = \Omega \cdot \nabla\mathbf{u} \tag{1.4}$$

When the vorticity is zero ($\Omega = 0$) the flow is irrotational. For an inviscid, irrotational flow the velocity can be expressed as the gradient of a scalar function. The scalar function represented by ϕ is called the velocity potential. Using the vector identity $\nabla \times \nabla\phi = 0$, and plugging in $\nabla \times \mathbf{u} = 0$ for the case of irrotational flow, results in the velocity represented as the gradient of a scalar, ϕ.

$$\mathbf{u} = \nabla\phi \tag{1.5}$$

The velocity must still satisfy mass conservation, and for the case of incompressible flow it can be shown that the velocity potential obeys Laplace's equation.

$$\nabla^2\phi = 0 \tag{1.6}$$

Rewriting the momentum equation in terms of the velocity potential ϕ, for the inviscid, irrotational case gives,

$$\nabla\left[\frac{\partial\phi}{\partial t} + \frac{1}{2}|\nabla\phi|^2\right] = \nabla\left(\frac{p}{\rho} + gz\right) \tag{1.7}$$

Integrating the above equation once with respect to the space variables results in the unsteady Bernoulli equation, given by,

$$\frac{p}{\rho} = gz + \frac{\partial \phi}{\partial t} + \frac{1}{2}|\nabla \phi|^2 + c(t) \tag{1.8}$$

where $c(t)$ is some arbitrary function of time. The gz term gives the contribution from hydrostatics, while the remaining terms are the hydrodynamic contributions to the total pressure, p.

1.2   Boundary Conditions

To complete the set of governing equations, initial and boundary conditions are necessary. Initial conditions depend greatly on the specific problem under consideration, while boundary conditions depend on the physical domain of the problem. Two main classes of boundary conditions are considered here, which are rigid impermeable and interfacial boundaries. Rigid impermeable boundaries include the wetted surfaces of solid objects, and in this discussion are assumed to maintain their shape. Interfacial boundaries include the air-water interface, or other immiscible fluid interfaces, and can be thought more generally as deformable boundaries. In these cases it is assumed that there is no spray or mixing between the two fluids of consideration. Three main assumptions are made here: pressure is constant across the interface between two fluids, once a particle is on a free surface it remains there, and there is no flow through an impervious boundary.

For the case of rigid impermeable boundaries it is assumed that there is no fluid flow across the boundary. If the boundary is not only impermeable, but also fixed, then the normal component of the fluid velocity must vanish. A common example of this is at the sea floor. Mathematically, it is given by,

$$u_n = \mathbf{u} \cdot \hat{n} = 0 \tag{1.9}$$

where $\hat{n}$ is the unit normal to boundary, and u_n is the normal component of the fluid velocity.

This zero-flux boundary condition can also be expressed in terms of the velocity potential and is shown in the equation below.

$$\frac{\partial \phi}{\partial n} = \nabla \phi \cdot \hat{n} = 0 \qquad (1.10)$$

There are many examples of impermeable boundaries that move, including floating objects such as wind turbine platforms. We let $\mathbf{V}$ be the velocity of the moving object. In the simplest treatment, the normal component of the fluid velocity must equal the velocity of the moving surface.

$$u_n = \vec{u} \cdot \hat{n} = \mathbf{V} \cdot \hat{n} \qquad (1.11)$$

For potential flows, this boundary condition is given by,

$$\frac{\partial \phi}{\partial n} = \nabla \phi \cdot \hat{n} = \mathbf{V} \cdot \hat{n} \qquad (1.12)$$

It is shown that the case of a fixed impermeable boundary is just a special case of the moving impermeable boundary case.

Interfacial boundaries are deformable, as in the case of the air-water interface. Here both the velocity potential, ϕ, and the location of the free surface, η, must be determined. Since there are two unknowns, two boundary conditions are needed to close the system. First, the kinematic free surface boundary condition are derived, followed by the dynamic free surface boundary condition.

The kinematic condition states that any particle sitting on the free surface will remain there always. This can be treated mathematically by letting η be the free surface elevation above some equilibrium level z_0, so that the vertical coordinate of the particle on the free surface is given by,

$$z = z_0 + \eta(x, y, t) \qquad (1.13)$$

Using the assumption that a particle on the free surface will remain on the free surface always, leads to

$$\frac{D}{Dt}(z - z_0 - \eta) = 0 = \left(\frac{\partial}{\partial t} + u\frac{\partial}{\partial x} + v\frac{\partial}{\partial y} + w\frac{\partial}{\partial z} \right)(z - \eta) \qquad (1.14)$$

The z-coordinate is independent of x, y and t, so that leaves the differentiation of η. Following the rearrangement of terms, we arrive at the kinematic free surface boundary condition, shown below.

$$w = \frac{\partial \eta}{\partial t} + u\frac{\partial \eta}{\partial x} + v\frac{\partial \eta}{\partial y} \text{ at the free surface} \qquad (1.15)$$

For small amplitude problems it may become useful to make approximations for small fluid velocities or slopes. These approximations result in a simplified expression for the kinematic free surface boundary condition, given by,

$$w \cong \frac{\partial \eta}{\partial t} \qquad (1.16)$$

Now, we look at the dynamic free surface condition. A normal force is required to balance the pressure difference across the interface to prevent disrupting the surface. Surface tension provides this normal force. The surface tension is proportional to the curvature of the interface, or the inverse of the radius of curvature. Looking at a two dimensional case, the mathematical representation of the pressure and surface tension balance is given by,

$$p - p_a = \sigma \left(\frac{1}{R_x} + \frac{1}{R_y} \right) \qquad (1.17)$$

where σ is the surface tension, R_x and R_y are the radii of curvature in orthogonal directions and p_a is the pressure above the free surface. Curvatures are given ap-

proximately by the second derivative of the surface height. Upon replacement, the dynamic boundary condition becomes

$$p - p_a = \sigma \left(\frac{\partial^2 \eta}{\partial x^2} + \frac{\partial^2 \eta}{\partial y^2} \right) \tag{1.18}$$

For ocean waves, the wavelength is typically long enough that surface tension plays an insignificant role in the physics. When this is the case, the pressure above the free surface must match the pressure just below the surface. Bernoulli's equation on the free surface, given in Equation 1.8, is combined with the kinematic condition written in terms of the velocity potential, shown in Equation 1.19. The resulting equation for the dynamic free surface boundary condition is shown below, in Equation 1.20.

$$\frac{\partial \eta}{\partial t} + \frac{\partial \phi}{\partial x} \frac{\partial \eta}{\partial x} + \frac{\partial \phi}{\partial y} \frac{\partial \eta}{\partial y} = \frac{\partial \phi}{\partial z} \quad \text{on } z = \eta \tag{1.19}$$

Taking a total derivative of the Bernoulli equation, using the assumption that p_a is constant, and rearranging, produces the dynamic free surface boundary condition given below.

$$\frac{\partial^2 \phi}{\partial t^2} + g \frac{\partial \phi}{\partial z} + \frac{\partial}{\partial t} (\vec{u})^2 + \frac{1}{2} \vec{u} \cdot \nabla \vec{u}^2 = 0 \tag{1.20}$$

The resulting formula is non-linear, and still leaves the position of the free surface as an unknown. It is shown that the problem of water waves is nearly impossible to describe analytically. We are left to solve the Laplace equation, as discussed earlier, which is a linear equation. However, because the boundary conditions are non-linear it becomes a very difficult problem to solve. The following section examines approximations that can be made in an effort to find useful analytical solutions.

1.3 Linearized Wave Theory

As previously noted, waves exist in many forms, including regular and irregular, linear and non-linear, and progression in varying depths. This section discusses the

simplest possible type of wave, the linearized or small amplitude wave, which forms the basis for all other waves. The assumptions for linearized wave theory discussed here are that the wave is a two-dimensional, progressive gravity wave, with a constant period, height and length, traveling over a horizontal, smooth sea bed. Additionally, the wave is assumed to be inviscid, incompressible, irrotational with no temperature of salinity gradients, and is in the absence of wind and surface tension effects.

We begin with the Laplace equation discussed in Section 1.1, and three boundary conditions to describe the sea bed, and the kinematic and dynamic boundaries given in Equations 1.22, 1.23 and 1.24, respectively.

$$\nabla^2 \phi = 0 \tag{1.21}$$

$$\frac{\partial \phi}{\partial z} = 0 \text{ at } z = -h \tag{1.22}$$

$$\frac{\partial \eta}{\partial t} + \frac{\partial \phi}{\partial x}\frac{\partial \eta}{\partial x} - \frac{\partial \phi}{\partial z} = 0 \text{ at } z = \eta \tag{1.23}$$

$$\frac{\partial \phi}{\partial t} + \frac{1}{2}\left[\left(\frac{\partial \phi}{\partial x}\right)^2 + \left(\frac{\partial \phi}{\partial y}\right)^2\right] + g\eta = f(t) \text{ at } z = \eta \tag{1.24}$$

As was mentioned in the previous section, finding solutions to the Laplace equation with these non-linear boundary conditions is very difficult. To simplify this problem, assumptions are made in an effort to linearize the governing equations. Small amplitude wave theory assumes that the wave height is much smaller than the wave length and the water depth, and neglects non-linear terms. The kinematic and dynamic boundary conditions, given by Equations 1.23 and 1.24, in the problem statement then become

$$\frac{\partial \eta}{\partial t} - \frac{\partial \phi}{\partial z} = 0 \text{ at } z = \eta \qquad (1.25)$$

$$\frac{\partial \phi}{\partial t} + g\eta = 0 \text{ at } z = \eta \qquad (1.26)$$

Now, combining the kinematic (KBC) and dynamic boundary conditions (DBC) results in

$$\frac{\partial^2 \phi}{\partial t^2} + g\frac{\partial \phi}{\partial z} = 0 \qquad (1.27)$$

and

$$\eta = -\frac{1}{g}\left(\frac{\partial \phi}{\partial t}\right)\Big|_{z=0} \qquad (1.28)$$

Via separation of variables, the velocity potential and surface elevation are found to be

$$\phi(x, z, t) = \frac{gH}{2kc}\frac{cosh[k(z+h)]}{cosh(kh)}sin[k(x-ct)] \qquad (1.29)$$

$$\eta(x, t) = \frac{H}{2}cos(kx - \omega t + \psi) \qquad (1.30)$$

where g is gravity, H is wave height, k is wavenumber, c is wave speed, h is water depth and ω is the angular frequency of the wave. It is important to note that non-trivial solutions for the velocity potential, which satisfy the boundary conditions given above, only exist when the dispersion relation is satisfied. The dispersion relation which uniquely relates the wave number to the wave frequency for a given water depth is given below, and it a result of the KBC given in Equation 1.27.

$$\omega^2 = gk \ tanh(kh) \qquad (1.31)$$

15

Table 1.2. Summary of Linearized Wave Theory Characteristics.

Characteristic	Mathematical Representation
Linearized KBC	$\frac{\partial \eta}{\partial t} - \frac{\partial \phi}{\partial z} = 0$ at $z = \eta$
Linearized DBC	$\frac{\partial \phi}{\partial t} + g\eta = 0$ at $z = \eta$
Velocity Potential	$\phi = \frac{gH}{2kc} \frac{cosh[k(z+h)]}{cosh(kh)} sin(\omega t - kx + \psi)$
Surface Elevation	$\eta = \frac{H}{2} cos(kx - \omega t + \psi)$
Dispersion Relation	$\omega^2 = gk\ tanh(kh)$
Horizontal Particle Displacement	$\zeta_p = \frac{H}{2} \frac{cosh(k(z+h))}{sinh(kh)} sin(\omega t - kx + \psi)$
Vertical Particle Displacement	$\eta_p = \frac{H}{2} \frac{sinh(k(z+h))}{sinh(kh)} cos(\omega t - kx + \psi)$
Horizontal Particle Velocity	$u = \frac{gH}{2c} \frac{cosh[k(z+h)]}{cosh(kh)} cos(kx - \omega t + \psi)$
Vertical Particle Velocity	$w = \frac{gH}{2c} \frac{sinh[k(z+h)]}{cosh(kh)} sin(kx - \omega t + \psi)$
Pressure	$p = -\rho g z + \frac{1}{2}\rho g H \frac{cosh(k(z+h))}{cosh(kh)} cos(kx - \omega t + \psi)$

Table 1.3. Classifications for deep, intermediate and shallow water. [36]

Depth Classification	Range
Shallow	$h < \frac{1}{20}\lambda$
Intermediate	$\frac{1}{20}\lambda < h < \frac{1}{2}\lambda$
Deep	$\frac{1}{2}\lambda < h$

Simplifying assumptions can be made for shallow and deep water. In shallow water, as kh tends towards zero, the hyperbolic tangent of kh approaches kh, leaving the dispersion relation for shallow water as $\omega^2 \cong gk^2h$. For deep water, kh approaches infinity, and the hyperbolic tangent goes to one. The dispersion relation for deep water then simplifies to $\omega^2 \cong gk$.

The determination of the velocity potential, surface elevation and dispersion relation provides enough information for the calculation of numerous other physical quantities relating to linearized wave theory. A sample of physical quantities are outlined below, and a summary of linearized wave theory characteristics are provided in Table 1.2.

The pressure is found by plugging the solution for the velocity potential into the unsteady Bernoulli equation. Keeping the initial assumption to neglect non-linear terms, the Bernoulli equation is simplified by dropping the second order term. The resulting expression for the pressure is

$$p(x, z, t) = \rho gz + \frac{1}{2}\rho gH \frac{cosh[k(z+h)]}{cosh(kh)} cos(kx - \omega t + \psi) \tag{1.32}$$

It is straightforward to determine the velocities in the x and y-directions by differentiating the velocity potential. The equations for the horizontal and vertical components of velocity are given below.

$$u(x, z, t) = \frac{gH}{2c} \frac{cosh[k(z+h)]}{cosh(kh)} cos(kx - \omega t + \psi) \tag{1.33}$$

$$w(x, z, t) = \frac{gH}{2c} \frac{sinh[k(z+h)]}{cosh(kh)} sin(kx - \omega t + \psi) \tag{1.34}$$

An expression for particle displacement follows from the calculation for particle velocities in the vertical and horizontal directions. Letting ζ_p be the particle displacement in the horizontal direction and η_p the particle displacement in the horizontal direction, and using the relations $u = \frac{\partial \zeta_p}{\partial t}$ and $v = \frac{\partial \eta_p}{\partial t}$, produces

17
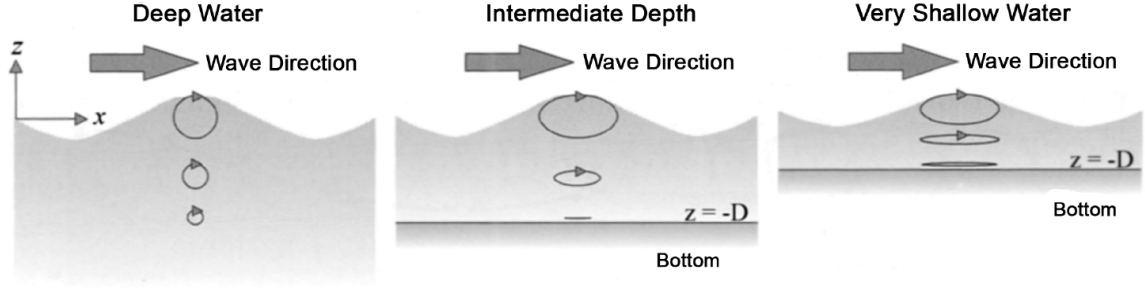
Figure 1.1. Particle orbital paths which vary depending on water depth. From Faizal, et al [48].

$$\zeta_p(x, z, t) = \frac{H}{2} \frac{cosh[k(z + h)]}{sinh(kh)} sin(\omega t - kx + \phi) \tag{1.35}$$

$$\eta_p(x, z, t) = \frac{H}{2} \frac{sinh[k(z + h)]}{sinh(kh)} cos(\omega t - kx + \phi) \tag{1.36}$$

The particles follow elliptical clockwise orbits in progressive gravity waves. The shape of the elliptical path depends on the depth of the water, as can be seen in the equations for particle displacements and velocities. The horizontal particle displacement and velocity decreases with depth following $cosh[k(z+h)]$. In a similar fashion, the vertical displacement and velocity decrease with $sinh[k(z + h)]$. The profiles of the particle paths in shallow, intermediate and deep water are illustrated in Figure 1.1. Classifications for shallow, intermediate and deep water are given in Table 1.3.

1.4   Non-linear Waves

Next, non-linear wave theories are discussed. A sample of non-linear wave theories are presented here, including Stokes, cnoidal and solitary waves. Fundamental differences between linear and non-linear solutions are highlighted. Following the discussion of these wave theories, a diagram is given to outline the regions of applicability of various wave theories.

1.4.1 Stokes Theory

In 1847 Stokes published a paper on non-linear gravity wave theory using perturbation analysis to find approximate solutions for periodic progressive waves of permanent form in intermediate and deep water [220]. He made the important finding that periodic wavetrains are possible in a non-linear system, and also that the wave speed depends on wave amplitude, unlike in the case for linear waves. Stokes waves often serve as the basis for irregular wave modeling, and are seen in later discussions of ocean wave modeling.

Analysis begins with the potential flow formulation previously discussed, starting with the Laplace equation and boundary conditions for the seabed, kinematic and dynamic free-surface. First, the free-surface conditions are expressed as a Taylor series expansion about a constant free surface elevation. For convenience and without loss of generality let the constant elevation be chosen as $z = 0$, which also ensures the expansion is done in proximity of the actual free surface elevation. Levi Civita proved the convergence of the series for small amplitude, steady wave motion [124]. The Taylor series expansion about $z = 0$ applied to the free surface boundary condition given in Equation 1.20, returns the expression

$$
\begin{aligned}
\left[\frac{\partial^2 \phi}{\partial t^2} + g\frac{\partial \phi}{\partial z}\right]_0 &+ \eta\left[\frac{\partial}{\partial z}\left(\frac{\partial^2 \phi}{\partial t^2} + g\frac{\partial \phi}{\partial z}\right)\right]_0 + \left[\frac{\partial}{\partial t}(\vec{u})^2\right]_0 + \\
&\frac{1}{2}\eta^2\left[\frac{\partial^2 \phi}{\partial z^2}\left(\frac{\partial^2 \phi}{\partial t^2} + g\frac{\partial \phi}{\partial z}\right)\right]_0 + \eta\left[\frac{\partial^2 \phi}{\partial z^2}(\vec{u}^2)\right]_0 + \\
&\left[\frac{1}{2}\vec{u}\cdot\nabla\vec{u}^2\right]_0 + ... = 0
\end{aligned}
\tag{1.37}
$$

Next, perturbation analysis is applied. Let $\epsilon = ka << 1$, so that we can expand η as

$$
\eta = \epsilon\eta_1 + \epsilon^2\eta_2 + \epsilon^3\eta_3 + ...
\tag{1.38}
$$

and let ϕ and u be expanded likewise. Substitution of these expansions into the Laplace equation and the three boundary conditions which have been expanded about $z = 0$, results in different ordered approximations to the solution of the non-linear wave problem. The first order approximation returns the linearized solution discussed in the previous section. The second order approximation is found by equating terms which are proportional to ϵ^2. It is found that ϕ_2 satisfies the Laplace equation and the seabed boundary condition. The dynamic and kinematic free surface boundary conditions can be written, but are omitted here. Higher order approximations can also be carried out, which grow in complexity and contain more terms as their order increases.

Following the Taylor series expansion of the boundary conditions and the perturbation analysis, we can apply these results to the case of progressive waves of permanent form. Due to the assumption of permanence of the wave, it follows that the wave has constant speed, and the solution for the surface of the wave must contain only combinations of the term $(x - ct)$, where c is the phase velocity or wave celerity. Using the assumptions of periodicity and symmetry, the wave height can be represented as a Fourier series of the term $(x - ct)$,

$$\eta = \sum_{n=1}^{\infty} A_n cos(n(x - ct)) \tag{1.39}$$

The wave heights for Stokes first and second order waves, respectively, are shown in the equations below.

$$\eta = Acos(kx - \omega t + \psi) \tag{1.40}$$

$$\eta = Acos(kx - \omega t + \psi) + \frac{H^2}{2L} \frac{cosh(kh)(2 + cosh(2kh))}{sinh^3(kh)} cos(2(kx - \omega t + \psi)) \tag{1.41}$$

20

A few important changes in the features of the waves due to non-linear approximations should be noted. The non-linear effects cause more peaked crests and shallower troughs, which more closely match the profiles of surface gravity waves. These changes are illustrated in Figure 1.2 below. Additionally, the wave speed now depends on both the amplitude of the wave as well as the wavelength. Finally, particle paths are no longer strictly elliptical, but now the particles travel in unclosed paths. This effect is known as Stokes drift, and it causes the particle orbits to translate over time.
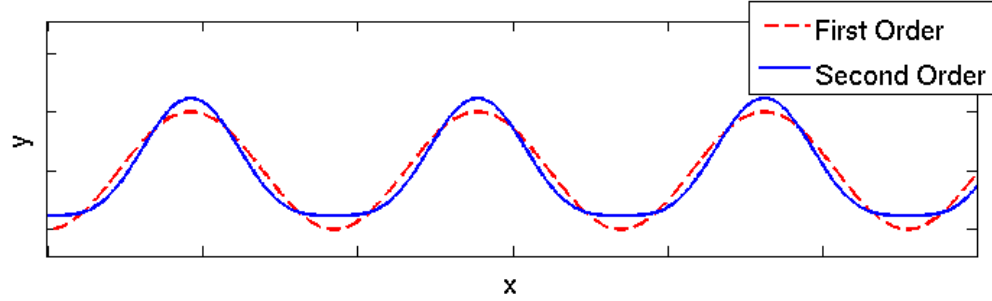
Figure 1.2. The surface elevation for first and second order Stokes waves. The second order waves demonstrate the non-linear effects of more peaked crests and shallower troughs.

1.4.2 Cnoidal Theory

In 1895 the Korteweg-deVries (KdV) equation was presented with the derivation of a nonlinear, exact solution called the cnoidal wave [112]. Cnoidal waves represent surface gravity waves with long wavelength to water depth ratios. These waves are often seen in ocean swells, and are marked by sharp crests and very shallow troughs.

The KdV equation in dimensional form is shown below,

$$\frac{\partial \eta}{\partial t} + c_0 \frac{\partial \eta}{\partial x} + \frac{3c_0}{2h} \eta \frac{\partial \eta}{\partial x} + \frac{c_0 h^2}{6} \frac{\partial^3 \eta}{\partial x^3} = 0 \tag{1.42}$$

where $c_0 = \sqrt{gh}$ and depth $d = h + \eta$. The solution for the surface elevation is

$$\eta(x,t) = \eta_2 + H cn^2 \left(\frac{x - ct}{\Delta} \Big| m \right) \tag{1.43}$$

where η_2 is the trough elevation, H is the wave height, c is the phase speed and cn is the Jacobi elliptic function. Without familiarity with elliptic functions, it suffices to acknowledge that cn is a periodic function. Thus, the solution returns a periodic wave train.

1.4.3 Solitary Wave Theory

In the limit of infinite wave length, the KdV equation discussed in the previous section gives a solution in the form of a solitary wave. Solitary waves were first observed and reported by Scott Russell in 1844 [208], and expressions describing this phenomenon were later developed by Boussinesq and Rayleigh, in 1871 and 1876, respectively [252]. Solitary waves consist of a single peak which maintains its form and speed as it progresses. Solitary waves are sometimes referred to as solitons, a term which was coined by Zabusky and Kruskal in 1965 [265]. An excellent review of equations which admit solitary wave solutions, and important applications of these waves, is given by Scott, et al [207]. It should be noted that while a variety of equations admit solitary wave solutions, the Navier-Stokes equations do not. A comprehensive review of solitary waves can also be found in the work of Miles [144]. Sun provides a discussion the non-existence of solitary waves in water with small surface tension [226].

The surface height of a solitary wave is expressed as,

$$\eta = \frac{H}{(cosh(\sqrt{\frac{3H}{4h^3}}(ct - \vec{x}))^2}$$

and the wave speed is given by,

$$c = \sqrt{g(H + h)} \tag{1.44}$$

where as before, H is the wave height, h is the water depth, g is gravity and $\vec{x}$ is the direction of the progressing wave.

1.5   Breaking Waves

Largely, wave breaking occurs due to wave crests becoming unstable. Many theories have been proposed to quantify wave breaking, including approaches based on wave steepness and acceleration. Breaking waves consist of the formation of a spilling region in front of the wave crest. Trailing behind the breaking wave is a turbulent wake in which the intensity decreases with distance from the wave crest. White-capping occurs because of air entrainment for particularly intense breaking waves.

Both Stokes and Michel came up with limiting configuration theories for breaking waves in 1880 and 1893, respectively [220] [139]. Stokes's breaking wave criteria included that the particle velocity at the wave crest equal the phase velocity, the wave crest reach a sharp angle of 120°, a wave height to wave length ratio of 1/7, and a particle acceleration of $0.5g$ at the wave crest [220]. Based on a limiting steepness criterion, Michel showed in 1893 that waves break when wave heights are greater than or equal to $0.027gT^2$ [139]. This was confirmed experimentally by Ochi and Tsai who found the empirical criterion $H \geq 0.020gT^2$ [161].

Later work by Longuet-Higgins gave a calculation demonstrating wave breaking at much smaller amplitudes than previously theorized [126]. An acceleration based criterion was proposed by Phillips that stated breaking would occur when the downward acceleration exceeded gravity [177]. Longuet-Higgins showed that white-capping occurs theoretically when the downward acceleration in all directions is within the Stokes 120° angle. Longuet-Higgins also derived that instabilities in regular waves occur when the wave steepness, ka, approaches 0.436. Rewriting this statement in terms of wave height gives $H = 0.022gT^2$ which is in good agreement with the work done by Michel and confirmed by Ochi and Tsai, mentioned earlier.

Wave breaking is classified into two types. Type I breaking occurs where the wave excursion (ξ_A) crosses the zero surface height line. Type II breaking takes place where the wave excursion (ξ_B) is above the zero line. An illustration of the two types of wave breaking is shown in Figure 1.3 below.
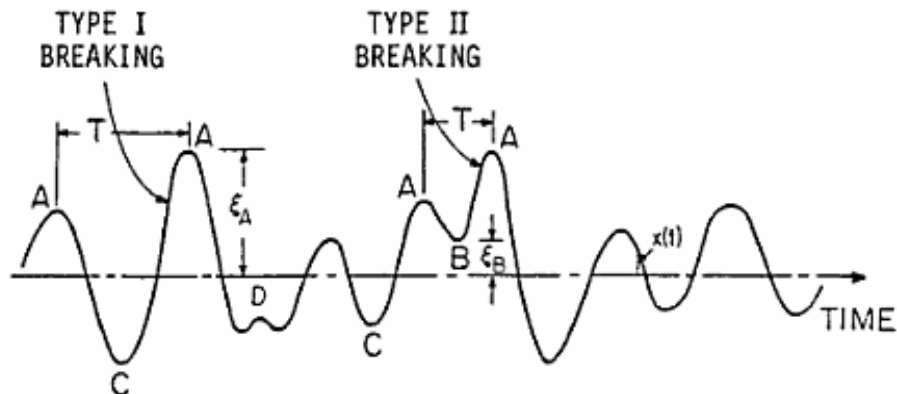
Figure 1.3. Type I and Type II wave breaking diagram by Ochi [160].

1.6 Regions of Wave Applicability

A variety of classic wave approximations have been discussed in this chapter. Understanding the limits of validity of each wave theory is important when selecting which equations to use. LeMéhauté compiled a useful diagram demonstrating the approximate regions of applicability, and is shown in Figure 1.4 [120]. The vertical axis shows the non-dimensionalized wave height plotted against the non-dimensionalized water depth on the horizontal axis. It is demonstrated that cnoidal theory is valid in regions of small wave height and water depth. In deeper water, linear wave theory is valid for small wave heights. As wave height grows, Stokes theory becomes applicable and the order of approximation grows with wave height. A line for breaking wave criteria is shown which bounds all the theories.

24
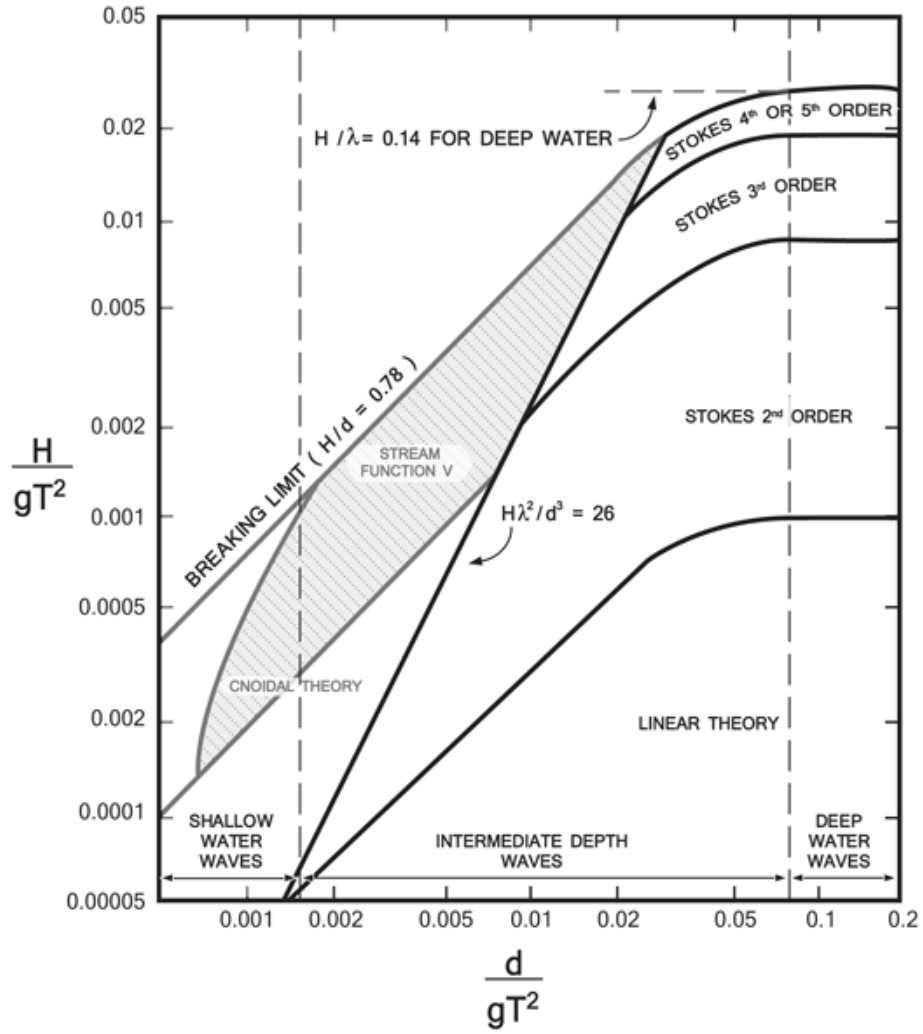
Figure 1.4. Approximate regions of applicability for different wave theories, depending on wave height and water depth, from LeMéhauté [120].

CHAPTER 2

OCEAN PHYSICS

The previous chapter treated waves as a deterministic process. In reality, the surface of the ocean is composed of waves of many different parameters. The instantaneous sea surface can be described as the summation of deterministic waves if they act independently and interact weakly. The profiles of wind-generated waves vary continuously over space and time in an irregular fashion. The description of the sea cannot be described on a single wave basis, but must be treated stochastically. Evaluation of statistical properties of waves can be done through frequency and probability domains. Waves in deep water follow a Gaussian distribution for their wave heights, while shallow water wave heights are non-Gaussian, but nonetheless can be described with a theoretical probabilistic distribution. The sea can be classified into ten sea states which increase with the significant wave height. The sea state classifications are shown in Table 2.1. This chapter begins with a discussion of the generation of ocean surface waves by wind. Spectral representation is covered, and commonly used ocean wave spectra are presented in some detail.

2.1 Ocean Wave Generation

Wind generated waves include both capillary and gravity waves. Capillary waves are ripples, where surface tension acts as the restoring force. Gravity waves are also wind driven, but as the name suggests, gravity acts as the restoring force. Gravity waves affect the motion and forcing on offshore structures. Therefore the discussion of wind generated ripples, or capillary waves is omitted here, but an excellent source

Table 2.1. Sea States. Adapted from the UK Meteorological Office Fact Sheet [1].

WMO Sea State Code	Significant wave wave height (m)	Characteristics
0	0	Calm (glassy)
1	0 to 0.1	Calm (rippled)
2	0.1 to 0.5	Smooth (wavelets)
3	0.5 to 1.25	Slight
4	1.25 to 2.5	Moderate
5	2.5 to 4	Rough
6	4 to 6	Very rough
7	6 to 9	High
8	9 to 14	Very high
9	Over 14	Phenomenal

on the topic can be found in G.I. Taylor's paper from 1940 [233]. A diagram of wave types with increasing wave period is demonstrated in Figure 2.1. The figure illustrates that capillary and gravity waves are wind generated, while other waves are generated by earthquakes, storms and planetary movement.

Phillips gives a comprehensive discussion on the generation of waves by wind in his text [178], which is summarized briefly here. Capillary waves are generated at the surface at very low wind speeds. These waves grow in space and time, until the wavelengths and amplitudes are large enough to categorize these waves in the gravity range, where the waves are on the order of centimeters. Once in the gravity range, continued growth is driven by forcing from wind pressure on the steep slopes of the waves. Additionally, shear stress from turbulent wind eddies, as well as tangential surface stress from the air spur further wave growth. Non-linear wave-wave interaction causes both smaller and larger waves to be formed. The generation of waves depends on the duration of the blowing wind as well as the distance from shore, or fetch. Additional details on the generation and growth mechanisms of waves by wind can be found in Jeffreys [87] [88], Miles [140–143], Sverdup and Munk [229], and Pierson [255].
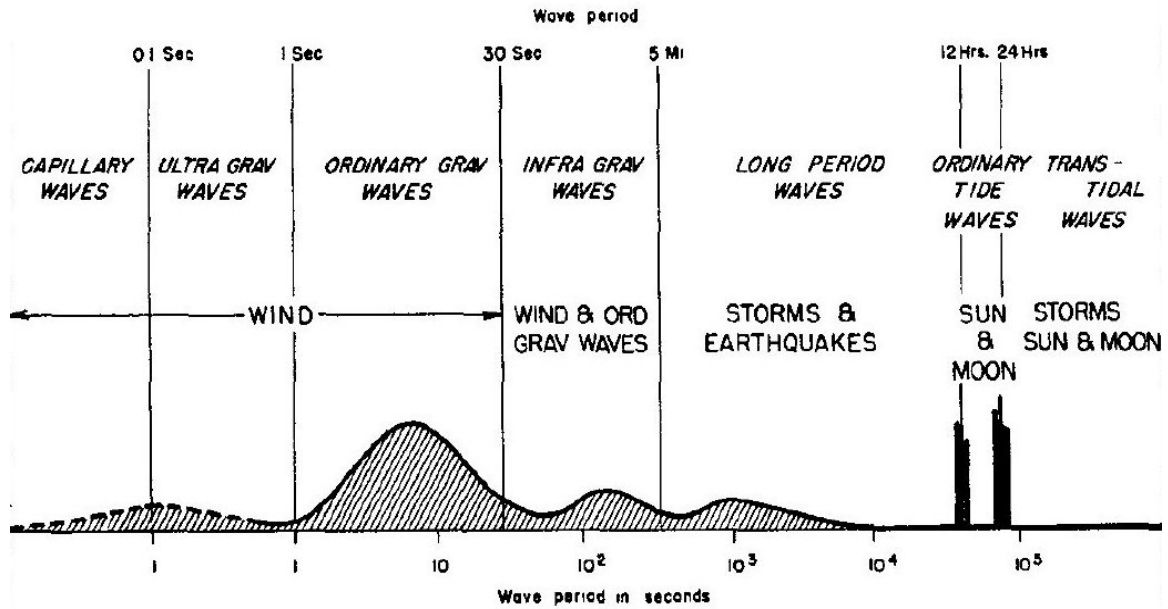
Figure 2.1. Waves classified by wave period from Munk [150].

2.2 Random Waves

Profiles of wind generated ocean waves vary randomly in both space and time. The wave height as well as period vary randomly in time. Randomly changing waves must be considered as a stochastic process in order to evaluate wave properties in frequency and probability domains. Only statistical measures can be used as significant wave characteristics or predictive parameters. Because of the random behavior of ocean waves, it is necessary to understand the both probabilistic aspects of waves and the spectral representation of ocean wave characteristics.

In deep water, waves heights are Gaussian random processes, which has been demonstrated from collected measurements of ocean waves [160]. However, in shallow water the wave heights do not follow a Gaussian random process, but can still be described with alternative theoretical probability distributions. Random seas are generally due to energy transfer between waves and wind. Variations in wave properties can be attributed to variation in the wind. In the case of swell, waves with small

28

wavelengths lose energy as they travel through space, causing less irregular waves to form over time.

The irregular surface height of ocean waves can be expressed by an infinite sum of sinusoidal wave components with differing wavenumbers (k), frequencies (f or ω) and directions (θ). These wave properties must be representative of the ocean state, which can determined by examining wave spectra.

To describe the surface of the ocean we begin with the profile of simple harmonic waves, which can be expressed as

$$\eta(x,y,t) = a\cos\left\{\frac{\omega^2}{g}(x\cos(\theta) + y\sin(\theta) - \omega t + \psi)\right\} \tag{2.1}$$

where a is the wave amplitude, ω is the wave frequency and ψ is the phase. Now, we consider the random sea as a superposition of an infinite number of sine waves with different amplitudes a_j, directions θ_j and frequencies ω_j. The profile of the random wave is written as,

$$\eta(x,y,t) = \sum_j a_j\cos\left\{\frac{w_j^2}{g}[x\cos(\theta_n)x + y\sin(\theta_n)y - \omega_j t + \psi_j]\right\} \tag{2.2}$$

Then, a spectrum that represents the contributions to the variance due to component waves with different speeds, frequencies and directions can be adopted. The potential and kinematic energy of waves can be represented with a spectral density function, otherwise known as a wave spectrum. The magnitude of the time averaged wave energy as a function of wave frequency is given in the spectral density function. The area under the spectral energy function gives the degree of sea severity. A very common measure of sea severity is given by the significant wave height, H_s or $H_{1/3}$, which is the average of the largest one-third of ocean waves. Sverdrup and Munk first introduced the term significant wave height in their discussion of random ocean

29

waves in 1947 [229]. H_s is equal to four times the square root of the area under the spectral density curve. These spectra are discussed in more detail in the next section.

2.3 Spectral Representation

Wave spectra allow for the probabilistic prediction of wave properties. A few basic assumptions are usually made, including that waves are steady-state, ergodic random processes, which are also Gaussian random processes. An ergodic process is one in which the statistics of an ensemble of time histories can also be determined from a single sample. Additionally, it is assumed that the spectra are narrow banded, that is, a sharp concentration exists around a specific frequency. Finally, wave peaks and troughs are statistically independent [160].

We begin the mathematical discussion of wave spectra by defining the auto-correlation of a signal, $x(t)$, which is given below.

$$R_{xx}(\tau) = \lim_{T \to \infty} \frac{1}{2T} \int_{-T}^{T} x(t)x(t + \tau)dt \qquad (2.3)$$

The auto-correlation is a measure of how similar a function is to itself at some shifted time τ.

The time average of wave energy can be found by evaluating R_{xx} at $\tau = 0$, as is shown below.

$$R_{xx}(0) = \lim_{T \to \infty} \frac{1}{2T} \int_{-T}^{T} \{x(t)\}^2 dt = \bar{P} \qquad (2.4)$$

To express the average energy in terms of wave frequency, ω, we can apply Parseval's theorem:

$$\int_{-\infty}^{\infty} x(t)^2 dt = \frac{1}{2\pi} \int_{-\infty}^{\infty} |X(\omega)|^2 d\omega \qquad (2.5)$$

where $X(\omega)$ is the Fourier transform of $x(t)$,

$$X(\omega) = \int_{-\infty}^{\infty} x(t)e^{-i\omega t} dt \qquad (2.6)$$

Using Equation 2.4 with Parseval's theorem, the average wave energy can be expressed as

$$\bar{P} = \lim_{T \to \infty} \frac{1}{4\pi T} \int_{-\infty}^{\infty} |X_t(\omega)|^2 d\omega \tag{2.7}$$

where it is now a function of wave frequency, ω.

The spectral density function of random waves $x(t)$ is then defined as,

$$S_{xx}(\omega) = \lim_{T \to \infty} \frac{1}{2\pi T} |X(\omega)|^2 \tag{2.8}$$

Now, the time average of wave energy can be written as

$$\bar{P} = \frac{1}{2} \int_{-\infty}^{\infty} S_{xx}(\omega) d\omega = \int_{0}^{\infty} S_{xx}(\omega) d\omega \tag{2.9}$$

where simplifications have been made because the spectral density function is an even function. The relationship above shows that the area under the spectral density function represents the average wave energy.

The Wiener-Khintchine theorem says that for a weakly steady-state wave, the auto-correlation and the spectral density functions are Fourier pairs [160]. The result is the often given relationship between the auto-correlation and spectral density, shown here.

$$S_{xx}(\omega) = \frac{1}{\pi} \int_{-\infty}^{\infty} R_{xx}(\tau) e^{-i\omega t} d\tau \tag{2.10}$$

$$R_{xx}(\tau) = \frac{1}{2} \int_{-\infty}^{\infty} S_{xx}(\omega) e^{-i\omega t} d\omega \tag{2.11}$$

This result is important because it relates the auto-correlation in the time domain to the spectral density function defined in the frequency domain.

The discussion above can be summarized into a few steps, and is presented as a single relationship, shown below. We began with a wave record $x(t)$, and assumed it to be a steady-state, ergodic random process. The auto-correlation function was

defined as $R_{xx}(\tau)$, given in Equation 2.3. The average of wave energy $\bar{P}$ was defined as $R_{xx}(0)$, which also gives the variance of the waves. Via Parseval's theorem, taking the Fourier transform of the auto-correlation returned the spectral density function. Finally, the Wiener-Khintchine theorem related the spectral density function in the frequency domain to the auto-correlation defined in the time domain. The previous equations can be summarized as the following relationship:

$$\int_0^\infty S_{xx}(\omega)d\omega = \bar{P} = R_{xx}(0) = \text{Variance}[x(t)] \tag{2.12}$$

Minkenberg, et al, examined the effects of regular and irregular waves sampled from a wave spectrum on the motions of offshore structures [147]. The regular waves used in their analysis had equivalent statistical properties to the irregular sea. It was found that the results calculated with the regular wave concept yielded erroneous results. The work concluded that spectral analysis techniques return more realistic results and should be used when modeling ocean physics.

2.4   Commonly Used Wave Spectra

To accurately predict the linear and non-linear responses of structures in marine environments, wave spectra representing a variety of desired sea states are needed. Predictions of responses of marine structures, including motions, moments and forces, rely on the accurate modeling of random seas. Many spectral formulations have been developed since the 1950s to describe sea states. Two of the most commonly used spectra are discussed here. Both the Pierson-Moskowitz and JONSWAP spectra were developed based on analyses of measured data from the ocean.

Pierson and Moskowitz analyzed measured wave data taken by accelerometers on British weather ships in the North Atlantic in 1964 [180]. Only data taken in fully developed seas were used in the analysis. A fully developed sea is reached at

the point of energy saturation in which there is a balance between the rate at which energy is gained from wind and lost by breaking or non-linear wave interaction. It was assumed that if the wind blew steadily over a long period of time and large area that waves would come into equilibrium with the wind, thus producing a fully developed sea. Five dimensionless spectra based on different wind speeds between 20 and 40 knots were produced, and an average of these was taken to find a general spectral formulation. The Pierson-Moskowitz spectrum is

$$S(\omega) = \frac{Ag^2}{\omega^5} exp\left[-B\left(\frac{\omega_0}{\omega}\right)^4\right] \tag{2.13}$$

where ω is the wave frequency, $A = 8.10x10^{-3}$, $B = 0.74$, $\omega_0 = g/U_{19.5}$, and $U_{19.5}$ is the wind speed measured at 19.5m above the sea surface. The Pierson-Moskowitz spectrum depends only on wind speed.

In 1968 and 1969 measurements were taken by the Joint North Sea Wave Project (JONSWAP) on a 160km line in the North Sea. Analysis of the measured data was conducted by Hasselmann, providing a new spectrum for wind generated waves in fetch limited seas [71]. It was found that the wave spectrum is never fully developed. The waves continue to develop as a result of non-linear interactions over long times and distances. The JONSWAP spectrum is a modification to the Pierson-Moskowitz spectrum to account for fetch, resulting in a sharper peak. The JONSWAP spectrum depends on wind speed as well as fetch. The spectrum is given by,

$$S(\omega) = \frac{\alpha g^2}{\omega^5} exp\left[-1.25\left(\frac{\omega_m}{\omega}\right)^4\right] \gamma^a \tag{2.14}$$

where,

$$a = -\frac{(\omega - \omega_m)^2}{2(\sigma\omega_m)^2} \tag{2.15}$$

and where the values for constants were determined from analysis of the collected data, and are listed below,

$$\gamma = 3.3$$

$$\alpha = 0.07\bar{x}^{-0.22}$$

$$\sigma = 0.07 \text{ for } f \leq f_m \text{ and } 0.09 \text{ for } f > f_m$$

$$\omega_m = 7\pi(g/\bar{U})\bar{x}^{-0.33}$$

$$\bar{x} = \text{ dimensionless fetch } = gx/\bar{U}^2 \qquad (2.16)$$

$$x = \text{ fetch length}$$

$$\bar{U} = \text{ mean wind speed}$$

$$g = \text{ gravity}$$

The γ term is called the peak enhancement factor. Analysis of the original data produces a peak-shape parameter value between 1 and 6, where γ is a random variable with a normal distribution. Generally the value is taken to be 3.3, which is the mean value taken from the normal distribution of γ. The α term specifies the growth of waves with distance, distinguishing the JONSWAP spectrum from the Pierson-Moskowitz spectrum. Furthermore, the ω_m term in the JONSWAP spectrum also relies on the dimensionless fetch. To demonstrate the differences between the two commonly used wave spectra, a plot of the two spectra is shown in Figure 2.2. The increased peakedness of the JONSWAP spectrum should be noted.
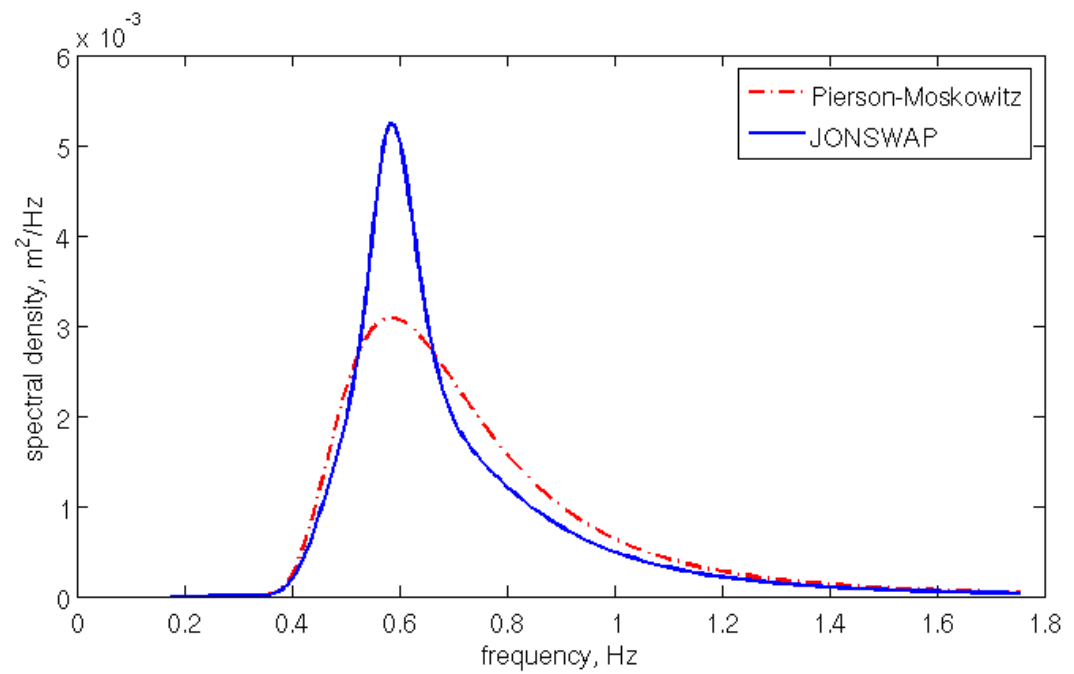
Figure 2.2. The Pierson-Moskowitz and JONSWAP spectra. Both spectra shown here have a significant wave height of 0.475 meters and peak spectral period of 4 sseconds.

CHAPTER 3

WAVE-BODY INTERACTION

This chapter addresses the physical characteristics of time dependent flow around and interacting with bodies. Idealizations and simplifications are made in an effort to describe the physics in a straightforward manner. The physics of fluid loading and the dynamic response of offshore structures is presented mathematically, and in some places empirical data are provided for better understanding. A table of important non-dimensional quantities is provided below, and is referred to throughout this chapter.

Table 3.1. Important non-dimensional numbers relating to fluid-structure interactions.

Dimensionless Number	Formula	Physical Significance
Reynolds	$Re = \frac{UD}{\nu}$	Characterize laminar and turbulent flow regimes
Froude	$Fr = \frac{U}{gL}$	Resistance of bodies moving through fluid
Keulegan-Carpenter	$KC = \frac{U_m T}{D}$	Compares the drag coefficient to inertial forces

First, static loads are discussed, which includes hydrostatics, gravity and current. Next, dynamic loads are presented. Wave loads are considered for small and large bodies. Radiation and diffraction in the context of linearized hydrodynamics are presented. A discussion of the effects of added mass in fluid-structure interactions is given next. Finally, the chapter concludes with a review of recent research efforts

in understanding offshore structures in the ocean. The next chapter presents a finite volume approach to modeling the loading and dynamic responses of structures in the ocean.

3.1 Static Loads

3.1.1 Gravity and Hydrostatics

We begin the discussion of fluid forces acting on a body with the simplest case possible, that of a body at rest. The structure experiences hydrostatic pressure acting normal to the submerged portion of its surface. The forces resulting from the hydrostatic pressure in the vertical direction are balanced by the gravitational force acting on the mass of the structure. The net force is zero for a structure in static equilibrium. This simple case is represented mathematically below.

$$F_{pressure} + F_{weight} = 0 \tag{3.1}$$

3.1.2 Current Loads

Current is mainly the result of wind blowing across the surface, pressure variations in the atmosphere and tides. Currents alter the shape and size of waves. Under the wave crest the current is stretched, and is compressed under a wave trough. Stretching formulas can be applied to better model the shape and size of waves in the presence of a current. A good reference on adjusting wave formulations in the presence of current can be found in Chakrabarti's text on offshore engineering [26].

Current is generally assumed to be time invariant, and despite being turbulent in most cases, it is often approximated by a mean value. While current may be considered constant in time, it cannot be approximated as constant in space where it may vary with water depth. Pressure distributions on the structure are induced by the current, which generate drag forces in the direction of the flow. These pressure distributions may not be symmetric about the structure due to vortex shedding.

Hogben and Standing summarized the effects of currents on large structures into three modes [74]. These include a modification to the wave speed which depends on the magnitude of the current, a drag force which can be treated by Morison's equation and lastly wave-making resistance. The latter involves the waves which are produced upon impact with a surface piercing body. Potential flow calculations can be carried out to model these effects.

3.2   Dynamic Loads

3.2.1   Wave Loads

Interaction of waves with solid bodies includes the effects of reflection, refraction and diffraction. Refraction accounts for the bending or turning of waves when passing between two mediums or fluids of differing densities. Diffraction covers the effect of scattering waves upon impact with an impermeable boundary. Radiation is also discussed, which treats the loads due to waves generated by a moving body. The shape, dimensions and relative motion of the body affects the magnification of these factors.

In wave-body interactions distinction must be made between small and large bodies. The character of the interaction differs significantly depending on the size of the body. Distinction between small and large bodies can be made by comparison between the size of the structure, D, and characteristic wavelength, $\lambda = 2\pi/k$, and wave amplitude, A. For small kD and a large value of A/D, the body is considered small. In this regime vortex shedding and flow separation dominate. Diffraction is insignificant for small bodies, as the bodies do not significantly alter the wave field. When kD is greater than order one, and A/D is small, diffraction is important and separation is insignificant [136]. A short discussion of small body interaction with the fluid is discussed here, followed by a more in depth discussion of large bodies interactions with the flow. An approximate mapping of the dominant loading regimes in

terms of wave height, structure diameter and water depth is provided in Figure 3.1 below. The figure represents a very specific set of conditions and should not be used as a general design guideline, but rather gives an idea for how wave and structure sizes influence the character of their interaction.
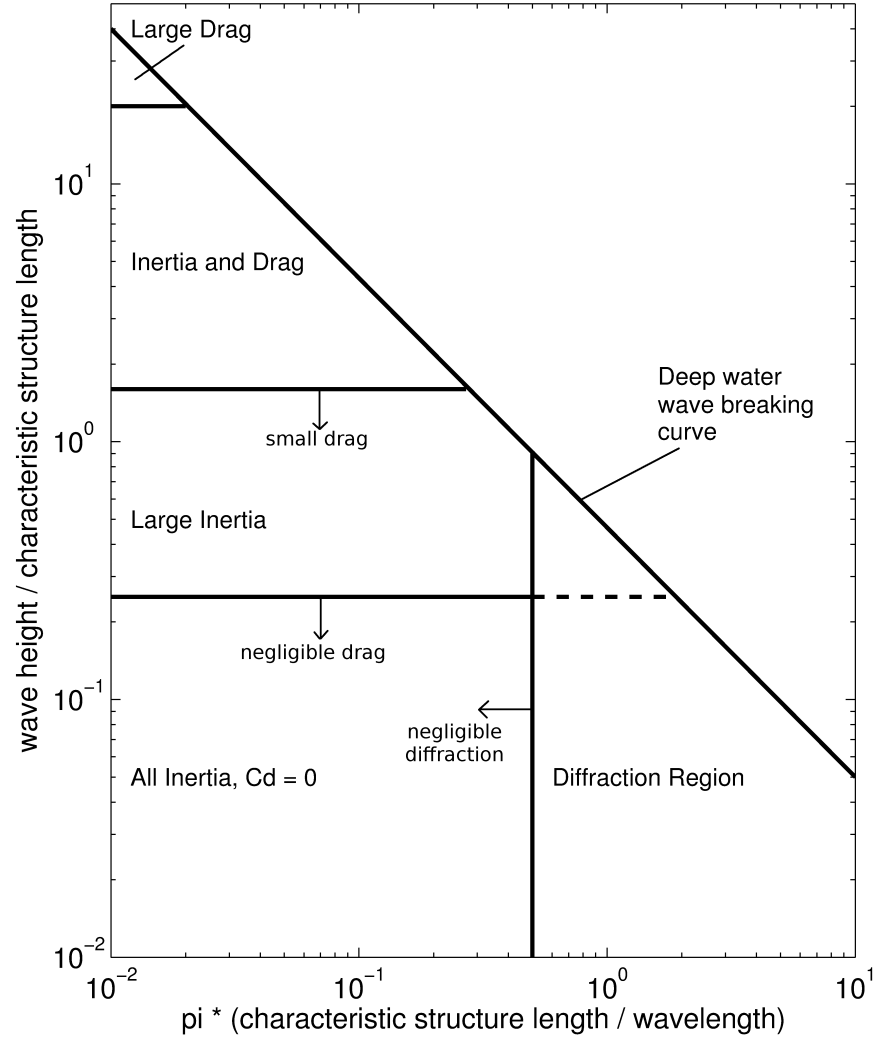
Figure 3.1. Classification of small versus large structures and their limits of applicability. The vertical axis shows H/D which is equivalent to the Keulegan-Carpenter number. The horizontal axis is the diffraction parameter, $\pi D/L$ [26]

The exact boundaries for the regimes where inertial, diffraction, drag and wave-breaking dominant are somewhat nebulous, but can be categorized in a general sense as shown in Table 3.2, which is for the case of a circular cylinder.

Table 3.2. Relative dominant wave loading regimes for a circular cylinder, adapted from Sarpkaya [201]. D is the diameter of the body, L is the wavelength, and H/D is the Keulegan-Carpenter number.

Dominant Regime	Range
Inertia	$0.01 < H/D < 0.25, \pi D/L < 0.5$
Small-drag, large-inertia	$0.25 < H/D < 1.5, \pi D/L < 0.5$
Morison region (comparable drag and inertia)	$H/D > 20$
Diffraction	$\pi D/L < 0.5$

Morison's equation is commonly used to determine the loading on offshore structures. It is valid for slender bodies, more specifically cylinders which pierce the water surface. Morison's equation is an empirically based calculation to determine the inline force of a body in an oscillating flow. The equation consists of two terms representing the drag and inertial forces of the body. While Morison's equation has many limitations, which is briefly mentioned here, it is still works surprisingly well for predicting loading on bodies in oscillatory flow.

Morison's equation in its simplest form is the sum of an inertial force in phase with the flow acceleration and a drag force proportional to the square of the velocity. The equation is given below.

$$F = \frac{1}{2}\rho C_d A_p |U|U + \rho C_m V_0 \frac{dU}{dt} \tag{3.2}$$

where ρ is the density of the water, C_d is the drag coefficient, A_p is the projected frontal area of the object, U is the fluid velocity, C_m is the inertia coefficient, and V_0 is the displaced volume of the object. Morison's equation can be modified for the case of a freely moving body, and furthermore in the presence of a current. Modifications

for the case of a freely moving body are discussed at the end of this section, following a brief description of the Froude-Krylov hypothesis.

While Morison's equation captures added mass, incident wave inertia and drag forces, it suffers from other limitations. Limitations of Morison's equation include the inability to account for fluctuating lift force, as well as capture the inline force accurately. Furthermore, it ignores memory effects, and uses GI Taylor's long wavelength assumption to simplify the treatment of diffraction [95]. It is inherently difficult to reconstruct the kinematics of the ocean due to uncertainties such as how to separate current and waves, omnidirectionality, and turbulence, among other parameters. Discrepancies between forces calculated with Morison's equation and measured forces can be attributed to both the form of the Morison equation and the uncertainties of ocean wave characterization.

If wave scattering is ignored then a simplified representation of the pressure field around the body can be found. The force calculated from this simplification is called the Froude-Krylov force. The Froude-Krylov Hypothesis assumes a sufficiently small body so that the pressure field is not affected by incident waves, such that diffraction effects can be ignored. The Froude-Krylov force is the force that would act on a body if the body were not there, that is, if the body were to make no changes to the flow field. The force is expressed as,

$$F^{FK}(t) = -\rho \int \int \frac{\partial \phi}{\partial t} n dS \qquad (3.3)$$

Closed form solutions for the Froude-Krylov force for a small sample of body geometries exist. A succinct summary of these solutions can be found in Chakrabarti [26]. The Froude-Krylov force is an over-simplification of the hydrodynamic loading on a body, and is in general not justified for use when more advanced computing resources are available. While the Froude-Krylov calculation is enticing due to its

simplicity, much can be gained from a few additional considerations about body-wave interactions.

Morison's equation can be modified for the case of a freely moving body. An additional term is included in the inertial force term, seen in Equation 3.2. To account for the moving body, the inertial and drag force terms are adjusted by $\frac{dv}{dt}$. The modified Morison's equation takes the form, where the Froude-Krylov terms appears as the last term on the right hand side,

$$F = \frac{1}{2}\rho C_d A_p |U - v|(U - v) + \rho C_m V_0 (\frac{dU}{dt} - \frac{dv}{dt}) + \rho V_0 \frac{dU}{dt} \qquad (3.4)$$

Morison's equation allows for an easy calculation of the forces on a small structure where pressure distributions due to complex flow and vortices would otherwise be difficult to calculate, and the Froude-Krylov force provides a simple treatment for the case where diffraction is ignored. But, if the flow remains attached to the structure, then it is actually easier to calculate the pressure field which causes the forces on the structure. For larger structures the flow around the body remains attached, and the incident wave scatters off the surface. In this regime of larger structures, Morison's equation assumptions are no longer valid.

For a linear treatment of the hydrodynamics of a floating object, the problem can be divided into three separate problems: radiation, diffraction and hydrostatics. The radiation problem gives the loads for an oscillating body in the absence of waves. The loads are due solely to waves radiating away from the body. The diffraction problem finds the loads for a non-moving body in the presence of incident scattering waves. Finally, the hydrostatics include the straightforward buoyancy and loads due to changes in the water-plane area. In the linearized treatment the three separate problems are mutually independent of each other. The total force is then given by

the sum of radiation, diffraction and hydrostatics, which are each discussed further below.

$$F^{Hydrodynamics} = F^{Diffraction} + F^{Radiation} + F^{Hydrostatics} \tag{3.5}$$

First, the diffraction problem for a vertical cylinder is considered. The hydrodynamic problem can be linearized by using the same assumptions discussed in Section 1.3. This leads to a potential flow based approach that models the linear diffraction off a vertical cylinder. In this analysis, on top of the usual assumptions of inviscid, incompressible, irrotational flow, it is assumed that the flow is unseparated, and we neglect surface tension, cavitation and gradients in temperature and density in the vertical direction. We return to the Laplace equation for the velocity potential. We take the same boundary conditions discussed in the linearized wave theory section, that is the kinematic and dynamic free surface, the seabed and body boundaries. We define ϕ_w to be the incident wave potential, and ϕ_s as the scattered wave potential. The sum $\phi = \phi_w + \phi_s$ must satisfy the Laplace equation. Furthermore, the Sommerfeld radiation condition must be satisfied [213], which says that the outgoing wave must be represented by the scattered wave potential at long distances. This is given mathematically by,

$$\lim_{R \to \infty} r^{1/2} \left[\frac{\partial \phi_s}{\partial r} - ik\phi \right] = 0 \tag{3.6}$$

where the incident wave potential is given by,

$$\phi_w = \frac{-igH}{2\omega} \frac{cosh[z(k+h)]}{cosh(kh)} e^{i(kx-\omega t)} \tag{3.7}$$

The body-surface condition is

$$\frac{\partial \phi}{\partial n} = \frac{\partial \phi_s}{\partial n} + \frac{\partial \phi_w}{\partial n} = 0 \Rightarrow \frac{\partial \phi_s}{\partial n} = -\frac{\partial \phi_w}{\partial n} \tag{3.8}$$

where n is the outward normal vector to the surface of the body. This is the same no-permeation boundary condition that was presented earlier. An expression for pressure is derived from the unsteady Bernoulli equation,

$$p = -\rho g z - \rho \frac{\partial \phi}{\partial t} \qquad (3.9)$$

The pressure distribution can then be determined, and the forces and moments calculations follow from there.

The above analysis is referred to as the diffraction problem. A similar analysis can be carried out to study the case of a body undergoing small oscillations and therefore radiating waves away from the body. The resulting motion and determination of wave amplitudes far away from the body can be studied, and is referred to as the radiation problem. Loads in the radiation problem include contributions from added mass and damping. An impulse in platform velocity causes waves to radiate. These radiating waves induce a pressure field which then results in a force which persists for all time while waves are radiating. Instead of the no-permeation boundary condition as was in the case of the diffraction problem, the normal derivative of the potential is prescribed by a non-zero value, and a similar analysis follows from there.

Closed form solutions to the linearized radiation and diffraction problems exist for a limited number of cases. Other geometries can be treated with integral methods to find approximate solutions, such as those based on Green's theorem. Force representations derived using Green's theorem are called the Haskind Relations, and details can be found in many texts on offshore engineering, including Sarpkaya and Issacson's book [202]. Additional methods for studying the diffraction and radiation problems exist, including hybrid element methods, as reviewed by Mei [136], and finite difference methods which are discussed in detail in the next chapter.

Generally wave diffraction reduces wave loads on the structure. It is important to note that even in the regime of diffraction dominated loading, flow separation

can occur. Viscous forces may be important especially around sharp corners where separation is likely to occur. This factor must be considered for each geometry.

3.2.2   Added Mass

In 1828 Bessel conducted experiments with spherical pendulums in air and water, and noticed that the period of oscillation increased when the pendulum was placed in water as compared to air [201]. Bessel attributed the increase in period to the effect of an added mass in the system. This so called added mass is described in terms of the fluid displaced by the moving body. When dealing with the flow around objects or the unsteady motion of bodies in water, we must consider the effect of added mass. An accelerating or decelerating body must move mass (a volume of fluid) as it moves.

Obviously the mass of the system does not change, but rather changes occur in the acceleration of deceleration of the fluid, an increase or decrease in kinetic energy, or a negative or positive change in inertia per unit mass. Due to these physical explanations, the term added mass is sometimes replaced with added inertia.

The added mass moment of inertia in a viscous fluid exists only for a brief moment immediately following an acceleration or deceleration of the fluid, or a change from an initially steady state to an unsteady state. The added mass effects exist only before separation and viscous effects come into play. Furthermore, the effects only occur for a small displacement of the body.

A simple analysis for the case of a floating object with small motions which obey a linear behavior is presented below to demonstrate the effects of added mass. A simple harmonic motion model with a driving force is can be represented with the following equation,

$$m\ddot{x} + b\dot{x} + kx = f(t) \tag{3.10}$$

45

where m is the mass, b is the damping coefficient, k is the spring constant, f is the force acting on the mass and x is the displacement of the mass. The effect of added mass acts in opposition to the motion of the mass, so the equation of harmonic motion is adjusted to reflect that change,

$$m\ddot{x} + b\dot{x} + kx = f(t) - m_a\ddot{x} \tag{3.11}$$

or by rearrangement,

$$(m + m_a)\ddot{x} + b\dot{x} + kx = f(t) \tag{3.12}$$

Now, instead of the natural frequency going as

$$\omega_n = \sqrt{\frac{k}{m}} \tag{3.13}$$

it becomes

$$\omega_n' = \sqrt{\frac{k}{m + m_a}} \tag{3.14}$$

Thus, the effect of added mass is to decrease the natural frequency and increase the period, just as Bessel observed in his pendulum experiments. The force due to added mass can be expressed in three dimensions most elegantly with tensor notation.

$$\bar{F}_i = [m_{ij}]\dot{u}_i \tag{3.15}$$

where i,j = 1,2,3,4,5,6 and the first three indices represent the linear degrees of freedom, and the last three indices are the rotational degrees of freedom. The added mass matrix, $[m_{ij}]$ gives the mass associated with a force in i^{th} direction due to an acceleration in the jth direction.

3.2.3 Impulse Loads

Much work has been done experimentally and theoretically on the wave impact loads on horizontal and vertical cylinders. Contributors to this topic include Miller [146], Faltinsen [49] [225], and Sarpkaya [200]. The flow field around a structure involving impacting waves is often very complicated. Empirical equations are often used in place of theory to calculate loads near the free surface due to breaking and broken waves.

For wave slamming, an empirical formula for a horizontal cylinder provides a rough estimate of the loading [26],

$$F = \frac{1}{2}\rho C_s A u_0^2 \tag{3.16}$$

where C_s is the wave slamming coefficient, ρ is the density of water, A is the cross-sectional area of the cylinder and u_0 is the maximum velocity in a wave cycle. The theoretical value of C_s is π and derivations of this value can be found in Sarpkaya's text [201]. Experimental work by Miller found a C_s value closer to 3.6 [146]. Further work by Sarpkaya showed that C_s depends greatly on the structural stiffness of the cylinder [200].

Furthermore, experiments on cylinders have been carried out to study the effects of breaking waves on structures. Ochi and Tsai conducted experiments with regular and irregular waves and found that the pressure field goes as

$$p = \rho \kappa_1 U^2 \tag{3.17}$$

where K_1 is 5.98 for breaking waves, and 2.74 for an already broken wave approaching the structure [161].

3.3 Design and Analysis of Loads

Two main methods of analysis and design include deterministic (extreme) and stochastic (nominal conditions) wave loading. Deterministic analysis gives low-cycle fatigue. Typically, a design wave is chosen, Morison's equation is implemented by vertically integrating over the surface of the object to determine loading. This case is often treated as pseudo-static, and is calculated in time domain. A design wave is assumed to be uniformly crested and travel with constant speed and shape. Stochastic loads are generally calculated in the frequency domain using a spectral analysis. A force transfer function is calculated to determine the loading. More recent work using finite volume methods has analyzed deterministic and stochastic loading in a different framework. These approaches and research efforts are discussed in the next chapter. For now, a review of other approaches can be found in the following section.

3.4 Wind Turbine Platform Concepts

Before delving into a review of the literature on loading of offshore wind turbine platforms, it bears noting the range and definition of proposed and exisiting platform concepts. Offshore turbines include monopiles in shallow water, jacketed structures in transitional water, and finally, floating concepts in deep water. Floating platforms include tension leg platforms (TLPs), semi-submersibles, spar buoys, and barges. Shallow water is generally considered to be less than 30 meters in depth, transitional waters extend from about 30 to 60 meters, and deep water is anything deeper than about 60 meters. A helpful way to categorize floating platform concepts is by their stablity strategy. TLPs are stabilized by mooring lines, spar buoys are ballast stabilized, and have catenary mooring lines, barges are buoyancy stabilized and also have catenary mooring lines, and lastly, semi-submersibles are stabilized by both buoyancy and the mooring lines. A more detailed review of floating platform concepts is given by Thiagarajan [237].

3.5   Previous Research

Some analytical solutions exist from linearized theory for basic geometries, such as circular cylinders. Other methods have been developed for more general cases, including the integral equation method and the hybrid element method, which are presented in a review by Mei [136]. More recently, finite volume methods have become more feasible, and these methods along with a review of recent research is presented in the next Chapter.

Integral equation methods using potential flow theory have provided exact analytical solutions for a small sample of geometries, and in more complicated cases, approximate results. Integral equation methods based on potential flow theory are popular due to their relatively inexpensive computational cost. Typically, the analysis begins with a single solution which satisfies the governing equations everywhere but on the surface of a geometry. Boundary conditions are applied on the surface of the body, resulting in an integral equation. In some cases an exact solution exists, but more commonly the surface is discretized and the solution is found numerically. The body surface is discretized into piecewise linear segments, often referred to as panels.

Work preceding floating offshore wind development includes research by Kleinman, who used a boundary value problem to model the generation of surface waves from a partially submerged body [110]. The linearized free surface condition is used with a radiation condition at infinity. In 1950 Fritz John gave an analytical solution for this problem under very strict assumptions, and Kleinman extends his work to show uniqueness for more general geometries. Two methods are introduced to modify the integral equation, including the addition of an integral on the water surface and another integral term representing only the submerged part of the floating body.

In 2005, Passon and Kühn presented a review of the state-of-the art simulation codes for offshore wind turbines [168]. A more recent review was given by Cordle and

Jonkman, in 2013, that summarizes the most popular design tools for simulating floating turbines [31]. The review includes discussion of FAST, Bladed, SIMO/RIFLEX, HAWC2, 3Dfloat and SIMPACK, which are discussed in more detail below.

There has already been a large effort to model the wave and wind loading on fixed bottom offshore wind turbines [7, 8] [28] [44] [216] [246]. Wave loading analysis on monopiles has largely been accomplished via Morison's equation, which is valid for vertically mounted cylinders. Research efforts in modeling floating offshore wind turbines have begun more recently, preceded by a history of research by the oil and gas industry, as well as the ship hydrodynamics community. Here, the focus is on work done for floating offshore wind turbines.

More recently, many wind turbine research efforts have made use of FAST, a nonlinear aero-hydro-servo-elastic computer aided engineering (CAE) tool, which can be coupled with HydroDyn to simulate both fixed bottom and floating offshore wind turbines and is described in detail in Jonkman's dissertation [95]. FAST continues to be developed, verified, and validated by the National Renewable Energy Laboratory (NREL) at the National Wind Technology Center (NWTC).

The latest release of FAST (version 8) provides a modularized framework, including a module for hydrodynamics called HydroDyn [92]. HydroDyn has the ability to model linear periodic waves as well as irregular waves sampled from various wave spectra. HydroDyn uses a combination of Morison's equation with potential-flow theory to model the loads on the platform.

The latest release of HydroDyn includes the added capability of calculating Morison's solutions on non-vertical and multiply interconnected members. Morison's equation includes a term for radiation-induced added mass, diffraction-induced wave excitation forces (with a long wavelength approximation), and and viscous drag forces. In the latest release of HydroDyn, each member of the platform is assigned a unique value for the viscous drag coefficient. Each member is discretized into segments, and

FAST outputs a viscous force per unit length at each node along the length of each member. The total force is found by integration along the length of each member, and then a summation of the force on each member.

Radiation and diffraction solutions based on linear frequency-domain analysis can be imported from a code like Wave Analysis MIT (WAMIT) [121]. WAMIT is a boundary integral equation method based on linear and second order potential theory, otherwise known as a panel method. The velocity potential and pressure fields are found on the submerged surface of the body. This model is used to solve the radiation problem, which generates a body-oscillation frequency-dependent set of coefficients, and the diffraction problem, which generates a vector of wave-frequency dependent coefficients. When WAMIT is used to provide potential-flow based solutions, Morison's equation provides drag effect solutions.

Verification of HydroDyn, with preprocessing input from WAMIT, is presented via code to code comparison by Jonkman [90]. Additional work by Jonkman and Matha demonstrated the dynamic responses of three types of offshore floating turbine platforms, including a spar buoy, tension leg platform and barge [94]. Sclavounos, et al, coupled WAMIT with the Aero-Hydro-Servo-Elastic design code FAST to study fluid loads on a floating wind turbine [249]. Sclavounos has also investigated non-linear loads on bodies in irregular steep waves using potential flow theory [206].

Cermelli, et al, modeled the hydrodynamics on a floating wind turbine using WAMIT [25]. The potential flow based panel method was also applied by Zambrano, et al, to demonstrate the feasibility of smaller floating wind turbines with semi-submerscible and tension leg platforms [266]. Gueydon, et al, simulated hydrodynamic loads using a panel method, coupled with catenary mooring lines and uniform wind, and found good agreement between numerical results and experimental results from a wave basin [67]. Wave drift on a semi-submerscible platform was modeling using three-dimensional potential flow theory by Pinkster and Huijsmans [182].

A comprehensive offshore code comparison collaboration (OC3) was conducted for the dynamic loading responses of a 5 MW wind turbine mounted on a spar buoy in a depth of 320 meters [93]. A variety of environmental conditions were selected to simulate different model features. Results from seven codes were compared, and each code is summarized in a table in the report. The hydrodynamics portion of each code consists of various combinations of Airy wave theory, linear potential flow with radiation and diffraction, Morison's equation and stream-function theory. None of the hydrodynamics modeling used in the code comparison includes finite volume methods, which are discussed in the following section.

Among the codes involved in the OC3 was the HAWC2 aero-elastic code developed at Risø-DTU, and the SIMO/RIFLEX code developed at MARINTEK. Work by Nielsen, et al, coupled HAWC2, which models fixed foundation wind turbines, with SIMO/RIFLEX, which simulates the dynamic response of marine structures, and found results to be in fairly good agreement with tank model experiments [158].

Although Morison's equation is most valid for cylinders that reach the ocean floor, or fixed-bottom wind turbines, it has been used for research on floating wind turbines as well. A spar buoy mounted wind turbine was modeled with a panel method and used Morison's equation to calculate hydrodynamics at instantaneous positions by Karimirad and Moan [102]. Further work by Karimirad presented hydroelastic code-to-code comparisons between his work using a combination of Morison's equation with a pressure integration method for the hydrodynamics of a tension leg spar buoy [101]. Fulton, Malcolm, and Moroz [57] and Withee [254] also used Morison's equation to model the hydrodynamics loads on tension leg platforms. Phuc and Ishihara modeled floating wind turbines as elastic bodies with an FEM code, using Morison's equation for hydrodynamics and quasi-steady theory for aerodynamics [179]. Mei gives a good review of earlier fluid-structure interaction work involving hybrid element methods for floating bodies that predates floating offshore wind turbine development [136].

CHAPTER 4

FINITE VOLUME METHODS

While the computational cost of CFD can be expensive for use as a design tool, it is still beneficial for its high-fidelity results. CFD has been more widely used to simulate wind turbine aerodynamics than hydrodynamics. Reviews of aerodynamic simulation tools have been given by Miller, et al, [145], as well as as a CFD focused review by Sanderse, et al [198]. However, as large-scale offshore wind development has grown in Europe, and begins to see development in other regions of the world, hydrodynamic modeling of offshore wind turbines has increased. Fixed bottom platforms for wind turbines, or monopiles, have been modeled with a variety of engineering tools as was discussed in the previous section. Additionally, wave run-up and loading on monopiles have been studied with CFD, and are outlined here. CFD research on the hydrodynamics of floating offshore platforms is growing, and is highlighted at the conclusion of this section.

This chapter covers finite volume methods for modeling multiphase flows. The discretization of the transport equation is presented as an example of the transformation of a set of continuous equations into a set of discrete algebraic equations. Individual terms are discretized, followed by a discussion of boundary conditions, and finally commentary on solving systems of algebraic equations. Next, a variety of finite difference methods for simulating multiphase flows are explored, including Volume of Fluid, Moment of Fluid, marker, and level-set methods. Finally, a review of recent CFD work in wave-structure interactions for wind energy and other applications is presented.

4.1 Finite Volume Discretization

The discretization of each term in the transport equation, including time, convection, diffusion and source terms is discussed here. Next, Neumann and Dirichlet boundary conditions are covered. The addition of boundary conditions provides problem closure, resulting in a system of algebraic equations. The section concludes with a brief discussion of solutions to linear algebraic systems.

4.1.1 Equation Discretization

The goal of finite volume discretization is to transform a set of continuous equations into a discrete set of algebraic equations. The problem domain must be discretized spatially, and in the case of transient analyses, also divided temporally. The spatial discretization is done by dividing the domain into control volumes, or cells. Temporal discretization is accomplished by division into discrete time steps in which the solution is determined at finite instances. Here, the governing equations are discretized to reformulate the problem into a set of algebraic equations. The algebraic equations are then solved to approximate the solution to the original set of equations. These approximations are done at specific places in space and time, as predetermined by a computational mesh and time-stepping regime.

The transport equation, shown below, is used as an example for equation discretization,

$$\underbrace{\frac{\partial \rho\phi}{\partial t}}_{time\ derivative} + \underbrace{\nabla \cdot (\rho \mathbf{U}\phi)}_{convection\ term} = \underbrace{\nabla \cdot (\Gamma \nabla \phi)}_{diffusion\ term} + \underbrace{S_\phi(\phi)}_{source\ term} \tag{4.1}$$

where ϕ is the quantity being transported, ρ is the density, U is the velocity, Γ is the diffusivity and $S_\phi(\phi)$ is a source term. The time derivative, convection, diffusion and source terms are labeled above. The equation above is reformulated into a finite volume discretization via integration over the control volume V_c and time,

$$\int_{t}^{t+\Delta t} \left[\int_{V_c} \frac{\partial \rho \phi}{\partial t} dV + \int_{V_c} \nabla \cdot (\rho \mathbf{U} \phi) dV \right] dt = \tag{4.2}$$

$$\int_{t}^{t+\Delta t} \left[\int_{V_c} \nabla \cdot (\Gamma \nabla \phi) dV + \int_{V_c} S_\phi(\phi) \right] dt$$

Using Gauss's theorem, most of the spatial integrals are converted from volume to surface integrals. The details of this transformation are shown in the following sub-section. The resulting finite volume discretizations must then be approximated using an appropriate numerical scheme.

4.1.2 Discretization of Terms

Gradient terms can be converted from volume integrals to surface integrals via Gauss's theorem. The value of the gradient is then approximated by summing the values of ϕ_f on every face f in the control volume. The resulting relation is given in Equation 4.3, below.

$$\int_{V_c} \nabla \phi dV = \int_S d\mathbf{S} \phi \approx \sum_f \mathbf{S} \phi_f \tag{4.3}$$

where $\mathbf{S}$ is the outward pointing surface area vector whose magnitude is equal to the area of the face, and $d\mathbf{S}$ is the outward pointing surface area differential.

The convection term is also discretized by converting the volume integral to a surface integral with Gauss's theorem, as is shown below.

$$\int_{V_c} \nabla \cdot (\rho \mathbf{U} \phi) dV = \int_S (\rho \mathbf{U} \phi) \cdot d\mathbf{S} \approx \sum_f \mathbf{S} \cdot (\rho \mathbf{U})_f \phi_f = \sum_f F \phi_f \tag{4.4}$$

where F replaces the term $\mathbf{S} \cdot (\rho \mathbf{U})_f$, which gives the mass flux through a face f, and ρ, U and ϕ have been interpolated from cell-centered values to face centered values. Interpolation can be performed with a variety of methods, including central differencing, upwinding and blended differencing. Central differencing is second order accurate but suffers from un-boundedness. Upwind differencing is only first order accurate, but maintains the boundedness of the solution. Finally, blended differencing

combines the two aforementioned methods to provide bounded solutions with decent accuracy.

Discretization of the diffusion term is treated similarly to the convection term. Again, Gauss's theorem is employed to convert from volume to surface integration, and the resulting expression is approximated by summation over the faces.

$$\int_{V_c} \nabla \cdot (\Gamma \nabla \phi) dV = \int_S d\mathbf{S} \cdot (\Gamma \nabla \phi) \approx \sum_f \Gamma_f (\mathbf{S} \cdot \nabla_f \phi) \qquad (4.5)$$

For orthogonal meshes, ∇_f is defined as

$$\nabla_f \phi = \frac{\phi_N - \phi_P}{|\mathbf{d}|} \qquad (4.6)$$

where the vector $\mathbf{d}$ is the distance between the cell center of interest, P, and the neighboring cell, N.

For non-orthogonal meshes the diffusion term is split into two pieces to preserve second order accuracy, the latter of which is a correction to the non-orthogonality.

$$S \cdot \nabla_f \phi = \underbrace{|\mathbf{\Delta}| \nabla_f^{\perp} \phi}_{orthogonal\ contribution} + \underbrace{\mathbf{k} \cdot (\nabla \phi)_f}_{non-orthogonal\ correction} \qquad (4.7)$$

where vectors $\mathbf{\Delta}$ and $\mathbf{k}$ must be determined, and satisfy $\mathbf{S} = \mathbf{\Delta} + \mathbf{k}$.

Finally, the source term is treated simply as a linearization, where S_E and S_I can depend on ϕ,

$$S_\phi(\phi) = \phi S_I + S_E \qquad (4.8)$$

Integration of the linearized source term over a control volume results in,

$$\int_{V_c} S_\phi(\phi) dV = S_I V_P \phi_P + S_E V_P \qquad (4.9)$$

where subscripts I, E and P denote implicit, explicit and belonging to cell P.

4.1.3 Temporal Discretization

To complete the discussion of the discretization of terms in the transport equation, the temporal term must be addressed. The temporal term is discretized with the Euler scheme, which can be treated either explicitly or implicitly. Discretization of the temporal term yields

$$\int_{V_p} \frac{\partial \rho \phi}{\partial t} \approx \frac{\rho^n \phi^n V^n - \rho^0 \phi^0 V^0}{\Delta t} \tag{4.10}$$

where n and 0 denote new and old times, respectively. The explicit or implicit nature of the Euler scheme is determined in the way the spatial terms are treated. For explicit Euler, the discretization of the spatial term uses the old values of the variables. That is, $\phi_p = \phi_p^0$ and so on. Explicit Euler is first order accurate and the stability of the method is limited by the Courant number, shown below. The method is unstable for Courant numbers greater than one.

$$Co = \frac{(\mathbf{v} \cdot \mathbf{n}) \Delta t}{|\mathbf{d}|} \tag{4.11}$$

When the discretized spatial terms use the newest time step values, the Euler scheme is implicit. For implicit Euler $\phi_p = \phi_p^n$, and so on. Implicit Euler is unconditionally stable and first order accurate.

4.1.4 Boundary Conditions

Boundary and initial conditions are necessary for closure of the problem. Initial conditions are only necessary for the case of transient problems. The two main types of boundary conditions are Dirichlet and Neumann, which prescribe the value of the dependent variable and of the gradient, respectively. Numerical treatment of the boundary is necessary when boundary faces are included in face summations. Boundary conditions are required for every boundary face and every dependent variable in a computational mesh.

Dirichlet, or fixed value, boundary conditions are implemented by direct substitution into the convection term when boundary values are required. For the diffusion term, Dirichlet boundary conditions must be converted from fixed values into gradients. This is accomplished via the equation below,

$$\mathbf{S} \cdot \nabla_f \phi = |\mathbf{S}| \frac{\phi_B - \phi_P}{|\mathbf{d_n}|} \tag{4.12}$$

where $\mathbf{S}$ is the surface area vector, ϕ_B is the value of the dependent variable at the boundary, ϕ_P is the cell centered value of the dependent variable, and $\mathbf{d_n}$ is the normal component of the distance vector from the cell center to the boundary face.

Neumann boundary conditions, or fixed gradient boundary conditions, are implemented by direct substitution when the face gradient is required. When the value of the dependent variable is needed on the face, the cell centered value must be extrapolated to the boundary. This is done with the following expression,

$$\phi_f = \phi_P + \mathbf{d_n} \cdot \nabla_f \phi = \phi_P + |\mathbf{d_n}| g_B \tag{4.13}$$

where g_B is the face normal gradient at the boundary.

4.1.5 Solving Systems of Linear Algebraic Equations

The discretization and linearization techniques discussed above lead to a linear algebraic equation for each control volume in the mesh. The linear algebraic equations depend on the exact choice of discretization technique and governing equations, but can be reformulated into the generic form,

$$a_P \phi_P + \sum_N a_N \phi_N = R_p \tag{4.14}$$

where a_P and a_N are coefficients associated with face interpolated values of the control volume P and its neighbors N, respectively. R_p represents contributions from

explicit terms, which include non-orthogonal corrections, explicit boundary conditions and source terms. The linear algebraic equations can then be recast into a system in the matrix form,

$$[A][\phi] = [R] \tag{4.15}$$

The matrix $[A]$ is generally a sparse matrix that contains the a_P terms on the diagonal, and the a_N on the off diagonals. Furthermore, it is a square matrix of dimension $N \times N$, where N is number of cells in the mesh. The $[\phi]$ vector is a column of the dependent variable, and $[R]$ is the vector of explicit contributions. Implicit terms contribute to the matrix coefficients in $[A]$ while explicit terms contribute to the source vector $[R]$.

The system of algebraic equations is then solved to determine the value of ϕ. Solution techniques fall broadly under two categories, direct and iterative methods. Direct methods solve the system in a finite number of arithmetic operations, where the required number of steps goes as N^3 where N is the number of equations/unknowns. Iterative methods are generally much cheaper computationally, but have restrictions on the type of matrices they can solve. Iterative methods begin with an initial guess and continue to improve on the approximation to the solution until a specified tolerance is reached. Matrices must be diagonally dominant to guarantee convergence for iterative methods. Oftentimes, conjugate gradient methods are used as the iterative method for systems of algebraic equations.

4.1.6 Governing Equations

Mass and momentum conservation equations were given in Section 1.1 to lay the groundwork for water wave theory. The Navier-Stokes equations for an incompressible fluid are revisited here to complete the discussion of finite volume discretization. Here, the equations are presented for a single-field formulation. The mass continuity and momentum equations are given in Equations 4.16 and 4.17, respectively.

$$\nabla \cdot \mathbf{U} = 0 \qquad\qquad (4.16)$$

$$\frac{\partial \rho \mathbf{U}}{\partial t} + \nabla \cdot (\rho \mathbf{U}\mathbf{U}) = -\nabla p + \nabla \cdot \tau + \rho \mathbf{f} \qquad\qquad (4.17)$$

where t is the time, $\mathbf{U}$ is the velocity vector, ρ is the density, τ is the stress tensor and $\mathbf{f}$ includes surface tension and other body forces, such as gravity.

The Navier-Stokes equations are supplemented by the stress tensor equation which obeys the Newtonian laws of viscosity, and is shown below.

$$\tau = \mu(\nabla \mathbf{U} + \nabla \mathbf{U}^T) \qquad\qquad (4.18)$$

These equations are revisited when detailing the Volume of Fluid method in the Section 4.2.1.

4.2 Eulerian Methods

Eulerian methods for multiphase flow modeling use a numerical grid that does not move with the fluid interface. The location of the fluid interface cuts through the cells in the mesh, and its location must be determined. There are two basic approaches in the determination of the interface location: interface tracking and interface capturing. Interface tracking explicitly describes the interface position. There are a variety of ways to do this, including use of supplemental Lagrangian surface-grids or marker particles. The interface capturing methodology does not explicitly track the interface. Instead, the interface location is determined implicitly, which can also be approached in a variety of ways. These include using volume fractions, as in the Volume of Fluid method, phase fields or distance functions, as are used in level-set methods.

This section describes some of the Eulerian methods for simulating multiphase flows. First, the Volume of Fluid (VOF) method is discussed, followed by the Moment of Fluid (MOF) method, level-set methods and finally marker methods.

4.2.1 Volume of Fluid

The Volume of Fluid (VOF) method is one of the most common methods for simulating multiphase flows. The VOF method is an interface capturing method in an Eulerian framework. Initial development of the method can be attributed to Woodward and Noh [159], Hirt and Nichols [155] and deBar [37].

In the simplest terms, the VOF method advects a fluid volume fraction on an Eulerian mesh. Each cell must have a fractional value between zero and one, where one represents fluid a, and zero represents fluid b. A pure cell is any cell which has a value equal of strictly zero or one. A mixed cell has a value between zero and one, meaning the cell is a mixture of the two phases and thus contains the interface between the two fluids. This information from the mixed cells is then used to reconstruct the interface between phases. The fluid volume fraction is advected with the flow via a transport equation. The transport equation is solved simultaneously with the mass and momentum conservation equations, which is elaborated upon shortly.

The mathematical representation presented here is for the flow of two immiscible, incompressible fluids, each with their own constant density and viscosity. The entire flow field is represented by a single set of conservation equations, where material properties vary discontinuously across the interface. Representations using two sets of conservation equations for each phase have also been done, but are omitted here.

As mentioned earlier, a volume fraction is used to represent the two fluids. The interface is represented as a mixture of the fluids instead of a sharp boundary. Physically the transition region is a sharp step, but is not treated as one in this method. The indicator function, α, is given by, [194]

$$
\alpha =
\begin{cases}
0 & \text{for a point inside fluid a} \\
0 < \alpha < 1 & \text{for a point inside transitional region} \\
1 & \text{for a point inside fluid b}
\end{cases}
$$

The indicator function, which is chosen to be the volume fraction, is advected with the flow, obeying a transport equation of the form,

$$\frac{\partial \alpha}{\partial t} + (\mathbf{U} \cdot \nabla)\alpha = 0 \tag{4.19}$$

Local material properties, such as density and viscosity, can be described using the indicator function as follows,

$$\rho = \alpha \rho_a + (1 - \alpha)\rho_b \tag{4.20}$$

$$\mu = \alpha \mu_a + (1 - \alpha)\mu_b \tag{4.21}$$

This method of determining local material properties, which jump in value across the interface, has its drawbacks. Taking the average of the viscosity as a simple weighted average of the indicator function can significantly reduce accuracy at the fluid interface [32]. An alternative to the arithmetic mean approach, given above, is to use a harmonic mean represented mathematically in the equation below [169] [185] [234].

$$\mu = \frac{\mu_a \mu_b}{\alpha \mu_a + (1 - \alpha)\mu_b} \tag{4.22}$$

Issues with numerical diffusion arise when convecting a step function such as the volume fraction. To combat these issues, compression of the interface can be achieved via an artificial compression term. This term, proposed by Weller [194], is shown in the third term below.

$$\frac{\partial \alpha}{\partial t} + \nabla \cdot (\mathbf{U}\alpha) + \nabla \cdot (\mathbf{U_r}\alpha(1 - \alpha)) = 0 \tag{4.23}$$

A velocity field, $\mathbf{U_r}$, compresses the interface. The compression term is only active in a thin region surrounding the interface, which prevents the compression

from significantly affecting the overall solution. Further details on the compression of the interface can be found in Rusche [194].

Pressure boundary conditions are simplified if the modified pressure is used as the dependent variable. The modified pressure is defined by subtracting the hydrostatic pressure from the pressure, given mathematically as

$$p^* = p - \rho \mathbf{g} \cdot \mathbf{x} \qquad (4.24)$$

Since the dependent variable has been changed, adjustments must be made to the momentum equation. The gradient of the modified pressure is taken, as shown in Equation 4.25, and then is substituted into the momentum equation shown in 4.26.

$$\nabla p^* = \nabla p - \nabla(\rho \mathbf{g} \cdot \mathbf{x}) = \nabla p - \rho \mathbf{g} - \mathbf{g} \cdot \mathbf{x} \nabla \rho \qquad (4.25)$$

In addition to modifying the pressure, the viscous stress term is also translated into a more convenient form.

$$
\begin{aligned}
\nabla \cdot \tau &= \nabla \cdot (\mu(\nabla \mathbf{U} + \nabla \mathbf{U}^T)) \\
&= \nabla \cdot (\mu \nabla \mathbf{U}) + \nabla \cdot (\mu(\nabla \mathbf{U})^T) \\
&= \nabla \cdot (\mu \nabla \mathbf{U}) + (\nabla \mathbf{U}) \cdot \nabla \mu + \mu \nabla(\nabla \cdot \mathbf{U}) \\
&= \nabla \cdot (\mu \nabla \mathbf{U}) + (\nabla \mathbf{U}) \cdot \nabla \mu
\end{aligned}
\qquad (4.26)
$$

Now the momentum equation can be rewritten as,

$$\frac{\partial \rho \mathbf{U}}{\partial t} + \nabla \cdot (\rho \mathbf{U}\mathbf{U}) = -\nabla p^* + \nabla \cdot (\mu \nabla \mathbf{U}) + (\nabla \mathbf{U}) \cdot \nabla \mu - \mathbf{g} \cdot \mathbf{x} \nabla \rho + \rho \mathbf{f} \qquad (4.27)$$

where the viscous stress term has been rewritten, and the final term represents the body forces without gravity.

The VOF approach evolves the volume of fluid in each cell, as the name suggests, but does not track the interface itself. In some cases, it may be desirable to geometrically reconstruct the fluid interface, for example, in scenarios where surface tension dominates. Geometric methods for reconstructing the interface are discussed first, including simple line interface construction (SLIC) [159] and piecewise linear interface construction (PLIC) [262]. Next, work by Ubbink and Issa [242] is discussed, where no explicit interface reconstruction is carried out. They proposed a method to avoid surface reconstruction altogether, as it can be computationally complex for unstructured meshes. Since the ocean is not dominated by surface tension, geometric reconstruction of the fluid interface is not required, such that Ubbink and Issa's approach is appropriate for modeling offshore wind turbines.

SLIC is a first order accurate reconstruction approach, that conserves volume, and was first presented by Noh and Woodward [159]. Fluid interfaces found in mixed cells are represented as compositions of one-dimensional components. Each component is represented as a straight line with is entirely perpendicular or parallel to the coordinate direction. Approximations of the interface are determined entirely by testing the volume composition of the two fluids in the cells neighboring the mixed cell of reference. Interfaces satisfy the volume fraction in mixed cells. It is shown in Figure 4.1 that SLIC does not accurately describe the true interface for many cases. The fluid front can easily become fragmented, as is demonstrated in Figure 4.1, and this deterioration of the interface representation can lead to flotsam and jetsam, or small remnants of mixed fluid zones.

PLIC is an alternative approach to SLIC. PLIC reconstructs the interface in a mixed cell as a line in two-dimensions or a plane in three-dimensions. Unlike the SLIC approach, PLIC allows for lines or planes to be aligned in any direction. Line segments representing the fluid interface are usually described in Hessian normal form, $\hat{n} \cdot \vec{r} + d = 0$, where $\hat{n}$ is normal to the line segment, $\vec{r}$ is a point on the
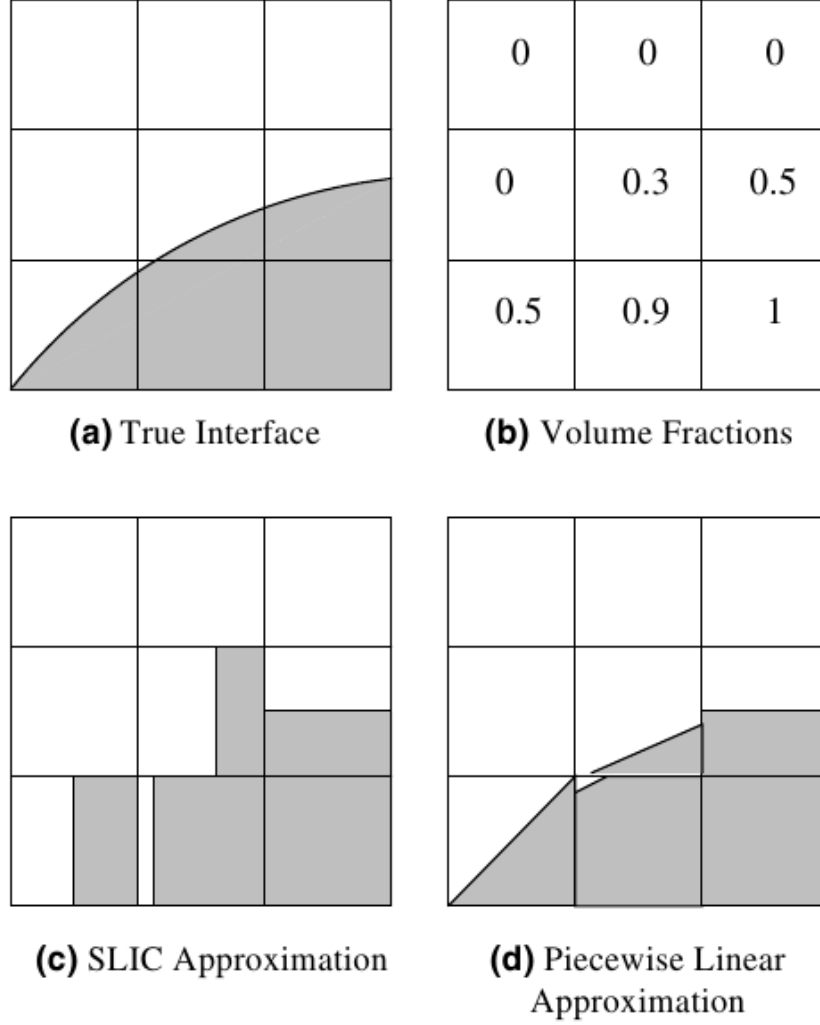
Figure 4.1. Volume of fluid representations of an interface(a), represented by volume fraction values (b), reconstructed with SLIC (c) and reconstructed with a piecewise-linear approximation (d). Reproduced from Pilliod and Puckett [181].

segment and d is the signed distance from the origin to the line segment. First the normal is computed, then the value for d satisfying the volume fraction of the cell is determined. This approach more accurately represents the interface, as shown in the Figure 4.1, despite the discontinuities between segments of neighboring cells. Errors of this method go as $O(\kappa h^2)$, where κ is the curvature of the true interface and h is the grid spacing [204].

Pilliod and Puckett proposed a second order accurate piecewise linear interface reconstruction algorithm. They demonstrated that a linear approximation to the interface is not sufficient to guarantee second order accuracy. They proposed the least squares volume-of-fluid interface reconstruction algorithm (LVIRA) and the efficient least squares volume-of-fluid interface reconstruction algorithm (ELVIRA), which use an error minimization approach to reconstruct the fluid interface exactly. The method reproduces lines and planes, in two-dimensions and three-dimensions, exactly, and allows the methods to maintain second order accuracy of the interface reconstruction [181].

Ubbink and Issa presented a non-geometric method to overcome the challenges associated with advecting a step function on an Eulerian grid [242]. These challenges include diffusion, dispersion and warping of the interface. The Compressive Interface Capturing Scheme for Arbitrary Meshes (CICSAM) method combines sharply resolved interfaces with boundedness of the volume fraction. Depending on the orientation of the interface with respect to the flow direction, the method switches between two high resolution discretization schemes. The method is fully conservative, implicit and theoretically second order in time.

Following interface reconstruction, and computation of volume fluxes from updated interface locations, the volume fraction is advected using the transport given in Equation 4.19.

4.2.2 Moment of Fluid

Dyadechko and Shashkov developed a Moment of Fluid method (MOF) which uses volume fractions as well as material centroid information to reconstruct interfaces [43]. The MOF method provides sufficient information to reconstruct an interface without the need for information from neighboring cells. MOF is able to resolve interface

features on the order of the cell size. The computed interface is chosen to match the volume fraction and approximate the reference material centroid as best as possible.
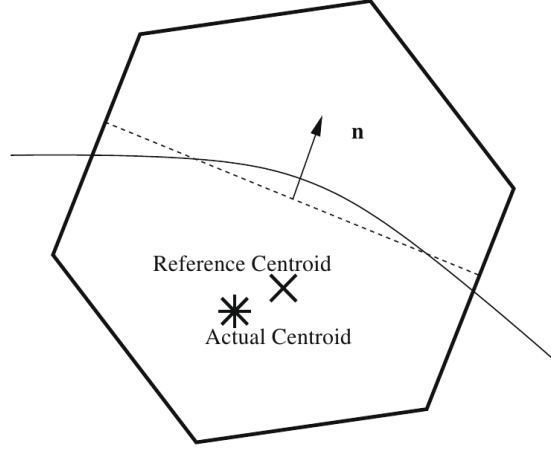
Figure 4.2. Representation of the MOF method in two-dimensions. The true interface is represented by the solid curved line, the dotted line represents the piecewise-linear reconstruction and the normal is label as $\hat{n}$. Reproduced from Shashkov and Ahn [9].

Letting Ω define a material region, the zeroth moment (volume) and the first moment are defined as,

$$M_0(\Omega) = \int_\Omega dV \qquad (4.28)$$

$$M_1(\Omega) = \int_\Omega \vec{x} dV \qquad (4.29)$$

The material centroid can then be represented in terms of the zeroth and first moments, as,

$$\vec{x}_\Omega = \frac{M_1(\Omega)}{M_0(\Omega)} \qquad (4.30)$$

The interface is computed to match the reference volume exactly and to approximate the centroid as closely as the possible. The interface normal, $\hat{n}$, is computed by minimizing the functional,

$$E_c^{MOF}(\hat{n}) = |\vec{x}_c^{ref} - \vec{x}_x(\hat{n})|^2 \qquad (4.31)$$

where $\vec{x}_c^{ref}$ is the reference material centroid and $\vec{x}_x(\hat{n})$ is the reconstructed material centroid with interface normal $\hat{n}$. The centroids are advected with the local velocity, and the reference material centroid is found from the volume weighted sum of these forward traced centroids.

The minimization of $E_c^{MOF}(\hat{n})$ is calculated as follows; first, an initial guess for the interface normal is calculated by defining a vector between $\vec{x}_c^{ref}$ and the actual cell centroid. The signed distance, d, is then calculated to match the reference volume in each cell exactly. The centroid of the resulting polyhedron is then computed, and the distance between the actual and reference centroids is determined.

Interface reconstruction in the MOF method is efficient due to the fact that no neighboring cell information is needed. Reconstruction of the interface in each cell is determined from volume fraction and material centroid of the reference cell only. Shashkov and Ahn extended the work of MOF to include an adaptive mesh refinement strategy [9]. The adaptive meshing is based on errors in the centroid positions. Furthermore, they extended MOF for multi-material cases in which the number of materials exceeds two.

4.2.3 Level-Set Methods

Osher and Sethian were the first to formulate a level-set method for calculating the motion of an interface under a velocity field [209]. Level set methods implicitly represent boundaries, or in the case of two phase flow, the interface between the fluids using a zero level-set of the function ϕ. The level-set function ϕ is a signed distance function. The interface is defined by $\Gamma(t)$, which exists in R^n and bounds a region Ω. The smooth level-set function ϕ is defined such that

$$\phi(\vec{x}, t) = 0 = \Gamma(t) \qquad (4.32)$$

$$\phi(\vec{x}, t) > 0 \text{ for } x \in \Omega \tag{4.33}$$

$$\phi(\vec{x}, t) < 0 \text{ for } x \notin \Omega \tag{4.34}$$

The motion of the interface is tracked by advecting the level-set function using a transport equation lacking a diffusion term. The dissipation must be carefully treated by use of an appropriate convection scheme.

The level-set field must be reinitialized at each time step following the evolution of Γ. The steady-state solution to the following equation is used to reinitialize the level-set field [133]

$$\frac{\partial \psi}{\partial t} + sign(\phi)(|\psi| - 1) = 0 \tag{4.35}$$

with the initial condition,

$$\psi(\vec{x}, 0) = \phi(\vec{x}, t) \tag{4.36}$$

The curvature of the interface is found by calculating the divergence of the normal gradient of ϕ at the interface. Mathematically this relation is given by,

$$\kappa = -\nabla \cdot \hat{n}, \text{ where, } \hat{n} = \frac{\nabla \phi}{|\nabla \phi|} \tag{4.37}$$

Properties of the two fluids, such as density and viscosity, are given by the smooth Heaviside function,

$$\rho = \rho_{liquid} + (\rho_{gas} - \rho_{liquid})H(\phi) \tag{4.38}$$

$$\mu = \mu_{liquid} + (\mu_{gas} - \mu_{liquid})H(\phi) \tag{4.39}$$

Adalsteinsson and Sethian introduced the narrow-band approach, which focuses the computational effort about the fluid interface region [4]. Similar work was also done by Peng, who developed an algorithm to track the evolution of the interface, that is, the level-set function [173]. A region is defined with a cut off width, γ, defining where the evolution of the level-set function is computed. This method is $O(N)$ where

69

N is the number of grid points inside of the cut-off region. The points outside of the cut-off region must be masked at each time step, and this step is $O(N^2)$.

Changes in the interface topology are well defined in the Level-set method. Additionally, level set methods are computationally inexpensive, as it sufficient to solve the level-set function only near the interface, as Peng demonstrated [173]. While level set methods are beneficial in these ways, they do suffer from mass conservation issues. A variety of hybrid methods have been proposed to combat issues with mass conservation as well as improved accuracy. Combinations of level-set and VOF methods have been put forth by Sussman and Puckett [228], Bourlioux [15], Sussman and Fatemi [227] and van der Pijl [244] which make an effort to overcome mass conservation issues. For improvement to the solution accuracy Enright proposed a hybridized method of level-set with particle methods [45]. Despite improvements in some areas, these approaches introduce artificial fluctuations in the interface curvature as a result of local corrections to the level-set field.

4.2.4 Marker Methods

The marker and cell method (MAC) uses Lagrangian marker particles which are advected with the local fluid velocity to locate the presence of a fluid interface. Marker particle methods were first developed by Harlow and Welch in 1965 [70]. Marker methods can be surface-based, in which particles are only on surfaces, or volume-based when markers exist in entire domain. Surface-based marker methods offer the benefit of being far less computationally expensive than volume-based methods.

Information is exchanged between the Eulerian grid and the Lagrangian particles at each time step by conservative interpolation. A typical computation begins by setting initial conditions and solving for the fluid momentum in the Eulerian grid. Then the momentum is transferred to the Lagrangian grid and advected. Following the advection of the momentum, surface tension forces are calculated and then in-

terpolated back to the Eulerian grid. Once the transferred forces are applied to the momentum equation, the next time step is computed and the the cycle repeats.

While surface-based methods are computationally less expensive, they suffer from the need for numerical surgery in the case of topological changes. Volume-based methods are able to avoid numerical surgery, but are more expensive. Marker methods are good at conserving volume. In general, marker methods are valued for the ability to capture subgrid scale features, such as fluid ligaments. However, grid refinement is often necessary to accurately calculate other physics anyway, negating the benefit of subgrid scale feature capturing. Kothe and Rider argue that practically the marker particle method is costly and suffers from accuracy issues due to the interpolation between the Eulerian grid and the particles [113].

Marker particles have been used with supplemental triangular surface meshes in an arbitrary Lagrangian Eulerian (ALE) framework by Unverdi et al [243], Tryggvason et al [240] [241] and de Sousa et al [35] to calculate surface tension on the supplemental mesh and transfer the solution back to the Eulerian grid. A variety of applications which use extensions of these methods have been performed. Esmaeeli, et al, simulated bubbly flows [46] [47], Juric, et al, utilized this method for boiling applications [98], and Glimm, et al, simulated Rayleigh-Taylor and Richtmeyer instabilities [62] [63].

4.3 Previous CFD Research: Wave-Body Interaction

As mentioned previously, there is a longer history of offshore structure hydrodynamics from both the oil and gas industry, as well as the ship hydrodynamics community. More recently, research efforts have begun to focus more closely on offshore wind farms, both with fixed bottom and floating platforms. Because so much of the hydrodynamics research on offshore wind turbines draws from the experience of oil and gas applications, and ship hydrodynamics research, the discussion of Navier-Stokes ap-

proaches to offshore wind begins with a broader scope. We'll work towards examining recent research in Navier-Stokes approaches to the hydrodynamics of offshore wind turbines by first exploring the broader problems of FSI coupling, multiphase flow modeling with FSI coupling, and then finally conclude with research on monopiles, and lastly on floating platforms.

4.3.1   Fluid-Structure Interaction

The choice in the overall computational scheme for FSI problems is non-trivial. Numerical instabilities are a well known challenge in FSI problems, where the computational method plays a major role in determining whether the system will be stable or not.

The computational approach for FSI problems can be divided broadly into two categories based on the coupling of the fluid and the structural equations. The first method is the monolithic approach in which the entire coupled system is solved implicitly and the solution is converged at each time step [59] [65] [73] [76]. Alternatively, partitioned solvers allow separate treatment of the fluid and the structure. These methods are beneficial due to their flexibility, and often are less computationally expensive as well.

Causin discusses numerical instabilities in loosely coupled FSI schemes in the context of a blood flow problem, but the ideas in his paper affect a wider range of FSI problems too [24]. Causin points out that numerical instabilities depend on both the density of the structure as well as the domain size. It is proposed that explicit couplings may be unconditionally unstable, and that implicit couplings should perform more stably. Förster, et al, provide a proof for the role of the density ratio in numerical instabilities in the sequentially staggered solution framework for FSI problems [54].

A variety of coupling schemes have been derived in the context of partitioned approaches [50]. In a sequentially staggered scheme, shown on the far left hand side of Figure 4.3, the codes are solved one after the other. In this approach, one code must use the solution of the other code from the previous timestep, making this method explicit. The center of Figure 4.3 illustrates a parallel staggered, explicit, approach, in which both codes are solved simultaneously. Both of these explicit approaches exchange information only once per time step. Lastly, the far right side of Figure 4.3 shows a strong coupling approach in which data is exchanged multiple times per time step. This iterative approach performs multiple coupling steps within each timestep, providing updated time step solutions for both codes making it implicit in nature.
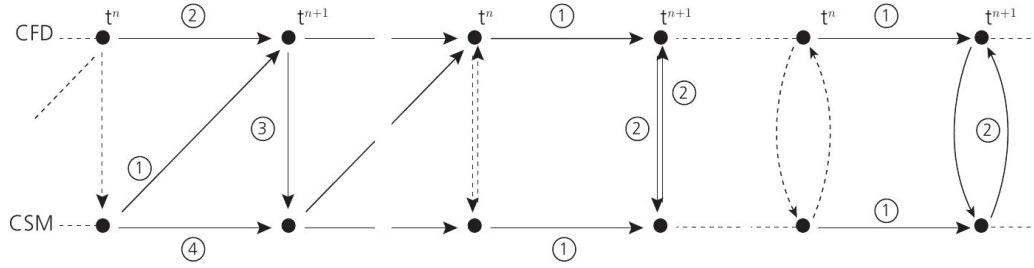
Figure 4.3. Partitioned schemes for loose and tight coupling of fluid and structural codes. The far left illustrates a sequential, staggered, explicit coupling scheme. The middle portion of the diagram shows a parallel, staggered, explicit approach. Finally, the far right side shows a strong coupling scheme, where an iterative approach couples the codes a number of times within each time step. From Ruprecht [193].

Work by Wall, et al, is an example of a iterative staggered, strongly coupled implicit approach to the FSI problem [248]. Wall, et al, simulated a basin with an elastic bottom. An approximate solution for the shape of the flexible bottom and the fluid pressure was determined from a staggered coupling scheme, and then the solution was iterated upon using updated boundary conditions. The fluid was computed with a free-surface that was treated with a deforming mesh. The equations for the fluid and structure are solved using a tightly coupled algorithm. The fluid and

73

structure equations are solved sequentially, in an iterative fashion. The deformation of the structure is updated in each iteration by using the fluid stress from the previous iteration. The fluid is updated following changes in the structure boundary. Iteration and under-relaxation are implemented to ensure convergence of the solution.

Malan and Oxtoby presented a fully coupled, partitioned FSI scheme which was computed in parallel [131] [132]. Their work used a dual-timestepping method in which the fluid and structure equations are solved simultaneously, but separately. At the fluid-solid interface, fluid traction is applied to the boundary of the solid body, and the body velocity is applied to the fluid. Following mesh motion, residuals are recalculated, and the solid and fluid solutions are recalculated until the residuals drop below the convergence criteria. Matthies and Steindorf also used a partitioned approach for solving an FSI problem [135] [134], and their work follows a very similar approach to that of Malan and Oxtoby. Their work used separate treatments for the fluid and the structural computations, and coupled the two components with an algebraic coupling condition. Habchi, et al, used a partitioned solver approach in which the fluid, structure and internal mesh motion were all treated separately [68]. The work simulated structural deformation due to incompressibility, as well as a flap excited by a Von Karman vortex street. Additional work using partitioned approaches for FSI problems have been done by Mok and Wall [149], Kuttler [116], Kassiotis [103], von Scheven [247], Dettemer and Peric [40] [41], Nicholls-Lee [154], Ruprecht [193] and Tezduyar [235] [236]. Partitioned approaches to the FSI problem are revisited below when discussing VOF approaches to FSI problems.

4.3.2 Dynamic Meshing

The numerical domain in the FSI problem can be treated in a variety of ways, one of which is through dynamic meshing in which the domain adapts to follow the movement of the structure. A brief overview of dynamic meshing classifications are

covered here, as well as mention of the challenges and difficulties related to moving meshes. These difficulties include factors such as mesh quality, robustness, efficiency, and numerical errors.

Dynamic meshing can be classified broadly into two categories – the first, where the mesh motion is known *a priori* and the second, in which the mesh motion is determined alongside the flow solution. Externally driven mesh motion includes cases like the prescribed motion of a wing, or a piston. The other type of dynamic meshing, in which the mesh moves with the flow involve cases like 6 degree-of-freedom body motion. Dynamic meshing can also be classified by two major mesh actions, which apply to both external and flow driven mesh motion. Mesh actions can be catergorized as mesh deformation or topological changes. Mesh deformation involves simply moving points, where topological changes alters the number of connectivity points, faces and cells. Furthermore, due to the changing number of cell volumes, topological changes require data remapping, which is prone to errors [83]. While mesh deformation is easier to implement and less prone to errors, sometimes it is not sufficient. Large mesh deformations and rotating motions can lead to mesh quality issues, necessitating topological changes to avoid numerical errors.

One of the main challenges in dynamic meshing is maintaining geometric validity, which includes mesh quality. Geometric validity requires all cells to be convex, and bounds mesh orthogonality to a specified tolerance [85]. Mesh quality can be judged by a variety of indicators, including but not limited to skewness, orthogonality, aspect ratio, smoothness, and condition number [20].

A variety of deformating mesh algorithms have been proposed. One of the most popular approaches to defining mesh motion is the spring analogy. Blom gives a review of the advantages and weaknesses of the spring analogy [14], and Farhat presents the addition of torsional springs to improve robustness of the method [50]. Other ap-

proaches to achieving robust mesh motion include Laplacian smoothing with varying diffusivity algorithms [232].

Issues arise with conservation of mass, and other conserved terms, when the mesh moves and mass fluxes are calculated with grid velocities. Difficulties with conservation can be overcome through the *Space Conservation Law* (SCL), which mathematically describes the conservation of space for a control volume that changes position and shape. The SCL gives the relationship between the rate of the change of the volume of a control volume and the velocity of its surface [53],

$$\frac{\partial}{\partial t} \int_{\Omega} d\Omega - \int_{S} (v \cdot n) dS = 0 \tag{4.40}$$

A more detailed discussion of the SCL is presented by Demirdzic and Peric [39], including an emphasis of the importance of satisfying the SCL and some test cases to demonstrate the point.

4.3.3 Finite Volume Methods with FSI

A variety of finite volume methods have been implemented to treat the fluid part of the FSI problem. Some methods treat the fluid problem with a free-surface, neglecting the air phase, while others simulate both the air and water with a fully two-phase treatment. Discussion of both the free-surface and fluid interface methods are mentioned here. Finite volume methods with FSI coupling have been applied to a variety of applications, largely outside of offshore wind energy. While the work reviewed in this section does not directly cover offshore wind applications, but rather presents similar FSI problems, the same methods can be applied to offshore wind modeling.

Immersed boundary methods provide one approach for solving the fluid flow problem in the presence of a body. Peskin first developed the immersed-boundary (IB) method for biological fluid dynamics applications in 1972, when he simulated cardiac

mechanics and blood flow [175]. Detailed reviews of the method have been given by Peskin [176] and Mittal [148]. Peskin's review provides a mathematically rigorous review of the method, while the latter review by Mittal covers applications of the method, including flow past a truck and sphere, a body tumbling in free fall and flow past flapping filaments. In general, the IB method solves the Navier-Stokes equation on a Cartesian grid. The body's effect on the fluid flow is treated with a force density which represents the force supplied by the surface of the body onto the fluid. This method eliminates the need for a body fitted grid. However, IB methods do suffer from various weaknesses, including challenges with stability, volume conservation and efficiency [153].

Gilmanov and Sotiropoulos implemented a hybrid Cartesian immersed boundary method to simulate flow past moving objects [61]. The code was validated using a rotating sphere. Simulations of flow past a undulating fish-like body and planktonic copepod were carried out. In all cases, the motion of the body was prescribed. Ilinca and Hetu presented results for the flow around rigid bodies using an IB method, but only for the case of static objects [77].

Further work with FSI coupling problems has been carried out without the use of an immersed boundary method. For example, Peric, et al, presented results for the motion of rigid bodies with a free surface RANS approach coupled with an iterative solution method for the 6 DOF motion [69]. The fluid flow was predicted with a commercial CFD software package, and was coupled with a user-coding interface for the 6 DOF motion. In each time step the fluid equations were solved first, followed by a predictor-corrector method for the motion of the rigid body by integration of pressure and shear forces along the body surface. The fluid velocity solution was re-solved after motion of the body, and a new time step was begun.

CFDShip-Iowa is a code that is frequently encountered in the literature for the modeling of ship hydrodynamics. The CFDShip-Iowa code uses the unsteady Reynolds

averaged Navier-Stokes (URANS) equations to solve for the liquid phase. A level-set method is implemented for capturing the free surface. The fluid flow equations are solved, and the forces and moments acting on the ship are found by integrating the elemental forces along the surface of the body. The ship is treated in a non-inertial ship-fixed reference frame with the origin located at the ship center of mass, on to which the forces and moments are projected. A predictor corrector approach is used to compute translational and rotational ship velocities. Rigid overset grids are used, and two to five iterations are performed to achieve convergence of the flow field and ship motions within each time step. Weymouth simulated a Wigley hull in regular waves with the CFDShip-Iowa code [251]. Good agreement was found between CFD predictions and experimental data for a wide range of Froude numbers. Experimental damping and added mass coefficients also showed agreement with the numerical work. Castiglione, et al, simulated a multi-hull catamaran in regular waves using the CFDShip-Iowa code [22]. Maximum response conditions were studied by varying the wavelengths at a fixed ship speed. The CFD predictions showed good agreement with experimental data.

Further development of the CFDShip-Iowa code was done by Yang, et al [260]. A level-set and immersed boundary (IB) method were combined with a sharp interface Cartesian grid solver for simulating ship hydrodynamics. A level-set method was used to find the solution for the free-surface, while an IB method was employed for simulating the motion of the ship. Wave fields around steady forward moving ship hulls were produced. This work was later extended with a strong-coupling scheme to solve fluid-structure interaction problems again in the framework of an embedded boundary [259]. In the later work, the fluid and the structure are treated as part of a single dynamical system where all governing equations are integrated simultaneously. More recently, Yang and Stern devised a simpler and more efficient formulation in which the fluid solver was moved outside of the predictor-corrector loop [261]. Pre-

scribed motion cases were provided as initial validation cases for this work. Strongly coupled interactions, such as vortex induced vibrations and galloping, were presented as well and were in good agreement with experimental measurements.

The Reynolds averaged Navier-Stokes code developed at MARIN, called ReFRESCO (Reliable and Fast RANS Equations (solver for) Ships, Cavitation and Offshore), has also been popular for ship hydrodynamics, as well as oil and gas platform simulations. ReFRESCO has been applied and validated for propeller flows, flow around complex ships, offshore structures in current and wind loads and submarine maneuvers and cavitating flows. Jaouen, et al, simulated the flow around a forced rolling body and investigated the added mass and damping coefficients [82]. The two-dimensional CFD predictions from ReFRESCO were compared with experimental data, as well as results from the commercial CFD package CFX, and excellent agreement was found between all three. Koop and Bereznitski presented results for a semi-submersible modeled with 10 different grids in three different headings (180, 150 and 90 degrees) [111]. The CFD predictions were compared with experimental data, and good agreement was found.

These same RANS based solvers can be applied to the problem of offshore wind turbines. The ship geometries can be replaced with offshore wind turbine platforms to examine the interaction of the waves and the structure. The loading on offshore wind platforms can be investigated in the same manner as is it on ships.

Ship hydrodynamics have also been modeled using the Volume of Fluid approach discussed in the previous section, with a deforming grid. Yang, et al, used a body-fixed reference frame with the origin located at the ship center of mass to simulate motion of a LNG carrier in regular waves [258]. A VOF method was employed which typically models two phase flow. However, Yang's work modeled only the water, and used extrapolation methods to compute the velocity and pressure fields of the air in order to properly model the fluid interface. In each time step the hydrodynamic

forces on the body were computed and then the position was updated, followed by a final update of the flow solution. Mesh topology changes were made when necessary.

Gerrits and Veldman developed, and named, the improved Volume-of-Fluid method (iVOF) for the study of sloshing liquid fuel in satellites [60].The iVOF method uses a structured, non-boundary fitted grid, allowing for the easy generation of the grid around complex structures. The authors argue that the iVOF method improves upon the original VOF method which suffers from the production of flotsam and jetsam, as well as gain or loss of water due to rounding the VOF function. In the iVOF method, a local height function is introduced in conjunction with the original VOF method. This work was extended by MARIN for the application of green water loading [52]. The iVOF method has since been used for anti-roll tank simulations [245], water entry problems for a wedge [109], dam break problems [250], free-hanging subsea structures in regular waves [21], and oil tension leg platforms in extreme waves [89].

Other work carried out with VOF methods includes the approach of body attached meshes, as opposed to deforming grid methods. Panahi, et al, have used VOF with a fractional step method to model a variety of hydrodynamics problems [165] [166]. In their work the mesh is fixed to the body, and moves with the body as the body moves due to forces and moments from the fluid flow. This method has been applied to sloshing, dam breaking with obstacles, as well as cylinder and wedge water-entry problems. Additionally, steady-state forward ship motion has been simulated with this method. All of the work mentioned has been validated with experimental data. Sato, et al, have also implemented a VOF method with a body attached mesh [203]. Ship motion in regular head waves for a Wigley Hull and Series 60 model was simulated. The pitch and heave amplitudes, as well as phase angles, were compared to experimental data and reasonable agreement was found.

Maki, et al, simulated the constant velocity impact of a wedge-shaped body using a VOF method and a one-way fluid-structure coupling approach in OpenFOAM [130].

More recent work by Piro and Maki presented a tightly coupled approach for fluid-structure interations [183]. In this approach information between the structure and fluid is exchanged in a manner that achieves better time accuracy. Under-relaxation and iteration are used at each time step. The under-relaxation factor is selected with a method presented by Causin, et al [24]. Three wedge entry problems are presented as validation cases; one with constant entry velocity of an elastic wedge, another is an entry and exit of a rigid wedge, and finally exit and entry of a hydroelastic wedge. While this work does not present a method for 6 DOF motion, the under-relaxation and iterative solution approach could be extended for freely moving bodies.

Again, these approaches can be applied to model offshore wind hydrodynamics. VOF coupled with a structural solver can simulate the two-phase flow of the ocean and the wind, while treating the platform geometry with a rigid body solver. These methods have been applied to ship hydrodynamics, as well as offshore oil and gas platforms, and can be extended to study offshore wind applications.

Other less common methods for modeling the fluid component of the FSI problem include the fictious domain method, and the constrained interpolation profile method, which are both mentioned here briefly. Fictitious domain methods have been developed for simulating fluid-structure interactions. Quantities are transferred between Eulerian and Lagrangian frames. The basic idea of the fictitious domain method is that the interior of the solid is assumed to be filled with a fluid. The fictitious fluid moves at the same velocity as the solid by a pseudo-body force, e.g. the Lagrangian multiplier. Shi and Lim simulated a variety of flexible bodies in fluid flows using a Lattice Boltzmann Method - Distributed Lagrangian Multiplier/Fictitious Domain (LBM-DLM/FD) method [211]. Yu and Shao also used a fictitious domain method to simulate flow past flexible bodies [264]. Hu and Kashiwagi studied the heave and pitch motion for a Wigley hull in regular head waves using a constrained interpolation profile method (CIP) [75]. This less common approach to fluid-structure interactions was

was first developed by Yabe [257]. Hu and Kashiwagi found good agreement between their numerical predictions and experimental data, except at large wavelengths.

While none of the work presented in this section directly modeled offshore wind applications, each approach can be extended to model the interaction of waves with offshore wind platforms.

4.3.4 CFD of Hydrodynamics on Wind Turbine Platforms

The majority of installed offshore wind turbines use fixed-bottom platforms in shallow waters, however, for transitional to deep water, floating platforms show great potential. Research on the hydrodynamics of monopile support structures has a longer history, due to the greater number of farms that have been proposed and installed with fixed bottom structures. More recently, research efforts have begun to study floating platforms, which are subject to increased motion due to current and wave interactions.

Just as there was a large effort to model wind and wave loading on monopiles with non-CFD engineering tools, there has also been ample work with CFD. Research on monopiles has focused around not only wave loads, but also wave breaking, which can play a significant role for structures in relatively shallow water. Wave run-up has also been a point of focus for research on gravity based foundations in shallow water.

Christensen, et al, presented research on extreme wave forces and wave run-up on monopiles [29]. The work implemented the Navier-Stokes equations, but neglected viscous effects, thus reducing the modeling to the Euler equations. A vertical cylinder placed on a sloping bed was modeled, highlighting the effects of breaking waves. It was shown that breaking waves greatly influence wave run-up and forces on the strucuture. Further work by Christensen was carried out to study irregular wave loading on gravity based foundations specifically sited on Thornton Bank in Belgium [30].

82

Bredmose, et al, simulated wave loads on a gravity wind turbine foundation using a 3D Navier-Stokes solver which treated the fluid interface with VOF [18]. Load predictions from CFD were compared with Morison's equation and good agreement was found for wave load history, but not for extreme loads. Later work by Bredmose and Jacobsen used a 3D CFD model to investigate extreme loads from breaking waves on monopile foundations [16]. CFD results were compared to load predictions from Morison's equation, and found that loads from CFD predictions were larger. Bredmose and Jacobsen presented further work on wave impacts on monopiles, again with a VOF method from OpenFOAM [17]. Wave run-up on monopiles was also investigated by Peng, et al, with the commerical CFD software ComFLOW [172].

Wave forces on a single cylinder, and on a pair of cylinders, which is representative of monopiles for offshore wind turbines, as well as oil and gas support structures, was modeled by Kamath, et al [100]. CFD results were computed with RANS and a level set method modeling the free surface of the water. Load predictions from CFD were compared with Morison's equation and MacCamy-Fuchs theory, and good agreement was found.

Additional research on wave impacts on monopiles was carried out by Zhou, et al, specifically for the Shanghai Donghai-Bridge offshore wind farm in China [269]. OpenFOAM was used to model waves with VOF and RANS, and wave run-up as well as load predictions were examined. Lara, et al, also studied wave interaction with single- and multi-piled structures using an OpenFOAM based approach [119].

CFD research on platforms other than monopiles has been carried out as well, though not in as great of volume. Koop and Bereznitski presented results for a semi-submersible modeled with 10 different grids in three different headings (180, 150 and 90 degrees) [111] using the REFRESCO code, which was discussed earlier. The CFD predictions for loads on the semi-submersible in current were compared with experimental data, and good agreement was found.

Vortex induced motions (VIM) are known to affect the fatigue life of platforms such as TLPs and semi-submersibles. Work has been carried out with CFD to study VIM on a variety of platforms in current and waves. Kim, et al, used CFD to investigate VIM on a TLP platform, building upon previous work on spar VIM [106]. Tan, et al, studied VIM on a multi-column floating platform [230]. Commercial CFD software was used to investigate VIM, and good agreement was found between calculations and experimental tank measurements. Lefevre, et al, presented VIM studies of a spar with strakes, pipes, chains and anodes using the Improved Delayed Detatched Eddy Simulation turbulence model [123].

The CFDShip-Iowa code, discussed earlier in the contect of ship hydrodynamics modeling, was utilized by Quallen, et al, to simulate a spar mounted wind turbine [184]. The spar buoy was simulated in free decay tests, as well as in regular waves. The crowfoot and added yaw-stiffness mooring line models were investigated. CFD results were compared to motion predictions from FAST, and good agreement was found for most of the degrees of freedom, with the largest differences seen in the yaw motion.

Free decay tests of a spar buoy were simulated by Beyer, et al, [12]. The multi-body aero-servo-hydro-elastic wind turbine simulation tool, SIMPACK, was coupled with the commercial CFD code, ANSYS-CFX, which was used to model the hydrodynamic loads. The hydrodynamic modeling in ANSYS-CFX used a VOF approach to treat the two-phase flow. Surge, sway, roll, pitch and yaw DOFs were enabled, and surge and pitch motions form a free decay surge motion test were compared between CFD and HydroDyn. Future work will look at more complex geometries, and interaction of geometries with incident waves.

Simulations of free decay tests of the DeepCWind semisubmersible were presented by Dunbar, et al, [42]. The authors modified the standard Volume-of-Fluid 6-DoF coupling code in OpenFOAM to enhance stability and accuracy. The solver tightly

couples the solutions for the fluid and structure by implementing subiterations in each time step, as well as relaxing the 6 DoF solution. Convergence at each time step is ensured, and the Aitken method is used to accelerate the solution, which is now more computationally expensive due to the subiterations. The heave and pitch free decay cases presented by Dunbar, et al, are compared against predictions from FAST and good agreement was found. The work does not include mooring lines, relaxation zones or an implementation of wave boundary conditions.

CHAPTER 5

VALIDATION OF THE CURRENT APPROACH

Because CFD is used as a foundation for developing and judging the accuracy of other models, significant effort has been invested in validating the predictive ability of the CFD model. The assessment of the CFD model includes validations of wave propagation in a numerical domain, force predictions on floating bodies, and finally free-body motion due to wave-body interaction.

First, validation cases for waves propagating through a numerical domain are presented. These cases include regular Stokes waves, as well as irregular waves representative of the ocean environment. Simulation results are compared to both wave theory, which is described in some detail in Chapter 1, as well as experimental measurements from the DeepCWind tank tests [34].

Next, the prediction of forces on immersed bodies is validated against a range of experimental data. Validation cases include stationary cylinders in uniform flow, regular waves, and finally irregular waves. Numerical results for these cases are validated against experimental data from Sarpkaya and Isaacson [202] and Niedzwecki [157], respectively. Additionally, the forced oscillation of a vertical cylinder in zero-mean flow is simulated, and the numerical results are compared to experimental data from Mercier [138].

Finally, validation of the six degree-of-freedom solver in OpenFOAM is presented. First, the straightforward case of a floating object displaced from its point of hydrostatic equilibrium is presented. The ability of the code to predict the equilibrium position of the floating object is demonstrated. Next, the free roll decay of a rect-

angular barge is presented, as well as the induced roll motion of the same body in waves. Numerical results are validated against experimental work by Jung [97].

5.1 Wave Propagation in a Numerical Domain

A sample of two- and three-dimensional simulations of wave-only tests were conducted. First, results from simulations of regular waves are presented, and the results are compared to theoretical values computed from Stokes wave theory, detailed in Chapter 1. Further examples are given of regular wave simulations corresponding to wave properties from the DeepCWind data set [34]. Additionally, a range of irregular wave cases are provided to demonstrate the ability to properly model waves that interact with the spar buoy, tension leg platform and semi-submersible platforms in the ocean environment. Validations of wave simulations are provided by comparing numerical results with experimental results measured in the DeepCWind tests, as well as statistical measures for the irregular wave cases.

This work models wave propagation with the Volume of Fluid approach, discussed in detail in Chapter 4. A wave library developed by Niels Jacobsen at the Technical University of Denmark is used in this work [80]. The wave library contains a variety of wave theories, including first, second, fifth order Stokes waves, as well as cnoidal, solitary and bichromatic waves. Additionally, irregular waves can be generated from the Pierson-Moskowitz and JONSWAP spectra.

The time-varying velocity, volume fraction and pressure gradient are prescribed on the inlet boundary throughout the simulation. Initial conditions can be prescribed as the user wishes. Unless otherwise noted, the simulations presented in this section had an initially quiescent flow field, that is zero velocity everywhere in the domain. It should be noted that it is also possible to prescribe a spatially varying velocity and pressure field as the intial condition, where the fields are calculated according to the wave theory selected by the user.

In modeling waves in a numerical domain it is important to avoid the spurious reflections off numerical boundaries. Jacobsen's wave generation toolbox includes the ability to specify relaxation zones as a method to mitigate artificial wave reflection in the computational domain. Explicit relaxation of the velocity and volume function is implemented to lessen the non-physical reflection of waves off boundaries such as outlets. Relaxation is accomplished via a weighting function which is placed in user specified relaxation zones. The weighting function [80] is given by,

$$\alpha_R(\chi_R) = 1 - \frac{exp(\chi_R^{3.5}) - 1}{exp(1) - 1} \text{ for } \chi_R \in [0; 1] \tag{5.1}$$

And relaxation is is applied with,

$$\phi = \alpha_R \phi_{computed} + (1 - \alpha_R)\phi_{target} \tag{5.2}$$

The relaxation zone implementation is illustrated in Figure 5.1.
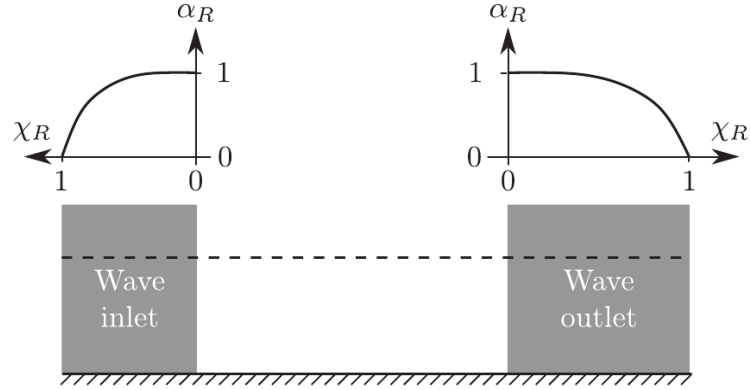
Figure 5.1. Illustration of the relaxation zones for an inlet and outlet. The variation in α (weighting function) and χ (lzone length) is shown above the relaxation zone boundaries. Figure taken from [80].

5.1.1 Regular Wave Modeling

Validation of the wave modeling begins with the simplest case of a regular Stokes wave propagating through a numerical domain. First, numerical wave profiles are validated against Stokes wave theory. Next, numerically generated regular waves are compared with experimental data, and excellent agreement is demonstrated.

In validating numerical solutions of the Stokes wave against linear wave theory, it is necessary to obey the assumptions of the theory. This is especially important in the limiting cases of shallow and deep water, where water depth classifications were made in Chapter 1, and are shown in Table 1.3.
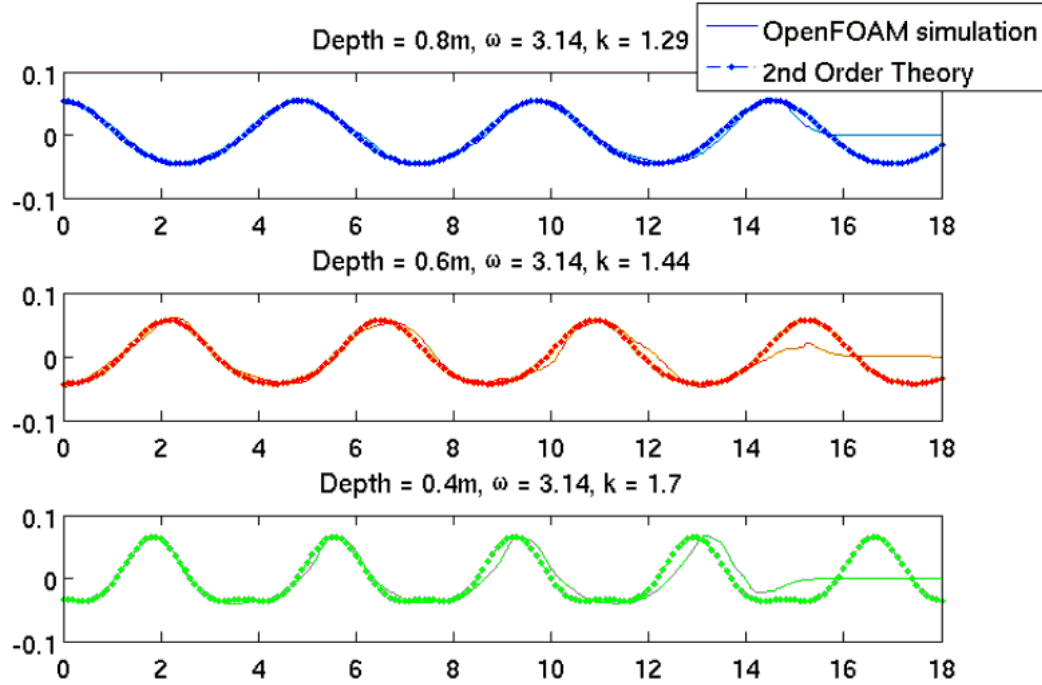
Figure 5.2. Profiles of 2nd Order Stokes waves with a frequency of 3.14 rad/s at varying water depths. The x-axis is the distance through the domain, and the y-axis gives the wave height. Numerical results are shown in the solid line, theoretical wave profiles are represented with dots. A relaxation zone begins at 15m, which accounts for the disagreement between simulation and theory at the far right end of the domain.

Linear wave theory approximations are valid in the shallow water limit when the ratio of wave height to water depth is small, as shown in Figure 1.4 in Chapter 1. In the deep water limit, these assumptions are valid when the ratio of wave height to wave length is small. When these assumptions are obeyed, the numerical solutions closely match analytical solutions, as expected. A sample of cases is presented to validate the wave generation codes used in this research against theory.

To examine the effect of water depth on the simulated wave fidelity, a variety of depths were modeled with an unchanging wave frequency. The results shown here demonstrate the ability to accurately model the wave numerically. All of the results shown in Figure 5.2 fall within the intermediate water depth classification.
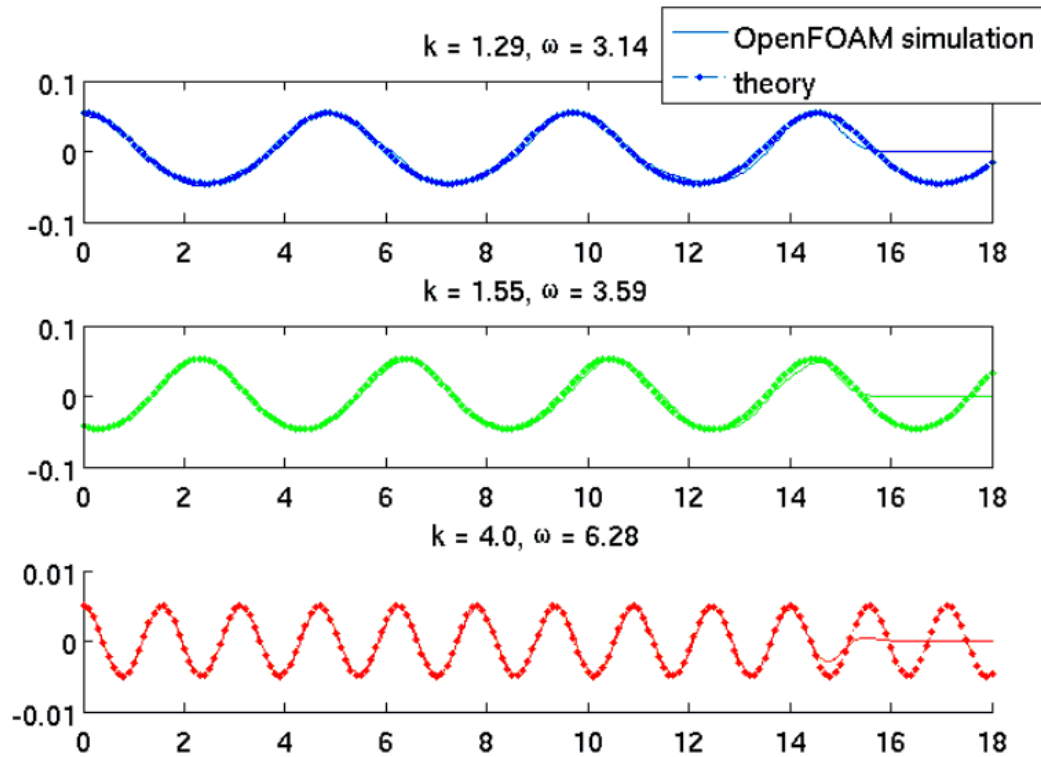
Figure 5.3. Profiles of 2nd Order Stokes wave in a constant depth of 0.8 m with varying wave frequencies. The x-axis is the distance through the domain, and the y-axis gives the wave height. Excellent agreement was found between theory and simulation. A relaxation zone begins at 15m, so only the data before 15m are expected to agree.

Additionally, simulations were carried out over a range of wave frequencies but with a constant water depth of 0.8 m. The results of these simulations are shown in Figure 5.3. The top two wave profiles displayed both fall in the intermediate water depth category, while the third wave falls in the deep water limit. In the case of the last wave, the ratio of wave height to wavelength is 0.06, which is appropriately small to obey the assumptions of linear wave theory. Again, the simulations show excellent agreement with the theory.
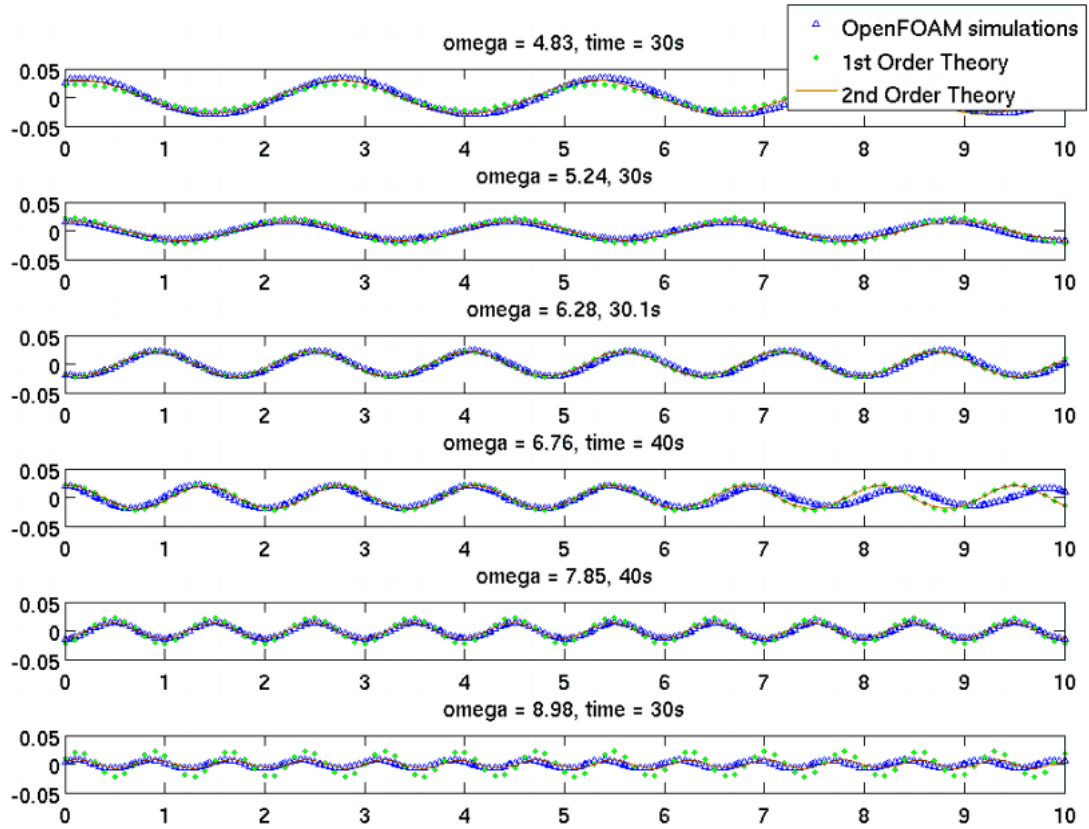
Figure 5.4. Regular waves traveling towards a barge located 20 m from the inlet. Simulations results are shown with triangles, 1st order theory is represented by dots, and the solid line displays the 2nd order theory. Excellent agreement was found between the numerical simulation and 2nd order theory.

Further simulations were done with a floating object inside the computational domain. Where the previous results were computed with relaxation zones at the

domain outlet, the following cases include the impermeable surface of the barge at the air-water interface. In these cases waves can and do reflect off the surface of the barge. The figure is provided to demonstrate the ability of OpenFOAM to capture the wave profile for a variety of wave frequencies and wave heights. In Figure 5.4, the data between 0 and 10 m has been enlarged to better exhibit the excellent agreement between theory and simulation, although the full domain was longer, with the barge located 20 meters from the inlet.

Overall, for a variety of water depths, wave heights, wave frequencies and wave numbers, excellent agreement has been found between 2nd order linear wave theory and the numerical results computed with OpenFOAM. Confidence in the model's ability to accurately capture regular wave propagation through a computational domain is high.

Following the validation of wave modeling against theoretical results, numerical results were then compared to experimental results from the DeepCWind tank tests [34]. DeepCWind model tests of the spar buoy, tension leg platform and semisubmersible platform were carried out with a variety of wave properties, both regular and irregular. This section describes results from regular wave simulations and the next section covers irregular wave simulations. Table 5.1 shows the regular wave properties from the DeepCWind Floating Wind Turbine Model Tests technical report [34]. A sample of regular wave cases was selected for simulation to demonstrate a range of wave properties that can be modeled with high accuracy. All work shown here is in the absence of the floating platform, which is consistent with the wave height measurements taken in the tank.

A mesh was generated to match the dimensions of the MARIN wave tank, and is shown in Figure 5.5. A 3d rectangular mesh was created with roughly 1.9 million cells. Cell refinement was concentrated around the air-water interface. The mesh was decomposed into 32 subdomains for simulation in parallel on 32 cores.

Table 5.1. Regular wave properties from the DeepCWind tank tests. Adapted from the DeepCWind technical report [34].

Wave case	Amplitude (m)	Period (s)	Wave frequency (rad/s)
Regular 1	0.960	7.5	0.8378
Regular 2	3.789	12.1	0.5193
Regular 3	3.568	14.3	0.4394
Regular 4	3.787	20.0	0.3142
Regular 5	5.152	12.1	0.5193
Regular 6	5.370	14.3	0.4394
Regular 7	5.561	20.0	0.3142
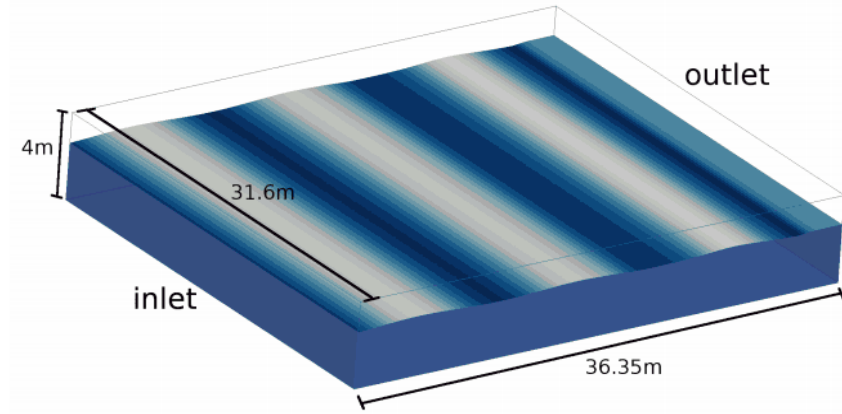
Figure 5.5. Computational domain illustrated with the fluid interface colored by surface elevation. The regular wave travels from left to right. Dimensions of the computational domain match those of the MARIN wave tank.

A set of validation cases is presented here to demonstrate the ability of the CFD model to accurately capture wave propagation seen experimentally. All of the properties given in Table 5.1 were scaled from prototype to model size using Froude scaling. First, the wave profile for the Regular 3 case is presented. The Regular 3 wave has an elevation of 3.568m and 14.3s period at prototype scale. The wave profile, from numerical and theoretical predictions, is shown in Figure 5.6 at four different times. It is shown that the simulation results are in excellent agreement with the profile determined using linear wave theory. It should be noted that relaxation zones were

implemented at the outlet to prevent wave reflection. The deviation in wave profiles between simulation and theory from roughly 32m to the outlet, at the far right, is due to the use of relaxation zones. The use of relaxation zones at the outlet is consistent with the experimental use of wave absorbing beaches.
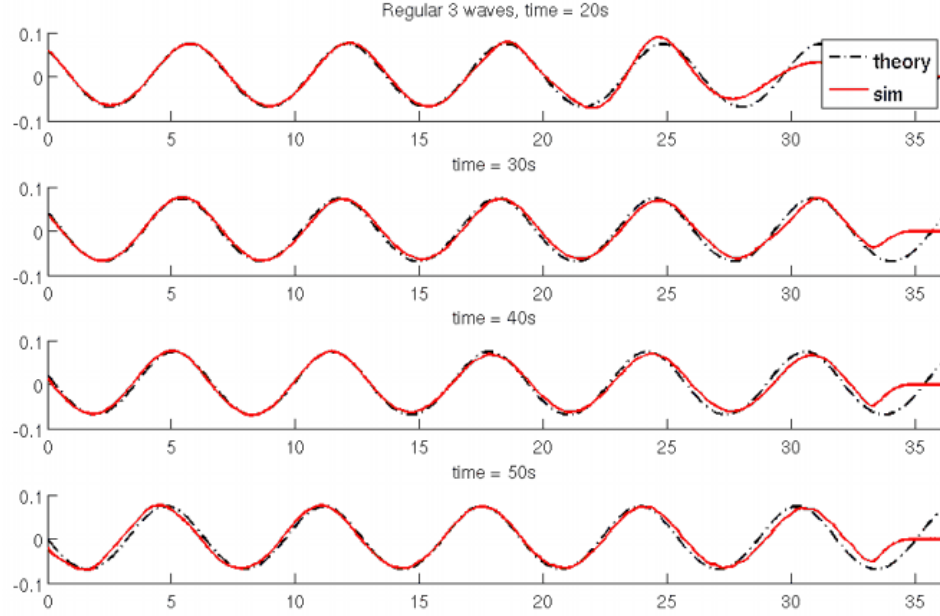
Figure 5.6. Wave profiles of the regular 3 wave at various times throughout the simulation.

Numerical and theoretical wave profiles for the Regular 7 wave were also compared. The Regular 7 wave has a 5.561m amplitude and a period of 20 seconds, before model scaling. Again, excellent agreement was found between the simulations and linear wave theory.

Regular wave simulations were post-processed in an effort to compare numerical results to experimental results, as opposed to theoretical results. Wave probes were used in the DeepCWind tests to measure wave heights at reference locations in the wave basin. The wave heights in the simulations were sampled at the same reference location in the wave tank where the wave probes were located in the experiments.

Here, the wave height of the Regular 3 wave is sampled in time, and is plotted against the experimental wave height time history provided by MARIN at the "wave 180" probe location. The wave height time history is shown in Figure 5.7. It is shown that the wave simulations in OpenFOAM are in excellent agreement with the wave heights measured by the wave probe in the tank tests.
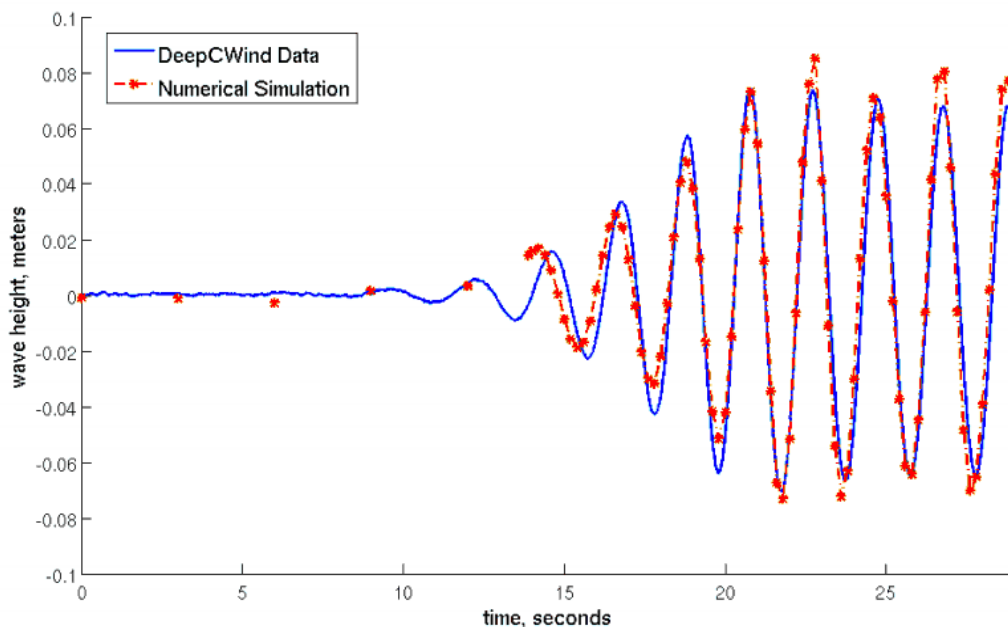
Figure 5.7. Excellent agreement was found between the wave height time history measured by MARIN, shown with a blue solid line, and the numerical results simulated with OpenFOAM, presented in the red dash-dot line.

This validation work is particularly significant because it demonstrates the ability to numerically propagate waves that agree well with waves generated experimentally. Moving forward, there is great confidence that the waves modeled numerically with OpenFOAM will match experimental waves. Furthermore, there is high confidence in the ability to simulate extreme wave cases that have not been produced experimentally but will be modeled numerically.

5.1.2 Irregular Wave Modeling

DeepCWind model tests were also carried out with irregular waves. Both the model tests and numerical simulations of irregular waves use the JONSWAP wave spectra. The irregular wave properties are listed in Table 5.2 below, again reproduced from the DeepCWind technical report [34]. Simulations of these irregular wave-only tests have been carried out. The Operational 2, Design/Survival and Bi-directional sea state tests were simulated. The results for the Operational 2 case are presented here.

Table 5.2. Iregular wave properties from the DeepCWind tank tests. The significant wave height, peak spectral period and peak enhancement factor (γ) value for the JONSWAP spectrum are presented in the table. Adapted from the DeepCWind technical report [34].

Environmental Condition	H_s (m)	T_p (s)	γ
Operational 1	2.0	7.5	2.0
Operational 2	7.1	12.1	2.2
Design/Survival	10.5	14.3	3.0
Bi-directional Sea State	7.0	12.1	2.2
	2.1	20.0	6.0

The Operational 2 and Design/Survival cases were simulated using the mesh from the regular wave simulations. Again, the simulations were computed in parallel on 32 cores. An image of the surface elevation for the Operational 2 wave is shown in Figure 5.8.

For validation, a time history of the surface elevation at the wave probe location was extracted from the numerical simulation. The simulated wave height time history for the Operational 2 wave is shown in Figure 5.9. Directly comparing the time histories of the wave heights for the numerical and experimental data does not provide significant insight since randomness is introduced through parameters such as phase angle. Statistical measures are necessary for comparing the predicted results from the simulation versus the measured results from the experiment.
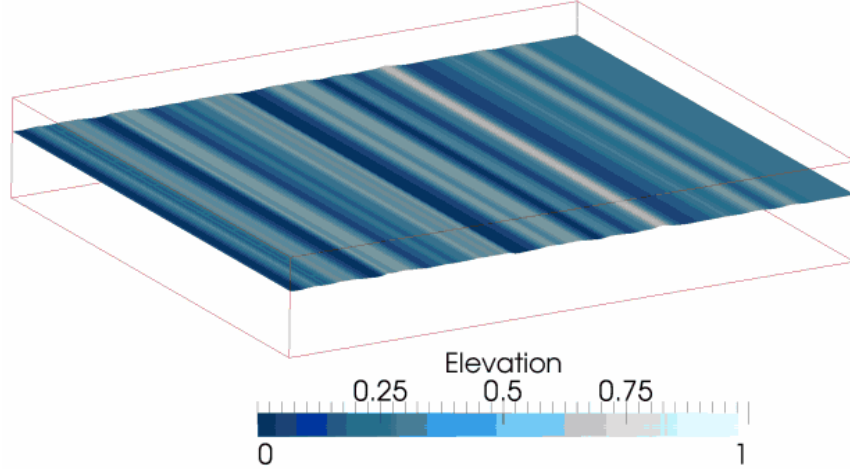
Figure 5.8. The Operational 2 wave shown at 30s of simulated time. The maximum and minimum surface elevations are shown as elevation values of one and zero, respectively.

The literature suggests that N, the sample size from the JONSWAP spectrum, should be at a minimum of 200 to ensure randomness of the time history [26]. The effect of sample size on both the significant wave height and peak spectral period was investigated in this work. Increasing the sample size leads to a greater sampling of points in the vicinity of the peak of the spectrum, which was found to be important for simulating irregular waves with the correct significant wave height and peak spectral frequency. An example of the numerically generated wave height time history for the Operational 2 wave is shown in Figure 5.9. This simulation was produced with a sample size of N = 200 from the JONSWAP spectrum. The window from 25 to 120 seconds is shown.

The peak spectral period was determined from taking the FFT of each of the wave height time histories, and determining the inverse of the peak of the frequency spectrum. The FFTs are plotted in Figure 5.10. It is shown that the waves generated with N=300 give the best agreement with the target peak spectral frequency, supporting the hypothesis that a large sample size from the JONSWAP spectrum is
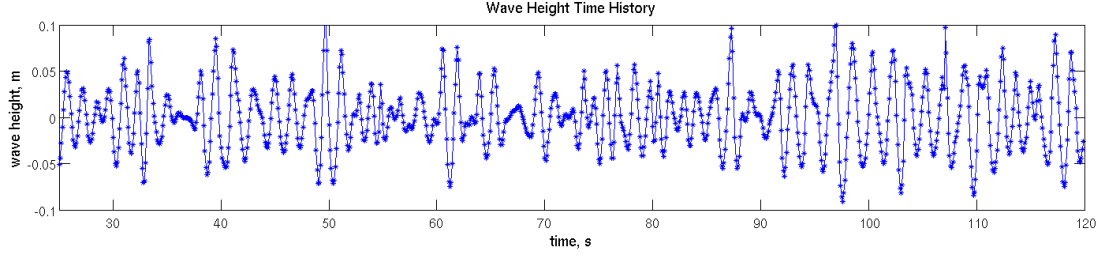
Figure 5.9. Numerical results from an irregular wave simulation. The wave height time history is shown between 25 and 120 seconds of simulated time. The wave heights here are shown at model scale. The results above are from a simulation with N = 200.
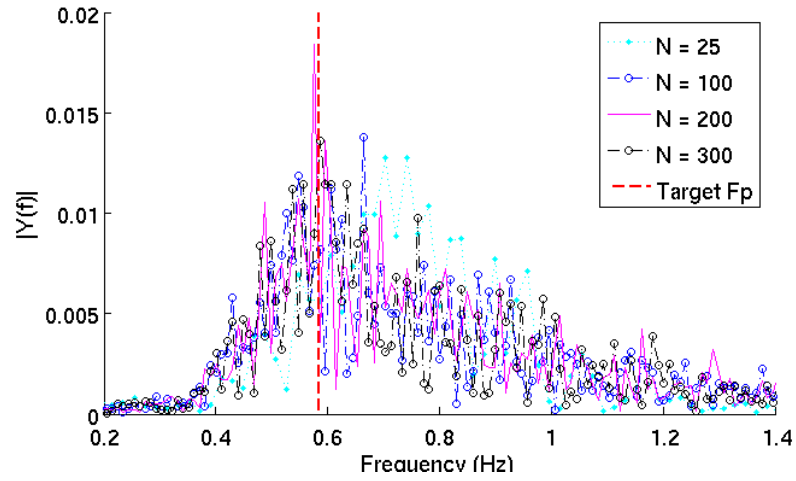
Figure 5.10. The FFT of the numerical wave height time history for the Operational 2 wave case. The input peak spectral frequency to the target JONSWAP spectrum is shown in the red dotted line. The FFTs for the four sample sizes are shown.

necessary. The peak spectral period was determined from FFT, which is very noisy, this could be another reason why the experimental and numerical values are not in excellent agreement.

The significant wave heights were calculated using the definition of four times the standard deviation of the wave height. The significant wave heights and peak spectral periods for the Operational 2 waves with sample sizes of 25, 100, 200 and 300 are given in Table 5.3. The significant wave height for the numerical simulations

gradually increases with the rise in sample size, and then dips for the N=300 case. The simulation carried out with 200 sample points from the JONSWAP spectrum returned the results most closely in agreement with the experimental data set. These simulations were carried out for relatively short time periods, and that is likely the reason for the slight disagreement between experimental and numerical significant wave heights. The numerical simulations were carried out to only 120s.

Table 5.3. Comparison of experimental and numerical significant wave heights and peak spectral periods for the Operational 2 wave case. Values are given at full scale, not model scale. The table demonstrates that increasing the sample size from the JONSWAP spectrum returns wave statistics that are in better agreement with the experimental data.

	Experimental	Numerical (N=25)	Numerical (N=100)	Numerical (N=200)	Numerical (N=300)
T_p	7.3	5.5	6.45	6.9	6.7
H_s	12.02	10.05	10.65	12.27	12.06

This work demonstrates that the sample size N from the JONSWAP spectrum plays an important role in the agreement between experimental and numerical wave statistics. Future work involving the interaction of floating platforms in irregular waves will take these findings into account.

Furthermore, this work demonstrates the ability of the CFD model to accurately simulate irregular waves sample from the JONSWAP spectrum. There is high confidence that the model is capable of generating high fidelity waves that are representative of the ocean, and even more specifically match experimental conditions from tank tests.

5.2 Validation of Hydrodynamic Load Predictions on Offshore Structures

In addition to the validation of the wave model, the code that predicts the loads on the floating structures must be validated. A sample of experimental data have been

selected from the literature, starting with the simplest case of a cylinder in uniform flow, and growing in complexity towards simulating free 6 DoF rigid body motion of a floating wind turbine platform in irregular waves.

A handful of validation cases are presented in this section. First, uniform flow past a stationary cylinder was simulated in an effort to match the drag coefficient versus Reynolds number curve by Sarpkaya and Isaacson, which is commonly used for selecting coefficients for FAST [202]. Next, the stationary cylinder was simulated in the presence of regular waves, and the results were compared to experimental data from Niedzwecki [157]. Finally, forced oscillation of a vertical cylinder was simulated and the results were compared to data presented by Mercier [138].

5.2.1 Drag coefficient versus Reynolds number curve

Uniform flow of water past a vertically mounted circular cylinder was simulated over a range of Reynolds numbers, and the resulting drag coefficients were calculated. A 0.254cm diameter cylinder with a height of 0.1 m was placed in a 0.6 m by 0.6 m domain.

An example force time history curve for the inline (drag) direction is shown in Figure 5.11. At early times the predicted force shows initial transient behavior before settling out to a periodic state. Once the periodic state behavior is reached, a sample window is created over an integral number of periods, and the average force is calculated. The sampling window is illustrated with the dotted lines, and the solid red line indicates the average force.

Each simulation used the same sized cylinder, but the uniform flow velocity was adjusted to change the Reynolds number. At low Reynolds numbers, direct numerical simulation (DNS) was employed. At higher Reynolds numbers a turbulence model was used, as the meshing requirements for DNS at high Reynolds numbers becomes unrealistically large.
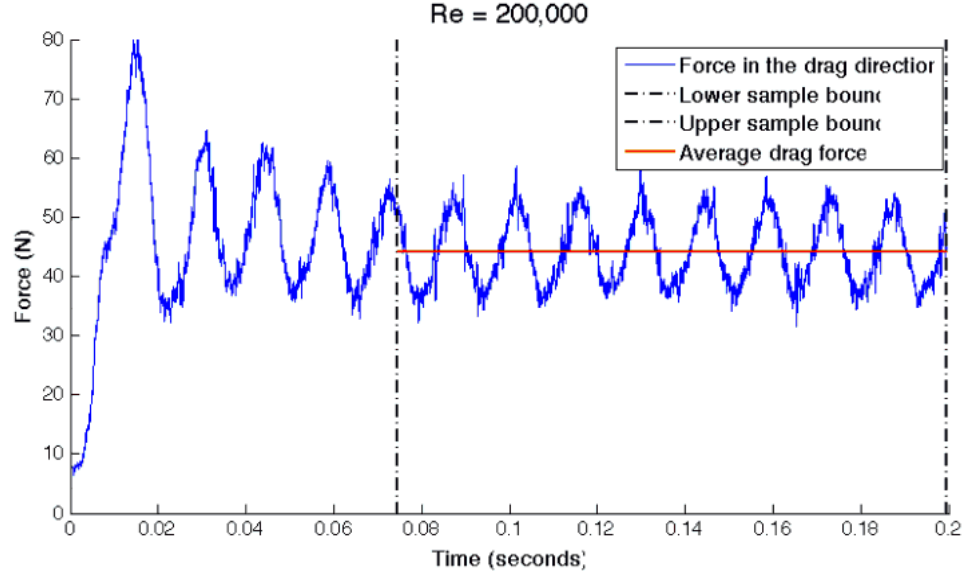
Figure 5.11. Example inline force time history for a stationary cylinder in uniform flow. The Reynolds number is 200,000 for this case. The dotted lines indicate the sample window for calculating the average drag force, which is illustrated by the solid red line. The Spalart-Allmaras turbulence model was used in this simulation.

The majority of results presented were simulated with the Spalart-Allmaras turbulence model. The k-Epsilon turbulence model was tested in some simulations, but the results exhibited excessive damping of the shedding vortices. Furthermore, the k-Epsilon RNG model was also tested, and again, there was excessive damping of the vortices. At this Reynolds number periodic behavior due to vortex shedding is expected. Detached Eddy Simulations (DES) were also carried out, and the results did not yield good agreement with experimental results. It was found that the Spalart-Allmaras turbulence model resulted in the best agreement between numerical and experimental data. These trends are demonstrated in the top plot in Figure 5.13.

Once the Spalart-Allmaras turbulence model was selected for simulations, a sensitivity study of the turbulent viscosity initial condition was performed. The results from this study are shown in the bottom plot of Figure 5.13. It was found that a turbulent viscosity value of 10^{-6} $Pa{\cdot}s$ for the initial condition yielded the best results.
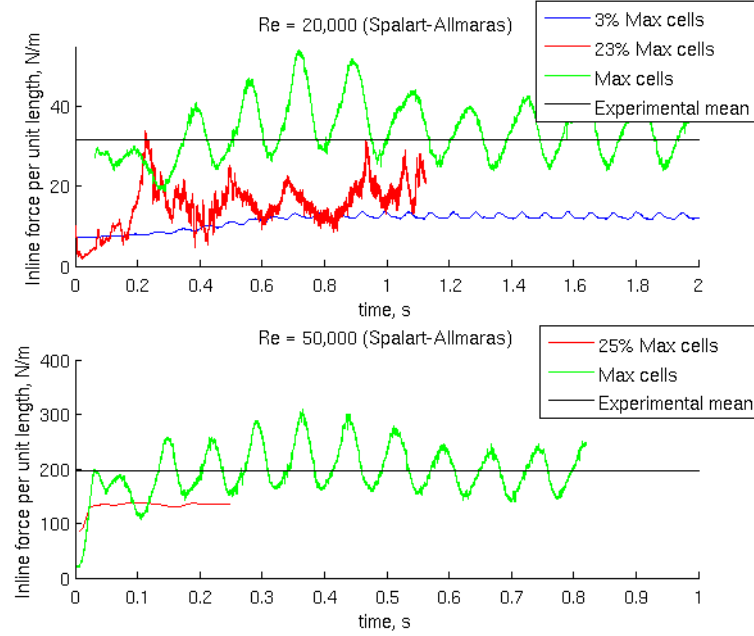
Figure 5.12. Examples of convergence testing at two Reynolds numbers. The top plot shows the inline force prediction at Re = 20,000 for three meshes, quantified again the mesh with the maximum number of cells. The same is shown on the bottom plot for simulations at Re = 50,000.

That is, the vortex shedding reached a quasi-steady state behavior, and the predicted mean inline force matched well with experimental results.

In addition to testing multiple turbulence models and carrying out a sensitivity study to the initial conditions of the Spalart-Allmaras turbulence model, convergence studies were also performed. Figure 5.12 shows force per unit length time histories at two Reynolds numbers. The top plot shows results at a Reynolds number of 20,000, and the bottom demonstrates the force predictions at 50,000. The experimental mean is plotted in the solid black line. In each case, the numerical results match well with the experimental value when the largest mesh was used.

The results for the drag coefficient over a wide range of Reynolds numbers are presented in Figure 5.14. It is shown that ample experimental and numerical work has been performed to study the drag coefficient across a wide range of Reynolds numbers.
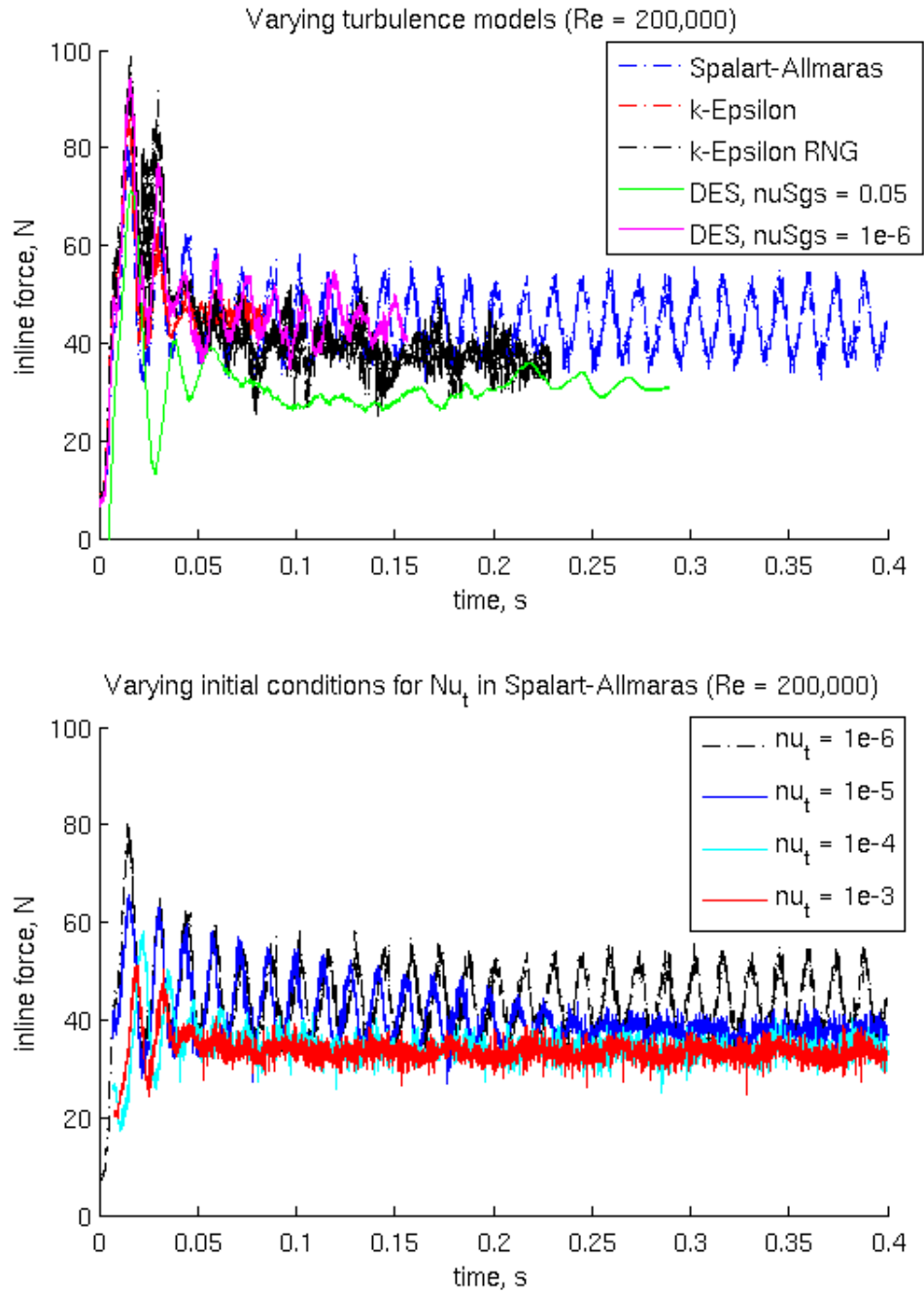
Figure 5.13. Inline force results from simulations with various turbulence models, shown on top. On the bottom, force predictions with varying initial values of ν_t are shown.
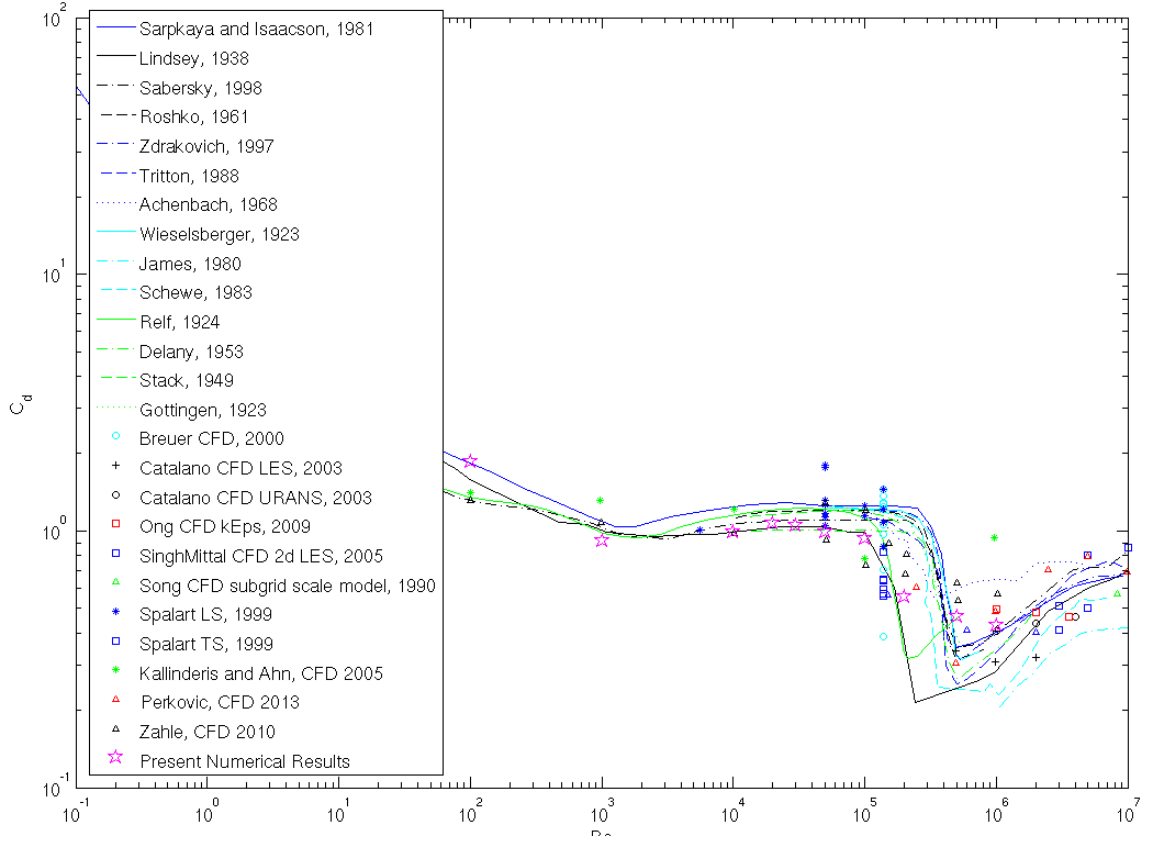
Figure 5.14. Drag coefficient versus Reynolds number curve for a smooth cylinder in uniform flow. Our numerical results calculated with OpenFOAM are shown with magenta stars. Other CFD work is shown with other symbols. Various experimental data is presented in the black, green and blue lines.

Reasonable disagreement still exists in the experimental work, and the numerical predictions vary widely, especially in the region of higher Reynolds numbers.

Figure 5.15 gives an overview of the entire Reynolds number range simulated in the present work, plus an enlarged view of the region of interest for floating wind turbine platforms, on the bottom plot. The numerical results are presented alongside experimental data from a variety of authors, as well as two sets of numerical results also generated with CFD. Experimental work is presented from 14 different authors [2], [38], [58], [81], [114], [156], [186], [191], [195], [199], [202], [205], [239], [253], [267].
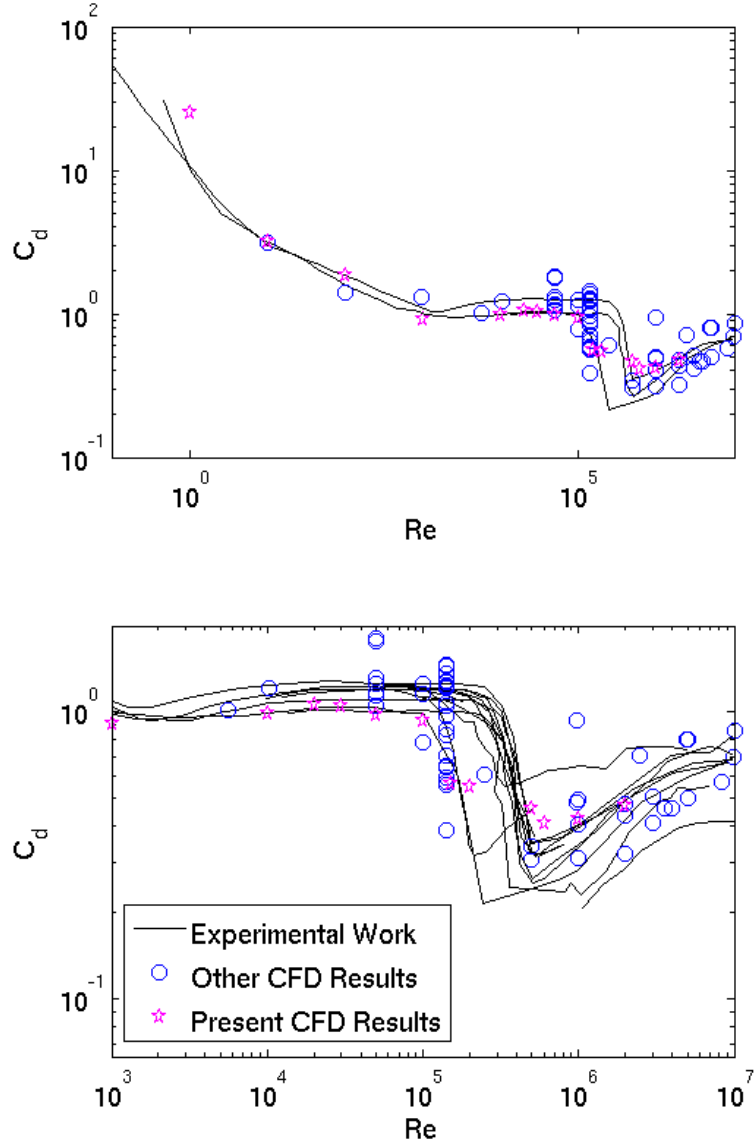
Figure 5.15. The drag coefficient versus Reynolds number results across the full range of Reynolds number studied, and in the region of interest where the Reynolds number is very large, shown on the bottom.

Results from CFD simulations are presented from 8 authors [19], [23], [99], [174], [212], [214], [238].

It can be seen in Figure 5.15, where the region of high Reynolds number flow has been enlarged, that there is a sizable scatter in experimental results. Furthermore, a large spread in numerical results from CFD simulations with varying turbulence
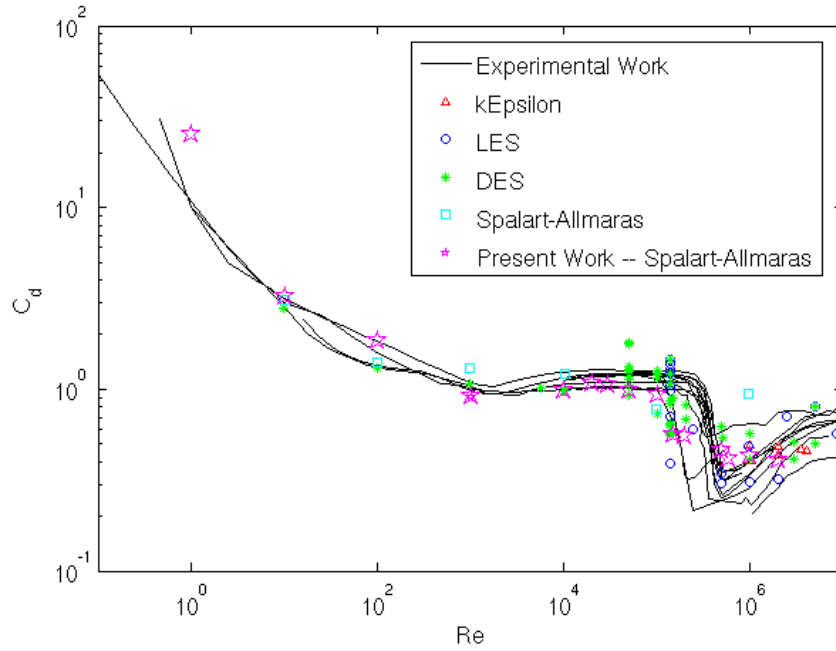
Figure 5.16. The present numerical results simulated with a Spalart-Allmaras turbulence model are compared to numerical results from the literature, categorized by turbulence model.

models is seen. The results from the present work fall among the other authors' accuracy of prediction, and at some Reynolds numbers the predictions from the present work do a better job. There is high confidence in the ability to simulate uniform flow past stationary bodies, and to predict loads accurately. This provides confidence in simulating offshore wind turbine platforms in current.

5.2.2   Static Cylinders in Regular Waves

The next validation case looks at regular waves propagating past a vertically mounted, stationary, surface-piercing cylinder. Niedzwecki carried out experiments with a cylinder of radius 0.057 m in a tank with a depth of 0.91 m [157]. Regular waves with a wide variety of wave properties were generated at the inlet. The experimental work presents the maximum force in the inline direction, as well as wave run-up on

the cylinder, both as a function of the scatter parameter, ka, where k is wave number and a is the cylinder radius. The case set-up is shown in the Figure 5.17.
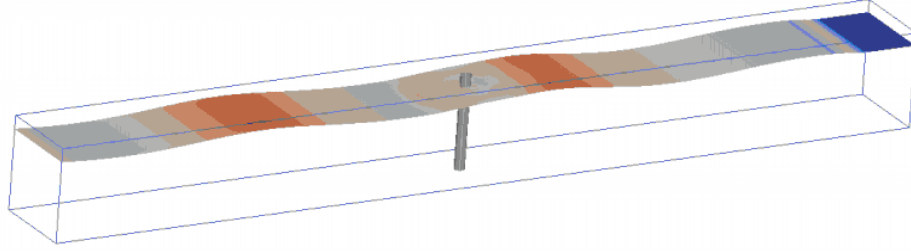
Figure 5.17. Numerical domain for the case of a vertical cylinder in regular waves. The boundaries of the domain match the experimental tank measurements in the work by Niedzwecki [157]. Waves propagate from left to right, past the surface-piercing cylinder in 0.91m depth.
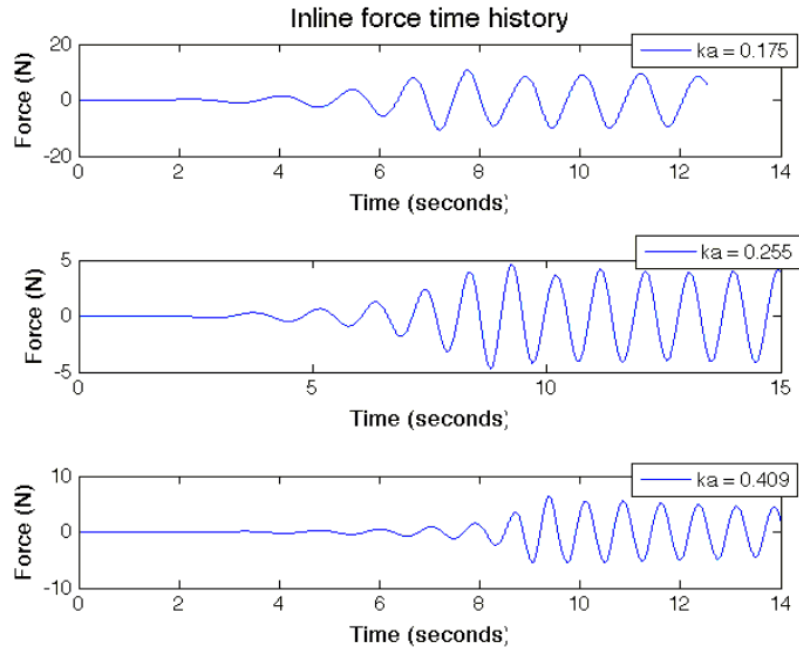
Figure 5.18. Three example inline force time histories for the surface-piercing cylinder in waves. The top case shows the inline force on the cylinder for a scatter parameter of 0.175, followed by cases with scatter parameters of 0.255 and 0.409.

A variety of regular waves were simulated, capturing a range of the experimental data. The wave heights and periods were varied to match the wave properties used experimentally. Three example time histories of the inline force on the cylinder are shown in Figure 5.18. It can be seen that the force on the cylinder slowly grows as the waves begin to propagate towards the cylinder. At later times, once the fully developed waves have reached the cylinder the force oscillates in a periodic state manner.
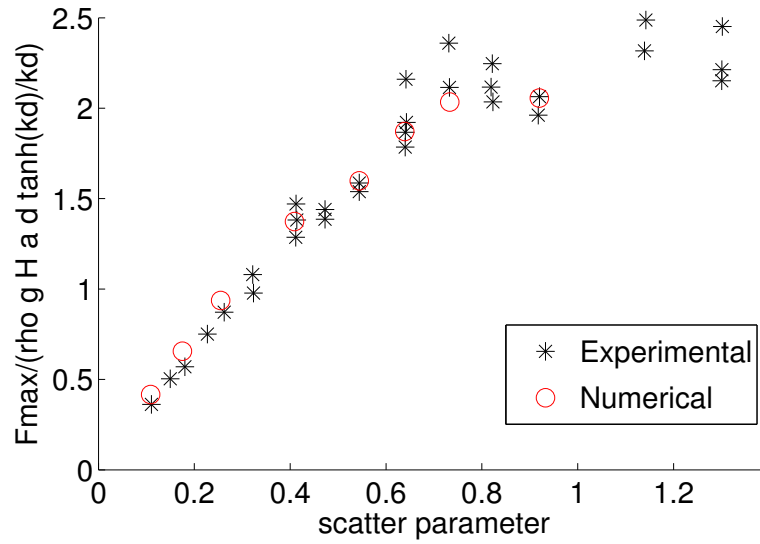
Figure 5.19. Numerical and experimental results for the maximum inline force on the vertical cylinder in waves, as a function of the scatter parameter. Experimental results are shown in black stars, and numerical results show excellent agreement in red circles. Experimental data extracted from Niedzwecki [157].

Figure 5.19 shows the numerical and experimental results for the maximum force in the inline (wave propagation) direction. It is shown that over a range of scatter parameters, ka, the predicted maximum inline force predicted by OpenFOAM is in good agreement with the experimental measurements presented by Niedzwecki [157].

Additionally, the experimentalist presented results for wave run-up amplification factor. Comparison between experimental and numerical wave heights provides con-
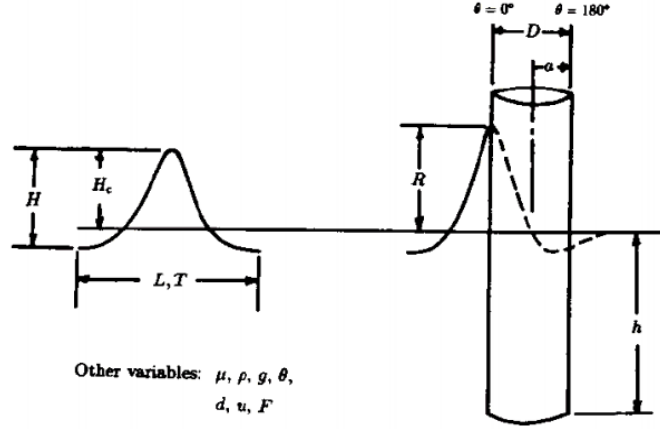
Figure 5.20. Definition of wave run-up parameters, taken from Niedzwecki [157]. The wave run-up is defined as the height of the water on the surface of the cylinder, measured from the still water level. The wave height follows the usual definition of trough to crest height. The amplification factor is calculated as the ratio of wave-run up to wave height, R/H.

fidence in the ability to accurately model the air-water interface. The wave run-up is illustrated in Figure 5.20, where R is defined as the height of the water on the cylinder measured from the still water level, and H is defined as the full wave height from trough to crest. The amplification factor is defined by the ratio of R over H. The numerical results were post-processed to determine the maximum fluid interface height on the surface of the cylinder, and the amplification factor was then calculated. The numerical and experimental results are shown in the left side of Figure 5.21. The experimental and numerical results show good agreement, however the wide scatter in experimental data does not present a convincing validation test. Additional data for the wave height around the cylinder proves to be a better measure against which to validate.

These additional data are presented as the water surface height around the cylinder as a function of theta. For the case where $ka = 0.175$, Niedzwecki gives the wave height for the run-up and run-down, where the wave is at its maximum and minimum, respectively, as a function of theta. Theta is zero at the front of the cylinder, and
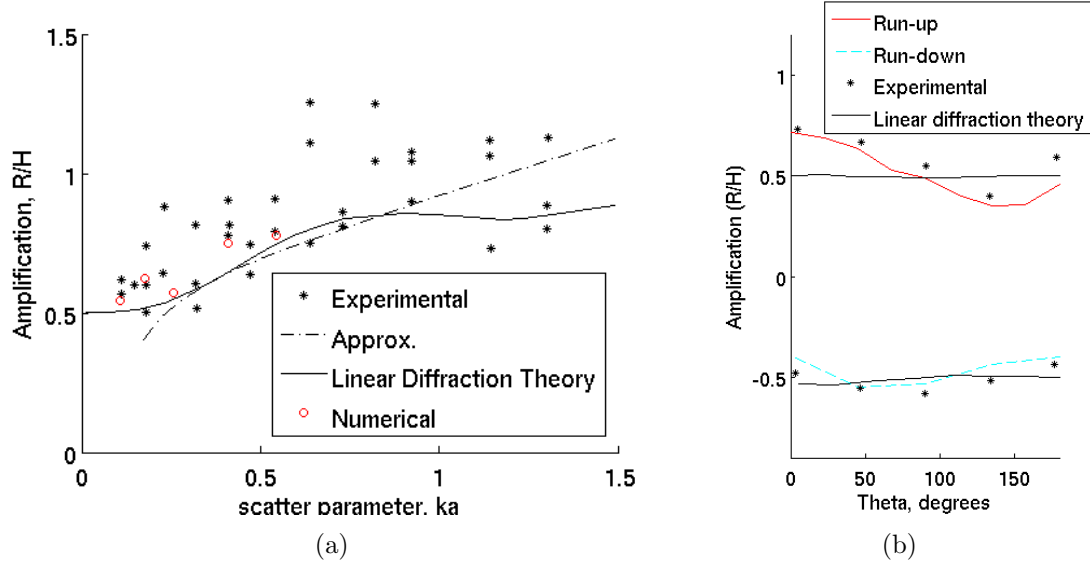
Figure 5.21. Amplification factor results for the stationary cylinder in regular waves. a) Wave run-up as a function of scatter parameter. The experimental results are shown in black stars, alongside the approximated fit shown in the dotted line, as well as the linear diffraction theory prediction. Numerical results from OpenFOAM as shown in red circles. b) Amplification factor around the cylinder as a function of theta. Numerical results are shown by the red and blue lines, indicating run-up and run-down, respectively.

180 at the back. Experimental measurements, results from diffraction theory and the present numerical water height predictions from CFD are shown in Figure 5.21 on the right. The results show that OpenFOAM predicts the surface height around the cylinder for both wave run-up and run-down with much better agreement to experimental results than diffraction theory was able to achieve.

5.2.3 Static Cylinders in Irregular Waves

Niedzwecki also took experimental measurements of the forces on the vertical, staionary cylinder in irregular waves. The JONSWAP spectrum was used for developing the random wave generated in the experimental tests. More specifically, the conditions were chosen to match storm conditions in the Gulf of Mexico [157]. Loading on the cylinder is presented as the root-mean-square (RMS) of the inline force.

Two simulations were carried out, matching two of the experimental cases. The wave parameters for the two simulations are shown in Table 5.4.

Table 5.4. Irregular wave parameters as inputs to the JONSWAP spectrum, and the experimental and numerical results for the RMS of the inline force.

Case	$H_s(cm)$	$T_p(s)$	γ	Experimental F_{rms}	Numerical F_{rms}
1	4.57	1.19	3.3	5.36	5.23
2	4.42	1.21	7.0	5.4	5.48
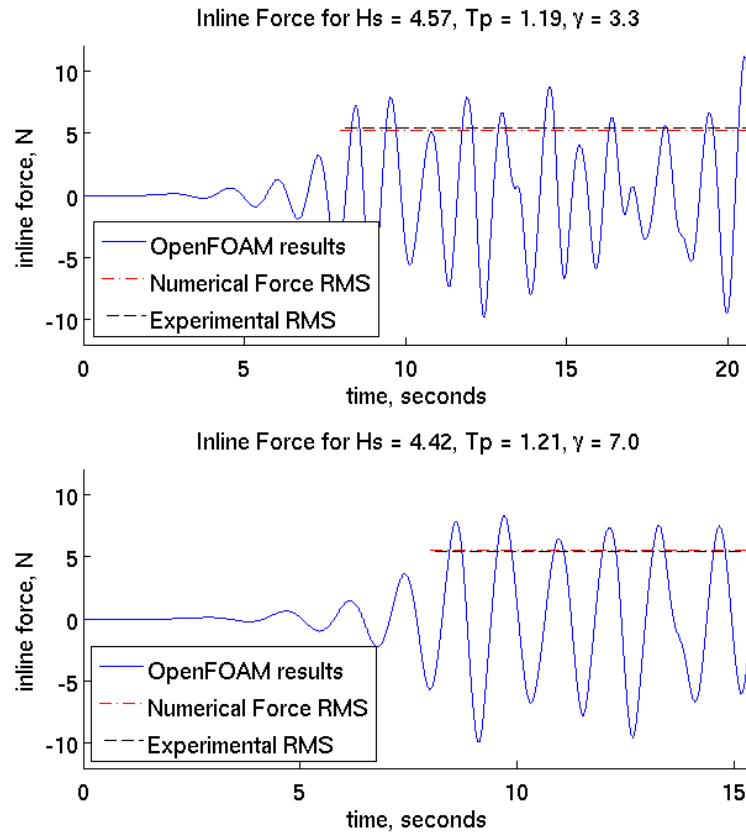
Figure 5.22. Inline force predictions from OpenFOAM for the two cases with wave parameters from Table 5.4. The numerical and experimental inline force RMS values are plotted to demonstrate their agreement.

The inline force time history is shown in Figure 5.22 for both of the cases outlined in Table 5.4. The top plot shoes the results for Case 1, and the bottom plot

demonstrates the results for Case 2. The RMS of the inline force was calculated for each case, once the fully developed waves reached the cylinder. The computed RMS value is plotted in a dotted red line alongside the experimentally determined RMS shown in the black dashed line. For both cases the RMS of the inline force are in excellent agreement. The RMS values of the inline forces are also presented in Table 5.4. The numerically predicted forces on the cylinder in irregular waves closely match experimental measurements, just as they did for the cylinder in regular waves. There is confidence in the ability to not only simulate propagating irregular waves in a numerical domain, but additionally to accurately predict loads on bodies due to incident waves.

5.2.4   Forced Oscillation of a Cylinder in Zero Mean Flow

The next validation case concerns the forced oscillation of a vertically mounted cylinder in zero mean flow. Numerical predictions are compared to experimental work carried out by Mercier [138]. The cylinder was oscillated at varying amplitudes, which match the experimental parameters. The case set-up is shown in Figure 5.23. A cylinder with a 1 inch diameter was oscillated at a range of amplitudes between 0.5 and 3.0 diameters. Mercier presents oscillographic records of the forces in the inline and transverse direction to the cylinder motion, over a range of amplitudes, all at a frequency of 1 Hz.
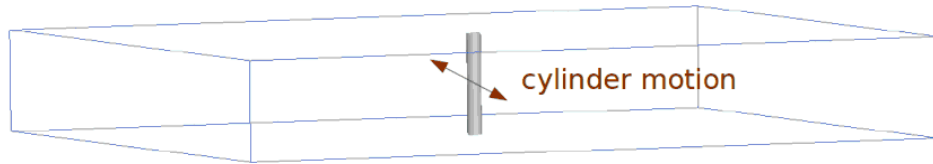
Figure 5.23. Numerical domain used to simulate forced oscillating cylinder in zero-mean flow. Dimensions are consistent with those used in the Mercier's experiments [138]. The cylinder is mounted vertically and oscillates transversely.
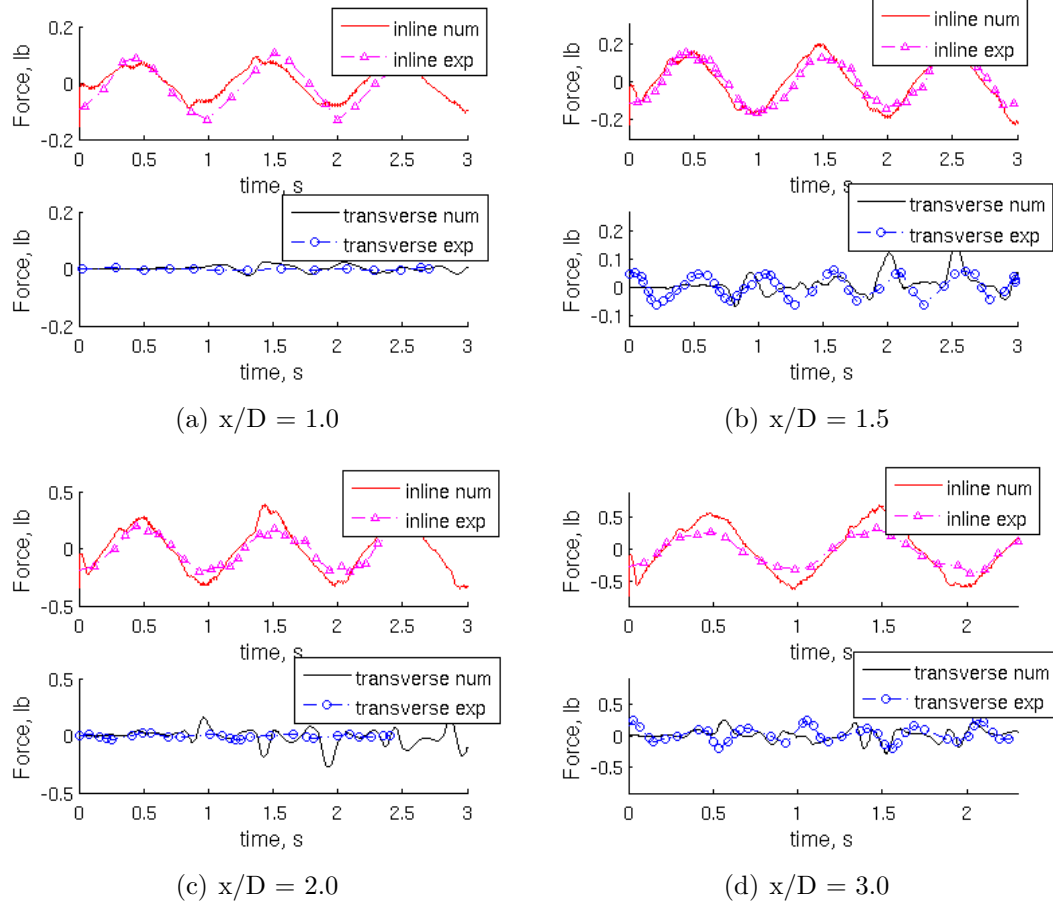
Figure 5.24. Inline and transverse forces on the cylinder with forced oscillation at 1 Hz. The amplitude of oscillation varies for the four cases shown, between 1.0 and 3.0 diameters. Experimental data taken from Mercier [138].

Results for the force on the cylinder in the inline and transverse flow directions are shown in Figures 5.24(a) through 5.24(d), below. Numerical results are presented for four different amplitudes of oscillation. It is shown that for a range of oscillation amplitudes, the numerical and experimental results are in good agreement in both the inline and transverse flow directions.

The inline forces predicted by the model show better agreement with the experimental data than the transverse forces. The forces in the transverse direction are known to be more difficult to measure precisely. This is due to the lift forces acting in the transverse direction, such that the object can wobble due to shedding vortices.

The amount of wobble depends on the stiffness of the object, as well as the strength of the mounting. It is difficult to recreate the exact degree of stiffness of the cylinder in the numerical simulation. In many cases, including this work, the cylinder is assumed to be completely rigid. This may explain the poorer agreement between numerical and experimental results in the transverse direction.

5.2.5 Hydrostatic Equilibrium Validations

To validate the 6DoF code in OpenFOAM, a basic hydrostatic equilibrium test was conducted with a square buoy. A variety of masses were chosen for the floating object, which was placed in a quiescent flow field with the same initial position for each case. The floating object was then allowed to move freely until settling into a position of hydrostatic equilibrium. The depth of the center of gravity was computed following the force balance given by Archimedes' principle. The five masses that were chosen and their corresponding depths of center of gravity are shown in Table 5.5.

Table 5.5. Floating object masses and depths of center of gravity.

Case No.	1	2	3	4	5
Mass (kg)	4.5	4.75	5.0	5.25	6.0
Depth of CG (m)	0.0550	0.0650	0.0750	0.0850	0.1150

The floating object is 0.25m x 0.25m x 0.1m, and the center of gravity is initially positioned at 0.075m below the water surface. Results for the five cases are shown in Figure 5.25. The red dotted lines indicate the theoretical depth of the center of gravity, while the blue solid lines represent the transient motion of the object as calculated by OpenFOAM. It is shown that as time passes the floating object oscillates around its theoretical equilibrium point, and eventually converges to a final position that agrees with the theory.
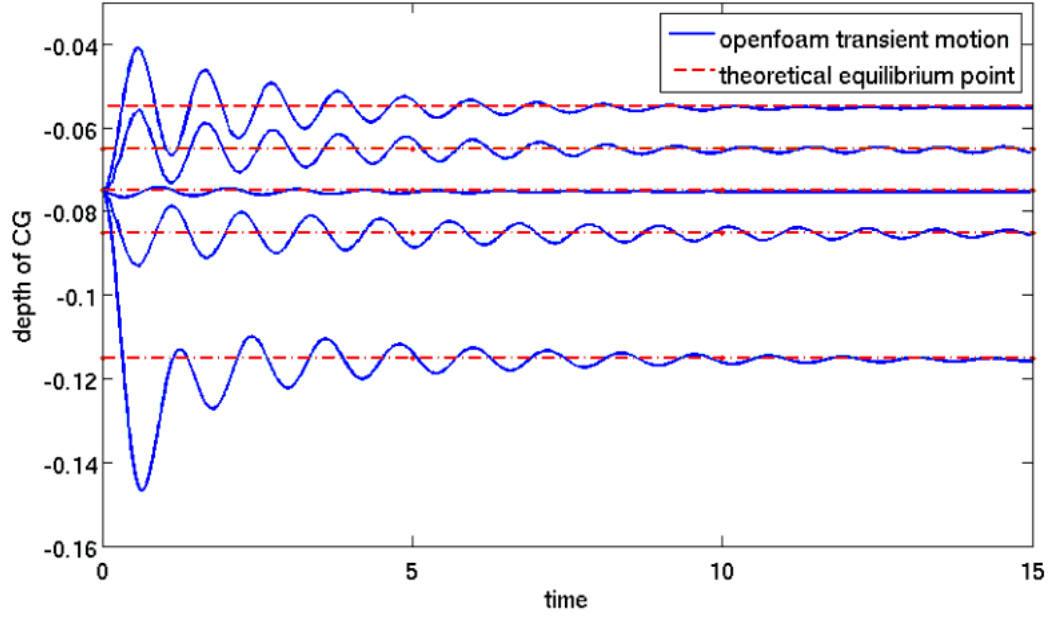
Figure 5.25. Time history, in seconds, of floating objects center of gravity position below water surface. Red dotted lines show theoretical hydrostatic equilibrium position, solid blue lines display transient motion of the center of gravity as it converges to the point of hydrostatic equilibrium.

5.2.6 Roll Motion of a Rectangular Barge

The free roll decay motion of a rectangular barge was studied experimentally by pre-tilting a barge to 15 degrees in a wave tank of still water, and allowing the barge to rock back and forth, or free roll decay, until reaching an inclination of zero degrees [97]. The wave tank used in the experiments was 35 m long, 0.9 m wide and had a water depth of 0.9 m. The barge was 0.3m long, 0.9m wide and 0.1 m tall, and placed 20 m from the wave maker. The barge was mounted to the walls of the wave tank with hinges located at the center of gravity. The case of the free decay of a rolling barge is illustrated in Figure 5.26, below, taken from Jung [97].

To examine the damping, the fluid viscosity was increased by a factor of 400. It was found that the damping was only minimally affected, leading to the conclusion that damping must be due to small waves transporting kinetic energy away from the
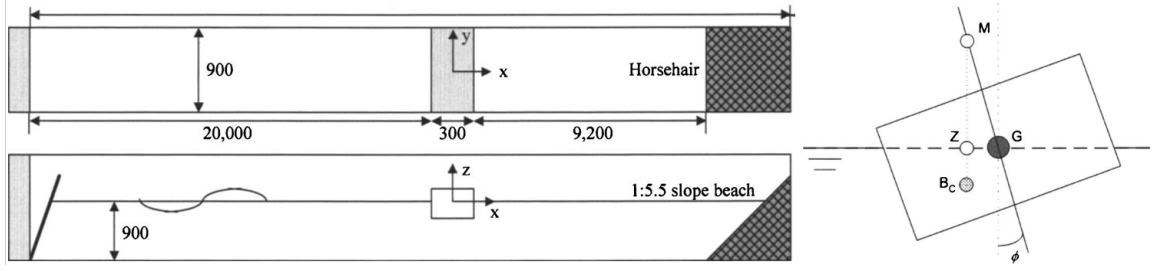
Figure 5.26. Experimental set-up for the rolling barge. The image on the left shows the wave tank, with the wave maker located on the left, and horsehair used on the right hand side to damp out reflecting waves. The image on the right illustrates the pre-tilted barge used as the initial condition for the free roll decay case. Images taken from Jung [97].

system. Therefore, the case requires a finer mesh than was previous used, in order to properly refine the small waves that radiate away from the barge as it rolls.

Finally, the frequency of oscillation is not affected by the damping, but rather other characteristics of the system. There is some doubt about the accuracy of the moment of inertia that was reported in the paper, and unfortunately the mass of the barge was not reported in the paper, nor in the corresponding dissertation.

In light of these findings, a series of new simulations were carried out in an effort to find better agreement between the experiment and the numerical predictions. First, a more refined mesh in the region of small wave radiation was generated. Additionally, an updated moment of inertia was calculated. The paper reports that the barge is constructed of acrylic. It was assumed that the barge is not constructed of solid acrylic, but rather as a solid box made from sheets of acrylic. (Confirmation of this from the paper's author is still pending). The material properties for acrylic sheets were found, and the resulting mass and moment of inertia were calculated. It was found to have a mass of 15.26 kg and moment of 0.125 $kg \ m^2$. Simulations were then carried out with a coarse and refined mesh, and with the newly calculated barge

116
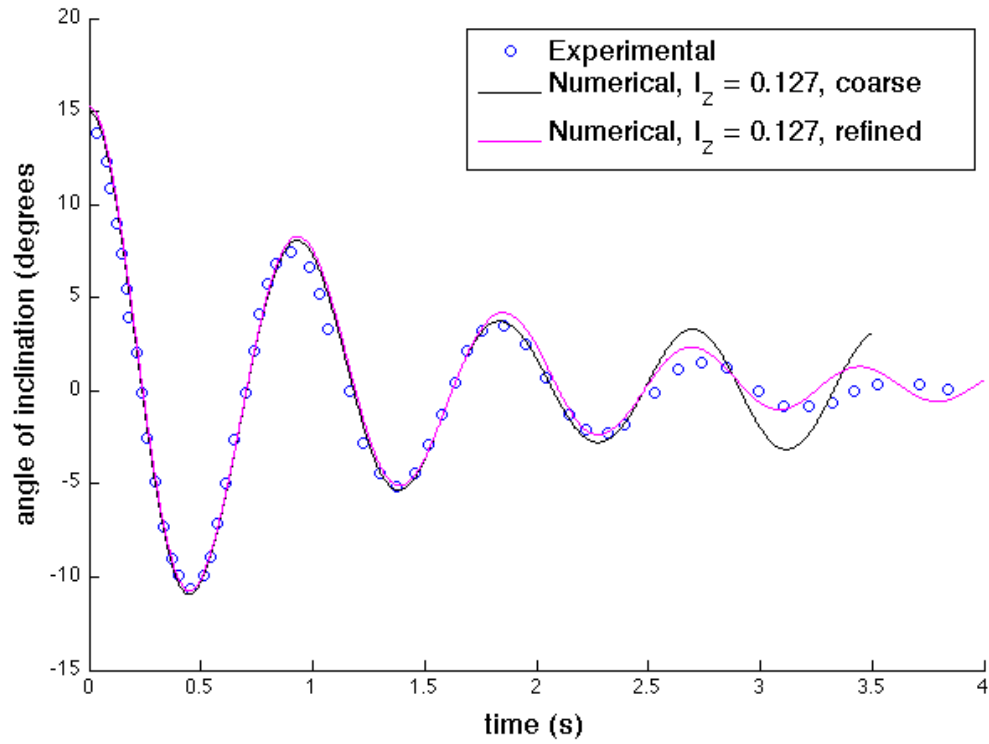
Figure 5.27. Results for the free decay roll motion of a rectangular barge in still water. The numerical results for a coarse and a refined mesh are shown in black and magenta, respectively. The experimental results are shown in blue circles.

properties. The results are shown in Figure 5.27. The numerical results show good agreement with the experimental data, especially for the more refined mesh case.

CHAPTER 6

FLOW PAST SURFACE-PIERCING CYLINDERS OF VARYING ASPECT RATIOS

6.1 Introduction

Understanding the flow behavior around finite surface-piercing cylinders with small aspect ratios is of fundamental importance to many engineering applications, including floating offshore structures. Very few studies have addressed the combined factors of a free-surface and truncated end of a cylinder. Flow past infinite, fully submerged cylinders is well understood, due to ample experimental and numerical studies [19, 23, 66, 99, 125, 128, 174, 191, 195, 202, 205, 215, 238, 256, 267]. Generous attention has been given to the isolated effects of finite cylinders, as well as surface-piercing cylinders. Far less research has been carried out, experimentally or numerically, on the simultaneous effects of a free end and free surface. Here, numerical investigations of surface-piercing, finite length cylinders are carried out over a wider range of aspect ratios than has previously been studied. The results are compared against experimental measurements, also performed by the authors. The effects of a free-surface and truncated end are discussed in terms of drag, lift and frequency content at at Re and Fr numbers not studied previously.

Previous to this work, insight about the combined effect of these factors has been presented by a very small number of studies including Hay [72], Goncalves [64] and Rosetti [189]. The present work uses both experimental and numerical results to extend the range of studies to include a wider range of aspect ratios than has previously been presented, and also provides insight about the critical aspect ratio when

a free surface is also present. Furthermore, the combination of the two factors is investigated, including which one, if any, is dominant across a range of aspect ratios. Additionally, sectional loads along the length of a cylinder with aspect ratio of 12 are given, providing insight about the flow behavior as it relates to a free surface and a free end. This investigation of loads as a function of length has not been previously presented for the case of a surface-piercing cylinder with a truncated end.

This work differs from previous work because it investigates the combined factors of a free-surface and free-end with numerical and experimental values across a wide range of aspect ratios not previously investigated. Furthermore, the present work provides loads as a function of cylinder length.

6.1.1 Surface-Piercing Cylinders

Surface-piercing cylinders have been investigated both experimentally and numerically. Experiments on surface-piercing cylinders were carried out by Akilli & Rockwell [10] and Chaplin and Teigen [27]. Akilli & Rockwell's experiments involved flow visualizations using visualization marker and particle image velocimetry [10]. Chaplin and Teigen found that the local drag coefficient on the cylinder decreased near the still water line, in other words, near the free surface [27].

Numerical work on the drag coefficients of surface-piercing cylinders has been carried out by Kawamura [105], Yu [263] and Suh [221]. In each of the papers, the drag coefficient for the cylinder in the presence of a free surface was found to be smaller than the subcritical constant value of 1.2 at Reynolds numbers below 1.4×10^5 for a fully submerged cylinder. This is consistent with the experimental findings from Chaplin & Teigen [27]. Previous work, both experimental and numerical, demonstrates that the presence of a free surface leads to a reduced drag coefficient.

In addition to effects on the drag behavior, the presence of a free surface has been shown to affect vortex shedding and lift forces. Yu found that vortex shedding was

suppressed near the free surface, which alters the lift forces acting along the length of the cylinder [263] . Experimental work by Inoue also found that vortex shedding was not seen near the free-surface [78].

6.1.2 Cylinders with Free Ends

Investigations of finite cylinders have been carried out both experimentally and numerically to investigate the effects of a free end on the overall flow regime. A thorough review of research on the flow field around free ends is given by Sumner [223].

Experimental studies have shown the drag coefficient decreasing with reducing the aspect ratio. This includes work by Sumner [224], who investigated a vertically mounted cylinder on a flat plate. Farivar [51] also studied drag coefficients of cylinders with small aspect ratios, and saw reductions in the drag coefficient. These relationships between drag coefficients and aspect ratio are consistent with other work in the literature by Sakamoto [197], Taniguchi [231], Okamoto [163], Luo [127], Iungo [79] and Okamoto [162]. Reductions in the drag coefficient of finite length cylinders has also been demonstrated numerically, including work by Lee [122], Pattenden [170] and Frohlich [56]. Further numerical work on cylinders with free ends can also be found in Majumdar [129], Afgan [6], Palau-Salvador [164] and Krajnovic [115].

Investigations of flow past finite cylinders of various aspect ratios has shown that the Karman vortex shedding is greatly affected by the free end of the body. Tip vortices that shed off of the truncated end of the cylinder interact with the Karman vortex shedding. Experimental measurements by Farivar [51] suggest that three different regions of shedding were present, indicated by different frequencies along the cylinder length. Kawamura [104] found that the Karman vortex shedding demonstrated dependence on the aspect ratio of the cylinder, such that at small enough aspect ratios periodic vortex shedding did not occur. The critical aspect ratio that marks the onset of Karman vortex shedding varies widely between authors, from 1

to 7 [51, 104, 162]. These results are consistent with observations by Sakamoto & Arie [196] and Park [167] which showed reductions in Strouhal number near the free ends of the cylinders. Unique flow behavior has been noted in work by Park [167], Adaramola [5], Rostamy [192], Roh [190] and Pattenden [171] that investigated flow past small aspect ratio cylinders, which exhibited changes in the frequency content of the loads.

6.1.3 Surface-Piercing Cylinders with Free Ends

Investigations of the combined effects of the free-surface on finite cylinders has been given far less attention. Only a small sample of work in the literature has addressed the combined factors of a free surface and a free-end. In these studies, the work has excluded studying loads as a function of cylinder length. Except for the work by Hay [72], the work has not examined aspect ratios larger than 2.

Hay [72] conducted experiments in a towing tank and data were collected for the mean resistance and water run-up on the cylinder. The results showed peaks in the resistance coefficients at small Fr_L around 1, and then tapering of the resistant coefficient to nearly 0.5. This study is notable for its breadth of experimental parameters. However, it excluded discussion of frequency, vorticity and any measurements that vary with depth.

More recently, Rosetti [189], presented experimental and numerical investigations of a surface piercing cylinder at an aspect ratio equal to 2 at $Re = 4.3 \times 10^4$ and $Fr = 0.31$. It was found that the free surface affected the flow, but the free end effects dominated. Irregular vortex shedding was observed, as a result of the low aspect ratio. The global drag of the finite, surface-piercing cylinder was found to be smaller than the infinite, surface-piercing cylinder, and also smaller than the infinite, fully submerged cylinder. The observed drag and vortex shedding phenomena are consistent with other work in the literature. The study focused on global loads,

excluding loads as a function of cylinder length. Furthermore, the study was limited to a single aspect ratio.

Goncalves [64], et al, presented thorough experimental results for varying aspect ratios up to 2 over a range of Re and Fr. The authors noted both a decrease in C_d and St with decreasing aspect ratio. In addition to load cell measurements, PIV measurements were also carried out. Visualizations of the flow around cylinders at a variety of aspect ratios were provided, showing the effects of a free end. The experimental data provided by Goncalves [64], complements the present work which presents numerical and experimental results up to $AR = 19$ with measurements at very small aspect ratios. Furthermore, this present work adds to the existing data by providing results at different Re and Fr.

6.2 Analysis Specifications

The present work examines the combined effects of a free surface and a free-end on cylinders with varying aspect ratios. Both numerical and experimental work was carried out over a range of aspect ratios from around 1 to 19, where the aspect ratio is defined as $AR = \frac{submerged\ length}{diameter}$. The cylinder diameter was held constant at 0.0127 m and the depth of submergence was varied to alter the AR. A uniform flow of 0.23 m/s was propagated past the cylinder.

The numerical and experimental work is compared in an effort to further validate the numerical model as well as provide insight into the flow around surface-piercing cylinders with free ends and varying lengths. All of the results presented here are for the case of a $Re = 2900$ and $Fr = 0.65$.

6.3 Experimental Method

The experiments were carried out in the re-circulating water tunnel of the Fluid-Structure Interaction Laboratory, with a test-section of 1.27 m $\times$ 0.5 m $\times$ 0.38 m
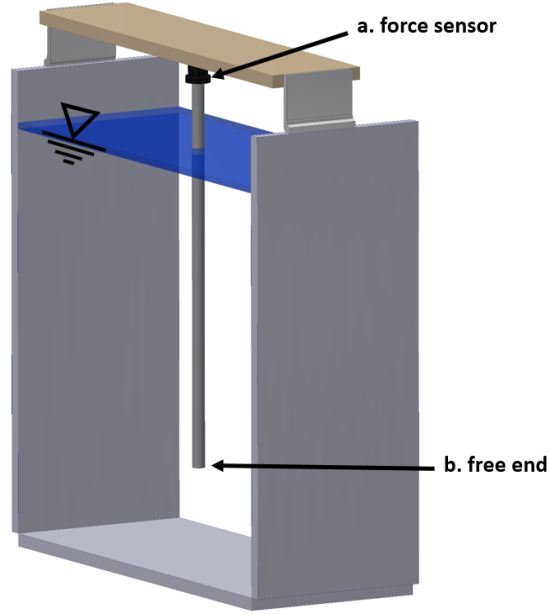
Figure 6.1. Schematic of the experimental set-up for the surface-piercing cylinder in the FSI water tunnel. The depth of submergence of the cylinder can vary, allowing for the study of the relationship between aspect ratio and drag coefficient.

and a turbulence intensity of less than 1% for up to a flow velocity of $U = 0.3$ m/s. A uniform circular cylinder with a diameter of $D = 1.27$ cm was tested. Tests were conducted at a constant flow velocity of $U = 0.23$ m/s, resulting in a constant Reynolds number of $Re = 2900$ (same as the Re number used in the numerical simulations). The cylinder could be placed in water at different immersed lengths, resulting in different aspect ratios, L/D, where L is the immersed length of the cylinder (Figure 6.1). Twelve different aspect ratios of L/D between 0.875 and 19 were tested. A six-axis force sensor (ATI-Nano17/IP68) was attached to the upper end of the cylinder and measured the total flow forces acting on the cylinder in three perpendicular directions. This force sensor had a capability of high precision measurement of small forces. The calibration SI-25-0.25 had a sensing range of 25 N in the F_x, F_y and 35 N in F_z direction with a resolution of $1/160$ N in all three directions. The single axis overload in F_{xy} and F_z were $\pm$ 250 N and $\pm$ 480 N,

respectively. T_{xy} and T_z had a single axis overload capacity of $\pm$ 1.6 Nm and $\pm$ 1.8 Nm.

Four experimental runs were performed for each aspect ratio. The results presented in this paper include error bars illustrating $\pm$ one standard deviation from the mean of the four measurements taken at each of the aspect ratios.

6.4 Numerical Method

6.4.1 The Numerical Domains and Boundary Conditions

Hexahedral meshes were generated for simulating the flow past the cylinders with varying aspect ratios. A mesh was built for each aspect ratio, where all meshes had a height of 0.55 m, width of 0.254 m and a length of 0.762 m. Each cylinder was located at 0.254 m from the inlet and 0.508 m from the outlet to allow room for the wake. Three layers of octree refinement were performed from the base mesh to the surface of the cylinder with an additional boundary layer on the surface of the cylinder. The boundary layer consisted of 10 layers. In addition to the increased refinement around the cylinders, the fluid interface region was refined with two layers of octree refinement in the vertical direction. The first layer of refinement fell within $\pm 0.025m$ of the still water level (SWL), and the second layer of refinement fell within $\pm 0.0125m$. The cell count of each mesh varied slightly due to the differing lengths of the cylinders and the resulting numbers of refined cells near each cylinder surface. The mesh sizes were all in the neighborhood of 3.3 million cells.

The bottom and sides of the domain were treated as no-slip boundaries, as well as the surface of the cylinder. The inlet was prescribed with uniform velocity of 0.2286 m/s in the water phase, and zero velocity for the air phase. The volume fraction was given as 1 below the SWL and 0 above, where 1 represents water and 0 is air. Pressure was prescribed to have a normal gradient of zero on every boundary except for the top boundary, which was set with a total pressure boundary condition. The simulations
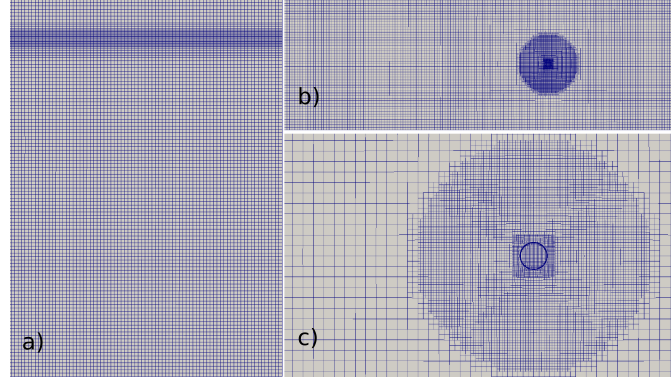
Figure 6.2. a) View of the numerical domain from the side. Increased cell refinement is located around the fluid interface. b) Overhead view of the numerical domain. Increased cell refinement surrounds the cylinder. c) An enlarged view of the near cylinder region, as seen from above.

presented here had an initially quiescent flow field (i.e. zero velocity everywhere in the domain).

A maximum Courant number of 0.5 was set, where $Co = U\frac{\Delta t}{\Delta x}$ and U is the velocity, and Δt, Δx are the discretized time and length intervals, respectively. The time step was adjusted according to the Courant number throughout the simulation, with an initial time step of 0.01 s.

The Spalart-Allmaras one-equation model, described in Spalart & Allmaras [217], was used to model the turbulence, with a Spalding wall function at the cylinder boundary, presented in Spalding [218]. The turbulence model was chosen based on the findings from the validation exercises discussed in the validation work presented in Section 5.

Load predictions on the cylinder were calculated by discrete integration of the pressure and viscous stresses along the body, by summing values on each cell face. Moments were calculated in a similar manner. The individual moments from pressure and viscous forces on each cell face, where the moment arm was calculated as the distance from the face center to the cylinder center of gravity, were summed to yield

a combined pressure and viscous moment on the body. The total moment is the sum of the pressure and viscous moments. The forces and moments were stored as three-component vectors in the x, y and z directions, and roll, pitch and yaw directions, respectively.

6.5 Results and Discussion

The results from experimental measurements and CFD simulations are presented here. First, the predicted drag forces from both simulations and experiments are presented. Next, the frequency content of the load predictions from CFD is examined. Flow field visualizations from CFD are presented to provide insight about the flow physics around these surface-piercing, finite length cylinders of varying aspect ratios. Additionally, CFD results for sectional loads along a cylinder with an aspect ratio of twelve are presented. Finally, the section concludes with a comparison of the present results with previous work from the literature for the isolated cases of a free surface or a free end.

6.5.1 Drag Forces

The non-linear relationship between the drag coefficient and the aspect ratio is shown in Figure 6.3 below. The agreement between the numerical predictions and the measured data from the experiments are shown across the entire range of aspect ratios studied. A maximum drag force of 0.07 N was measured experimentally, at the aspect ratio of 19.

The drag coefficient is given by,

$$C_d = \frac{2F_d}{\rho U^2 A},$$ (6.1)

where F_d is the time averaged drag force, ρ is the density of water, U is the freestream velocity, and A is the frontal projected area of the cylinder, which changes with aspect

ratio. The numerical and experimental results show the same trend in drag coefficient versus aspect ratio. The drag coefficient is roughly constant for aspect ratios of 3 and above. A large drop in the drag coefficient appears at an aspect ratio of 2, in both the experimental and numerical work. The reason for the drop in drag coefficient at $AR = 2$ is investigated further through computational flow visualizations in a later section.
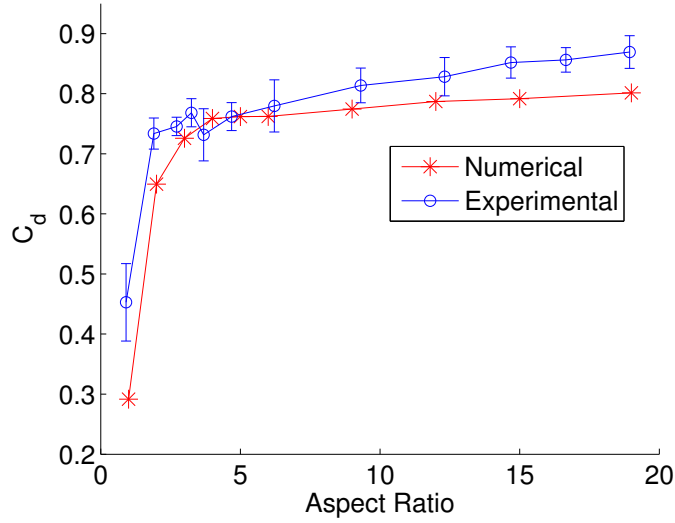
Figure 6.3. The drag coefficient at different aspect ratios. The numerical results are shown in red stars, and the experimental results are given in blue circles.

The calculated drag coefficients from the present work's CFD predictions and experimental measurements are plotted against results from the literature in Figure 6.4. The drag coefficients for the cylinder of varying aspect ratios from the present work are shown with red stars and blue circles, for the numerical and experimental work, respectively. Additionally, drag coefficients from the present numerical work for a fully-submerged, infinite cylinder are shown in magenta stars. Experimental results from the literature for infinitely long cylinders are shown in the figure [2, 99, 156, 174, 191, 202, 239, 267]. Drag coefficients from fully-submerged cylinders
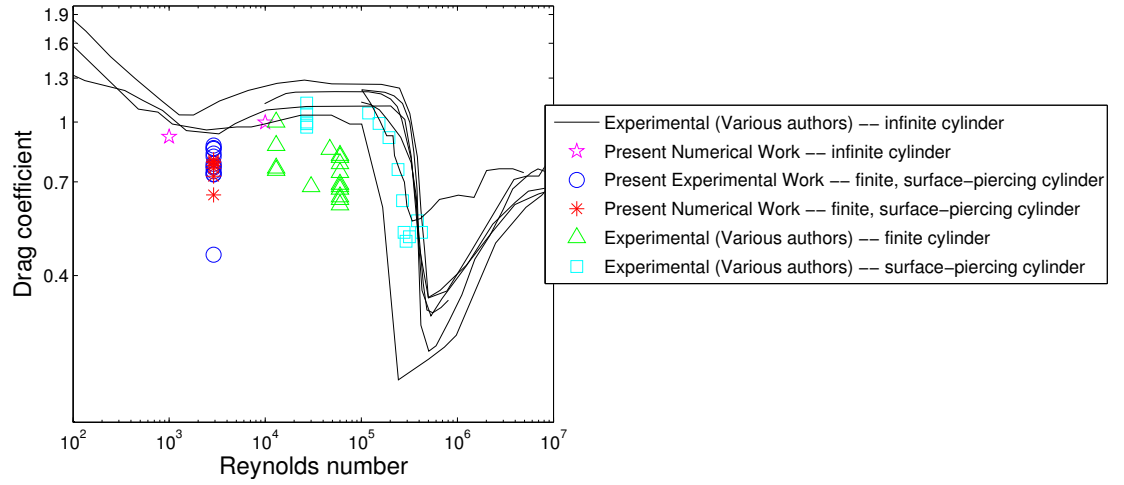
Figure 6.4. The drag coefficient of a vertical cylinder across a range of Reynolds numbers, determined experimentally and numerically in both the literature in the present work.

with free ends, of varying aspect ratios, are shown [51, 162, 163, 197, 224, 231]. Drag coefficients for surface-piercing cylinders are shown as well [27, 105].

Overall, the drag coefficient for infinite, fully-submerged cylinders is greater than the drag coefficients for other cylinders in the same Reynolds number range. Previous work from the literature shows that surface-piercing cylinders have a slightly lower drag coefficient than fully submerged cylinders, which can be seen by comparing the black lines to the cyan squares in Figure 6.4. It has been demonstrated in the literature and in the present work that surface-piercing cylinders have even greater reductions in drag coefficients near the free surface. This result is not reflected in the plot of the total drag coefficients, but is demonstrated in Figure 6.13 which examines loads as a function of cylinder length.

The global drag coefficients for finite length cylinders show a greater decrease in value compared to the surface-piercing cylinders. It is shown that the presence of a free end for these finite cylinders has a greater effect on the total drag than does the presence of a free surface. This can be noted by comparing the cyan squares

with the green stars in Figure 6.4. The present work shows that the combined effects
of free ends and a free surface results in reductions in the drag coefficients that are
more similar to the finite cylinder results. The reduction in the drag coefficients are
of similar value. In the present work, the very low drag coefficients were found at
the smallest ARs studied. The blue circle with $C_d = 0.45$ is for the case of $AR = 1$. Again, this highlights the large effects of the free end and free surface on the drag
loads. As the AR increases, the C_d predictions in the present work approach the C_d
values for the infinitely long, fully-submerged cylinder.
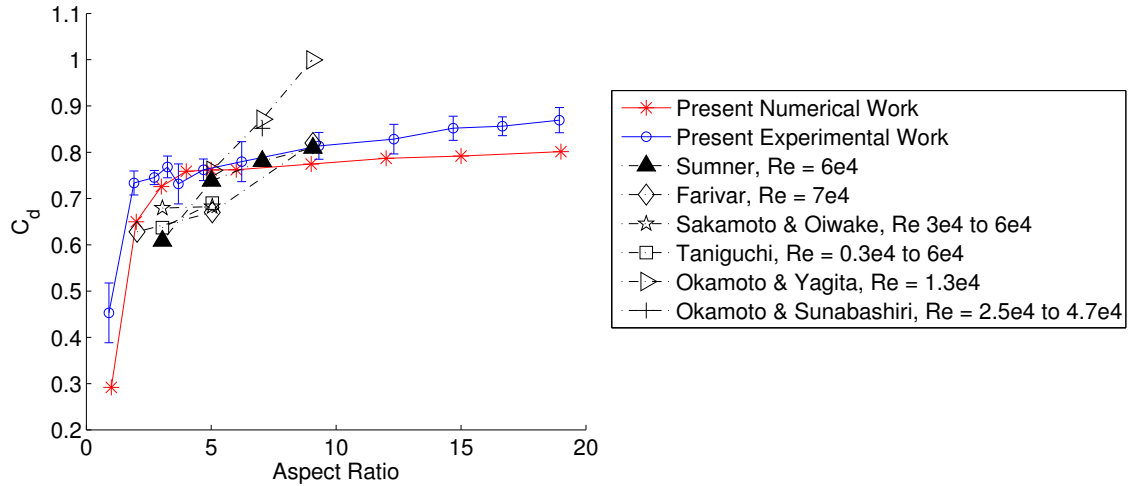
Figure 6.5. The relationship between drag coefficient and aspect ratio from the
present work as well as previous work from the literature [51, 162, 163, 197, 224, 231].

To further investigate the combined effects of the free end and free surface on
the drag behavior of cylinders, the relationship between the aspect ratio and drag
coefficient is examined. In Figure 6.5 the present work is compared against results
from previous work, where the cylinders had free ends, but did not pierce a free
surface. (Experimentally, this can be achieved by mounting the cylinder vertically to
the floor, such that the free end is located at the top.)

Sumner [224] presents results that show initial signs of C_d plateauing between AR = 5 and 10, while the results by Sakamoto [197], Okamoto [162, 163] and Taniguchi [231] fall in too narrow of a range of ARs to capture the plateau effect. The present work shows agreement with the general trends of lower drag coefficients at low aspect ratios, but also demonstrates a plateau at high aspect ratios. The differences between authors is most likely due to the different Re numbers at which these studies were performed. Overall, this comparison demonstrates that drag coefficients smaller than values for infinite cylinders at the same Re numbers are found for cylinders with free ends, excepting some results from Okamoto [163].

The discrepancies between previous work in the literature and the present work is likely due to the fact that the previous work investigated vertically mounted cylinders on flat plates, such that the free end was located at the top of the cylinder. In these works, the cylinders were partially immersed in a boundary layer attached to the floor, or flat plate. In the present work, the hard surface of the floor is replaced with a deformable water-air fluid interface.
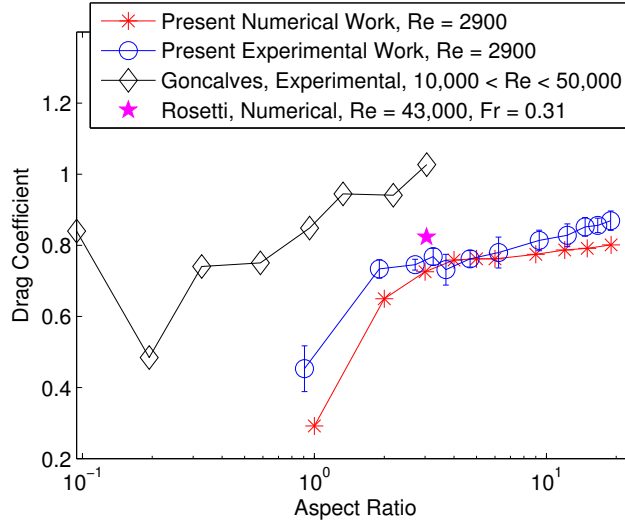
Figure 6.6. Comparison of the numerically and experimentally determined drag coefficients from the present work, against numerical results by Rosetti [189] and experimental work by Goncalves [64].

Finally, experimental and numerical results from the present work are compared against numerical results by Rosetti [189] and experimental work by Goncalves [64]. The differences between work by Goncalves [64] and the present study indicate that load results are not universal, but rather that they depend greatly on the Fr and Re numbers. Future work will seek to understand this discrepancy in results, whether the difference is due to the Fr or Re, or a combination of the two.

6.5.2 Frequency Content

Fast Fourier transforms (FFTs) of the transverse force time histories from CFD were computed. The resulting FFTs are presented as a function of the Strouhal number, $St = fD/U$, where f is the vortex shedding frequency, D is the cylinder diameter and U is the uniform flow velocity. For a cylinder with $Re = 2900$, the St is expected to be 0.2 [3]. The FFTs shown in Figure 6.7a show very strong peaks around $St = 0.2$ for the high aspect ratio cases of $AR = 15$ and 19. A less dominant peak is shown at $St = 0.18$ for the $AR = 9$.
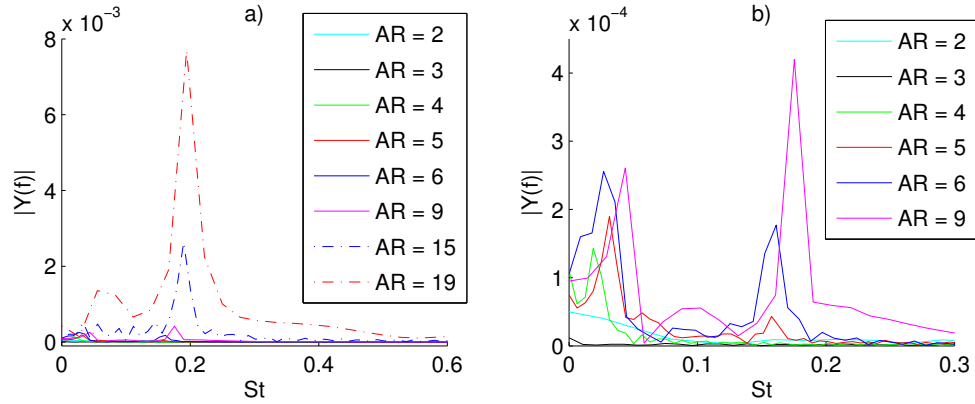
Figure 6.7. FFTs of the transverse force signal for cylinders with aspect ratios of 3, 9, 15 and 19.

An enlarged view of the FFTs is given in Figure 6.7b. At an aspect ratio of 6 a small peak is shown at St = 0.15, which is a slight reduction from the St numbers for

larger aspect ratios. For aspect ratios 4 and 5, peaks are found at very low St. Finally, for $AR = 2$ and $AR = 3$ there exist no peaks in the FFTs, suggesting the absence of a strong oscillatory transverse force signal, and thus a lack of regular vortex shedding at these low aspect ratios. This analysis of the frequency content of the tranverse forces demonstrates that the vortex shedding begins to be suppressed at an aspect ratio of 6, as the St decreases from the theoretical value of 0.2 for an infinite cylinder. The vortex shedding is increasingly supressed as the aspect ratio is reduced, such that at an aspect ratio of 3 there exist no dominant frequencies in the vortex shedding.

Kawamura [104] noted the absence of Karman vortex shedding at $AR = 4$, while Okamoto [162] noted suppression of vortices at $AR = 2$, which are roughly consistent with the present work's finding. The present work finds that Karman vortex shedding is suppressed at $AR = 3$ and below. Additionally, Sumner [224] found a reduced Strouhal number of 0.16 for cylinders with aspect ratios of 3, 5, 7 and 9 as compared to the value of 0.2 for infinite cylinders. The present work also demonstrates a reduced Strouhal number at $AR = 9$. However, at $AR = 3$ and below, periodic vortex shedding was not observed. This difference is likely due to the presence of a free surface which did not exist in Sumner's study.

6.5.3 Visualizing the Flow

Here, flow field visualizations are presented in an effort to understand the underlying physics of the flow around surface-piercing, finite cylinders with varying aspect ratios. The previous subsections demonstrated non-linear relationships between the aspect ratio and the drag coefficients. Furthermore, the frequency content of the loads showed a dependency on the aspect ratio. Visualizations of streamlines and vorticity fields around the cylinders of various aspect ratios are presented here, and provide insight about the reasons for the load characteristics seen in the numerical predictions and experimental measurements.
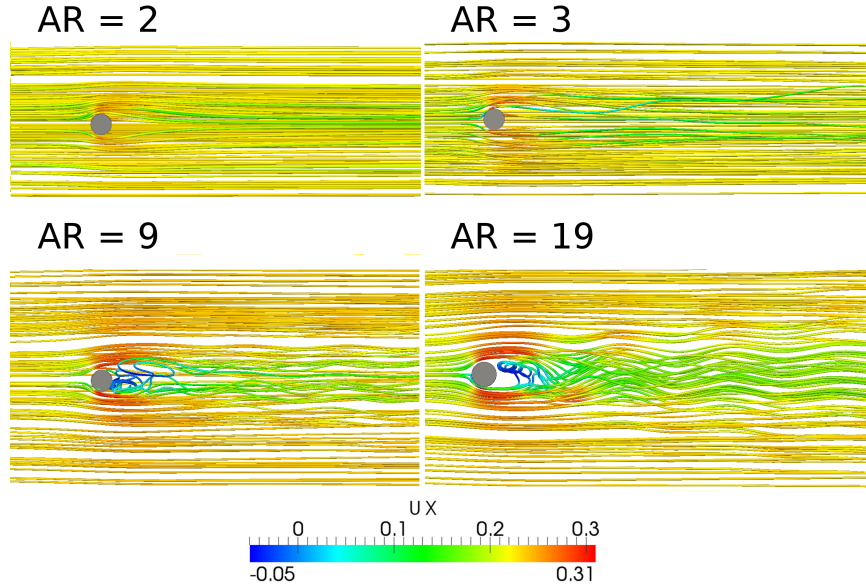
Figure 6.8. View from above of streamlines moving from left to right past four cylinders of varying aspect ratio, including AR = 2, 3, 9 and 19.

Views of the streamlines around cylinders with aspect ratios of 2, 3, 9, and 12 are shown in Figure 6.8. The cylinders with an aspect ratio of 2 and 3 do not appear to generate any vortices along the length of the cylinder. However, vorticies are still generated from the free end. At an aspect ratio of 9, vortex shedding occurs. The magnitude of the oscillation in the wake increases with increasing aspect ratio.
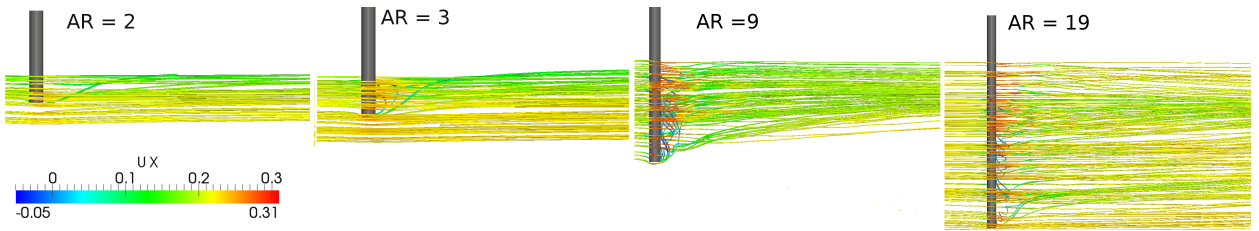
Figure 6.9. Streamlines past cylinders with four different aspect ratios, view from the side. The flow travels from left to right.

The streamlines are shown from the side in Figure 6.9. From this perspective, the absence of vortex shedding along the length of the cylinder in the $AR = 2$ and 3 cases

is illustrated again. With increasing aspect ratio the vortex shedding again increases in magnitude. Near the free surface there is a lack of vortices in all cases, suggesting the free surface suppresses vortex shedding altogether. The ability of the free surface to deform, as opposed to a solid wall, alters the flow in this region. Surface waves are observed in both the experimental and numerical work. Further away from the fluid interface, and moving towards the free-end of the cylinder, the vortex shedding increases, such that the $AR = 19$ case exhibits vortex shedding clearly.

The side view of the streamlines also shows the portion of the flow that travels under the free-end of the cylinder and then moves upwards on the downstream side. The ability of the flow to travel beneath the cylinder because of the free end, as opposed to solely around the cylinder for the case of an infinite cylinder, is likely the main contributor to the reduced drag coefficient of finite cylinders.
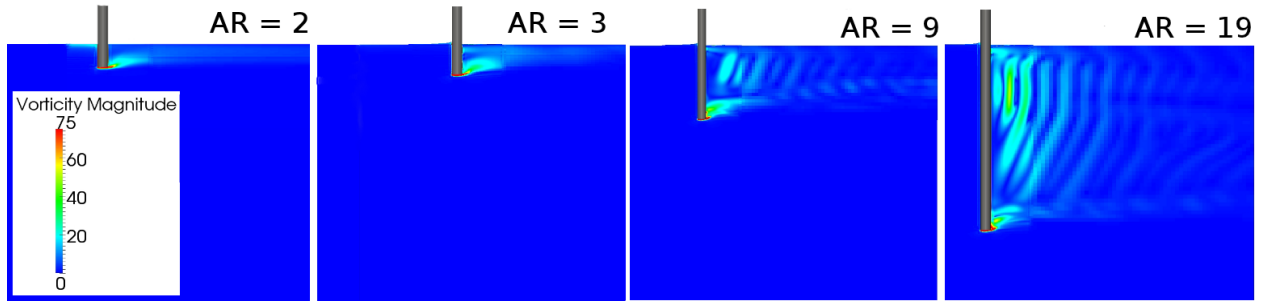
Figure 6.10. Vertical slices through the numerical domain illustrating the vorticity fields around cylinders of aspect ratios 2, 3, 9 and 19, flow travels from left to right.

The vorticity was computed from the CFD results. Vertical slices taken through the cylinder and parallel to the fluid flow are shown in Figure 6.10. At the small aspect ratio of 3, the vortex structure appears to be smeared out compared to the vortex structures behind cylinders with larger aspect ratios.

For the case of the large aspect ratio of 19, shown on the lower right, different regions of vortex shedding appear. Near the free surface the vorticity is very small. Along the upper-middle segment of the cylinder the vorticity oscillates periodically

and parallel to the cylinder. Moving down to the lower-middle section, the vorticity remains oscillatory but the variation no longer occurs parallel to the cylinder, but rather at an angle. Finally, at the free-end of the cylinder there exists a different vortex structure altogether which is small and creates its own wake pattern. The tip vortices appear to interact with the Karman vortex shedding that occurs along the middle span of the cylinder. This effect is manifested in angled vortex sheets towards the bottom-middle section, while the top-middle section shows perfectly vertical vortex sheets.
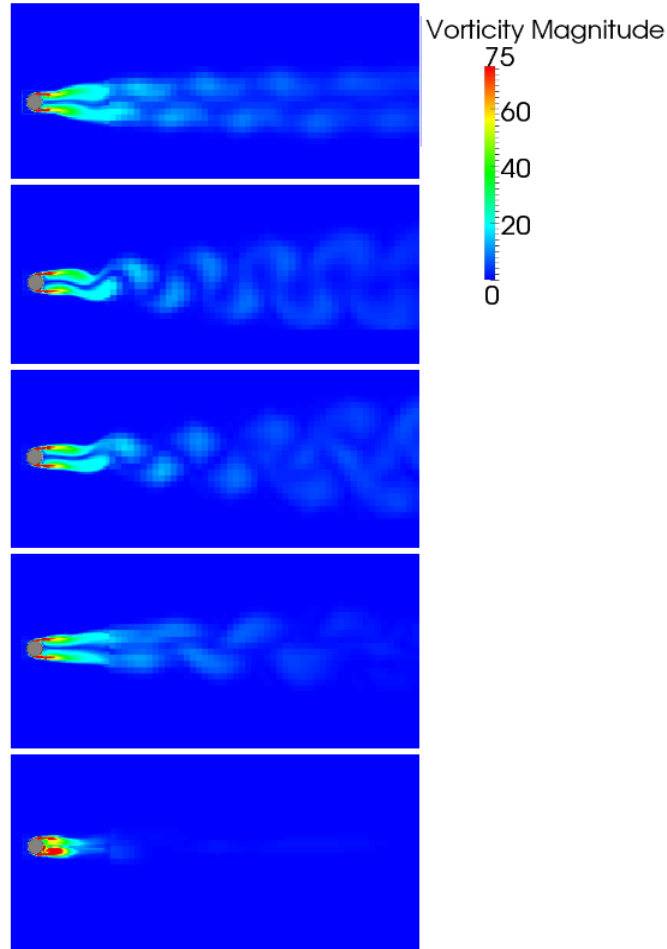
Figure 6.11. Horizonal slices through the numerical domain of a cylinder with aspect ratio 9. The slices are taken at 10, 30, 50, 70 and 90% of the cylinder's depth.

Horizontal slices of the vorticity field around a cylinder with $AR = 9$ are shown in Figure 6.11, at increasing depths below the still water level (SWL). The slices are taken at 10, 30, 50, 70 and 90% of the cylinder's depth, from top to bottom in the figure. The vortex shedding patterns differ along the length of the submerged cylinder. Near the free surface, shown in the top image, two vortices trail behind the cylinder and create a narrow wake. Moving down the length of the cylinder into deeper water, the wake widens. Near the free-end of the cylinder, illustrated in the bottom image, the wake structure disappears and two vortices with large vorticity magnitudes are seen.

When the cylinder has a small aspect ratio, the vortex shedding, which is suppressed near the free surface, dominates over nearly the entire length of the cylinder. However, there does remain a region of high vorticity at the free end, seen both in the vorticity fields and also demonstrated by the streamline visualizations that show the tip vortices coming off the bottom of the cylinders. For the cases of $AR =2$ and 3, the aspect ratio is so small that a middle region does not exist, such that high vorticity from the free end dominates the flow behavior on the entire length of the cylinder. For each of these cases there exists a region of relatively high vorticity at the free end, from which tip vortices are shed. The marked drop in drag coefficient for the $AR = 2$ case is also a likely result of the vortex shedding coming entirely from the free end, combined with the flow propagating past the cylinder from below and around the two sides.

6.5.4 Sectional Forces

Here, CFD predictions for the sectional forces along the length of a cylinder with $AR = 12$ are presented. A numerical mesh was generated with multiple patches (where a patch is a collection of boundary faces) along the length of the cylinder in order to investigate the loading on the cylinder as a function of its length and

distance from the free surface. Each patch was a 3d cylindrical section. The patches were stacked vertically such that the eight patches comprise the entire geometry of the cylinder with $AR = 12$. It is possible to achieve spatial resolution as small as each face on the cylinder's surface. However, dividing the surface into eight patches achieved sufficiently detailed resolution in space, while also averaging out statistical noise.

The patch names are defined in Figure 6.12, where the portion of the cylinder that touches only air is named "air". The patch named "Fountain" is located just above the still water line (SWL) but does touch water due to wave run-up on the front side of the cylinder. The patches that are located beneath the SWL are named "Water1" to "Water7" with increasing depth. The patches vary in length, such that patches near the ends are shorter, and patches along the middle span are longer. The exact length of each patch is provided in Figure 6.12.
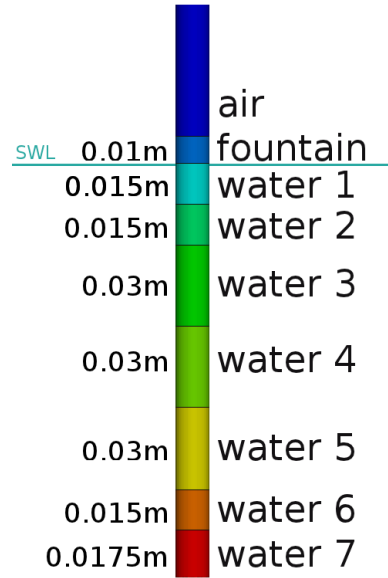
Figure 6.12. Surface patch definitions for the cylinder with aspect ratio 12. The SWL sits at the base of the "fountain" patch. The patches under the SWL are labeled "Water 1" to "Water 7" with increasing depths.

Sectional drag coefficients were computed for each patch, given by,

$$C_d(z) = \frac{2F_d(z)}{\rho U^2 A(z)} \tag{6.2}$$

where $F_d(z)$ is the time averaged drag force at a single patch and A(z) is the frontal project area of the corresponding patch located at the same height, z.
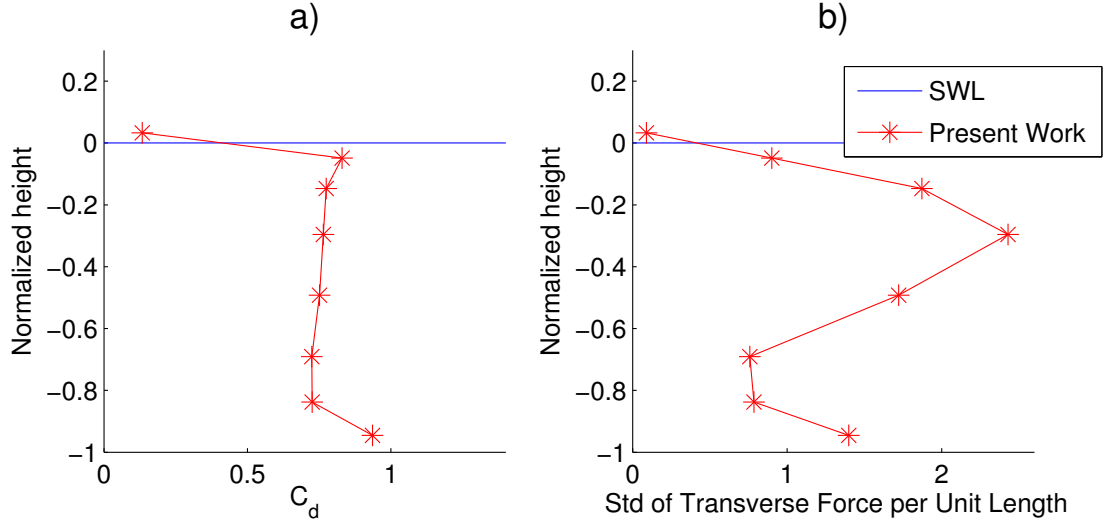
Figure 6.13. a) Sectional drag coefficient along the length of the cylinder. b) Standard deviation per unit length of the fluctuating lift forces along the length of the cylinder. A peak in the standard deviation of the transverse force is seen near the middle of the cylinder span, with another smaller peak located near the free end.

The time averaged sectional coefficients along the cylinder length are shown in Figure 6.13a. The drag coefficient is nearly uniform along the length of the cylinder. However, near the free surface the drag coefficient decreases rapidly, a trend that is consistent with previous studies found in the literature, e.g. [27], [105], [263], [221]. Additionally, an increase in the drag coefficient can be seen at the bottom of the cylinder where the flow is altered due to the tip vortices from the free end.

The present work is compared against drag coefficient results for surface-piercing cylinders in Figure 6.14. Numerical results from the present work are shown in red
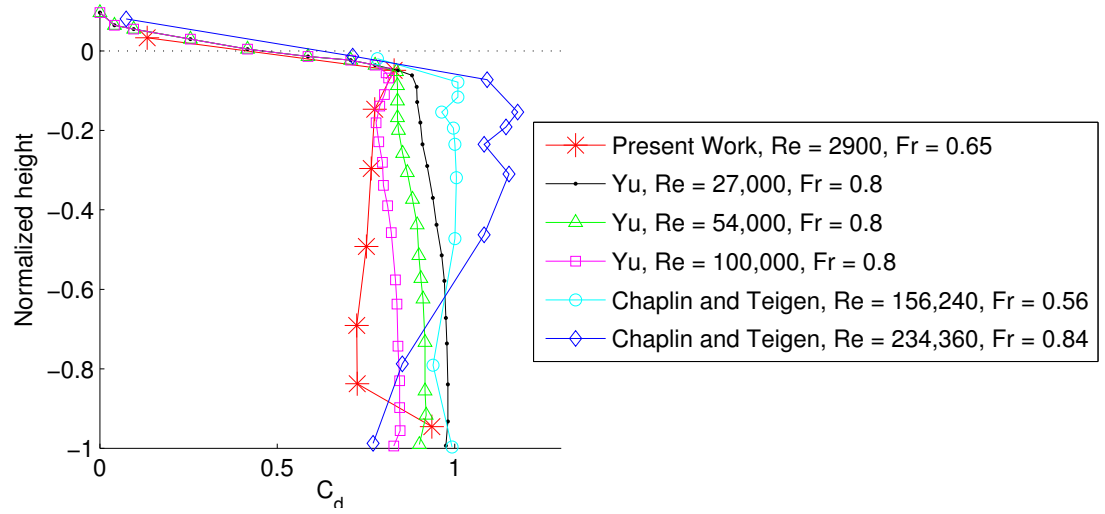
Figure 6.14. Sectional drag coefficients from the present work are shown in red stars. Sectional drag coefficients from surface-piercing cylinders without free ends are shown in black, green, magenta, cyan and blue ([27, 263]). The dotted line indicates the location of the SWL.

stars. Data from Yu [263] and Chaplin & Teigen [27] in the same vicinity of Fr, but larger Re, as the present work are also plotted. The sectional drag coefficients from the present work show the same trend from the top of the cylinder to nearly the bottom. At the bottom the drag coefficient increases, unlike the values from the previous work where the bottom of the cylinder was attached to a floor or a splitter plate, instead of being a free end. It is also shown that the predicted C_d values vary with dependence on both Re and Fr.

The standard deviation per unit length of the fluctuating lift force was calculated for each patch along the length of the cylinder. The results are presented in Figure 6.13b. A peak in the magnitude of the oscillatory lift force signal is seen near the middle of the cylinder's length. The magnitude of the fluctuating lift force is smaller near the free surface and near the free end, though not at the free end. At the end of the cylinder a local maximum in the lift force magnitude is seen, likely due to tip vortices shedding off of the free end. The relative magnitude of the lift force oscilla-

tion is indicative of the degree of vortex shedding. The standard deviations given on the right in Figure 6.13 match well with the visualizations of the vorticity present in Figure 6.10. The computed standard deviations of the sectional fluctuating lift force reiterate the presence of vortex shedding in the middle span of the cylinder, the lack of vortices near the free surface and lastly, the tip vortices from the free end, which were all seen in the visualizations of vorticity in Figure 6.10.

Next, FFTs of the sectional transverse forces were computed, and are presented as a function of the St in Figure 6.15a. The largest peaks are seen for patches "Water2", "Water3" and "Water4", the three patches located along the middle span of the cylinder. This is the region where the vorticity field illustrated the greatest degree of vortex shedding, as well as the region where the peak in the standard deviation of the transverse force was found. Furthermore, these peaks are found at $St = 0.2$, the expected value for cylinders at the Re studied in this work.

Reduced peaks around $St = 0.2$ can be seen for the patches "Water1" and "Water5", the patches that surround the middle span of the cylinder. These are the regions that mark the beginning and the end of the region of strong vortex shedding. The FFTs as well as the standard deviation of the transverse force indicate that these regions see periodic vortex shedding, but that the vortices are smaller in magnitude than those between "Water1" and "Water5". Finally, the patches near the free-end of the cylinder, "Water6" and "Water7", show small peaks just below $St = 0.2$, as well as larger peaks closer to $St = 0.05$. The "Water7" patch gives the larger peak at the low St, which alongside the streamline and vorticity visualizations, suggests the tip vortices shed periodically and at a lower frequency than the vortices in the main wake.

The St number as a function of cylinder height is shown in Figure 6.15b, against data presented by Farivar [51] and Fox & West [55]. In Farivar's work the free end was located at the top, so the data have been mirrored for comparison to the present
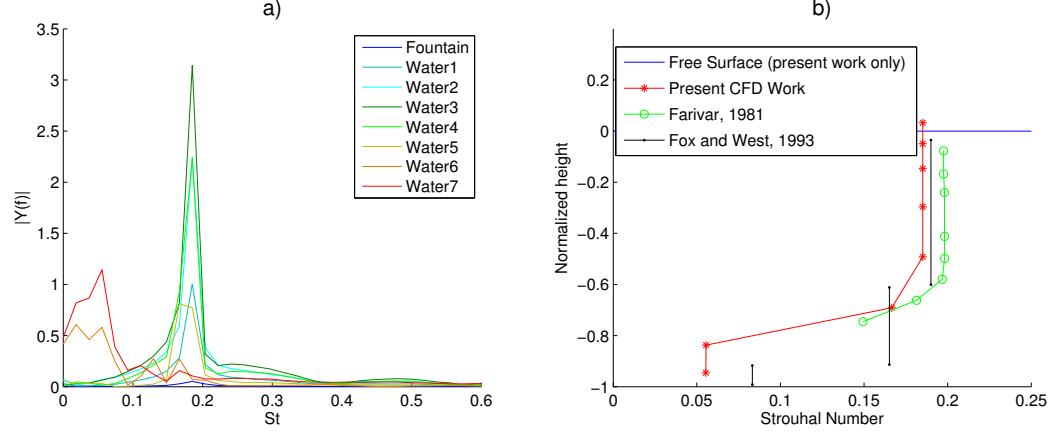
Figure 6.15. a) FFTs of the transverse force signal from each of the patches. Larger peaks in the FFT of the transverse force are observed for patches around the middle span of the cylinder, indicating where the periodic vortices are largest and most pronounced. b) The St as a function of cylinder height, compared against results from Farivar [51] and Fox & West [55]

work which modeled the free end at the bottom of the cylinder. The normalized height of zero represents the location of the free surface in the present work. Again, the work by Farivar [51] did not include a free surface. The free ends are located at a normalized height equal to negative one. Fox & West's work studied a cantilevered cylinder attached to a wall [55]. The free end of the cylinder in their work corresponds to the normalized height of negative one in Figure 6.15b. The general trends in St as a function of distance from the free end of the cylinder match well. St numbers near 0.2 are observed for the end furthest from the free end, while near the free end, the St numbers are much lower. The flow travelling over the free end interferes with the Karman vortex shedding, and leads to a reduction in the shedding frequency in that region.

6.6   Summary and Conclusions

CFD simulations of flow past surface-piercing cylinders with aspect ratios from about 1 to 19 were performed at $Re = 2900$ and $Fr = 0.65$. The drag forces predicted

141

from CFD simulations were compared against experimental measurements, across a wide range of aspect ratios from 1 to 19, and good agreement was found. It was found that the combined effects of a free surface and a free end affected the magnitude and frequency of loads on the cylinder, with a dependency on the aspect ratio.

At higher aspect ratios the drag coefficient was found to be nearly constant with a value near 0.75 from numerical simulations, and 0.85 from experimental work. A sharp drop in the drag coefficient was observed at $AR = 2$, as the flow can travel under as well as around the cylinder. Tip vorticies were seen to dominate at small aspect ratios, while more pronounced vortex sheets were observed behind cylinders with larger aspect ratios. The Strouhal number decreased with the aspect ratio such that for the cases of $AR = 3$ and below, the lift force exhibited almost no periodicity at all.

Sectional load investigations, a new contribution to studies of the combined effects of free surface end free ends, further corroborated flow field visualizations. The magnitude of the lift force was shown to peak near the middle of the cylinder span, with a local maximum at the free end where tip vortices shed. Near the free surface the magnitude of the lift forces was shown to die off entirely, as a result of the supression of vortices near the free surface. Reduced Strouhal numbers were found for locations near the free end, indicating a different frequency of vortex shedding from the tip than from the center span of the cylinder.

The presence of a free-surface and a truncated cylinder end affects the structural loading, in both magnitude and frequency. These alterations to the loading behavior are dependent on the aspect ratio, such that at small depths of penetration, the drag is greatly diminished and the periodicity of loads from vortex shedding is absent. Understanding the flow behavior around bodies in the presence of these factors is of great importance to many engineering applications, such as offshore structures. The

design of offshore structures should consider the implications of these factors of drag
and frequency of loads.

CHAPTER 7

LOADS ON A STATIONARY SEMISUBMERSIBLE IN STEADY CURRENT

7.1 Introduction

A variety of computer-aided engineering (CAE) tools, based largely on engineering models employing potential-flow theory and/or Morison's equation, are currently being used to evaluate hydrodynamic loading on floating offshore wind turbine platforms [90, 94]. Evaluation of the validity of these tools is a necessary step toward proper modeling. In this chapter, the open-source computational fluid dynamics (CFD) package, OpenFOAM, was used to provide high-fidelity simulations of wind turbine platforms in steady current and waves to assess the validity of potential-flow and Morison solutions.

FAST [91], which employs engineering models, is the National Renewable Energy Laboratory's (NREL) wind turbine CAE tool. In this work, hydrodynamic load predictions from FAST's hydrodynamics module, HydroDyn, are compared with results from OpenFOAM for a fixed semi-submersible platform. The OC4-DeepCwind semi-submersible analyzed in the International Energy Agency (IEA) Wind Task 30 project is used for this study [187]. The effects of the wind turbine were neglected.

HydroDyn uses a combination of Morison's equation with potential-flow theory to predict loads on offshore structures, including floating platforms. Morison's equation is more valid for small members where viscous and inertial effects dominate. Potential-flow theory is more appropriate for larger members where radiation and diffraction effects are more important. The interaction between the individual components of

the structure is neglected. This means that the loads on the individual components are summed, but the large components do not influence the hydrodynamic loads on the small components and vice-versa. In CFD simulations the forces and moments are predicted entirely by the flow field such that interaction effects are intrinsically accounted for, but with large computational expense.

To study the implications of the assumptions in HydroDyn, both FAST and Open-FOAM were used to simulate a series of cases using a variety of wave and current conditions. Simulations of the semi-submersible were performed in each tool, and load predictions are compared. To specifically address the issue of body-size classification as well as component interaction, three geometries were used in the CFD study of the semi-submersible. The first geometry contains the entire semi-submersible geometry. The second and third geometries contain only the small and only the large members, respectively. The assumptions in HydroDyn are assessed based on the comparison of load predictions against results from OpenFOAM. Even though HydroDyn is used in this study, the results are likely applicable to other engineering codes that employ similar models.

7.2   Analysis Specifications

The OC4-DeepCwind semi-submersible platform geometry was selected in this study because it is composed of both small and large components relative to the waves encountered in the ocean environment, meaning that viscous drag, static pressure, dynamic pressure, and inertial loads all contribute to the loading on the structure. (Radiation added mass and damping are neglected in this study of a stationary platform.) The specifications of the semi-submersible geometry meshes are outlined here, followed by a description of the simulated environmental conditions. Simulations performed in OpenFOAM were conducted at 1/50th the scale of the prototype semi-submersible, such that the dimensions of the CFD mesh match the dimensions

of the semi-submersible employed in the the DeepCwind tank testing campaign. The FAST simulations were carried out with full prototype scale length dimensions, but are effectively treated at model scale because of the chosen drag coefficients. To properly compare the HydroDyn results with those from OpenFOAM, the drag coefficient used in FAST is derived from the model-scale Reynolds number, and the drag coefficient is chosen to be 1.0. All dimensions, forces, and other data from OpenFOAM are presented at prototype scale, scaled using Froude scaling. The Froude number is given by $Fr = \frac{u^2}{gL}$, where u is the fluid velocity, g is gravity, and L is the characteristic structure length. The scaling relationship between model and prototype is upheld by $Fr_{model} = Fr_{prototype}$. Although the Froude scaling method cannot be applied in conjunction with Reynolds number scaling, it does properly scale inertial effects [26]. This inconsistency was avoided by using a model-scale Reynolds number for the FAST simulations.
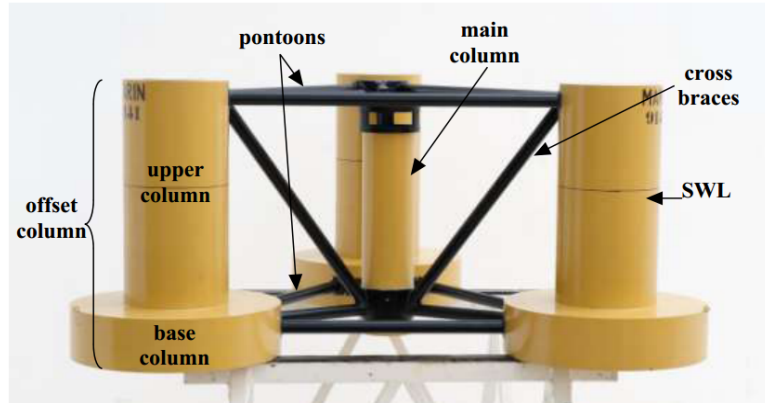
Figure 7.1. The model-scale semi-submersible, built at 1/50th the size of the prototype, from the DeepCwind tank tests with component definitions labeled [187]. Note: SWL is the still water line

7.2.1 Semi-Submersible Specifications

Discussions of the tower or turbine properties are neglected because these simulations omitted the wind turbine. The semi-submersible structure, built at model scale

Table 7.1. Specifications of the semi-submersible structure [187]

Depth of platform base below SWL (total draft)	20.0 m
Centerline spacing between offset columns	50.0 m
Length of upper columns	26.0 m
Length of base columns	6.0 m
Diameter of main column	6.5 m
Diameter of offset (upper) columns	12.0 m
Diameter of base columns	24.0 m
Diameter of pontoons and cross braces	1.6 m

and used in the DeepCwind tank tests, is shown in Fig. 7.1 with labeled components. The three large cylinders are referred to as the offset columns, and are split into the upper and base columns. The center of the semi-submersible consists of a single main column that is connected to the offset columns with pontoons and cross braces. Additionally, the still water line (SWL) is indicated on the right offset column. The dimensions of the individual components, at prototype scale, are given in Table 7.1.

7.2.2 Representative Geometries

HydroDyn predicts wave and current loads on offshore structures using Morison's equation in conjunction with potential-flow theory. For small members, where it is assumed that viscous and inertial forces dominate, Morison's equation is most appropriate. For the larger members, where diffraction effects become dominant, potential-flow theory is more valid (based on a preprocess using a panel method such as WAMIT). To study the implications of the applicability of Morison's equation and potential-flow theory as they relate to the component size, CFD simulations were performed on three representative geometries that include all components, only the small components, and only the large components. High-fidelity results from the three CFD meshes are compared against results from HydroDyn where the distinction between body size alters the limits of applicability for the CAE model equations. In

OpenFOAM, the validity of the model equations does not change based on structure size, so the representative geometry is changed instead.

First, a mesh representing the entire semi-submersible platform was generated. The surface of the semi-submersible is shown in the top of Figure 7.2, where an increased level of refinement can be seen around the SWL. This mesh is referred to as the "Full Geometry" throughout this study. Next, the offset columns were isolated from the pontoons, cross braces, and main column, to generate the geometry shown in the bottom right of Fig. 7.2, where again, a region of increased mesh refinement exists around the SWL. This mesh is referred to as "large components only." Finally, the cross braces, pontoons, and main column compose the "small components only" mesh, which is shown at the bottom left of Fig. 7.2. The following sections give more detail on categorizing the individual components as small or large.
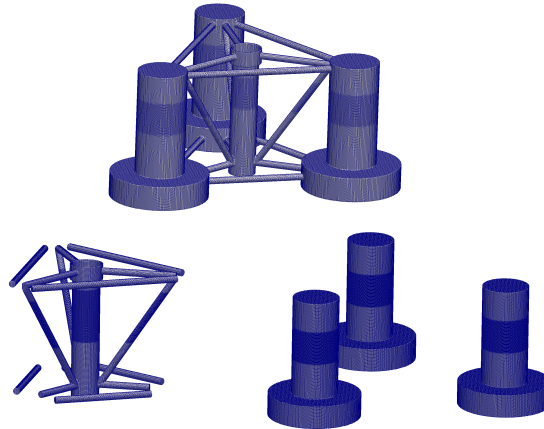
Figure 7.2. The surfaces of the semi-submersible from the full geometry, large components only and small components only numerical meshes for CFD, in clockwise order from the top

7.3 Methods

7.3.1 FAST

FAST is a nonlinear aero-hydro-servo-elastic CAE tool used for wind turbine design. The new FAST (version 8) modularization framework, which is used in the research presented in here, breaks the code into several modules including HydroDyn for hydrodynamics. HydroDyn uses a WAMIT potential-flow panel method model as a preprocessor and internal frequency-to-time-domain transforms for time-domain-based potential-flow solutions, as well as an internal Morison's equation solver for drag effects [91]. In addition, the new release of HydroDyn adds the capability to calculate Morison's equation for multiple interconnected and (nonvertical) platform members.

The WAMIT model developed for this platform is a high-resolution surface model that includes all platform members. This model is used to solve the radiation problem, which generates a body-oscillation frequency-dependent set of coefficients, and the diffraction problem, which generates a vector of wave-frequency dependent coefficients. In this research, the platform is fixed, so there are no forces from radiation, which is caused by platform motion. Furthermore, in current-only cases, there are no waves, so the total force contribution from potential-flow theory is zero.

Morison's equation in its full form includes a term for diffraction-induced wave excitation forces (with a long wavelength approximation), radiation-induced added mass, and viscous drag forces. Only the viscous drag force term of Morison's equation is calculated in this research because the other forces are computed using the potential-flow model. Using the new capabilities of FAST 8, a viscous drag coefficient is specified for every member of the platform. FAST outputs a viscous force prediction per unit length for several nodes along each member. The resulting viscous forces are integrated along the length of each member and summed to produce a resulting total force from Morison's equation. The Morison solution treats each member as

an isolated component, neglecting the effects of direct interaction between members. This is not the case for WAMIT, where the diffraction solution includes the effects of direct interactions between members.

7.3.2 OpenFOAM

This section briefly describes the CFD methods that were used to simulate the semi-submersible platform in current and waves. A VOF method was used to simulate the two-phase flow. Further details about the CFD methodology can be found in Chapter 4 of this document.

As mentioned previously, three meshes were generated representing the full geometry, small components only, and large components only. Each mesh consists of roughly 3 million cells, with increased mesh refinement located around the SWL and near the surface of the semi-submersible body. The model-scale domain begins roughly 9.4 m from the body, extends 4 m past the body in the wave propagation direction, and is 6.3 m wide. The domain depth is 4 m, which matches the depth of the DeepCwind tank tests, and classifies the waves in the deepwater region. At prototype scale, this is equivalent to a mesh that begins 470 m from the body, extending 200 m behind the body, with a depth of 200 m, and a domain width of 315 m. The bottom and sides of the domain are treated as no-slip boundaries. The inlet was treated with varying velocity, volume fraction, and pressure gradient, according to the wave theory being simulated.

The wave library developed for OpenFOAM by Jacobsen, et al, was used in this work [80], as discussed in Chapter 5. In this study, only Stokes first order wave theory and steady currents are used. This work implemented relaxation zones at the domain outlet, also discussed in Chapter 5.

The time-varying velocity, volume fraction, and pressure gradient were prescribed on the inlet boundary throughout the simulation. Initial conditions can be prescribed

as the user wishes. The simulations presented here had an initially quiescent flow field (i.e. zero velocity everywhere in the domain).

Turbulence was modeled with the Spalart-Allmaras one-equation model [217], with a Spalding wall function at the semi-submersible boundary [218].

The load on the body was predicted by integrating the pressure and viscous stresses along the body in a discretized manner. The pressure and viscous forces from each cell face on the surface of the body were summed to find the total pressure and viscous force, respectively. The pressure and viscous forces were then combined to yield a total force on the body. The total moment on the body was calculated as the sum of the moments resulting from pressure and viscous stresses, where moment arms are calculated as the distance from face centers to the structure center of gravity. The total moment was determined in the same manner as the total force. The results are stored as three component vectors, in the x, y, and z directions and in the roll, pitch, and yaw directions for the forces and moments, respectively.

Experimental tests of the model-scale semi-submersible were carried out at the Maritime Research Institute Netherlands (MARIN) under the DeepCwind project, but only for the case of the freely moving body [34]. The simulations carried out in this work model the structure as fixed in place, therefore direct compararisons of these numerical results to the tank test data cannot be made.

In the absence of experimental data to directly validate the semi-submersible work against, comparable experiments to the case of a fixed semi-submersible in waves and current are used in their place. The CFD model has been validated against a suite of experimental work published in the literature, as discussed in Chapter 5. The CFD work here was simulated at model scale, where the experimental and numerical results are in excellent agreement.

Table 7.2. Current Conditions. The current velocities for the three cases are given at model and prototype-scale. The Reynolds numbers for the four major components of the semi-submersible are presented at model and prototype scale

	Case 1	Case 2	Case 3
Model-Scale Vel.	0.042 (m/s)	0.084 (m/s)	0.14 (m/s)
Model-Scale Re.			
Pontoons	1,356	2,713	4,524
Main Column	5,512	11,024	18,382
Upper Columns	10,176	20,352	33,936
Base Columns	20,352	40,704	67,872
Prototype-Scale Vel.	0.3 (m/s)	0.6 (m/s)	1.0 (m/s)
Prototype-Scale Re.			
Pontoons	480,000	960,000	1,600,000
Main Column	1,950,000	3,900,000	6,500,000
Upper Columns	3,600,000	7,200,000	12,000,000
Base Columns	7,200,000	14,400,000	24,000,000

7.4   Environmental Conditions

A series of current-only cases were carried out. The current velocity ranges from 0.3 m/s to 1 m/s at prototype scale, and these velocities are scaled down to model scale with Froude scaling. This range of current velocities was selected because it matches the conditions most likely to be found in the ocean environment. The values for the current velocities are given in Table 7.2, at both model and prototype scale. Additionally, the Reynolds numbers for each of the four major components of the semi-submersible are given at each of the current velocities.

A more detailed discussion of validation cases is given in Chapter 5, where Fig. 5.15 demonstrates the ability to predict the drag coefficient of a vertical cylinder over a range of Reynolds numbers. Confidence in the ability to predict loads on bodies in steady flow, such as current, is high.

7.5   Results and Discussion

7.5.1   Global Loads

Inline and transverse force predictions are presented for the semi-submersible in a current with velocity of 0.6 m/s in Fig. 7.3. OpenFOAM results are presented from simulations with the three representative geometry meshes described earlier. Results from the large component-only mesh, small component-only mesh and the full geometry mesh are shown by the solid blue line, dashed red line, and light blue line, respectively. Force predictions from FAST are represented by the dash-dotted black line.
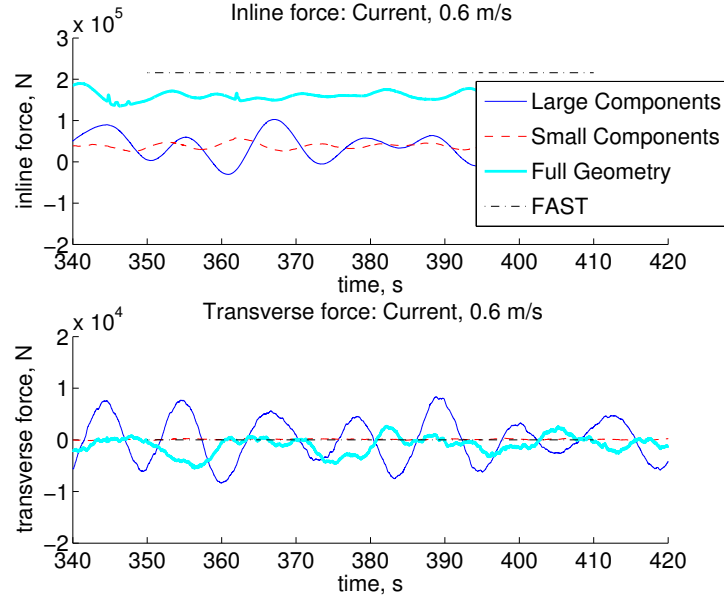
Figure 7.3. Inline and transverse force results from OpenFOAM and FAST. Results from the large components only, small components only and full geometry meshes are shown for OpenFOAM. FAST predicts a larger inline force, but smaller transverse force compared to OpenFOAM.

The inline force prediction from FAST is larger than any of the inline force results from OpenFOAM. One possible reason for these differences is due to the numerical treatment of shadowing effects. The simulations in OpenFOAM naturally account for
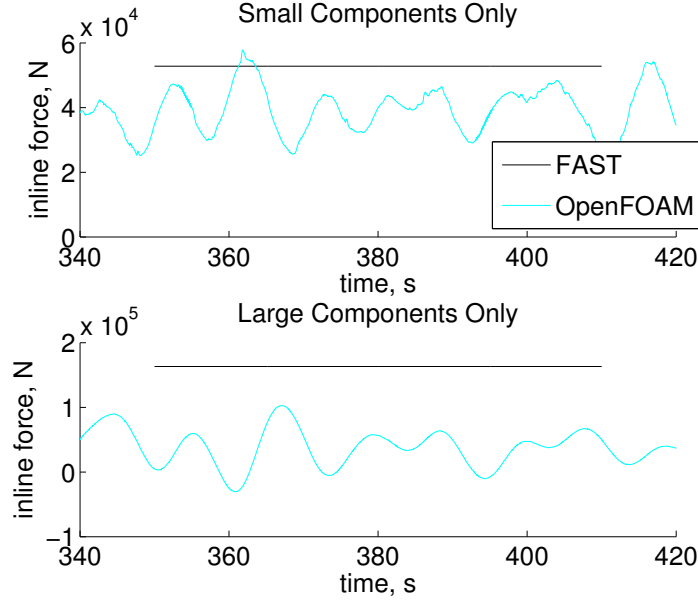
Figure 7.4. Inline force predictions from FAST and OpenFOAM for only the small components, and only the large components in a current of 0.6 m/s. FAST predicts a larger force on both small and large components.

shadowing effects, in which downstream members are shadowed by upstream members, decreasing the load. These shadowing effects are not accounted for in FAST, and each member is assumed to interact with an undisturbed flow. Future work examines the shadowing effect in more detail. The discrepancy may also be due to the fact that OpenFOAM predicts drag coefficients that are between 2.0% and 8.4% lower than the value of 1.0 used in FAST. It may also be the case that a drag coefficient of 1.0 in FAST is not appropriate for all members. FAST predicts a constant zero force in the transverse direction, which is not representative of the true time-varying physics that result from vortex shedding, just as it is expected from the Morison formulation. The results from OpenFOAM properly capture the time-varying nature of the transverse force, unlike the FAST results that do not model the vortex shedding and associated lift forces.

In addition to looking at the total hydrodynamic loading on the semi-submersible, forces on individual components are examined. The total forces on the small components, which include the pontoons, cross braces, and main column, are summed from the FAST output and compared to the results from the OpenFOAM simulation with the small components-only mesh. Additionally, the sum of the forces on the large components in FAST are compared to the results from the large components-only mesh in OpenFOAM. The comparison of inline forces in a current of 0.6 m/s is shown in Fig. 7.4. For both the small and large components, FAST predicts larger inline forces, where the difference is greater for the case of large components. This is consistent with the expectation that Morison's equation predicts forces more accurately for small components. Again, the larger predicted forces from FAST may be the result of neglecting shadowing effects of upstream members sheltering downstream members, or also the difference in drag coefficients between FAST and OpenFOAM.

Figure 7.5 summarizes the overall effect of the velocity on the force predictions from the three steady current cases by comparing the mean of the forces in the inline and transverse directions. In current, FAST predicts constant forces in the inline and transverse directions. OpenFOAM predicts oscillating forces, which more closely match the physics. Error bars on the OpenFOAM results indicate the standard deviation from the mean because of the time-varying nature of these signals. Only the full geometry results from OpenFOAM are considered here. Again, FAST predicts a larger inline force than OpenFOAM, which could be a consequence of shadowing effects being neglected in FAST.

FAST predicts a zero transverse force across all current velocities. OpenFOAM shows a slight nonzero mean that results from noise in the transverse force signal. The standard deviation in the transverse force prediction from OpenFOAM (shown by the error bars in Fig. 7.5) demonstrates that the two codes are in fair agreement for the mean transverse flow predictions. Transverse force prediction in OpenFOAM
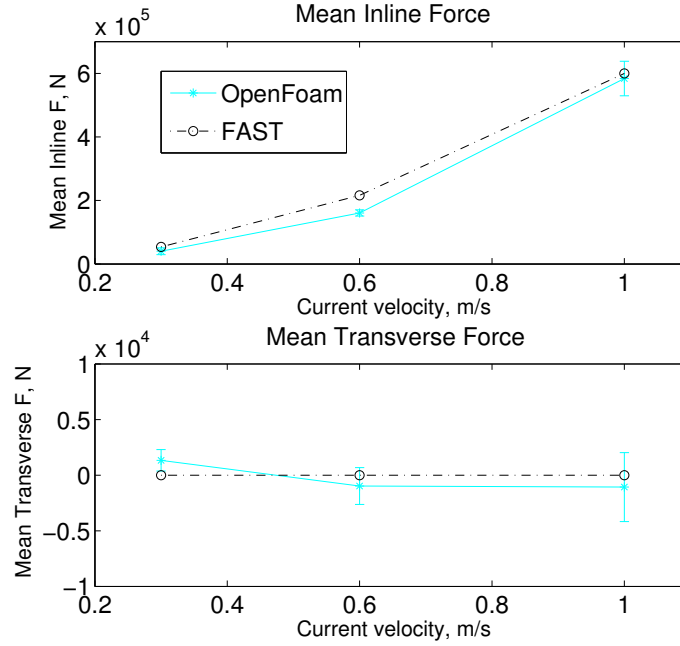
Figure 7.5. Trends in the inline and transverse force predictions in steady current. The mean of the inline and transverse forces from both codes is plotted against increasing current velocities. Error bars on the OpenFOAM results illustrate the standard deviation from the mean because the inline and transverse forces are actually oscillating signals.

does capture lift forces, which are not computed in FAST because it uses Morison's equation.

The full geometry load prediction from OpenFOAM does not equal the sum of the results from the large components only and the small components only meshes. This is likely due to the complex flow patterns that result from the fluid interacting with the structural components in the interior region of the semi-submersible. The accelerating flow around and through the full geometry mesh results in an increased load prediction on the structure.

7.5.2 Geometric Factors Affecting the Drag

It was hypothesized that discrepancies in load predictions from the previous work could be due to a variety of factors, including shadowing effects, treatment of interaction between individual members, or even the selection, or prediction, of drag coefficients. In each of the OpenFOAM simulations discussed in the previous work, the geometry considered was treated as a single patch, meaning each simulation produced only one global force prediction.

This study presents loads on individual members of the semisubmersible and highlights the effects of shadowing, interaction between structure members, and the importance of carefully selecting drag coefficients for engineering models. This work focused only on drag because the previous work validated the radiation/diffraction solution of the potential-flow solution through comparison of wave-loading simulations in HydroDyn and OpenFOAM. This study followed that previous work, trying to understand why OpenFOAM did not match HydroDyn well for the current-only case, where drag is important, and the key features that cause these loads to differ from those seen for submerged, infinite cylinders. Drag effects are also important in severe sea states.

For this study, loads on separate structural members were investigated to better understand the significance of shadowing and interactions between members, as well as the influence of a free surface and free ends. CFD is used to examine the influence of a complex geometry on the drag of a structure as compared to the experimental measurements for submerged, infinite cylinders. Insight about the role of shadowing is provided through CFD force predictions and flow visualizations. The roles of the free surface, free ends, and wake effects are discussed in terms of inertial and drag loads on the semisubmersible. The implications of these factors on loading predictions in engineering tools are addressed with regard to modeling assumptions and approximations in HydroDyn and other similar codes.

In addition to assessing the mean drag predictions on the semisubmersible, the CFD solution can also quantify the importance of the transient loads induced by vortex shedding. Time histories of the load predictions in the inline and transverse directions, as computed with CFD, provide information about the magnitude and frequency of the oscillatory loads. These time varying loads merit further attention because of their potential fatigue impacts and absence in Morison-based engineering models.

This work serves to better inform those that use engineering tools when selecting drag coefficients for offshore structures that differ from infinitely long, fully submerged cylinders. CFD simulations presented here provide improved understanding of the drag behavior of more complex structures, and this knowledge can be extended to engineering models, such as HydroDyn.

Often, the drag coefficient input to HydroDyn, and other similar engineering tools, is chosen based on the Reynolds number alone. Moreover, the drag coefficient is often determined based on previous experimental work on fully submerged, infinitely long cylinders. The semisubmersible components are neither infinitely long nor fully submerged, and it was hypothesized that these factors alter the drag coefficient, which is discussed later in this paper.

In fact, previous work from the literature demonstrates that the drag coefficient on a circular cylinder can be sensitive to many factors, including the presence of a free surface, and a free end of a body. In addition, the presence of multiple members disrupts the flow such that the drag characteristics are altered as well. If tools are not capable of modeling this disturbed flow, the parameters must be used to approximate this influence. Insight is gained from a review of previous work that has investigated these individual factors on cylinders. Furthermore, the results provided confidence in the drag coefficient predictions from CFD in this study where multiple factors were

combined. Indeed, these factors do alter the drag behavior on the semisubmersible in the current conditions considered here, as discussed below.
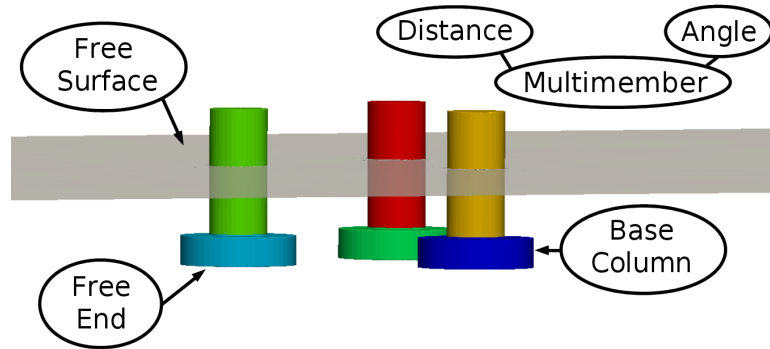
Figure 7.6. Contributions to the drag coefficient of the semisubmersible platform for offshore wind turbines.

Various authors have examined the effects of a free surface on the drag behavior of vertical cylinders. In all of these works, vertical cylinders that pierce the free surface of an air-water interface were studied. Experimental work by Chaplin and Teigen [27] demonstrated that the drag coefficient decreases near the free surface of the water. Numerical work by Yu [263], Kawamura [105] and Suh [221] found drag coefficients that were smaller than the drag coefficient for fully submerged cylinders in the same flow conditions. There is numerical and experimental evidence that the presence of a free surface decreases the drag coefficient on vertical cylinders.

The role of free ends has also been investigated numerically and experimentally. Experimental studies by Sumner [224] demonstrated reduced drag coefficients for cylinders with a free end about which the flow could accelerate. Sumner's work investigated drag in uniform flow conditions, but the same effects were found in waves. Niedzwecki [157] performed experiments on truncated cylinders in regular and random waves and found that the normalized drag on truncated cylinders was lesser than that on infinitely long cylinders.

Drag behavior on bodies consisting of multiple members has also been investigated. Sumner provides a thorough review of dual-cylinder configurations [222]. For cylinders placed in a tandem configuration, in which one cylinder is directly upstream of the other, it was found that the upstream cylinder has a lower drag coefficient than it would if the cylinder were isolated. Furthermore, at certain distances, the downstream cylinder can experience a negative drag. When cylinders were arranged side-by-side, a certain spacing existed where the drag reached a minimum. Finally, when the cylinders were staggered, certain angles and spacings existed in which drag minima are seen. In all of these scenarios, the wake behind the first cylinder alters the flow field such that the drag behavior is different from that of an isolated cylinder.

Overall, the effects of a free surface, free end, and multibody configuration are shown to cause a decrease in drag coefficient on a vertical cylinder. There is reason to believe that these same factors are the causes for decreases in the drag coefficient of many members of the semisubmersible structure as well—such as the upper, base, and main columns, which are shown in a later section. This study examines the combined effects of the free surface, free end, and multibody configuration of the semisubmersible on the drag behavior.

7.5.3 Sectional Loads: Numerical Set-up

CFD simulation results are presented for the simplified OC4-DeepCwind semisubmersible in current-only conditions. Results are first presented to compare load predictions between the three offset columns. Then the loading is discussed in further detail by examining differences in loads between the upper and base components of the offset columns. The trends in drag loads are presented quantitatively in the first two sub-sections. Next, the quantitative findings in the drag behavior are explained through various flow visualizations. Finally, mean inline force predictions from Hydro-

Dyn are presented, with the drag coefficients determined from CFD at three current velocities.

In the simulations, the semisubmersible platform is oriented such that one column is located in front and centered, and the other two columns are downstream and parallel to one another. The column that is upstream of the others is called the front column, and the two downstream columns are called the right and left columns, according to their position relative to the front column when looking in the direction of the current flow.

Simulations were carried out in current-only conditions, at a uniform velocity of 0.085 m/s, at model scale. This corresponds to a current velocity of 0.6 m/s at prototype scale. Additionally, simulations were performed with HydroDyn, using the same environmental conditions and semisubmersible orientation as the CFD simulations. The results from the two codes are presented for comparison in Section 4. These flow conditions correspond to Froude number of 0.055, where $Fr = \frac{U}{\sqrt{gL}}$. The Reynolds numbers are given in Table 7.3.

Table 7.3. The Reynolds numbers of the upper and base columns, at model and prototype scale. The Froude number is 0.055 at both scales.

	Model Scale Re	Protoype Scale Re
Upper Column	20,361	7,200,000
Base Column	40,704	14,400,000

Meshes were generated with increased mesh refinement near the surface of the semisubmersible body and also around the fluid interface. Three unstructured meshes were generated, with 1.94, 2.88, and 5.06 million cells each. Sensitivity of the model to grid density was again tested for the computational meshes used in this study. The results of this mesh convergence study are given in Figure 7.7. It was found that the inline force predictions show convergence after a mesh size of 2.88 million cells. A y+ value of 61 was used on the surface of the columns, which is appropriate given the use

of the Spalding wall function. A vertical slice through the coarsest numerical domain is presented in Figure 7.8. The entire numerical domain is illustrated in Figure 7.9.

The offset columns, in the absence of the main column, pontoons, and cross braces, of the geometry were selected for further investigation because of their more simplistic form. The absence of cross braces and pontoons reduces the complexity of the flow, allowing for better understanding of the fundamental flow behavior. Meshes were generated for CFD simulations consisting of only the three offset columns. The reults presented in the Loads on Individual Offset Columns section used a mesh with three isolated surface patches, while the results in the Loads on Upper and Base Columns section are from a mesh with six surface patches.
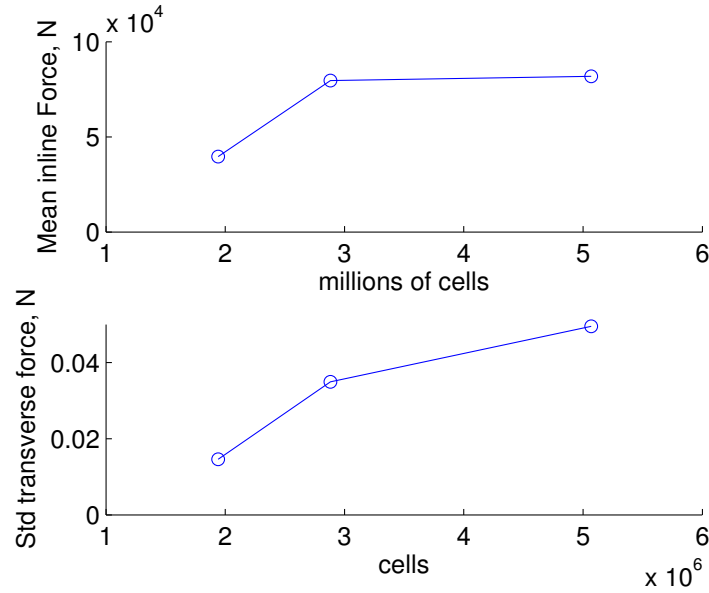
Figure 7.7. Mesh convergence results for the mean inline force and the standard deviation of the transverse force, in the top and bottom plots, respectively.

The bottom and sides of the domain are prescribed as no-slip boundaries conditions on velocity. The pressure and volume fraction are zero-gradient at the walls and the floor. An atmospheric boundary condition is used for the top, in which the pressure changes with velocity, as prescribed by the *totalPressure* condition in Open-
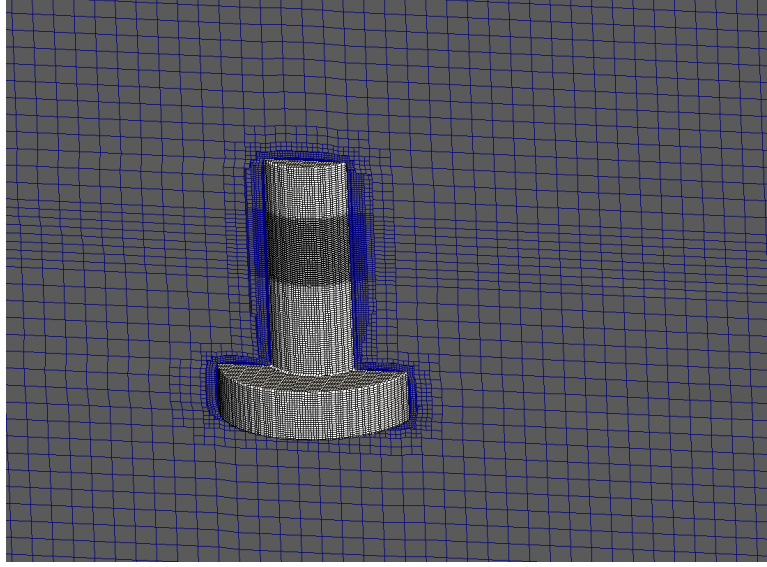
Figure 7.8. Vertical slice through the domain to illustrate the increased level of mesh refinement around the free surface, as well as the refinement surrounding the body.
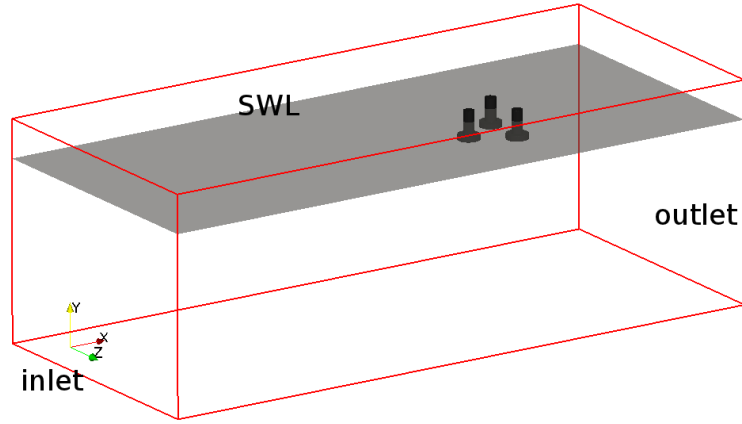
Figure 7.9. Computational domain for the simplified OC4-DeepCWind semisubmersible in uniform flow.

FOAM. A uniform velocity is prescribed in the water phase at the inlet. The volume fraction is given as 1 below the still water line (SWL) and 0 above, where 1 represents water and 0 is air. The internal domain is initialized with a zero-velocity flow field.

The maximum Courant number ($Co = U\frac{\partial t}{\partial x}$, where U is the velocity and ∂t, ∂x are the discretized time and length intervals) was set to 0.5. An initial time step

of 0.01s was given, and the timestep was adjusted automatically according to the Courant number through the simulation.

7.5.4 Sectional Loads: Individual Offset Columns

The CFD results for the inline and transverse forces on each of the individual offset columns are shown in Figure 7.10. The results are shown between 250s and 350s, once the initial transients, due to the quiescent initial conditions on velocity, of the simulation have subsided. The top plot shows the inline force predictions on the front, right and left columns. A lag in the peaks of the forces can be seen in the right, and left column loads, as compared to the front column. The bottom plot displays the transverse force predictions on the three columns. The magnitude of the transverse forces on the right and left columns is greater than on the front column, which is likely a result of flow diffraction and vortex shedding on the downstream columns. Furthermore, it is interesting to note that the transverse forces on the two downstream columns are completely out of phase with each other, indicating symmetrical vortex shedding off of the trailing columns.

To investigate the inline force predictions further, the mean force predictions on each column, from OpenFOAM, are calculated. These mean inline forces are shown in the first three bars of Figure 7.11. The red error bars indicate one standard deviation from the mean, to illustrate the degree to which the periodic force signal oscillates about the mean. The bar on the far right of Figure 7.11 shows the inline force prediction from HydroDyn. HydroDyn calculates the inline force as a mean value, without any time-varying oscillation, so the standard deviation of the signal is zero. The bar labeled $C_d = 1.0$ shows the result from a HydroDyn simulation where the base and upper columns are each assigned a drag coefficient equal to one. The drag coefficient of 1.0 corresponds to the model-scale Reynolds numbers of the upper and base columns. These drag coefficients for input to HydroDyn are selected from a
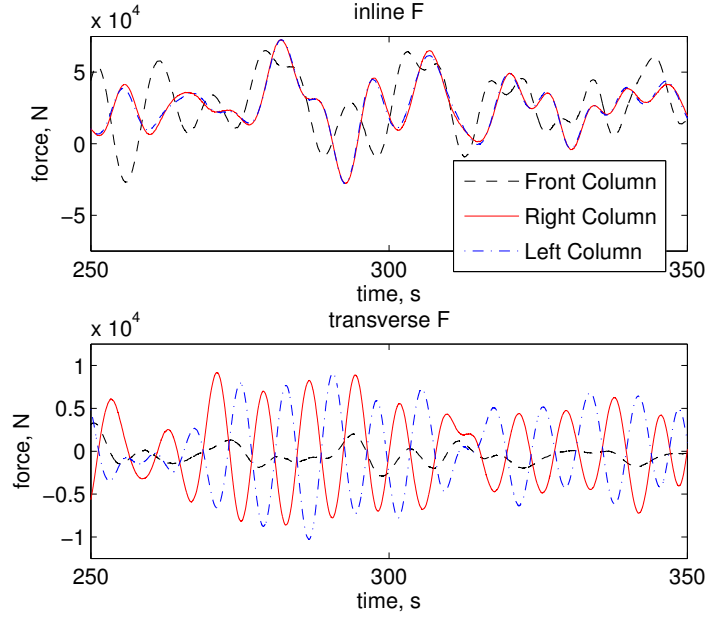
Figure 7.10. Inline and transverse force predictions from OpenFOAM. The load predictions are shown in black, red, and blue for the front, right, and left columns, respectively.

straightforward Reynolds number versus drag coefficient curve. Without consideration of the free surface, free end or multimember effects, it was expected that a drag coefficient equal to 1.0 would be most appropriate for the model-scale simulations carried out in this work, but that was not found to be true in practice.

The mean inline force predictions from OpenFOAM are very similar for each of the three offset columns, and not surprisingly, are in near perfect agreement for the two downstream columns. The agreement between HydroDyn and OpenFOAM is not very good when the drag coefficients are set to 1.0.

These findings illustrate three main points. First, the OpenFOAM results seem to indicate that shadowing effects do not play a major role in the loading on the structure, as demonstrated by the very similar inline forces on the front, right, and left columns. However, this finding is questioned in the next subsection when loads on individual members are investigated. Second, these results point to the pivotal
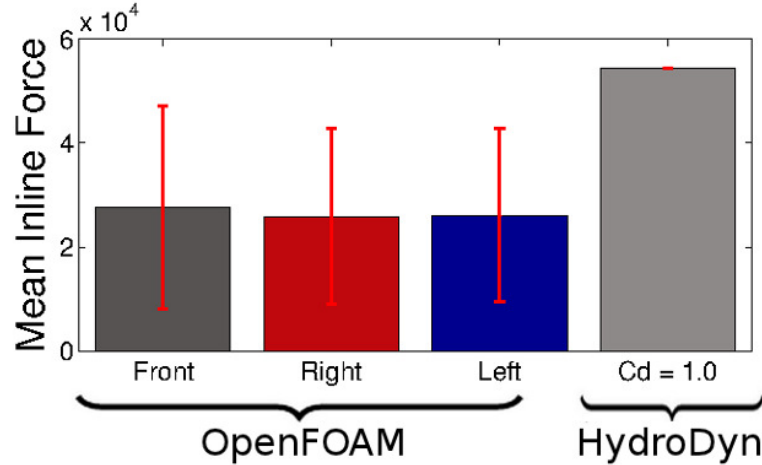
Figure 7.11. Mean inline force predictions from OpenFOAM and HydroDyn. The three bars on the left show the results from OpenFOAM. The bar on the right shows predictions from HydroDyn, for the inline force on a single column. Error bars indicate one standard deviation in the time-varying force signals from OpenFOAM.

role the drag coefficient plays in loading predictions in current-only conditions. It is possible that OpenFOAM is underpredicting the drag on the body; however, prior validation work showed great accuracy in the drag prediction in this Reynolds number range. The drag coefficient selection in HydroDyn could be at fault. It may be too simplistic to select the drag coefficient from a simple Reynolds number relationship, especially one that is based on an infinitely long, fully submerged cylinder. Third, the time variation of load is the result of vortex shedding, not modelled by the viscous drag term from Morison's equation.

7.5.5   Sectional Loads: Individual Members

To further investigate the inline forces on the offset columns of the semisubmersible column, the loads on the upper and base columns of the front and trailing offset columns are examined individually. Whereas the results in the previous section would indicate roughly uniform loading on each offset column, the results here show that loading varies greatly depending on upstream versus downstream location, as well

at proximity to the free surface. While these reuslts are for a specific geometry in a single flow condition, we hypothesize that these factors will affect loads on other geometries in similar flow conditions, such that careful attention must be given to selecting input parameters to engineering tools.
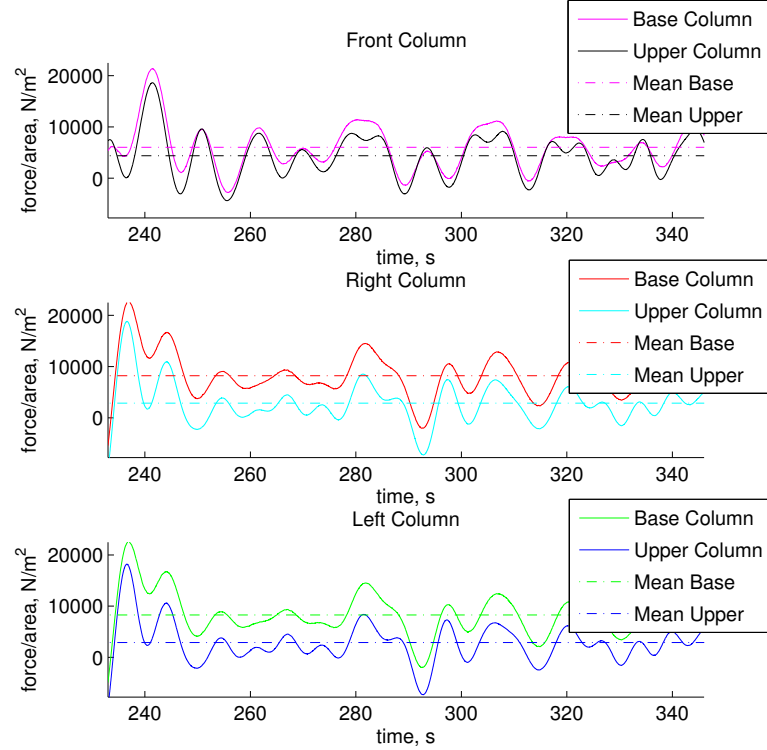
Figure 7.12. Forces per unit area on the front, right, and left columns are shown in the top, middle, and bottom plot, respectively in a current of 0.6 m/s. Solid lines show the time varying loads, and the dash-dot lines show the mean value used for computing the drag coefficient.

Again, simulations in OpenFOAM were carried out in current-only conditions with a uniform velocity equal to 0.085 m/s at model scale, corresponding to 0.6 m/s at prototype scale. The force predictions, per unit area, are presented in Figure 7.12. The forces per unit area on the front, right, and left columns are shown in the top, middle, and bottom plot, respectively. The magenta, red, and green lines show the loads per unit area on the base columns, and the black, cyan, and blue lines illustrate
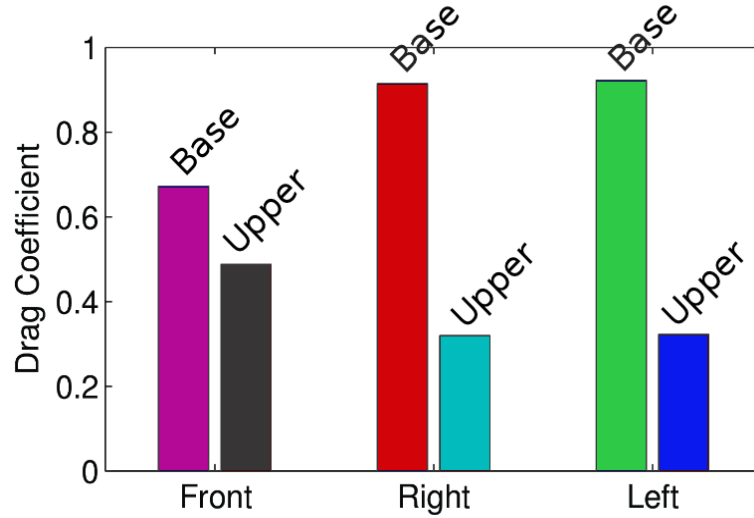
Figure 7.13. Predicted drag coefficients from an OpenFOAM simulation of the three offset columns in a current flow of U = 0.6 m/s at prototype scale. The results for the base columns are shown in blue, and the upper columns are represented in red. The mean inline forces are illustrated with the dashed lines.

loads per unit area on the upper columns. Solid lines show the time varying loads, while the dash-dot lines show the calculated mean load. The loads per unit area on the base and upper columns are very similar for the front column. The downstream columns, however, give different loads per unit area for the base and upper columns. This indicates that the wake behind the front column is somehow affecting the loading on the body in a way that varies vertically.

The variation in loads between the upstream and downstream columns is not accounted for in HydroDyn where there is no model for shadowing of members, such that equal loads are predicted on each column. Additionally, the load predictions from HydroDyn do not vary in the vertical direction when modeling current-only conditions. Finally, HydroDyn does not compute time-varying loads for the current-only conditions, despite the fact that vortex shedding does occur in this flow regime.

The predicted drag coefficients from OpenFOAM are calculated for the base and upper columns for each of the three offset columns, based on the upstream undis-

turbed velocity. The results are presented in Figure 7.13. At the Reynolds number simulated here, the drag coefficient versus Reynolds curve for an infinitely long, fully submerged cylinder indicates that the drag coefficient should be roughly 1.0. The predicted drag coefficients from OpenFOAM are all below 1.0. The drag on the base columns increases for downstream members, while the drag on the upper columns decreases. These initially surprising results merit further investigation through flow visualization. The findings from flow visualization, and a brief survey of the literature discussed earlier, reveals that these predictions from OpenFOAM are likely correct. The following subsection provides and discusses flow field visualizations.

7.5.6 Flow Visualizations

Here, visualizations of the velocity and pressure fields are presented to provide insight about the drag coefficients discussed above. The values in this section are presented at model scale—the scale at which the CFD simulations were performed. Additionally, the visualizations presented here are instantaneous values and have not been time averaged. These visualizations highlight a variety of factors that may contribute to smaller predictions in the drag coefficient than previously anticipated. These factors include the presence of a free surface, free end effects of the body, and the multimember structure. As discussed earlier, the literature suggests that each of these factors can lead to decreases in the drag behavior on the semisubmersible structure.

A side view of the streamlines around the offset columns in current-only conditions is shown in Figure 7.14 where the flow moves from left to right. This visualization highlights the velocity drop near the body, and furthermore, near the free surface. Additionally, the flow is shown to accelerate as it passes under the geometry. Finally, the velocity near the free surface is further reduced after passing the front column, just before it reaches the two trailing columns. This single image highlights that the
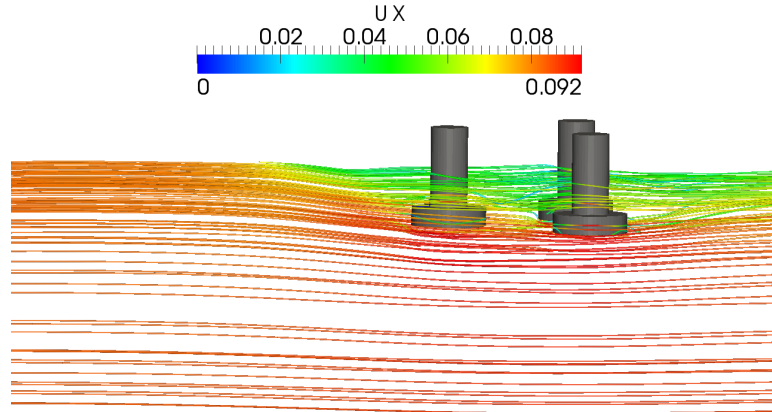
Figure 7.14. A side view of the streamlines where the flow travels from left to right. The flow slows as it approaches the body and near the free surface. Acceleration of the flow can be seen as the streamlines pass under the body.

free surface, free ends, and multimember arrangement all appear to alter the drag behavior of the semisubmersible, as compared to that of an infinite cylinder.

Streamlines that are seeded nearer to the free surface are shown in Figure 7.15. They provide a better visualization of the vortex shedding in the wakes of the three offset columns. Again, reductions in the velocity in the current direction are seen near the free surface as the flow approached the body. Also, the effects of the multibody arrangement are illustrated in the increasing reduction in flow velocity behind the front column and before the trailing columns.

Horizontal slices at increasing depths—0.1, 0.2 and 0.3 m below the SWL—are shown in Figure 7.16. The velocity magnitude is presented at three depths of submergence, where the magnitude increases with increasing depth. This reiterates the trend shown in Figure 7.14 where the flow is seen to slow near the free surface. The reduction in fluid velocity near the free surface where the body sits explains the reduced drag coefficient on the upper columns, as compared to the base columns that see a higher flow velocity. Again, the presence of the free surface is shown to affect the flow field near the structure.
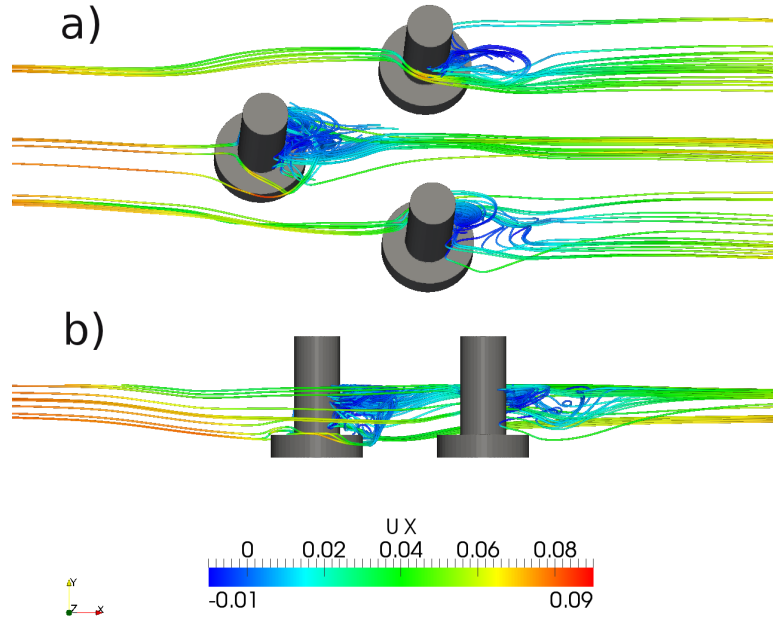
Figure 7.15. a) Bird's eye view of the streamlines past the simplified semisubmersible geometry, in a 0.085 m/s current flow traveling from left to right, at model scale. b) A side view of the streamlines.
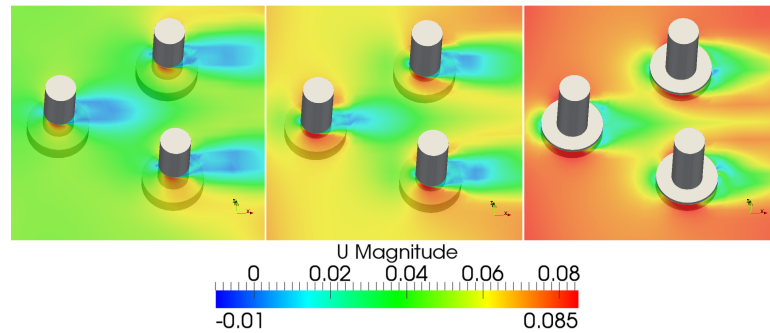
Figure 7.16. The velocity magnitude at three horizontal planes, located at 0.1, 0.2, and 0.3 m below the SWL, from left to right, shown at 42 s. The current direction is from left to right. The increasing velocity with increasing water depth highlights the role of the free surface in the fluid flow near the structure.

Next, velocity vectors at the three depths—again, at 0.1, 0.2, and 0.3m below the SWL—are shown in Figure 7.17, from top to bottom, respectively. Again, a reduced velocity is seen near the free surface near the structure. With increasing water depth, the velocity increases. This image sheds light onto the effects of the

171
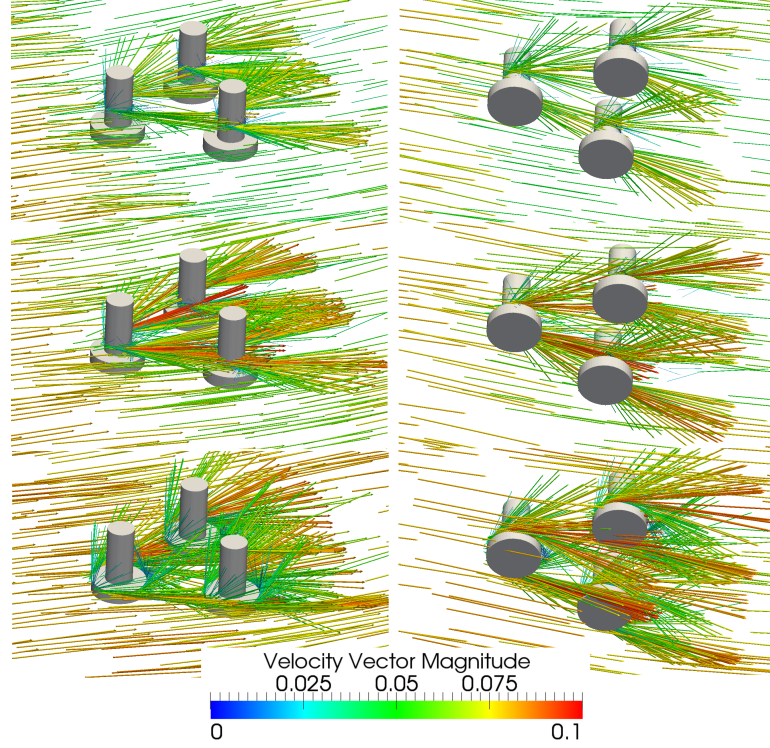
Figure 7.17. Velocity vectors at three depths below the free surface, 0.1, 0.2, and 0.3 m, from top to bottom respectively. The right column of images shows a view from an angle above, while the left column illustrates the view from an angle below the semisubmersible. The vectors are colored by magnitude.

multibody arrangement by illustrating the vector magnitudes and directions as they come off of each offset column. Perhaps most notable is the large magnitude velocities that point downwards from the front column onto the trailing base columns. These velocity vectors help to explain the increase in the drag on the trailing base columns.

Largely, the total pressure field is dominated by hydrostatics. To investigate local changes in the pressure, the hydrostatic component is subtracted from the total pressure, leaving a modified pressure term, $\tilde{p}$, that is p without $\rho g z$. This is described mathematically below, where p is defined as the total pressure, giving the modified pressure,

$$\tilde{p} = p + \rho g z \tag{7.1}$$

where z is negative in the downward direction, hence the plus sign. The total pressure is many orders of magnitude larger than the modified pressure, $\tilde{p}$, term due to the dominance of the hydrostatics. However, the hydrostatic pressure varies only in the vertical direction (z), such that ∇p_x and ∇p_y are dictated entirely by changes in the modified pressure. In this work, which focuses on drag loads, it is the changes in the x-direction of the pressure field that are of primary concern. Therefore, despite the dominance of the hydrostatics on the total pressure, variations in the modified pressure, specifically in the x-direction (current direction) are significant.

Isosurfaces of the modified pressure field, $\tilde{p}$, are shown in Figure 7.18. This image illustrates surfaces of constant pressure, without the contribution of the hydrostatic pressure. It is shown that lower pressure regions exist directly in front of the front column, and behind the trailing columns, as indicated by the dark blue pressure shell with a value of 3 Pa. The isosurfaces increase in magnitude inside of the three offset columns, most specifically on the front side of the trailing columns. This is shown with the red isosurface illustrating a pressure of 5.5 Pa. These variations in the modified pressure highlight the effects of the multicolumn arrangement of the semisubmersible where the field appears to be directly affected by the presence of the downstream columns.

The changes in the modified pressure term help to explain why the flow diverts downwards as it travels downstream, because the flow avoids the region of higher pressure that forms in between the three offset columns. The fluid motion is seen to move downwards after passing over the base column of the front pile. It then heads toward the base columns of the trailing columns with increased velocities, as is depicted in Figures 7.14 and 7.17. To further illustrate the increase in velocity, Figure 7.19 shows the magnitude of the velocity field mapped onto the pressure isosurfaces presented in Figure 7.18. Additionally, accelerations in the flow field are seen as the flow travels
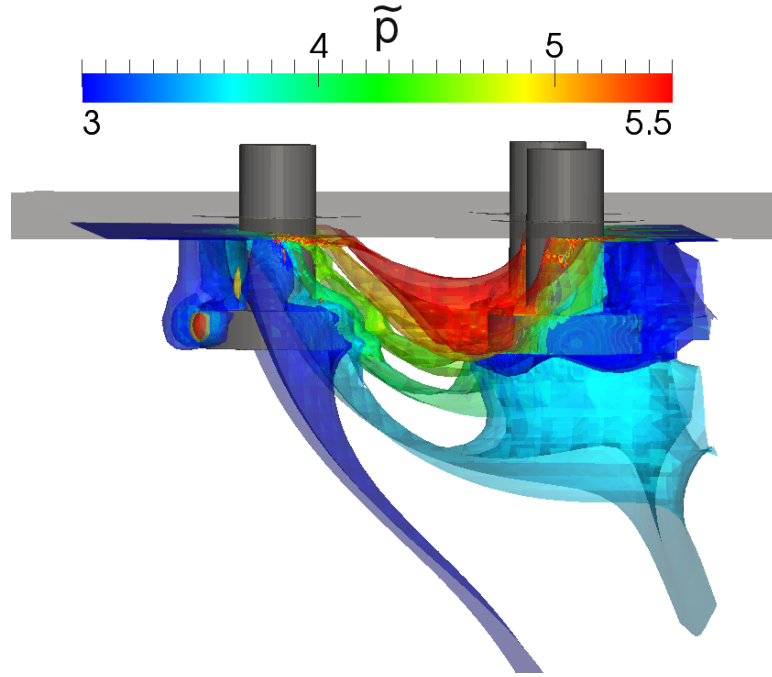
Figure 7.18. Isosurfaces of the modified pressure term, $\tilde{p}$. A region of higher pressure is shown in between the three columns, which is believed to drive the flow downwards towards the trailing base columns.

beneath the base columns, further explaining the increased drag on the base columns on the trailing columns and highlighting the role of the free ends of the structure.

The presence of a free surface, free ends and multibody arrangement is shown to play a role in the overall drag loading on the semisubmersible. A reduction in the velocity near the free surface as the flow approaches the body leads to overall lower drag coefficients on the upper columns. Flow accelerations beneath the structure, cause by the free ends, are shown to cause higher drag on the base columns in general. The multibody arrangement leads to increases in the fluid velocity coming off the front columns and heading downwards, causing increased drag on the base columns of the trailing piles. It is shown that the geometric differences between an infinitely long cylinder and the semisubmersible structure alter the drag predictions on the latter
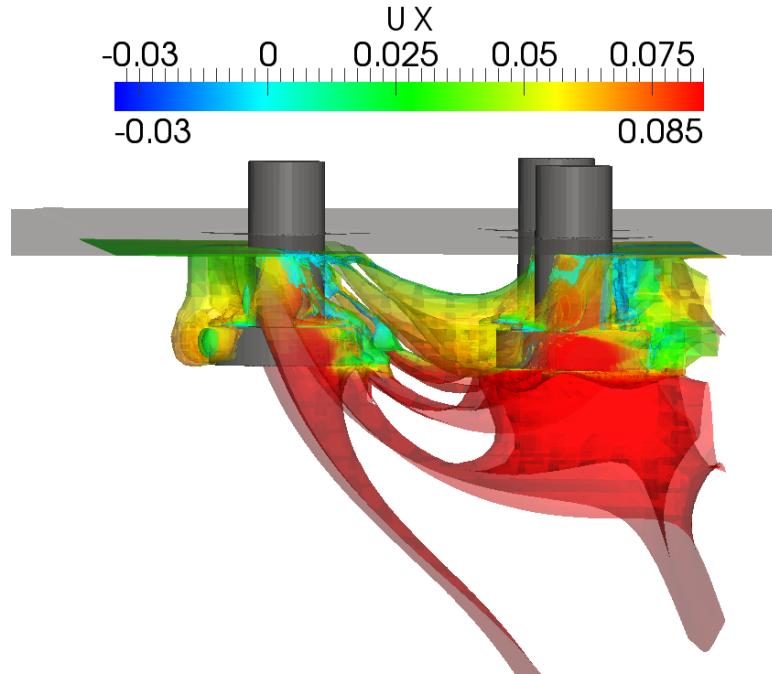
Figure 7.19. The x-component of velocity mapped onto the pressure isosurfaces illustrated in Figure 7.18.

structure. These factors should be taken into consideration when selecting the most appropriate drag coefficients for input to engineering tools.

7.5.7 Isolated Offset Column

To better understand the effects of the multimember arrangement of the semisubmersible, a single, isolated offset column was simulated in 0.6 m/s current velocity. The resulting force predictions on the isolated offset column are compared against the loads on columns that are part of the multimember arrangement. Loads on the isolated column are presented here, alongside the predicted loads on the front and trailing columns discussed earlier.

The drag coefficients of the base column, upper column, and entire offset column, as predicted by CFD, are presented in Figure 7.20. The predicted drag coefficient for the base member of the isolated offset column falls between the predicted drag
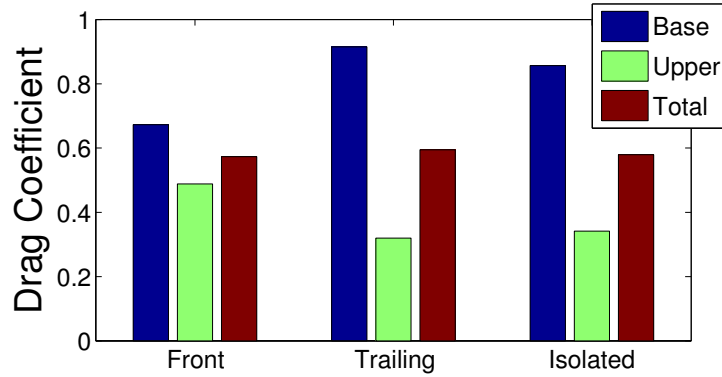
Figure 7.20. Drag coefficient predictions for the base column, upper column, and entire offset column for the front, trailing, and isolated columns of the semisubmersible.

coefficients for the front and trailing columns' base members. The same trend exists for the upper member as well. This finding indicates that the presence of other members does alter the drag behavior on any one member.

7.5.8 HydroDyn with Updated Drag Coefficients

The geometric complexities of the semisubmersible have demonstrated sizable effects on the drag behavior, as compared to that of an infinitely long cylinder. It may be the case that CFD simulations must be performed *a priori* to running simulations with engineering tools that use drag coefficients as inputs. To assess how far we can extend drag coefficients computed at a single current velocity, in this case at 0.6 m/s, the drag coefficients presented earlier were input to HydroDyn, and simulations were performed with current velocities of 0.3 and 1.0 m/s, for stationary semisubmersibles. The drag coefficients are given in Table 7.4, taken from Figure 7.13, and the results are presented here.

Table 7.4. Predicted drag coefficients from CFD, used as input to HydroDyn.

	Upper	Base
Front	0.488	0.673
Trailing Right	0.320	0.915
Trailing Left	0.322	0.922
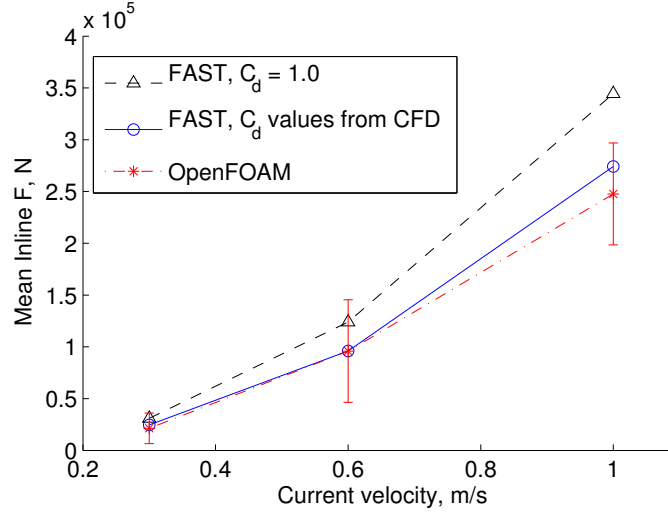
Figure 7.21. Comparison of mean inline forces from OpenFOAM and FAST at three current velocities. FAST results when all members were assigned a drag coefficient of 1.0 are shown in black, while FAST results with drag coefficients from Table 7.4 are shown in blue. OpenFOAM results are given in red, where error bars indicated one standard deviation in the time-varying load.

The mean inline force predictions from OpenFOAM at 0.3, 0.6, and 1.0 m/s current velocities are shown in Figure 7.21, alongside the load predictions from two sets of FAST simulations. The first set of FAST simulations used drag coefficients of 1.0 for each member, while the second set of simulations used the drag coefficients listed in Table 7.4. As expected, the agreement between OpenFOAM and FAST is much better when the drag coefficient inputs to HydroDyn are taken from the CFD predictions. More importantly, the agreement improves for the 0.3 and 1.0 m/s current velocity cases, even when the drag coefficients are derived only from a 0.6 m/s case. This points to the ability to extrapolate drag coefficients computed from similar, but different, flow conditions.

7.6   Model vs. Prototype Scale Simulations

CFD simulations of the semisubmersible in steady current were performed at model scale (as well as wave cases in the following section) instead of prototype scale,

the scale at which FAST simulations were carried out. There are multiple reasons for simulating CFD at model instead of prototype scale. One of the motivations is that the DeepCwind wave tank experiments were done at model scale (1/50th prototype size), such that comparison with experimental data would be more direct. Next, previous validation exercises for uniform flow past infinite cylinders gave slightly better agreement between drag coefficients from the literature and our CFD simulation at Reynolds numbers in the model scale region. Finally, model scale simulations are less computationally expensive since boundary layer cell refinement increases with rises in the Re.

Table 7.5. Model and prototype scale velocities and Reynolds numbers, as well as aspect ratios of the upper and base columns.

	Aspect Ratio (H/D)	Re model scale (U = 0.085 m/s)	Re prototype scale (U = 0.6 m/s)
Upper Column	1.16	20,000	7.2 million
Base Column	0.25	40,000	14.4 million

Given that CFD and FAST simulations have been performed at different physical scales, and then results have been Froude scaled to match, we must ask whether this is an acceptable approach. The goal here is to assess the impacts of running CFD simulations at model scale instead of prototype scale. Using the simplified semisubmersible geometry, so that results can be compared to the member level drag coefficient predictions discussed earlier, prototype scale simulations were carried out in a steady current at 0.6 m/s. The steady current velocities and Reynolds numbers are given at model and prototype scale in Tabl 7.5, along with the aspect ratios of the upper and base columns. Load predictions, including both drag forces and frequencies, from prototype scale CFD simulations are compared against model scale simulation results that have been Froude scaled post-simulation.
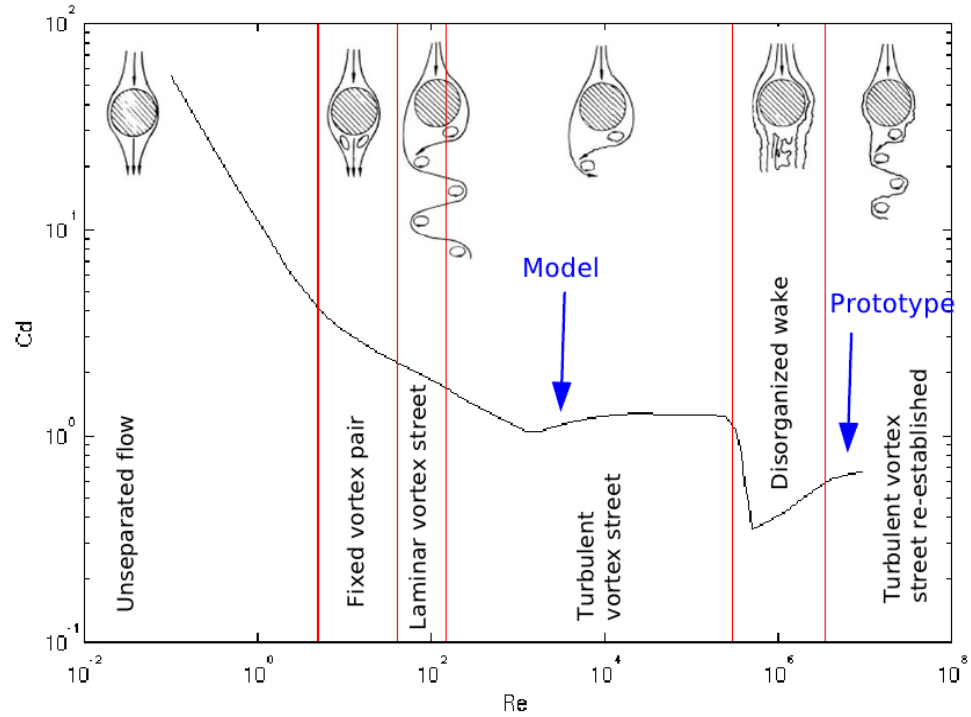
Figure 7.22. Re vs C_d for an infinite surface piercing cylinder. Schematics of the flow regime as a function of Re are also shown. The Re for model and prototype scale simulations of the semisubmersible are labeled.

The Reynolds numbers in this specific comparison of model to prototype scale simulations are illustrated in Figure 7.22 on top of a Re versus C_d for an infinite, fully submerged cylinder. Additionally, schematic drawings of the flow past infinite, fully submerge cylinders as a function of the Re are shown. Both the model and prototype scale Re simulated here indicate that turbulent vortex shedding should occur, and that the frequency content of those vortices may differ. It is important to note that these expectations are based on what has been observed for infinite, fully submerged cylinders, which vary greatly from the surface-piercing semisubmersible.

7.6.1 Drag Coefficients

First, a mesh convergence study was carried out for the prototype scale simulations. The mesh convergence study was done in two stages, first convergence of the

overall mesh was assessed, followed by a mesh convergence study of the cell refinement around the fluid interface. The results from the mesh convergence study are shown in Figure 7.23 and show that convergence was reached with a cell count near 6 million.
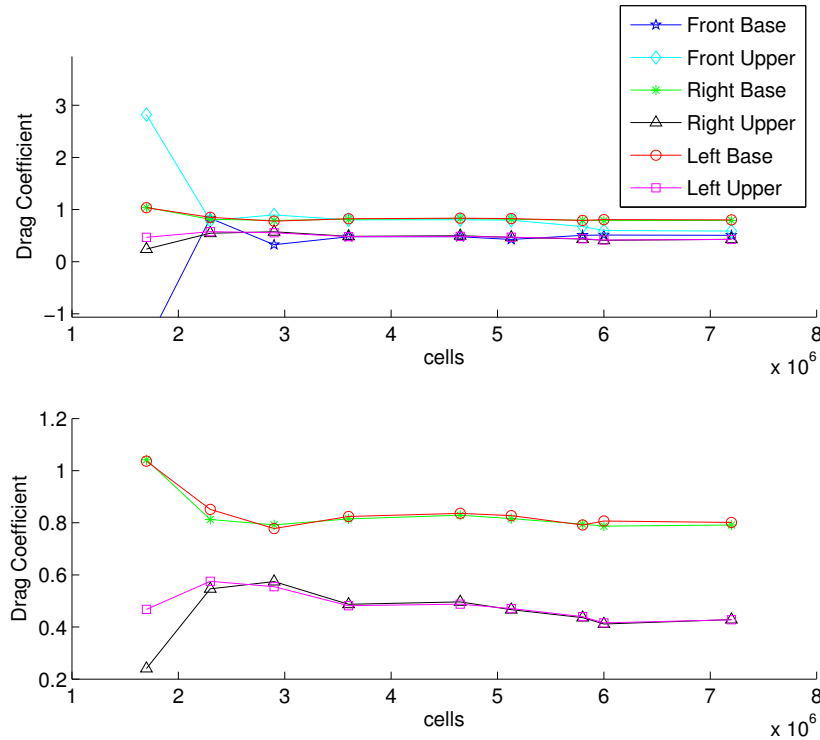
Figure 7.23. The drag coefficient as a function of the cell count. Mesh convergence was reached around 6 million cells.

The final drag coefficient predictions from prototype scale simulations are presented alongside results from a model scale simulation. The drag coefficient was computed for each member treated in the simplified semisubmersible geometry. In general, the prototype scale simulations predicted a smaller drag coefficient than the model scale simulations for base columns. The opposite trend was found for the upper columns, where the prototype scale simulations found larger drag coefficients.

From the standpoint of Figure 7.22, finding a larger drag coefficient for any of the members at prototype scale may be surprising. However, the surface-piercing semisubmersible differs so greatly from a fully submerged, infinite cylinder. Differ-

ences in trends between the infinite cylinder and the semisubmersible should in fact be expected, as was discussed in the previous sections.
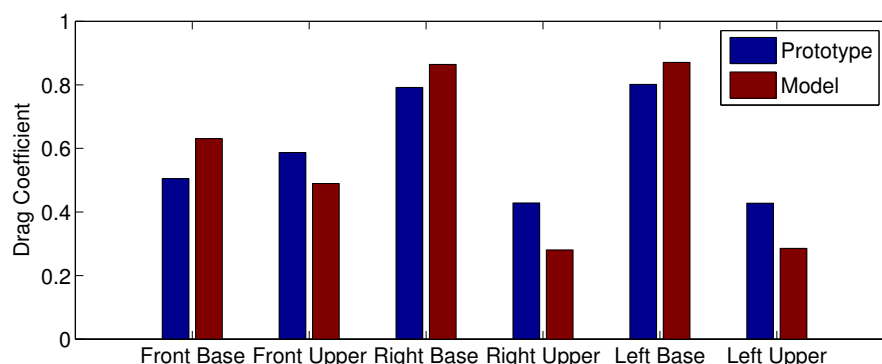
Figure 7.24. Drag coefficient predictions from simulations performed a prototype and model scale, in blue and red bars, respectively. Drag coefficients are larger on the upper columns and smaller on the based columns at prototype scale.

Remember that this is only one case of comparison, and it is a specific one. For other geometries the prototype and model scale Re will fall on different areas of the Cd vs Re curve – but basing any scaling effects off of that curve should be called into question anyway.

7.6.2 Frequency Content

In addition to comparing the drag coefficient predictions at model and prototype scale, the frequency content of the inline forces is compared. Because of previous research investigating surface-piercing cylinders with free ends, discussed in Chapter 6, we have high confidence in our ability to accurately predict the vortex shedding frequency using the Spalart-Allmaras turbulence model (see Figure 6.7).

The Strouhal number ($St = fD/U$) for each member of the simplified semisubmersible is plotted from model and prototype scale simulations in Figures 7.25(a) and (b), respectively. In both the model and prototype scale simulations more pronounced peaks in the Strouhal numbers were found for the trailing columns. Furthermore, in

both model and prototype scale simulations a distinction was found between Strouhal numbers for the upper and base components of the offset columns. The Strouhal numbers for the base columns are higher than those found for the upper columns. That is, the vortex shedding frequency from the base columns is greater.
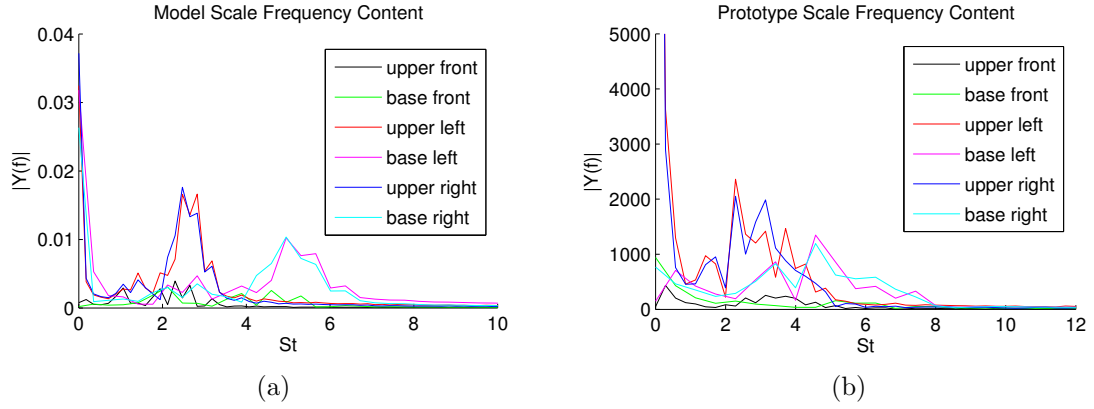
Figure 7.25. a) Strouhal numbers for upper and base columns simulated at model scale, b) prototype scale Strouhal numbers.

Strouhal numbers for smooth, infinite cylinders fall between roughly 0.1 and 0.47 across a wide range of Re, as illusrated in Figure 7.26(a). This range is much lower than the Strouhal numbers that were computed from CFD simulations of the semisubmersible, by an order of magnitude. Again, the semisubmersible geometry is very different from that of an infinite cylinder.

Perhaps it is more appropriate to compare Strouhal numbers from the semisubmersible against those from a sphere. The aspect ratios of the upper and base columns are 1.16 and 0.25, respectively, where the aspect ratio of a sphere would be one. Strouhal numbers measured from experiments of flow past spheres is given in Figure 7.26(b). Two branches of Strouhal numbers occur for the sphere, termed the high-mode and low-mode St. The experimental data for spheres show a much wider range of Strouhal numbers than what was seen for a cylinder, beginning at roughly

0.2 and extending to nearly 10. The St values computed for the semisubmersible at model and prototype scale fall within the range observed for spheres.
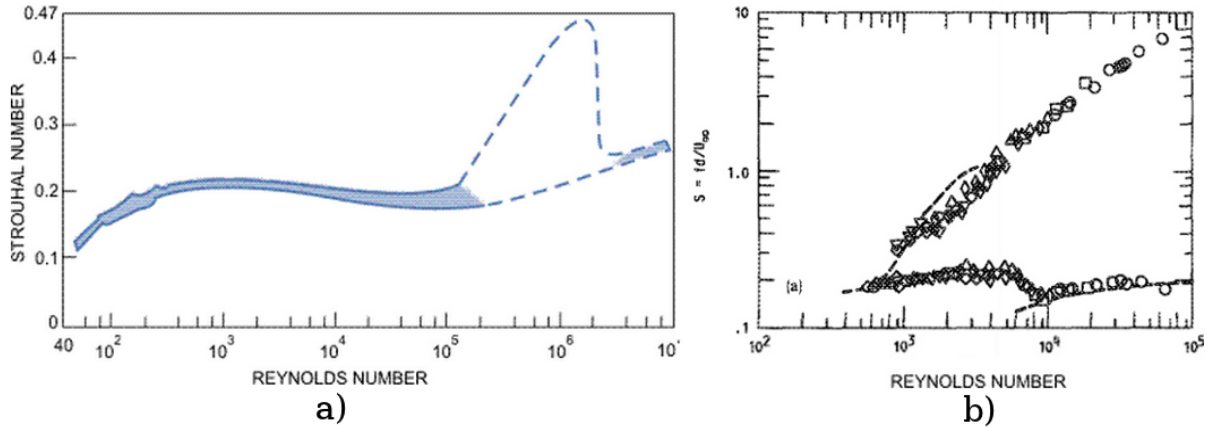
Figure 7.26. a) Strouhal numbers for a cylinder, reproduced from Blevins [13]. The upper band shows Strouhal numbers for smooth surface, while the lower bound exhibits values for rough surface. b) Strouhal numbers for a sphere, reproduced from Kim and Durbin [107].

7.7   Summary and Conclusions

A series of current-only cases was simulated using HydroDyn and OpenFOAM. Comparison of load predictions from the two codes showed larger drag forces from FAST than from OpenFOAM. Further work was performed to gain an understanding of the code-to-code discrepancies in load predictions. The combined effects of a free surface, a free end and the multiple member arrangement were investigated. Simulations were carried out to study the loads on individual members of the semisubmersible, providing insights into the effects of shadowing. High-fidelity flow field visualizations were generated to better understand the underlying physics of the flow interacting with the complex geometry of the semisubmersible.

The drag loads were compared quantitatively, and the results from CFD revealed drag coefficient predictions far below the values for an infinitely long, fully submerged

cylinder at the same Reynolds number. Flow visualizations from the CFD simulations were presented to explain the geometric factors leading to changes in the drag behavior. It was shown that the presence of a free surface as well as free ends leads to reductions in the drag coefficient as compared to infinitely long cylinders. Additionally, the multimember arrangement also lead to decreases in the drag loads. The work demonstrated the large impact of these geometric factors on the prediction load behavior, and argues that careful selection of input parameters for engineering tools is necessary.

HydroDyn, and other codes that use Morison's equation, predict only mean forces. They do not capture time varying loads, which occur due to vortex shedding in both the inline and transverse flow directions. These oscillatory loads could have a significant impact on the fatigue of the semisubmersible and other similar offshore structures. The OpenFOAM results exhibit a very large variation in inline loads, as shown by the error bars in Figure 7.11.

Since the model-scale Reynolds number is much smaller than the full-scale Reynolds number, this mismatch in values was considered for the semisubmersible in steady current. Drag coefficient predictions on the upper and base columns of the semisubmersible were compared between model and prototype scale simulations. At prototype scale larger drag coefficients were found for the upper columns, and smaller values were seen for the base columns than was observed at model scale.

Due to the sensitivity of the loads to various geometric factors, as well as the added complexity of their combined effects, it is likely necessary that CFD simulations be performed for each unique geometry to determine load coefficients for input to engineering tools.

CHAPTER 8

LOADS ON A STATIONARY SEMISUBMERSIBLE IN REGULAR WAVES

8.1 Introduction

In addition to simulating the semisubmersible in a range of current conditions, a variety of wave conditions were investigated. Because the semisubmersible is treated as a stationary body there are no radiation effects, but diffraction is important. First, operational conditions in sea state 3 to 5 are simulated in CFD and the results are compared with FAST predictions. Next, higher sea states are simulated in CFD to investigate the importance of flow separation when KC > 2.

8.2 Operational Conditions

8.2.1 Environmental Conditions

The properties for three simulated wave cases are shown in Table 8.1. The simulated wave cases span a wave height range from 1.95 m to 2.75 m, and a range of periods from 7.5 s to 8.8 s, at prototype scale. The wave simulations carried out in this work fall between sea states 3 and 5.

8.2.2 Categorization of Component Size

The four major components of the semi-submersible can be mapped onto a plot of the Keulegan-Carpenter number versus the diffraction parameter, which depend on both the wave parameters and structure size (in the transverse direction). Mapping the components by Keulegan-Carpenter number and diffraction parameter classifies

Table 8.1. Simulated regular wave conditions at prototype scale

Simulated Case	T (s)	H (m)
Regular 1	7.5	1.95
Regular 2	7.7	2.35
Regular 3	8.8	2.75

each member as small versus large by the dominating physics in that loading regime. The Keulegan-Carpenter number and diffraction parameter are calculated for each of the four components - pontoon, main column, upper column, and base column - over the range of sea states simulated here. The regions where each semi-submersible component fall are illustrated in Fig. 8.1, where the sea state increases upward and toward the left. The figure demonstrates that the base columns and the upper columns, which comprise the offset columns, fall mostly in the diffraction-dominated region for the sea states considered here. The pontoons fall almost entirely in the inertia and drag dominated region. The main column spans both sides of the divide between inertia-, drag- and diffraction-dominated regimes.

The classification of structures in Fig. 8.1 demonstrates the relationship between structure size and dominating physics. The figure is divided by a vertical line that separates the inertia- and drag-dominated regime where Morison's equation is valid, from the diffraction-dominated regime where a panel method code is more appropriate. First, the figure shows that the base and upper columns should be considered as large components, because they are largely dominated by diffraction effects. This is consistent with the decision to include those members in the large components only mesh discussed previously. In addition, the pontoons/cross braces fall in the inertia- and drag-dominated region, which justifies including those members in the small components only mesh. The potential-flow approach is valid everywhere except where viscous effects are important. For this reason, the main column can be modeled with potential-flow theory or Morison's equation, and was classified as a
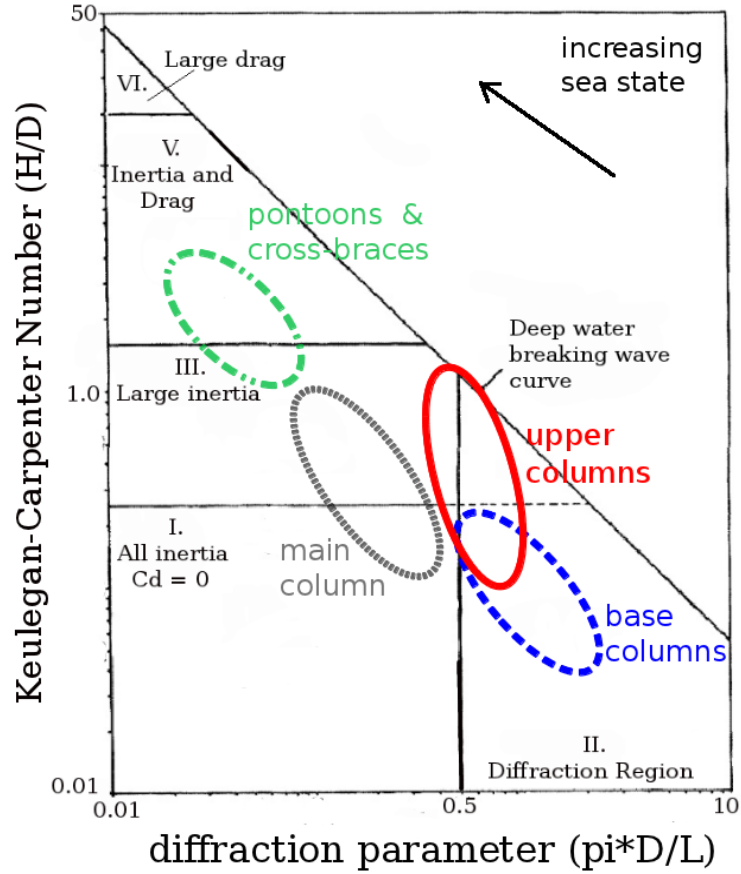
Figure 8.1. Classification of small versus large structures and their limits of applicability. The vertical axis shows H/D, which is equivalent to the Keulegan-Carpenter number, and the horizontal axis is the diffraction parameter. The four major components of the semi-submersible are mapped onto the figure over a range of sea states from 3 to 5, which encompass the range of environmental conditions studied in this work. Adapted from Chakrabarti [26]. H is the wave height, L is the wave length and D is the characteristic structure diameter

small component in this work. This selection of small and large components is not unique. Second, Fig. 8.1 illustrates that the simulated wave properties divide the individual components into different dominant load regimes. This allows for the study of the assumptions made in HydroDyn where model equations are based on the size of individual components.

8.2.3 Results and Discussion

The current-only cases provide insight about the Morison's equation component of FAST. The regular wave cases shed light on the potential-flow theory portion of FAST. Load contributions from Morison's equation are negligible compared to diffraction forces for the regular wave cases investigated in this work. FAST calculates the diffraction forces from coefficients produced in WAMIT. Contributions from Morison's equation and diffraction are compared in Fig. 8.2. Radiation forces are omitted from the figure because they are zero for this case of the nonmoving structure.
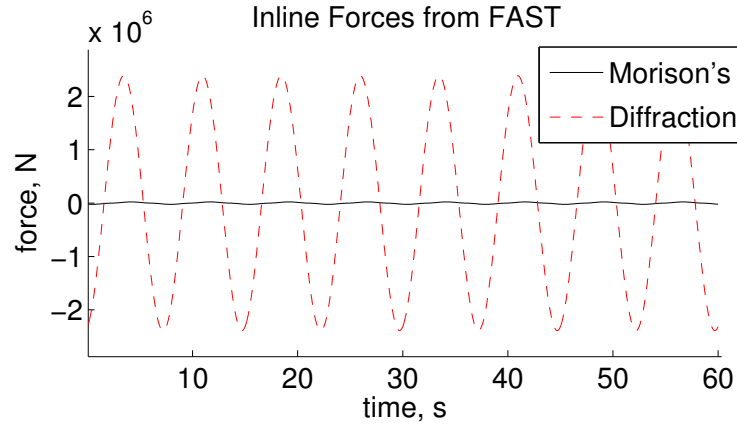
Figure 8.2. Inline forces from FAST. The solid black line shoes the forces resulting from Morison's equation, and the red dotted line represents loading from diffraction, calculated in HydroDyn. The plot illustrates that drag forces calculated with Morison's equation are negligible compared to diffraction for the semi-submersible in Regular 2 waves.

OpenFOAM and FAST results from the Regular 2 wave case, with properties given in Table 8.1, are shown in Fig. 8.3. The inline-force results from FAST and the full geometry case in OpenFOAM show excellent agreement. Previously with the steady current simulations there was sizable disagreement between the inline force predictions, but now the load contributions from drag are negligible compared to contributions from diffraction. The semi-submersible is now in a regime where diffraction effects are dominant, unlike in the current cases. The diffraction forces
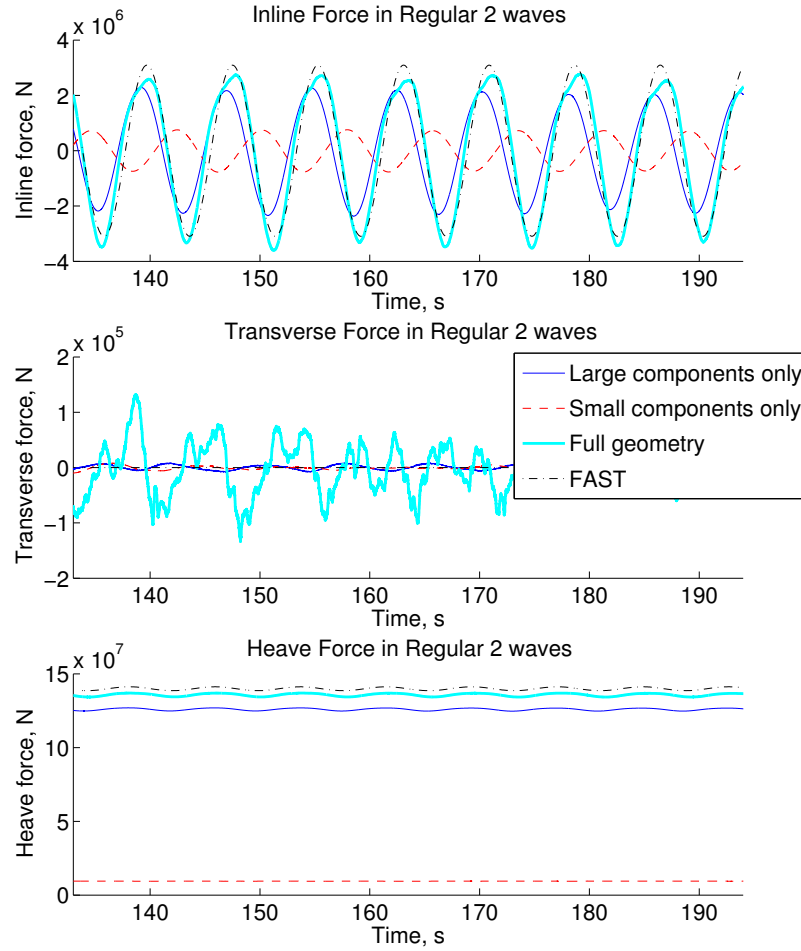
Figure 8.3. Inline, transverse and heave force results from OpenFOAM and FAST. Results from the large components only, small components only and full geometry meshes are shown for OpenFOAM. FAST and OpenFOAM show excellent agreement for the inline force, while the transverse flow prediction is much greater from Open-FOAM than it is from FAST. The heave force prediction is larger in FAST than it is in OpenFOAM.

from WAMIT include the interaction between members such that shadowing should play a lesser role. Again, the differing drag coefficients in FAST and OpenFOAM may be the cause for discrepancy in force predictions. As was the case for current, FAST predicts a constant zero transverse force; OpenFOAM gives a time varying
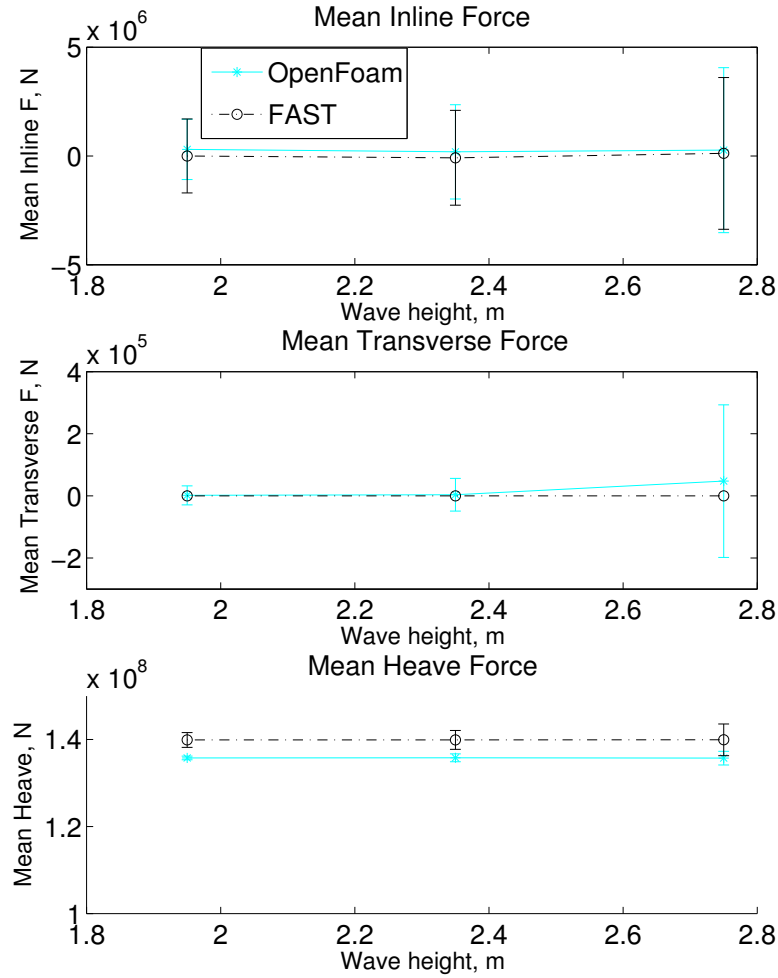
Figure 8.4. Trends in the mean inline, transverse, and heave force predictions in regular waves. The mean values of the inline force predictions with increasing wave height are demonstrated in the top plot. The mean transverse and heave forces are given in the middle and bottom plots, respectively. Standard deviation from the mean in OpenFOAM is illustrated with error bars. Excellent agreement was found between FAST and OpenFOAM inline loading predictions. The transverse force prediction from FAST is zero for all wave heights, and increases with increasing wave height in OpenFOAM. The mean heave force prediction is larger from FAST for across all wave heights studied here.

transverse force. The heave forces are also presented, where FAST predicts a slightly larger force compared to OpenFOAM for all representative geometries. As expected,

the large components only and small components only meshes predict smaller heave forces, which is a direct result of their smaller volume and surface area.

Results from the two codes are compared across the range of wave heights simulated in this study, and are illustrated in Fig. 8.4. The means of the inline, transverse, and heave forces from both FAST and OpenFOAM's full geometry mesh are shown in the plots from top to bottom, respectively. The error bars indicate the standard deviation from the mean force. The inline force predictions from FAST and Open-FOAM are in excellent agreement across the range of wave heights. The transverse force predicted by OpenFOAM grows with increasing wave height, yet remains zero in the FAST output. The heave force prediction is larger in FAST than OpenFOAM, across all wave heights studied here. Unlike with the current cases, where the absence of shadowing effects in FAST may be the source of large discrepancies in inline force results between the two codes, the inline force predictions from the two codes agree well for the semi-submersible in waves. Again, the lack of a lift force in FAST causes disagreement between the two codes, just as it did for the current cases. The discrepancy in lift force predictions is more important for the current-only cases, and less important for wave cases where drag and lift forces are negligible compared to diffraction loads. Even though the OpenFOAM results demonstrate that the transverse force is of smaller magnitude than the inline force, the loading in the transverse direction should not be ignored.

8.3   Higher Sea States

Load predictions on the semisubmersible from OpenFOAM and FAST were found to be in good agreement for waves classified as sea states 3 to 5. The relative importance of flow separation can be determined based on whether the KC number is less than or greater than 2 [187]. When the KC number is larger than two, flow separation becomes important. Below that threshold potential flow theory applies. In the sea

states presented earlier, the KC numbers for each of the strucutural members were below 2. Here, simulations at a higher sea state was carried out in OpenFOAM and FAST to assess load predictions when flow separation becomes important.

Sea state 6 was investigated here, with $H_s = 6.0$ m and $T_p = 12$ s. This sea state was chosen based on an analysis of the KC values as a function of water depth and sea state for the OC4-DeepCwind semisubmersible [187]. The analysis shows that flow separation occurs for the main column at a sea state of 6, and for the offset columns at a higher sea state of 7. The cross braces and pontoons flow separation is important beginning at a sea state of 5.
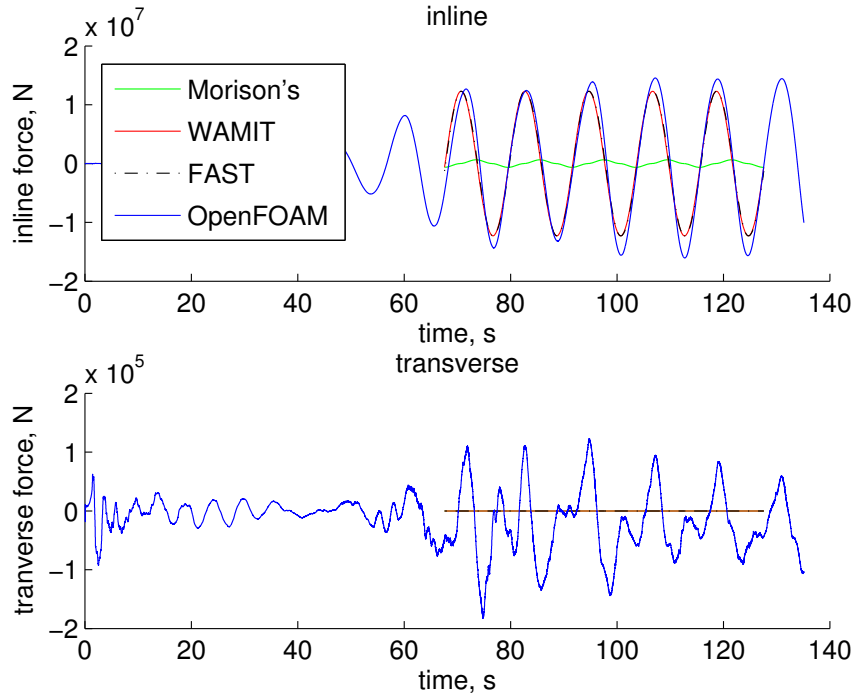
Figure 8.5. Comparison of inline and transverse load predictions between Open-FOAM and FAST at a sea state of 6. $H_s = 6$m, $T_p = 12$s. Results presented at prototype scale.

The CFD simulations were performed at model scale, and include all members of the semisubmersible geometry. FAST simulations were performed at prototype scale.

All results are presented at prototype scale, where the CFD results have been Froude scaled.

Time histories for the inline and transverse load predictions from OpenFOAM and FAST in the sea state 6 wave conditions are shown in Figure 8.5. In this case, the CFD simulation predicts higher peaks and troughs than FAST does. In the previous section a time history of forces on the semisubmersible in a sea state of 4 was given in Figure 8.3. For this lower sea state, OpenFOAM predicted slightly smaller peaks in the inline forces than FAST did.

8.4   Summary and Conclusions

A code-to-code comparison was carried out between the HydroDyn module in FAST, a CAE tool for assessing hydrodynamics loads on offshore wind turbines, and OpenFOAM, a high-fidelity CFD software package. A fixed semi-submersible was simulated in wave-only conditions to assess differences from load predictions in the two codes. Confidence in the ability to accurately model rigid bodies in current and wave conditions with OpenFOAM, based on previous validation exercises, is high.

The wave-only conditions were simulated for a range of wave heights and periods. In these cases, the inline-force predictions from HydroDyn and OpenFOAM were in excellent agreement, but the HydroDyn results did not capture any lift forces. The magnitude of the transverse force is smaller than the inline force, but it is nonetheless significant. The ability to capture shadowing effects and transverse forces from vortex shedding would enhance HydroDyn's load predictions, and other engineering codes that employ similar assumptions and theories.

The loading predictions from the two codes was in much better agreement for the wave cases than it was in steady current. The loads on the stationary body in waves are dominated by diffraction, which is treated with a panel method, potential-flow based model in HydroDyn. In waves, the drag forces captured by Morison's

formulation are nearly negligble compared to the diffraction loads. The lessened importance of Morison's formulation means that poorly selected drag coefficients have a diminished effect on the overall load prediction.

CHAPTER 9

LOADS ON SLANTED CYLINDERS

9.1 Introduction

In HydroDyn, loads on slanted members are calculated in the normal direction to a member. To assess the impact of this assumption, simulations of slanted cylinders were carried out in OpenFOAM. Understanding the impact of this assumption in HydroDyn is critical to ensuring accurate load predictions on offshore platforms, especially for geometries such as the semi-submersible platform which contains multiple slanted members. Moreover, the cross-braces of the semi-submersible are surface-piercing, which has the potential to further complicate the flow and loading. Here, loads on slanted cylinders are examined, and contrasted with those for vertical cylinders at the same Reynolds numbers.

Previous work in the literature has explored flow around, and loading on, slanted cylinders. The majority of this research has investigated fully-submerged slanted cylinders. King [108] and Lam [117] performed experiments on fully submerged slanted cylinders, while numerical work has been presented by Zhao [268], Lam [117] and Jordan [96]. These works found that the drag coefficient, based on the velocity and force components normal to the cylinder, was independent of the cylinder's angle of inclination. This effect is called the independence principle (IP).

More recently, Shao, et al, performed experiments and numerical simulations to study slanted cylinders that pierce a free surface [210]. In this research, the authors found that the IP did not hold. Rather, the drag coefficient increased with increasing angle of inclination. Furthermore, the work found that with increasing angle of in-

clination the vortex shedding became more irregular. This irregularity of the vortex shedding is not only a result of the angle of inclination, but also due to the presence of a free surface. The effects of a free-surface on a vertical cylinder have been studied experimentally [10, 27, 78] and numerically [105, 221, 263], and have found that the free-surface can lead to reductions in the drag coefficient, as well as irregular vortex shedding.

While the work of Shao, et al, provide important insight into the drag and lift behavior past a slanted cylinder, their work is limited to a single depth of submergence and a single orientation in the side-side direction. In order to understand the ramifications of the slanted cylinder assumptions in HydroDyn, as they apply to the semi-submersible structure, further studies were necessary.

9.2 Analysis Specifications

The simulation parameters are outlined in Table 9.1. The cases are represented visually in Figure 9.1, where specific cross braces of the semisubmersible are highlighted in red, demonstrating the relative angle of the slanted cylinder. In each of the simulations the slanted cylinder was simulated in the absence of other members. The diameter of the pontoons are crossbraces are 1.6 m at prototype scale, which were simulated at model scale with diameters of 0.032 m. The Reynolds number for the flow normal to the cross braces is 2092.

Table 9.1. Parameters of the slanted cylinder simulations performed in OpenFOAM.

Case	Velocity (m/s)	Pitch (deg)	Yaw(deg)	Comments
A	0.084	39	0	Fully-submerged
B	0.084	39	0	Surface-piercing
C	0.084	39	45	Surface-piercing
D	0.084	39	90	Surface-piercing
E	0.084	39	180	Surface-piercing
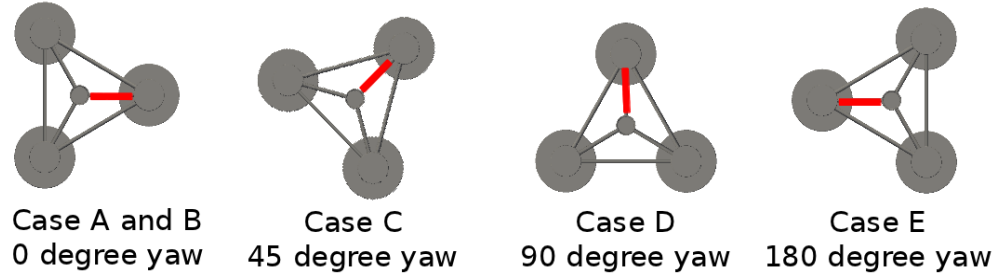
Figure 9.1. Orientations of the slanted cylinders simulated in OpenFOAM. Cross braces are highlighted in red to illustrate the orientation of the cylinder as it relates to the semisubmersible geometry. Cases B, C, D, and E are shown from left to right, respectively. Flow travels from left to right.

The literature suggests the presence of a free-surface further complicates the flow regime and loading on the slanted cylinders. To test that loads on surface-piercing cylinders differs from those on fully-submerged cylinder, and thus breaks the IP assumption, Cases A and B, pitched at 39 degrees, to match the angle of the cross-braces in the semi-submersible, were carried out. These cylinders have a zero yaw angle.
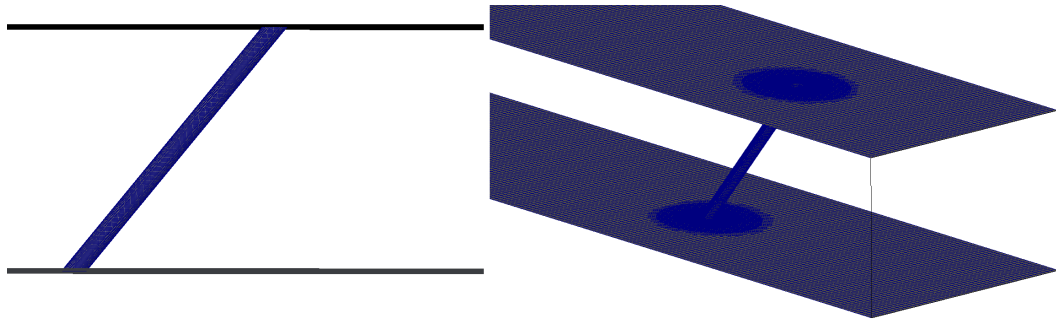
Figure 9.2. The mesh used for Case A, with 0 degree yaw and 39 degree pitch, seen from the side and at an angle. The flow travels from left to right.

Since the cross braces of the semisubmersible are surface piercing, the remainder of simulations focused on surface-piercing cylinders. To validate our model's ability to accurate predict sectional loads on slanted members, two cases (Cases B and E) were performed to match work previously carried out by Shao, et al, [210].
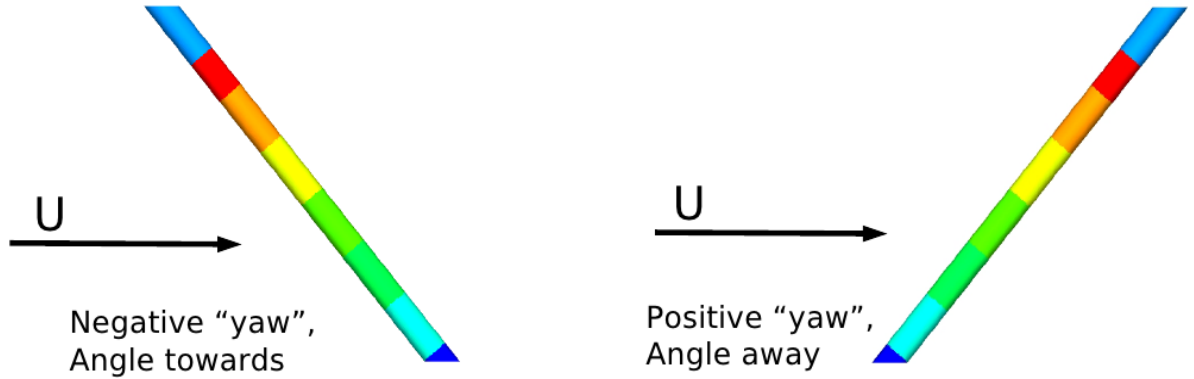
Figure 9.3. Schematic of cases B and E. Multiple surface patches were generated to allow investigation of the loads as a function of cylinder length. These cases correspond to work by Shao, al [210], allowing for validation of our model.

Following validation of sectional loads on slanted cylinders, two more simulations with different yaws were carried out. The original case was yawed 45 degrees (Case B), and then 90 degrees (Case C). The 90 degree yaw angle corresponds to the cylinder being perfectly transverse to the flow. In this case, it would appear that the assumption in HydroDyn to calculate loads simply from the normal component of the flow should be perfectly valid. However, the pitch angle of the cylinder could potentially alter the wake formation, and in turn affect the drag and lift behavior. Assessment of this effect was explored. Trends across the orientations of the slanted cylinder were investigated.

9.3 Surface-piercing versus Fully-submerged Cylinders

To confirm Shao's finding that the angle of inclination alters the load components normal to the cylinder, such that the independence principle is not upheld, Cases A and B were simulated and compared. In cases A and B the angle of inclination of the cylinders in the pitch and yaw direction are identical. The flow velocity past each cylinder in each case is identical. However, in case A the cylinder is fully submerged

and in case B the cylinder pierces the free surface. In each case the length of cylinder in the water phase was the same.
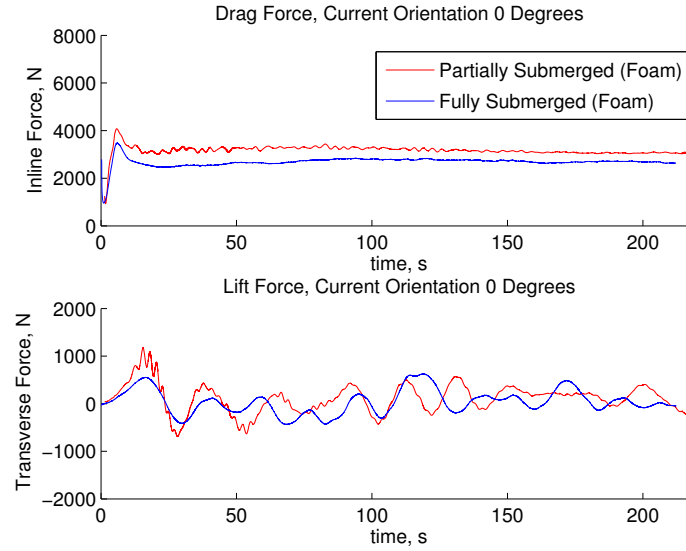
Figure 9.4. Comparison of drag and lift force time histories for cases A and B, where the yaw angles and pitch angles were both 0 and 39 degrees, respectively. Case A was a fully submerged cylinder while case B simulated a surface-piercing cylinder.

The results from the simulations of cases A and B are presented in Figure 9.4, where Case A is shown in blue and Case B in red. The results are presented at prototype scale. The drag coefficients found in this work are consistent with the previous findings of Shao, et al. A higher drag prediction is found for the cylinder that pierces the free surface.

Streamlines around the cylinders simulated in Cases A and B are shown in Figure 9.5. The images show streamlines with different characteristics, where the streamlines are smoother for the case of the surface-piercing cylinder. In Case B, the free-surface, which forms the upper bound on the water phase, can deform. However, in Case A the upper bound on the water phase is a rigid wall. These differences in boundary conditions alter the flow behavior around the cylinder, and ultimately the loads on the structure.

In Case B, the streamlines are smoother, indicating that less vortex shedding is occuring as compared to Case A. This is analogous to a lower Reynolds number flow where the flow remains unseparated and the drag coefficients are larger. With increasing the Reynolds number, the flow around a cylinder transitions from unseparated flow, to laminar vortex sheets and finally to a turbulent vortex street, which results smaller drag on the cylinder. These same effects are being observed in Cases A and B, where the larger drag corresponds to the case with less vortex shedding.
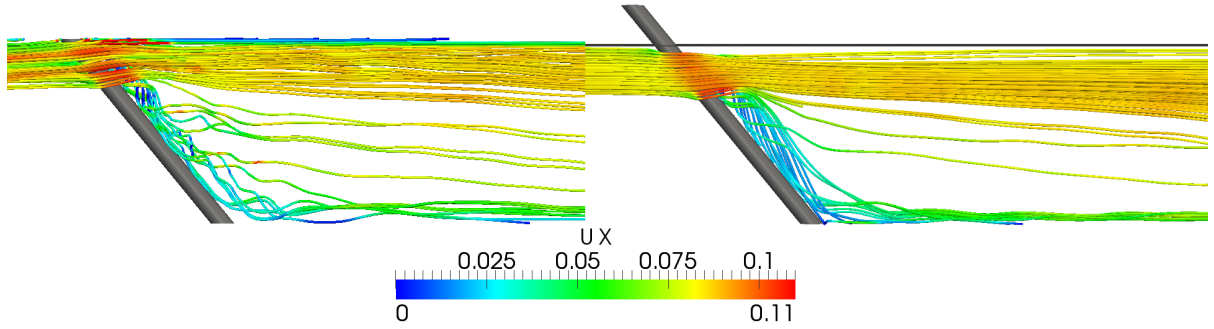
Figure 9.5. Visualization of Cases A and B, on the left and right, respectively. In case A, the cylinder is fully submerged and in case B it pierces the free surface. The streamlines are colored by the x-component of the velocity.

9.4   Validation of Loads of Slanted Members

Prior to simulating cases C and D, validation of cases B and E are carried out by comparing results with data presented by Shao, et al. Results from the Open-FOAM simulations of slanted cylinders at various orientations are discussed in terms of frictional drag coefficients and the drag coefficient without hydrostratics.

The frictional drag coefficient is given by

$$C_{Df} = \frac{2F_{Df}}{\rho U_n^2 A} \tag{9.1}$$

where F_{Df} is the frictional force in the direction normal to the cylinder axis, ρ is the density of the fluid, U is the free stream velocity and A is the frontal project area of the cylinder.

The drag coefficient without hydrostatics is given similarly by

$$C_{Dp} = \frac{2F_{Dp}}{\rho U_n^2 A} \tag{9.2}$$

where again the force is taken in the direction normal to the cylinder axis. Here F_{Dp} includes forces due to dynamic pressure and viscous terms, but omits the hydrostatic pressure.
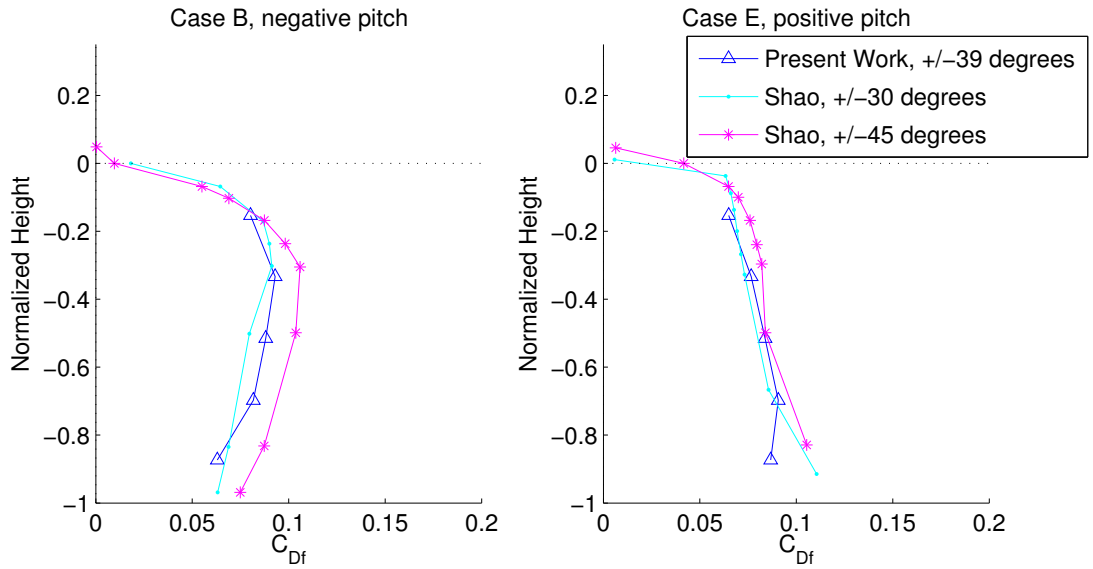
Figure 9.6. Frictional drag coefficients, C_{df}, as a function of cylinder height. The present work is shown in blue, and Shao's work is given in cyan and magenta at similar angles [210].

First, frictional drag coefficients for Cases B and E are compared against the similar cases presented by Shao, et al [210] as a function of the normalized vertical height of the cylinder. In Shao's work cylinders were oriented at 30 and 45 degrees, while our work was carried out with cylinders pitched at 39 degrees to match the

cross braces of the semisubmersible. The results are shown in Figure 9.6. Case B, where the cylinder is angled into the flow is shown on the left, and the case with the cylinder oriented away from the flow direction is shown on the right. In each of the orientations the present work falls roughly between Shao's predictions.
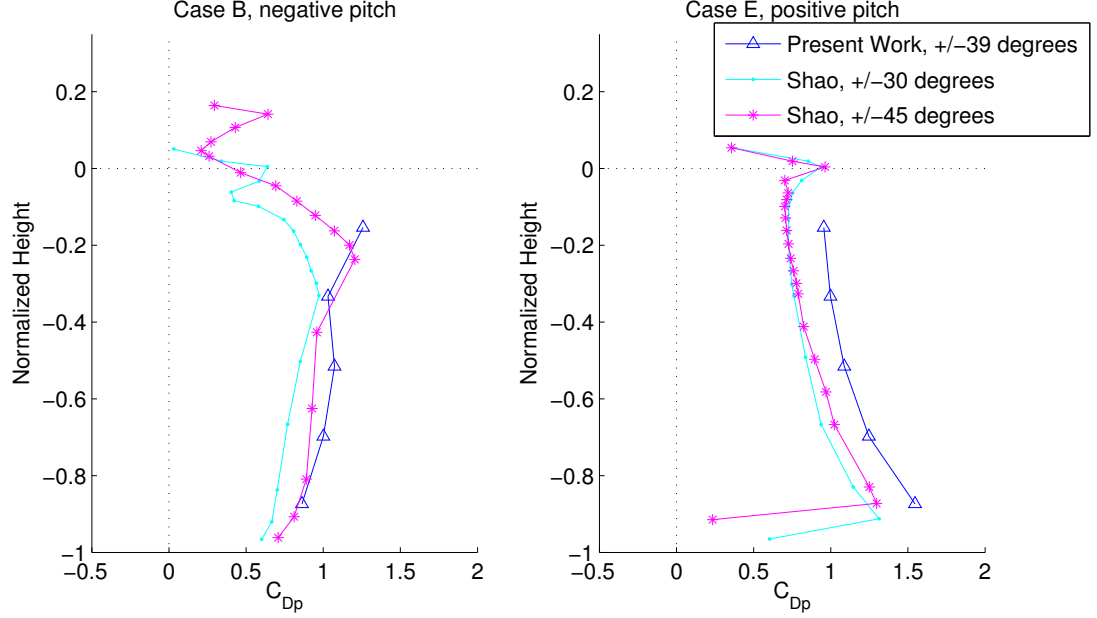
Figure 9.7. Drag coefficients without hydrostatics, C_{dp}, as a function of cylinder height. The present work is shown in blue, and Shao's work is given in cyan and magenta at similar angles [210].

Next, the drag coefficients without hydrostatics are compared, again as a function of the normalized cylinder height. The results are presented in Figure 9.7. The C_{dp} for the cylinder angled into the flow shows good agreement with Shao's results. There is a larger difference in C_{dp} values for the cylinder that is angled away from the flow, but the overall trends match very well, with a peak value near the cylinder base.

Overall, excellent agreement was found in the trends of C_{df} and C_{dp} as a function of cylinder height for both orientations of the cylinder when compared to data from Shao [210]. The agreement gives us confidence in our ability to accurately predict

sectional loads on slanted members. The CFD model can be extended to study other orientations of cylinders in crossflow.
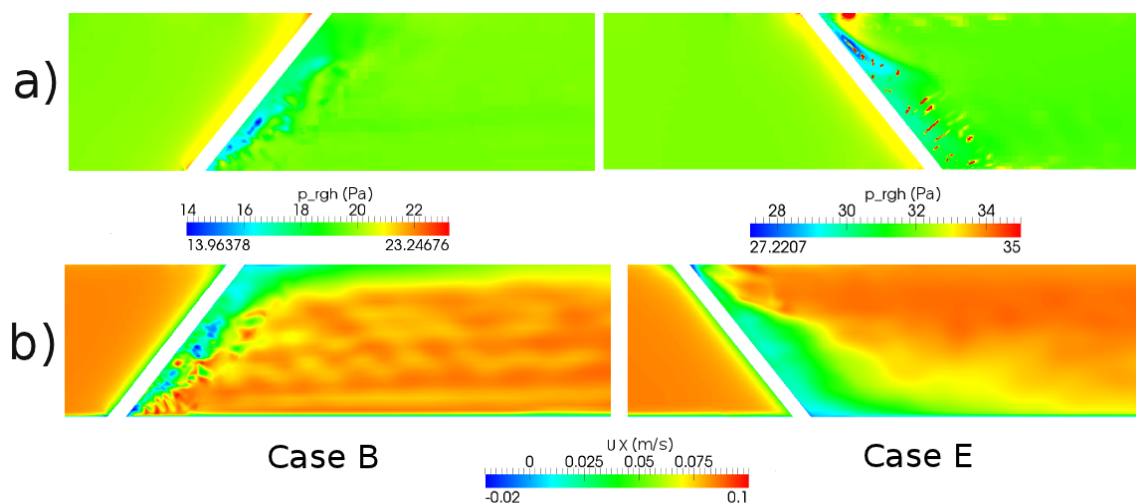
Figure 9.8. a) A vertical slice of the modified pressure fields for Cases B and E, on the left and right, respectively. b) Vertical slices of the x-component (flow direction) of the velocity. Flow travels from left to right.

Visualizations of the modified pressure (total pressure without hydrostatics) and the velocity are shown in Figure 9.8 for Cases B and D. The vertical slices through the numerical domains illustrate the mirrored flow fields that occur when the orientation of the cylinder is swapped. In case B, on the left hand side of the figure, a low pressure region forms near the base of the cylinder, while in case E the low pressure region forms near the top of the cylinder. These mirrored effects are also shown in the velocity fields, where the wake behind case B shows a larger velocity deficit near the top of the cylinder, and the reverse is true for case E. These patterns in the flow fields between the two cases is corroborated by the drag data presented as a function of the cylinder height, as discussed above. The C_{dp} term increases near the free surface for case B, while it decreases as it nears the free surface in case E.

9.5 Loads on Slanted Cylinders in Four Orientations

Following validation of the results for a fully submerged versus surface-piercing cylinder, and also two orientations of surface-piercing cylinders (Cases B and E), the model was used to investigate two further orientations. In cases C and D the cylinders were orientated with a yaw angle of 45 and 90 degrees, respectively. The results for C_{df} and C_{dp} from Cases B through E are now compared, and are shown in Figure 9.9, again as a function of the cylinder height.
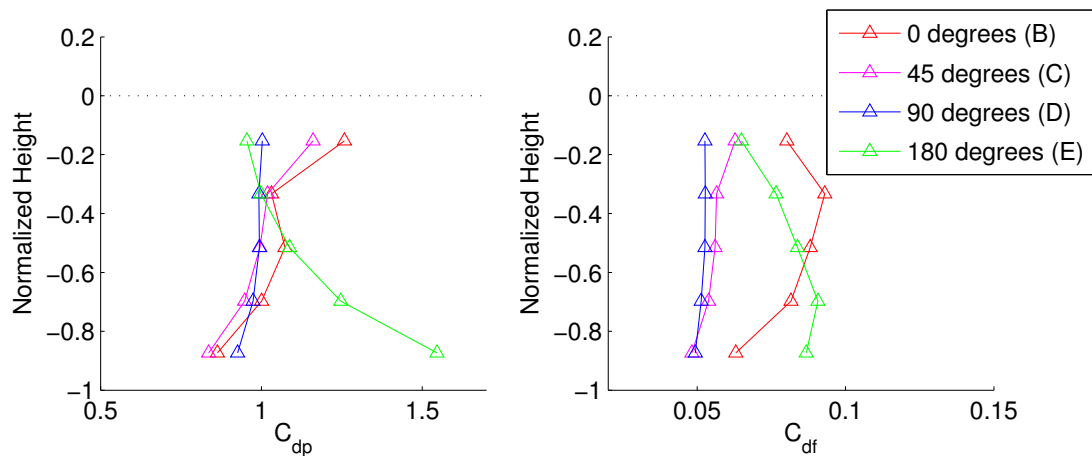
Figure 9.9. Drag coefficients neglecting hydrostatics are shown on the left, and frictional drag coeffients are given on the right, both as a function of the normalized cylinder height. All four yaw angles are presented.

The drag coefficient as a function of cylinder length, without hydrostatics, is presented on the left hand side of Figure 9.9. This figure demonstrates the dependence of drag not only on the yaw angle of the cylinder, but also on the proximity to a floor and a free surface. The free surface in this figure is represented with a dotted black line. The 0 and 180 degree yaw angle results were presented in the previous section. Now, cases C and D have been added. These two cases show more uniform drag predictions along the length of the cylinder than the 0 and 180 degree yaw angle cases.

Additionally, the frictional drag coefficient is presented for all four of the simulations, again as a function of the cylidner length shown on the right hand side of Figure 9.9. Again, the results for Cases C and D were found to be more uniform along the length of the cylinder. Overall, the frictional drag coefficient is much smaller than the drag coefficient due to dynamic pressure, such that any variations in the frictional drag can be neglected. However, variations in the pressure based drag coefficient should not be neglected. It is advisable to prescribe drag coefficients that vary along the length of a member when choosing inputs for engineering tools.
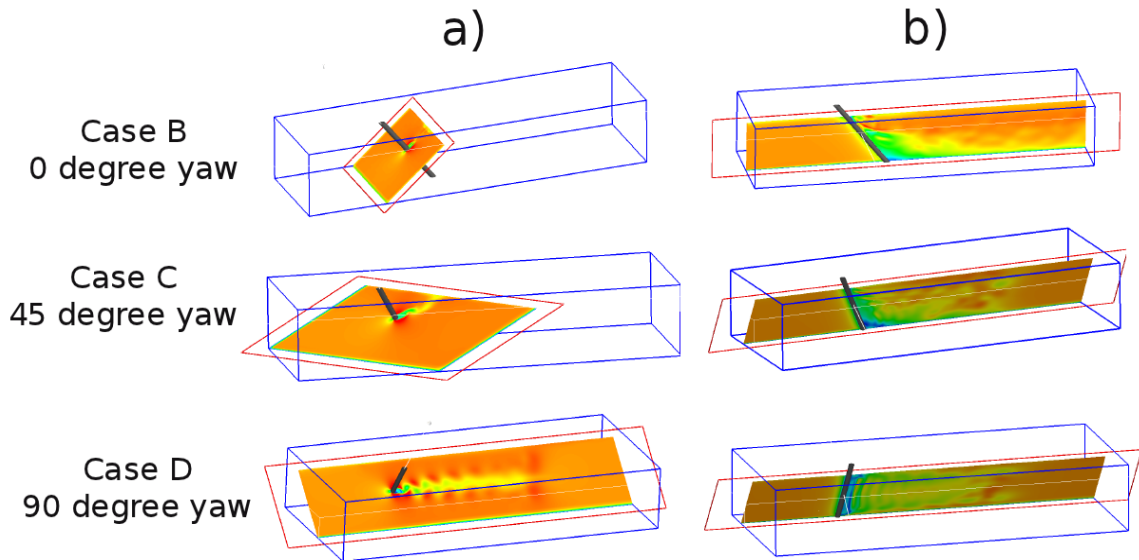
Figure 9.10. Visualizations of the flow around Cases B, C and D. In a) slices are taken perpendicular to the cylinder axis, and in b) the slices are made to align with the angle of the cylinder, along the flow direction.

To better understand the drag coefficient predictions from these four simulations, visualizations of the velocity fields around the cylinders are provided in Figure 9.10. Two slices were taken through the domains of cases B, C and D (E is omitted here because it is the mirrored case of B, which was discussed earlier). These slices are made normal to the cylinder axis and then along the cylinder axis, in line with the flow direction. Again, Case B shows a wake behind the cylinder that varies greatly along

the length of the cylinder, corroborating the variation in drag prediction as a function of height. In Case C, there is some variation in the wake in the vertical direction. As the yaw continues to increase, as it does in Case D, the wake appears uniform in the vertical direction, corroborating the drag coefficient predictions in Figure 9.9.

9.6   Summary and Conclusions

The CFD model was validated against previous results presented by Shao, et al, [210]. This included testing the independence principle (IP), by comparing a cylinders in the same orientation where one was fully submerged and the other pierced a free-surface. In this comparison we confirmed that the presence of a free-surface alters the loads on a slanted cylinder, such that the loads are actually increased as compared to a fully-submerged cylinder. Next, cylinders at two yaw angles in the vicinity of previous studies by Shao, et al, were simulations and the results matched well with values published in the literature.

Upon completion of the validation exercises, the model was used to simulate two new yaw orientations of the pitched cylinder. The results from this study were presented alongside the previous simulation results, where the drag was given as a function of cylinder length. It was found that the drag coefficient depended on the yaw orientation of the cylinder relative to the flow direction, in a way that varied with the cylinder length.

For yaw angles of 0 and 180 degrees, the results were found to be roughly opposite each other. At a 0 degree yaw angle, the drag coefficient increased near the free surface, while the converse was true to the cylinder yawed at 180 degrees. In all of these cases, the drag coefficient (taken normal to the cylinder axis and neglecting hydrostatics) were near 1.0 along the center of the cylinder span. At the Reynolds number studied here, Re = 2092, a drag coefficient of 1.0 would be expected for a fully-submerged, vertical, infinite cylinder. This indicates that selecting drag coeffi-

cients from the standard Reynolds number versus drag coefficient look up table would actually provide appropriate inputs for coefficient-based engineering tools.

However, consideration of more complex physics near the cylinder ends must be taken into consideration. This work demonstrates that the flow around the cylinder is altered by proximity to a floor as well as a free-surface. These effects can be large enough that the drag coefficients at the ends of the cylinder deviate greatly from the drag coefficients near the center span. Selecting drag coefficients as input to engineering tools should be done carefully, and it is suggested that variable drag coefficients should be assigned along the length of members.

CHAPTER 10

MOTION OF THE SEMISUBMERSIBLE

10.1 Introduction

Validation against experimental data from the DeepCWind tank tests, as well as code comparison between OpenFOAM and HydroDyn, are important steps in providing better understanding and knowledge about the assumptions and approximations of HydroDyn, and other similar CAE tools. While code-to-code comparisons can provide verification of the codes, comparisons to experimental data have the potential to validate the codes. The lessons from the code comparison, with the experimental data, contribute valuable improvements to CAE tools, such as HydroDyn. Many other CAE tools for offshore wind turbine modeling exist worldwide and can also be improved from the findings of this work.

The work presented here is a continuation of a step-by-step comparison between OpenFOAM hydrodynamics simulations and predictions from FAST and experimental data. Through slowly increasing case complexity, individual factors that may contribute to disagreements in load predictions on offshore floating platforms for wind turbines can be assessed. This thesis project began with validation cases of wave propagation and load predictions, and has grown in complexity. Previous work examined the impacts of CAE model predictions depending on body size and the effects of shadowing on downstream members for the stationary semi-submersible. The work in this chapter adds further realism to the comparison by allowing the body to move. Results from free decay simulations of the OC5 semisubmersible are presented and compared to CFD predictions, focusing on radiation and viscous damping. Addition-

208

ally, motion of the semisubmersible in waves is simulated, and results are compared against predictions from HydroDyn.

10.2 DeepCWind Experimental Measurements

A variety of measurements were taken in the DeepCWind tank tests [34,188], and they are outlined in Table 10.1. Measurements include wave heights taken at two locations in the tank with resistance type wave probes. These measurements were used in the numerical wave propagation validation discussed in Chapter 5. Platform translational and rotational motion measurements were taken with an optical measurement device. From these optical motion measurements, translations at the center of gravity were derived. Forces on the platform were not measured. Comparisons between OpenFOAM and the tank test data use displacement data, and CFD can supplement the tank data by providing force predictions.

Table 10.1. Measured and derived quantities of the semi-submersible platform tests in the wave tank, adapted from [188].

Description	Sensor
Wave height next to and at platform location	Resistance type wave probe
Translational motion of floater	Optical measuring system
Rotational motion of floater	
Accelerations on columns	Piezo-type accelerometers
Mooring tension	Ring shaped force transducers

The physical properties of the system (including the tower and rotor-nacelle assembly) and the floating platform used in tank tests are provided in Table 10.2.

10.2.1 Free Decay Test Experiments

The DeepCWind tank tests included free decay experiments of the semi-submersible in surge, sway, heave, pitch, roll, and yaw. The model scale platforms were pulled or rotated from the zero-position and released. These tests were performed with and without wind, where all of the cases studied numerically here exclude wind.

Table 10.2. System and floater structural properties from OC5 tank tests, neglecting moorings, reported at prototype scale [188].

Property	System Value	Floater Value
System Mass	1.3958e7 kg	1.2919e7 kg
Draft	20 m	20 m
CM location below SWL	8.07 m	14.09 m
Roll inertia about CM	1.3947e10 $kg\ m^2$	7.5534e9 $kg\ m^2$
Pitch inertia about CM	1.5552e10 $kg\ m^2$	8.2236e9 $kg\ m^2$
Yaw inertia about CM	1.3692e10 $kg\ m^2$	1.3612e10 $kg\ m^2$

Table 10.3. Initial offsets and natural periods from the free decay tests of the OC5 semi-submersible in the MARIN wave tank [188].

MARIN Test No.	Description	Initial Offset	Natural Period (s)
901012	Surge	6.3 m	106.7
901014	Heave	2.13 m	17.5
901016	Pitch	4 deg.	32.5
901016	Yaw	11.2 deg	80.8

The free decay tests of the semi-submersible in the wave basin are outlined in Table 10.3. The initial offsets and natural periods are reported for each of the six free decay tests that were performed. The experimental free decay tests were carried out with and without the sensor cables attached in the OC4 test campaign, and it was found that the presence of the sensor cables affected the damping primarily in surge, roll and pitch [34].

10.2.2 Wave Experiments

The DeepCWind tests of the OC5 semisubmersible also included load cases of the platform in regular and irregular waves. The case studied here focuses on the response of the semisubmersible in waves, without wind. The regular wave tests were carried out for 20 minutes, while the irregular wave cases were performed for 180 minutes, where much longer time are required due achieve statistically significant data from

the inherently random irregular waves. The wave parameters for the OC5 load cases are given in Table 10.4.

Table 10.4. Wave tests of the OC5 semi-submersible in the MARIN wave tank [188]. Values presented at prototype scale.

MARIN Test No.	Case Description	Wave Height (m)	Wave Period (s)	
902001	Regular wave 1	7.1	12.1	
902002	Regular wave 2	10.5	14.3	
MARIN Test No.	Case Description	Significant Wave Height (m)	Peak Spectral Period (s)	Gamma γ
906001	Operational wave	7.1	12.1	2.2
907001	Design wave	10.5	14.3	3.0

10.3 Numerical Simulations

This chapter introduces body motion to the hydrodynamic study of offshore floating wind turbines, increasing the complexity of computations significantly. FSI coupling methods are briefly reviewed, followed by a discussion of results from Open-FOAM.

10.3.1 Numerical Fluid-Structure Interaction Coupling

As discussed previously, in Chapter 4, the method of fluid-structure interaction (FSI) coupling is important to the stability and accurate solution of the fluid and structural motion predictions. There are various ways to treat the FSI problem, including partitioned and monolithic approaches. Amongst the partitioned approaches, in which the solutions of the fluid and structure are determined sequentially, the degree of coupling can vary. In loosely coupled codes it is common for the fluid solution to be calculated first, followed by the structure solution, and then the dynamics simulation marches to the next time step. This coupling can be tightened by iterating

between the fluid and structure solutions within a single time step until a convergence criterion is reached, adding greater stability and accuracy.

Some common coupling methods including Aitken relaxation, Picard iterations and Arnoldi-type algorithms [86]. Perhaps the most common method is the Picard method which consecutively solves the fluid and structure solution, where the coupling is explicit. The Aitken method dynamically relaxes the 6 DoF solution to accelerate the coupled solution of the fluid and structure [116]. Finally, the Arnoldi method uses flow and structural solutions as a preconditioning step before converging the solution with a matrix-free solver.

In OpenFOAM, various treatments for the FSI coupling exist. The standard Volume-of-Fluid (VOF) solver with mesh motion is interDyMFoam. In this solver, the coupling is very loose. The equations for the fluid are solved, followed by the forces, moments and then resulting motion of the body. Then the solver moves to the next time step. This loose coupling can lead to unrecoverable instabilities. This instability has been well explained and documented by Förster and her colleagues [54], and is termed an "added mass instability".

In the extend branch of OpenFOAM, a new solver was created to enhance code stability and increase solution speed. This solver was developed by Wikki and is called navalFoam [84]. The navalFoam solver follows a similar structure to interDyMFoam, OpenFOAM's VOF-solver for moving meshes. The implicit nature of the navalFoam code leads to enhanced code stability. The FSI coupling, however, remains loose. The alpha, or volume fraction, field is solved, either explicitly using multidimensional universal limiter with explicit solution (MULES), as is done in the standard interDyMFoam, or implicitly (where MULES guarantees boundedness of the phase fraction). Under-relaxation on the alpha field is employed, and the solution is iterated over a user-prescribed number of cycles. Under-relaxation is also employed for the velocity solution, according to a relaxation factors for velocity and a final velocity it-

eration as prescribed in the fvSolution dictionary. The dynamic pressure is explicitly under-relaxed for the momentum corrector, except for the final corrector. Following correction of the momentum, the static pressure is then calculated, which includes the hydrostatic pressure field. This can be done either by summing the dynamic pressure solution with the hydrostatic pressure or implicitly, again with under-relaxation. The code is also written to allow a limit on the magnitude of the velocity by direct user input of an upper bound. While this solver maintains solution stability, it can lead to inaccurate motion predictions due to the use of loose coupling between the fluid and structure. The stability of the solver is necessary but not sufficient for guaranteeing long, accurate 6 DoF motion simulations.

More recently, interDyMFoam was updated by Dunbar, et al, [42] to add tight FSI coupling. The new solver is called relaxationDyMFoam, and it was developed for the ESI branch of OpenFOAM. The momentum equation and PISO loop remains unchanged from the standard interDyMFoam solver. Increased code stability is provided entirely through tightening the FSI coupling. Solution subiterations and Aitken dynamic relaxation were implemented to improve code stability. Convergence of the solution is checked within each time step, following a subiteration loop. To accelerate the solution, Aitken relaxation was used for the 6 DoF solution.

However, the tightly-coupled solver developed by Dunbar, et al, does not include wave generation boundary conditions. Wave boundary conditions can be implemented by installing swak4Foam and using a groovyBC boundary condition. Here, the user can write expressions for fields, such that a few lines of code can prescribe sinusoidal motion of the color function, velocity and pressure fields at the inlet. This method is easy to implement, however, previous work in this dissertation found that waves reflecting off of boundaries quickly led to poor wave time histories. The wave library, waves2Foam, developed by Jacobsen [80] includes relaxation zones, as discussed in Chapter 5. These relaxation zones provide the necessary damping to mitigate spu-

rious wave reflections from domain boundaries. Because these relaxation zones are necessary to achieve accurate wave fields, the wave library from waves2Foam was coupled to the tightly-coupled solver, relaxationDyMFoam, creating a new solver which I named relaxWaveFoam.

This chapter presents simulation results from navalFoam (extend branch), relaxationDyMFoam (ESI branch), and relaxWaveFoam illustrating the importance of the FSI coupling method in the prediction of accurate motion of bodies interacting with a fluid.

10.3.2 Parallel Processing Challenges

Due to the large three-dimensional meshes required for simulating floating wind turbine platforms in water, CFD simulations must be performed in parallel. In OpenFOAM, parallel simulations are performed with a message-passing interface (MPI) library.

In this work, challenges related to parallel processing in the extend branch of OpenFOAM were confronted. The code showed a dependency on the number of domain decompositions, or in other words, number of processors used in computation. For example, cases could reach long simulated times on 48 processors, but the same case would crash at early simulated times on 80 processors. The inability to decompose simulations on a large number of processors limits not only the speed of simulation, but also in some sense the size of meshes, in terms of cell counts. These limitations on mesh sizes mean that adding refinement to regions such as the surface of the body and the fluid-interface was hindered. The implications of these mesh challenges are discussed further, below, in regards to the numerical results.

In addition to the issue of processor count, the moving meshes in the extend branch produced degenerate cells leading to unrecoverable code crashes. In these instances it was found that degenerate cells were occurring at processor boundaries.

The degeneracy of the meshes is unrelated to the actual fluid solution, but is instead a by-product of the dynamic meshing which does not guarantee mesh quality.

10.3.3 Numerical Analysis Specifications

The CFD simulations were performed at model scale, as they were for stationary simulations discussed in previous chapters. The experiments were performed at model scale as well, but all values were scaled with Froude scaling in the reported data. The physical properties of the semisubmersible used in the numerical simulations are given in Table 10.5, and are presented at model scale (1/50th of prototype scale, and Froude scaled).

Table 10.5. Physical properties of the semisubmersible used in the CFD simulations, values are presented at model scale.

Property	Value
System Mass (without main column)	104 kg
System Mass (with main column)	109.6 kg
System Mass (all members)	110 kg
Draft	4 m
CM location below SWL	0.26 m
Roll inertia about CM	44.63 $kg\ m^2$
Pitch inertia about CM	49.76 $kg\ m^2$
Yaw inertia about CM	44.81 $kg\ m^2$

A simplified version of the semisubmersible geometry was used in some of the CFD simulations. This most simplified geometry neglects the cross braces, pontoons and main column of the semisubmersible, and includes only the three offset columns, which are composed of the upper and base columns. The simplified geometry was chosen to allow future comparisons with MIT's fluid-impulse theory that are to be conducted with a simplified geometry. For the pitch free decay test an additional mesh was created which included the main column, which allows for a better understanding of the impacts of including or neglecting that member. Finally, a mesh of the full

geometry, that is, including the main column, pontoons and cross-braces, was used for simulating the motion of the semisubmersible in waves.
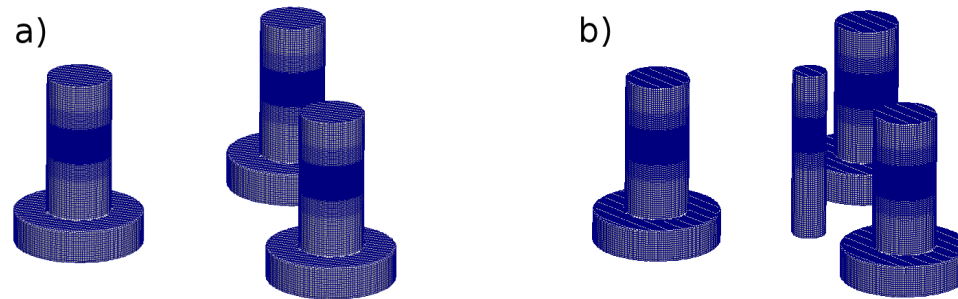
Figure 10.1. a) Surface of the semisubmersible mesh without the main column, pontoons or crossbraces, b) from numerical mesh that includes the main column.

The meshes are shown in Figure 10.1, and follow the same mesh criteria that were discussed in previous chapters. Again, mesh refinement was employed nearest to the semisubmersible geometry, and also along the fluid interface region. The full geometry mesh is described in more detail in Chapter 8.

Boundary conditions for the free decay tests and motion in waves were very similar to those employed in the stationary semisubmersible simulations discussed in earlier chapters. For the free decay tests the flow field was initially quiescent, that is, the velocity was zero everywhere in the domain. Any velocities in the flow were created by the motion of the semisubmersible structure. In the wave cases, the velocity and liquid volume function were prescribed on the inlet to generate waves through the domain, as was done previously.

A new boundary condition for point motion was added to allow for dynamic motion of the semisubmersible. This field describes the point motion of the mesh. As the semisubmersible moves, points not only on the body patch move, but also surrounding points. The mesh is smoothed using a Laplacian equation of the mesh radiating from the body, with a diffusivity-based algorithm for describing the degree of mesh deformation. In this work, a distance-based quadratic diffusivity model was

216

employed, such that the largest mesh deformations occur at the body patch and diffuse quadratically with increasing distance from the patch.

Furthermore, these simulations employed relaxation zones to damp out spurious reflections from domain boundaries. Further details on the relaxation zone implementation can be found in Chapter 5. For the free decay tests, relaxation zones were placed on the four side domain boundaries, and in the wave cases one relaxation zone was used at the domain outlet.

In this work, when the navalFoam solver was used, only three degrees-of-freedom of motion (DOFs) were allowed, which included surge, heave and pitch. The roll, yaw and sway degrees of freedom were turned off in order to enhance stability of the simulations. In my previous work with 6 DOF simulations, I found that added mass instabilities, well documented by Förster, et al, [54], lead to code crashes. Turning off three of the DOFs for the semisubmersible in free decay and wave motion is acceptable because pitch, heave and surge are the dominant motions of the body.

Mooring lines are simulated with the spring restraint model in OpenFOAM. The linear spring model was adapted to include constant pre-tension values and non-linear spring constants, in addition to the already existing linear spring terms. For free decay tests the motion of the body is small enough that the restoring force-displacement curve from the mooring lines is very linear in the narrow band of small displacements. In larger amplitude motions, such as the case of motion in extreme wave events, non-linear restoring forces are provided by the mooring lines, such that adding non-linear terms to the spring model was necessary. The three mooring lines in the OC5 tank tests are attached at the top of each base column, and each line, fairlead and anchor are located 120 degrees apart. Values for the mooring line spring constants were taken from the Phase II OC4 report [187]. In the extend branch of OpenFOAM the spring code in OpenFOAM treats the mooring as attached to a single point, so a torsion spring was also added, to provide rotational restoration in pitch. In the ESI

branch of OpenFOAM the spring restraint code is structure to allow an arbitrary number of springs, such that three springs were attached to the base column of the semisubmersible, at 120 degrees apart, to mirror the mooring lines in the tank tests.

10.4   Free Decay Tests: Results and Discussion

As part of the continued approach of increasing case complexity, free decay tests are carried out, introducing body motion but in the absence of waves and/or current. The free decay are performed to provide insight about the code's ability to properly model the rigid body natural frequencies and associated damping. Damping of large amplitude motion is dominated by viscous forces, while radiation damping has a greater influence on small motions. These comparisons can provide useful insight and guidelines for future improvements to the modeling tools.

10.4.1   Pitch Free Decay

Here, simulations performed with navalFoam of the semisubmersible in pitch free decay are presented. Validation of the rolling barge, presented in Chapter 5, was performed with the navalFoam solver and excellent agreement was found between the experimental measurements and code predictions. This agreement gives us confidence in the ability to predict rotational motion of a floating body.

In the pitch free decay cases, the semisubmersible was pre-tilted to 4 degrees to match the experimental initial condition. The semisubmersible was then allowed to pitch back to its equilibrium position. Initial offsets in the other degrees-of-freedom were set to zero in the numerical simulations, which was not always the case in experiment tests. Numerically, the initial offsets were done only in the degree-of-freedom of interest, such that pitch free decay tests had an initial pitch offset, but in no other.
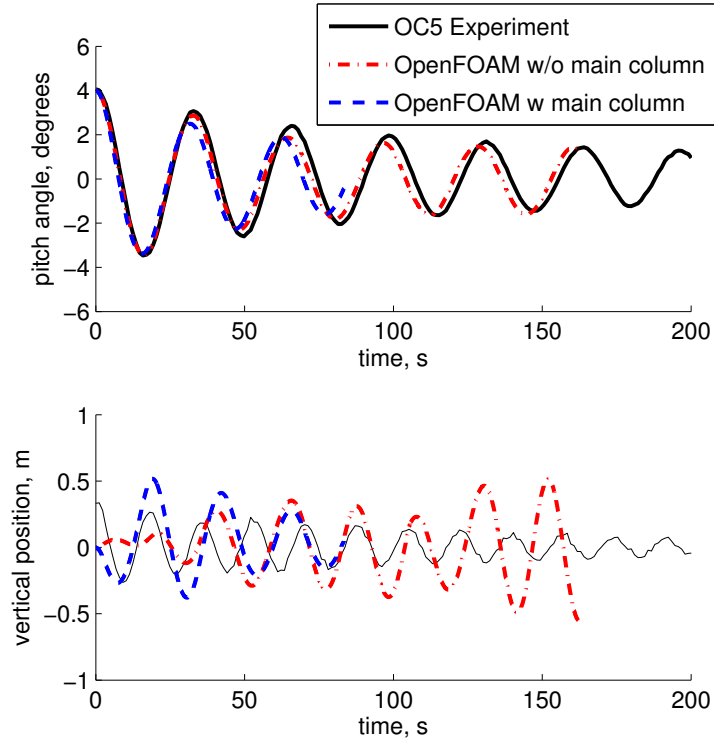
Figure 10.2. Pitch displacement of the semisubmersible in the pitch free decay test, shown in the top plot. The black line shows experimental measurements. Numerical results from navalFoam for the meshes with and without the main column are shown in dashed blue and dash-dotted red lines, respectively. The heave displacement from the same free decay test is shown in the bottom.

For the pitch free decay cases, two geometries were simulated, both similifications of the OC5 semisubmersible platform. The first excludes crossbraces, pontoons and the main column, while the second geometry includes the main column. The surface of the semisubmersibles from the two numerical meshes are shown in Figure 10.1. Comparison of the results from the two simplified geometries provides insights into the effects of including a main column.

Figure 10.2 shows the experimental results in black, and numerical results from the meshes with and without the main column in blue and dotted red lines, respectively. Good agreement was found between experimental measurements and CFD predictions

219

for the pitch degree-of-freedom. The heave degree-of-freedom did not find as good of agreement, where the numerical magnitudes of motion were larger, as well as the frequency. There are a variety of reasons for these discrepancies, including differences in the system properties, such as the geometry, and also the simplified mooring line model. Additional sources of discrepancy are summarized in Section 10.6.
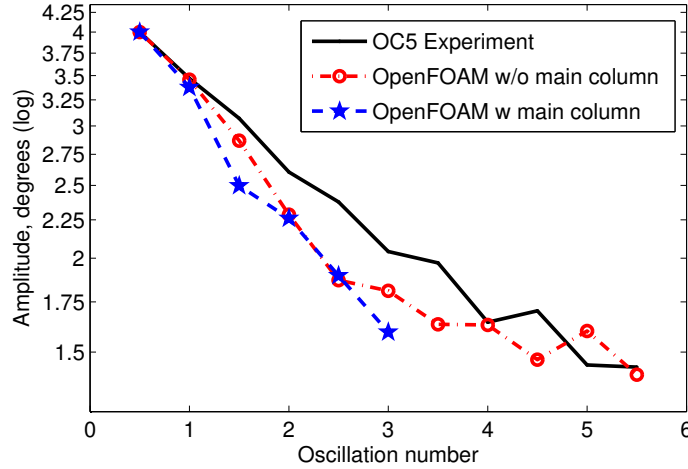
Figure 10.3. Damping of the pitch degree-of-freedom in the pitch free decay test. Experimental results shown in black, numerical results shown in red circles and blue stars for the geometries excluding and including the main column, respectively. All numerical results were computed using navalFoam.

The experiments found a pitch natural period of 32.1 seconds. Numerically, pitch natural periods of 31.6 and 32.7 seconds were predicted for the geometry with and without the main column, respectively. The two simplified geometries straddle the experimentally determined natural frequency nearly equally. The mesh with the main column found a slightly faster natural period than the experimental value.

The damping of the motion of the semisubmersible at each half cycle is compared between experiments and CFD predictions. The results are shown in Figure 10.3 as a function of the amplitude of pitch motion from the zero-position and the oscillation

number. The predictions from CFD show a slightly larger damping than was seen experimentally.
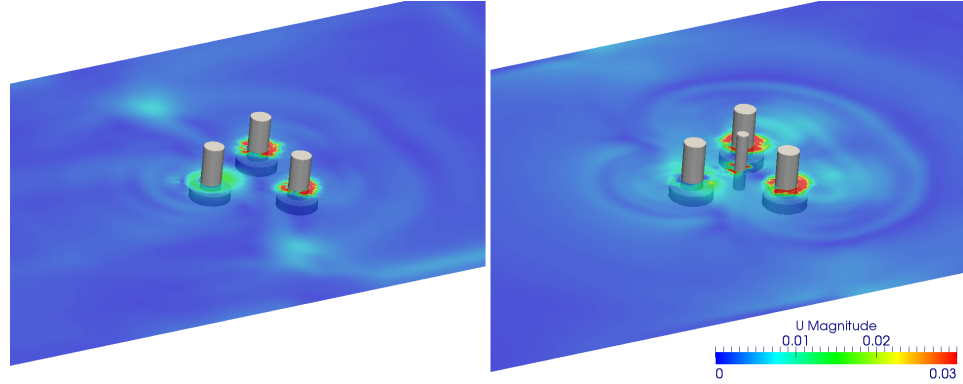
Figure 10.4. Horizontal velocity slices through the numerical domains, where the mesh with main column included is shown on the right hand side. Waves from radiation can be seen traveling to the left and right of the semisubmersible due to the pitching motion. Both slices were taken at t = 31.8 seconds. Results shown are from navalFoam solver.
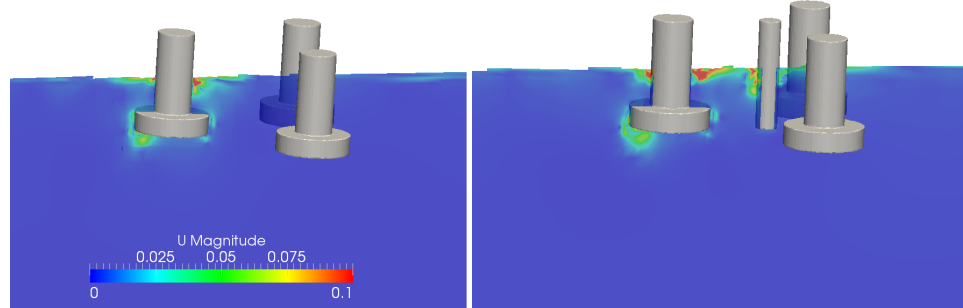
Figure 10.5. Vertical slices through the domains of both of the simplified geometry simulations illustrating the velocity magnitudes. Both slices were taken at t = 31.8 seconds. Results shown are from navalFoam solver.

Instantaneous snapshots of the flow around the semisubmersible in the pitch free decay tests are shown in Figures 10.4 and 10.5. Horizontal slices through the domains of the meshes with and without the main column are shown. The radiating waves can be seen traveling away from the pitching semisubmersible. Vertical slices, shown in Figure 10.5 display the velocity magnitudes and illustrate the vortices that are

generated off of the base column of the geometry. Again, the images show the case of the simplified geometry excluding and including the main column.

10.4.2 Heave Free Decay

Next, navalFoam was used to simulate heave free decay motions of the semisubmersible. In this work, the semisubmersible was pulled to 2.13 m below its position of hydrostatic equilibrium. Three DoFs of motion were allowed, including pitch, heave and surge.

Numerical predictions from navalFoam are presented alongside experimental measurements in Figure 10.6. The simulations of pitch free decay tests showed good agreement with experimental measurements, however, numerical agreement was found to be poor for the heave free decay test.
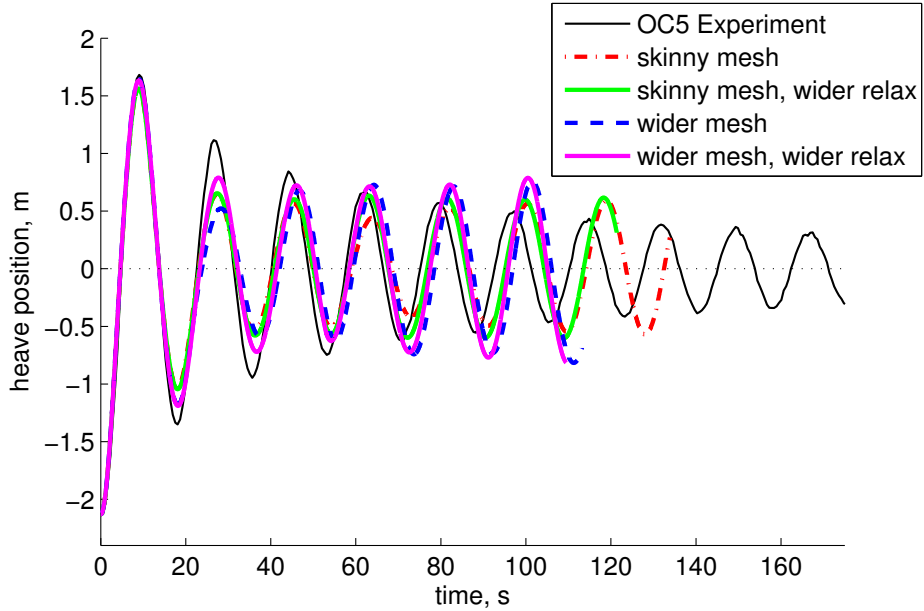
Figure 10.6. Heave displacements of the semisubmersible in the heave free decay test. The black line shows experimental measurements. The red dash-dotted line shows the results for the skinny mesh with small relaxation zones, and the results with wider relaxation zones are shown in green. For the wider mesh cases, the results with smaller relaxation zones are presented in dashed blue and with wider relaxation zones in solid magenta. All results shown here are from navalFoam solver.

Simulations with varying mesh domain sizes were carried out, that is, the distance from the body to the domain boundary were increased. These cases are called the skinny mesh and the wider mesh. Additionally, the width of the relaxation zones were varied to test for the effects of the radiating waves spuriously reflecting off the domain boundaries. For the wider mesh cases, the relaxation zone was doubled in width from one simulation to the other. The domain sizes and the width of the relaxation zones are shown in Figure 10.7, and it is shown that while the results differ from one another, none of them agree well with experiments.

In particular, the first few cycles of oscillation show reasonable agreement, with better agreement for the case of the widest mesh with the widest relaxation zones. As the number of oscillation cycles increases the damping of the numerical solution diverges from the experimental predictions, and in some cases the amplitude of oscillation actually increases with time.
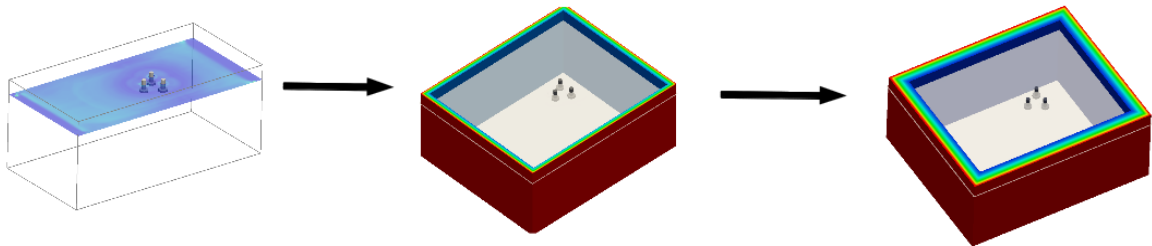
Figure 10.7. The skinny mesh is shown on the left, which was then expanded to make the wider mesh shown in the center. The width of the relaxation zones was doubled from the middle image to create the relaxation zone scheme illustrated on the far right.

The source of this reamplification of heave motion was initially thought to be produced by a non-physical reflection of radiation waves bouncing off of the domain boundaries. This was studied by increasing the distance to domain boundaries and increasing the width of the relaxation zones, neither of which ameliorated the reamplification issue adequately.
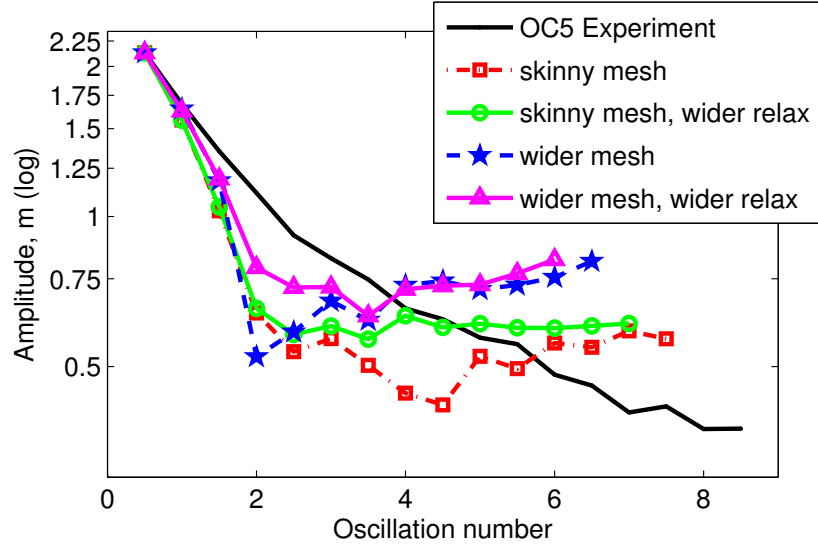
Figure 10.8. Damping of the heave degree-of-freedom in the heave free decay test computed with navalFoam solver. Experimental results shown in black, numerical results are shown in red, green, blue and magenta for the four cases present in Figure 10.6.

Damping of body motion at small amplitudes is due to the transfer of energy from the moving structure to the radiating waves. Without proper resolution of the fluid interface, these radiating waves may not be captured accurately, which could lead to poor prediction of the damping. To capture the radiation waves in these free decay tests, very refined cells around the fluid interface may be required, because the radiating waves are mere ripples. As discussed earlier, the mesh size was limited due to problems with the parallel processing of moving meshes in OpenFOAM. Thus, some of the damping issues seen with the heave decay cases could be due to the inability to properly capture the radiating waves.

Unlike the damping predictions, the natural frequency of the motions was predicted well by navalFoam. The experimental results found a heave natural frequency of 17.5 seconds, while the numerical results predicted a natural frequency of 17.8 seconds.
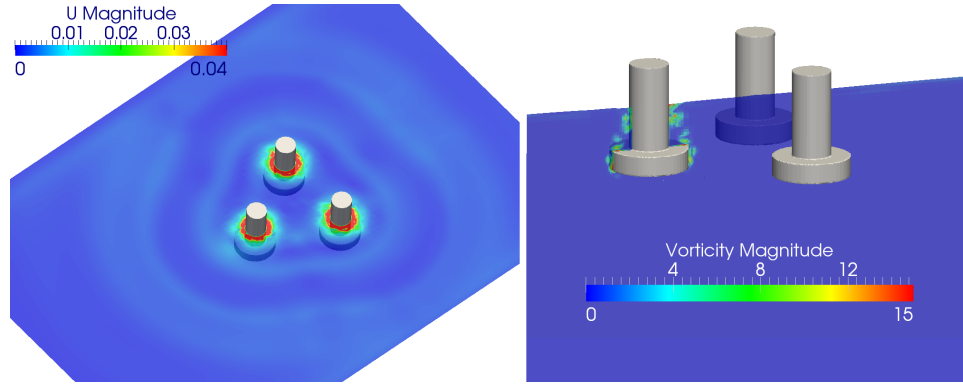
Figure 10.9. On the left, a slice through the domain, just below the free-surface, illustrates the velocity magnitude around the semisubmersible in a heave free decay simulation. On the right, the vorticity field is shown on a vertical slice through the domain. Both images are taken at t = 18.4 seconds. Results shown are from navalFoam solver.

The poor agreement between the heave free decay motion predicted from CFD and the experimental measurements can also be attributed to the loose FSI coupling in the navalFoam code. The code produces stable simulations due to the under-relaxation of pressure and velocity, as well as the implicit nature of the code. Because of this stability, long run times can be achieved, barring any crashes related to the parallelization of the moving meshes.

A sample of images from the flow fields around the semisubmersible in heave free decay are shown to illustrate the velocity and vorticity, in Figure 10.9. The velocity magnitude shows ripples traveling away from geometry. The vorticity field shows that the base columns generate vortices as the semisubmersible heaves up and down.

10.4.3 Surge Free Decay

Next, navalFoam and relaxationDyMFoam were used to simulate the surge free decay tests of the semisubmersible. In the experiments, the semisubmersible was displaced 6.3 m in the surge direction. The initial displacements in the other DoFs were assumed to be zero in the numerical simulations.

The numerical predictions from navalFoam and relaxationDyMForm for the surge decay motion are shown in Figure 10.10, and are compared against the experimental measurements from DeepCWind.

Numerous simulations were performed with navalFoam, the loosely-coupled FSI solver. The best predictions are shown in Figure 10.10, where the results show incredibly poor agreement with experimental data. The semisubmersible surge forward and backwards before reaching the equilibrium position. The mooring lines were modeled with a linear spring, where only one spring could be specified, but the spring constant consisted of three components in the x, y and z-directions. The poor predictions from navalFoam can be attributed to multiple factors, including the loose-coupling of the fluid and structure solutions.

Next, the tightly-coupled solver relaxationDyMFoam was used to simulate the free decay of the semisubmersible in the surge direction. The mooring lines were again modeled using a linear spring restraint. However, the spring model in the ESI branch of OpenFOAM differs from that in the extend branch. Instead of a single spring with a 3-component spring constant, the ESI branch allows for an arbitrary number of springs, each with a uniform spring constant. In practice however, implementing multiple springs simultaneously led to crashes. In experiments, the semisubmersible had three mooring lines, attached at 120 degree intervals. Instead, a single linear spring was used in the simulations, leading to poor prediction of the surge free decay motion. This issue is especially pronounced in the pitch motion, where a single mooring line attached from the center of the semisubmersible to a location on the tank bottom causes the barge to pitch in the negative direction. In reality, three mooring lines exist, and need to be simulated in order to avoid this false pitch motion. However, the code is not stable for more than one spring, such that including all three mooring lines in the simulations was not possible.
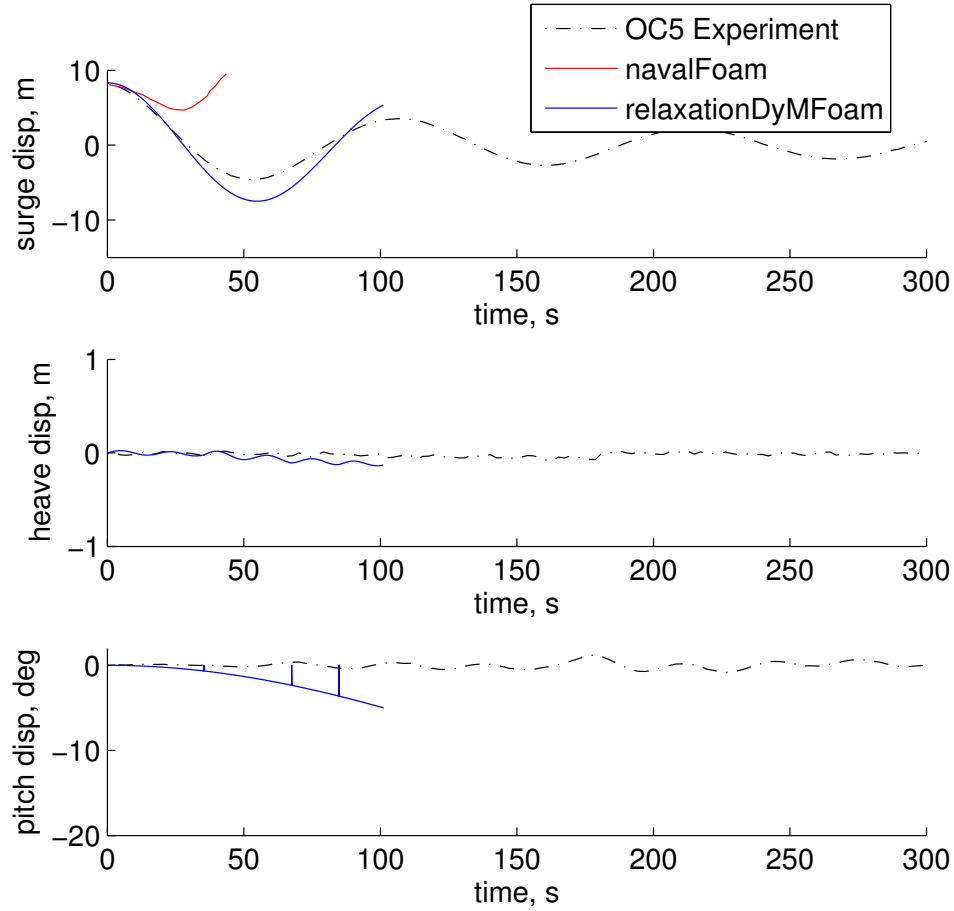
Figure 10.10. Surge free decay motion predictions from navalFoam and relaxationDyMFoam compared against experimental measurements from the OC5-DeepCWind tank tests.

The results from the relaxationDyMFoam simulations show much better agreement with experimental measurements relative to the results from navalFoam. Nonetheless, due to the challenges of the spring restraint code, namely the instability when using multiple springs, the surge free decay case remains a difficult case to simulate numerically.

10.4.4 Two-Dimensional Heave Test of a Buoy

To further investigate the effects of mesh refinement and wave reflections off domain boundaries, a parametric study was performed with navalFoam of a simple two-dimensional heaving square buoy in a quiescent flow field. The parameters included mesh refinement, domain length and relaxation zone size. The barge had a width and height of 0.25 m, with a 4.5 kg mass. The depth of the barge was 0.1 m (because 2d simulations in OpenFOAM actually have a dimension into the page). These dimensions and mass mean that the center of the barge should have a draft of 0.18 m in its position of hydrostatic equilibrium. The results plotted here are given in terms of displacement from the position of hydrostatic equilibrium, such that a displacement of zero means the barge has reached its theoretical equilibrium position. Neither springs nor moorings were used in any of the two-dimensional barge simulations.

First, a mesh refinement study was carried out. Because radiating waves provide the damping of the body motion, the level of mesh refinement at the fluid interface and near the barge was studied. It was hypothesized that inadequate refinement was causing poor capture of radiation waves, and therefore leading to erroneous prediction of the damping. A base mesh of 22,500 cells was used, and then refined with octree-refinement everywhere to generate a mesh with 86,150 cells. That mesh was then refined around the fluid interface in both directions to generate a mesh with 103,190 cells. Another mesh was generated with additional refinement surrounding only the barge, resulting in a mesh with 107,810 cells. Finally, a very well refined mesh was generated with 668,360 cells. The inlet and outlet were located at 36 diameters from the barge in either direction.

The results from these five meshes are shown in Figure 10.11. These results show that increasing the mesh refinement not only affects the degree of damping, but actually impacts the position to which the barge decays. Even more suprisingly, not
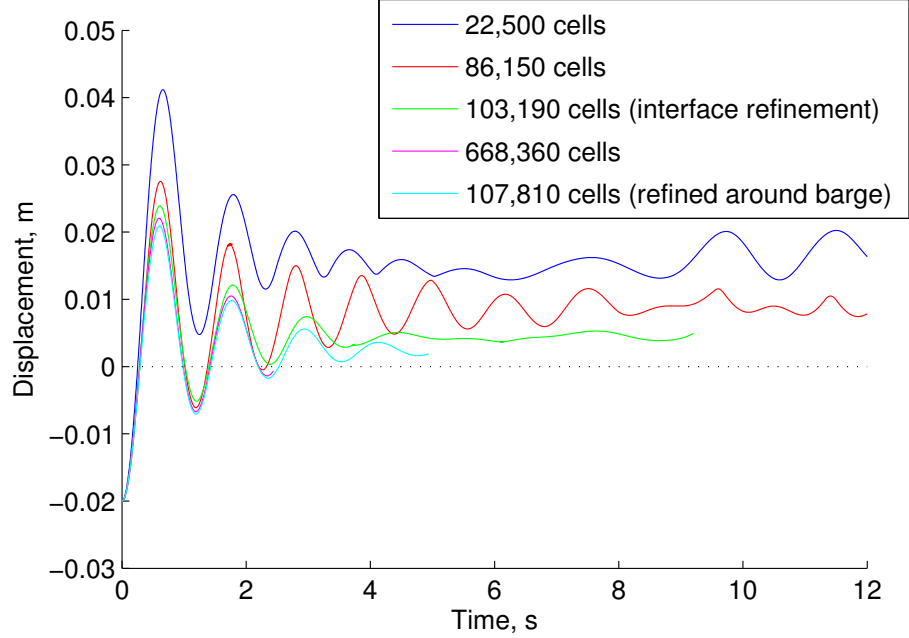
Figure 10.11. Heave free decay results for a two-dimensional square barge in still water. Results from five meshes are shown, with each mesh's cell count shown. The position to which the barge decayed to varied depending cell refinement. The correct position of hydrostatic equilibrium was not reached. All results shown here are from navalFoam solver.

only does the refinement affect the computed equilibrium position, but in none of the cases does the barge decay to its theoretical position of hydrostatic equilibrium, indicated by the dotted black line at 0 displacement.

Next, the computational domain size was varied to study the potential ramifications of placing the domain boundary too close to the body. This was also done to investigate the effects of reflecting waves off of nearby and farther away domain bounds. A short, long and medium length mesh were generated. The short mesh had the barge placed such that the inlet and outlet were located roughly 12 diameters from the barge on either side. The medium mesh had domain boundaries located at 20 diameters from the body, and the largest mesh had a distance of 36 diameters from body to boundary. The meshes used in this study were of medium refinement,

relative to the mesh refinement study discussed above, such that the longest mesh had 86,150 cells.
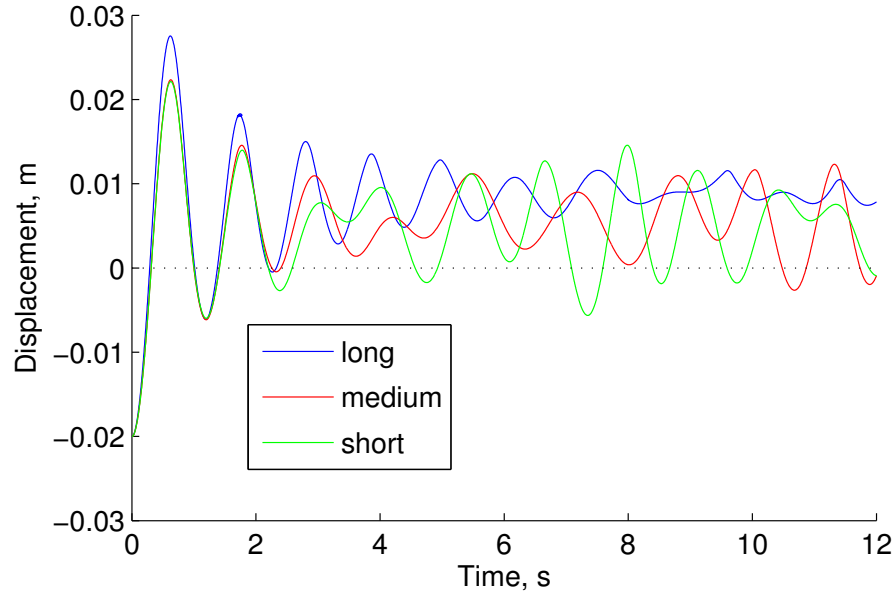
Figure 10.12. Heave decay predictions from simulations with three different domain lengths. The short, medium and long meshes have 12, 20 and 36 barge diameter distances from the boundaries, respectively. All results shown here are from navalFoam solver.

The results from the domain length study are presented in Figure 10.12. Again, the barge does not reach its theoretical position of hydrostatic equilibrium for any of the domain lengths. Looking at the results just in terms of the motion damping, it is clear that the longest mesh predicts the greatest damping. Reamplification of the motion is seen in the results from the short and medium length mesh, indicating that reflections off nearby domain boundaries may have a large effect on the predicted motion. Spurious reflections of waves off of the inlet and outlet may be constructively interfering with radiation waves from the body, such that the motion is reamplified.

Finally, the size of the relaxation zones was varied to study the impacts of their lengths on the motion prediction. Symmetric relaxation zones were placed at the inlet and out of the domain. The relaxation zones were 0.5, 1 and 1.5 m wide for

the small, medium and large cases, respectively. Additionally, the results for a case without any relaxation zones are presented for comparison. The results are shown in Figure 10.13.
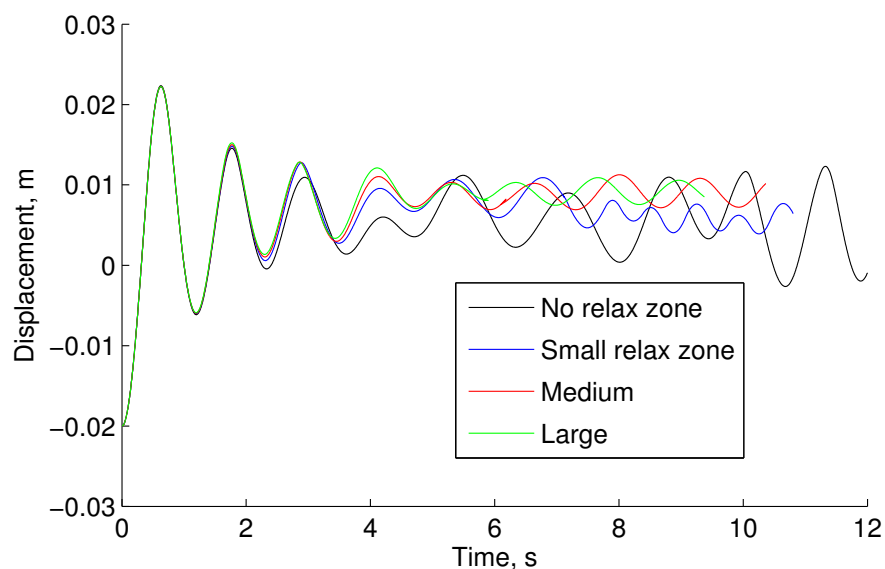
Figure 10.13. Results from simulations where the length of the relaxation zone was varied. The relaxation zones were 0.5, 1 and 1.5 m in length for the small, medium and large cases, respectively. All results shown here are from navalFoam solver.

The presence of relaxation zones has a large influence on the results, as indicated by the comparison of the results against a simulation without relaxation zones, shown in the black line of Figure 10.13. The case with the smallest relaxation zones predicts high frequency motions of the barge at later times, which may be caused by spurious reflections interacting with the radiation waves. The frequencies of motion predicted by the cases with medium and large relaxation zones is more uniform. However, the motion of the barge appears to reach a constant amplitude of oscillation, which is non-zero. And yet again, none of the results decay to the theoretical position of hydrostatic equilibrium.
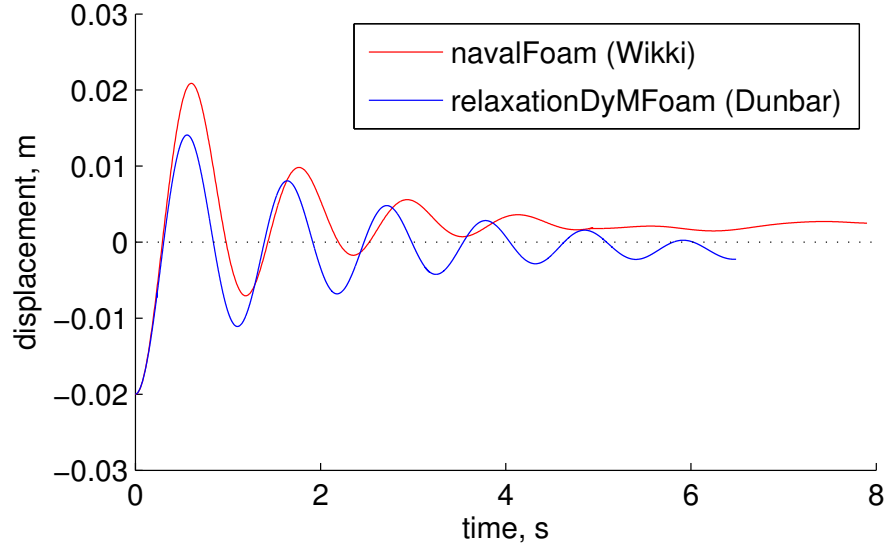
Figure 10.14. Predicted heave decay motion of a 2d barge in still water using the navalFoam and relaxationDyMFoam solvers.

None of the cases of the two-dimensional heaving barge simulated with navalFoam returned the correct solution for the location of hydrostatic equilibrium. This was a surprising result following the successful validation of the rolling barge simulated with navalFoam and compared against experimental data by Jung [97] presented in Chapter 5. The same case was simulated with relaxationDyMFoam developed by Dunbar, et al [42] with the 86,150 cell mesh. The results from the same meshes simulated with navalFoam and relaxationDyMFoam are shown in Figure 10.14. The comparison exhibits the navalFoam prediction reaching the incorrect position of hydrostatic equilibrium, while the relaxationDyMFoam result oscillates symmetrically around a 0-displacement, or equilibrium position. In addition to the difference in displacement magnitudes and center of oscillation, the results show different frequencies of motion.

The results from relaxationDyMFoam yield a more accurate prediction of the hydrostatic equilibrium than what is predicted by navalFoam. The more tightly coupled FSI method implemented in relaxationDyMFoam produces stable and accurate

results, where the loose coupling but implicit fluid solves provides only code stability, but not accuracy of body motion.

10.5 Motion in Regular Waves: Results and Discussion

Investigations of regular wave loads on the semi-submersible structure provide the next step in building complexity of the cases. Looking at regular waves in the absence of wind isolates the study to just hydrodynamics modeling. The regular wave cases include contributions from Morison's equation and potential flow theory when computed with HydroDyn. As opposed to the preliminary work which simulated the semi-submersible as a stationary body, this work introduces radiation. The agreement between HydroDyn and OpenFOAM is now subject to diffraction, radiation and viscous loads, further complicating the problem.

10.5.1 FAST Results

FAST simulations were performed for a simplified version of the semisubmersible geometry. A WAMIT model was used that included only of the upper and base columns, and neglected the cross-braces, pontoons and main column. For the Morison's calculation, only the offset columns and main column were included. The drag coefficients input to OpenFOAM were selected based on previous CFD simulations presented in Chapter 7. These values were 0.56 for the main column, 0.61 for the upper column and 0.68 for the base column. The FAST results show a large degree of start-up transients, particularly for the surge degree-of-freedom. This start up transients is also seen in experimental measurements, particularly for the surge DoF.

10.5.2 CFD Results: Loosely Coupled Solver

Here, a simulation using navalFoam of three DoF motion of the semi-submersible in regular waves is presented. The regular waves simulated here have a wave height of 7.1 m and a period of 12.1 s, at prototype scale. Again, the CFD cases were performed
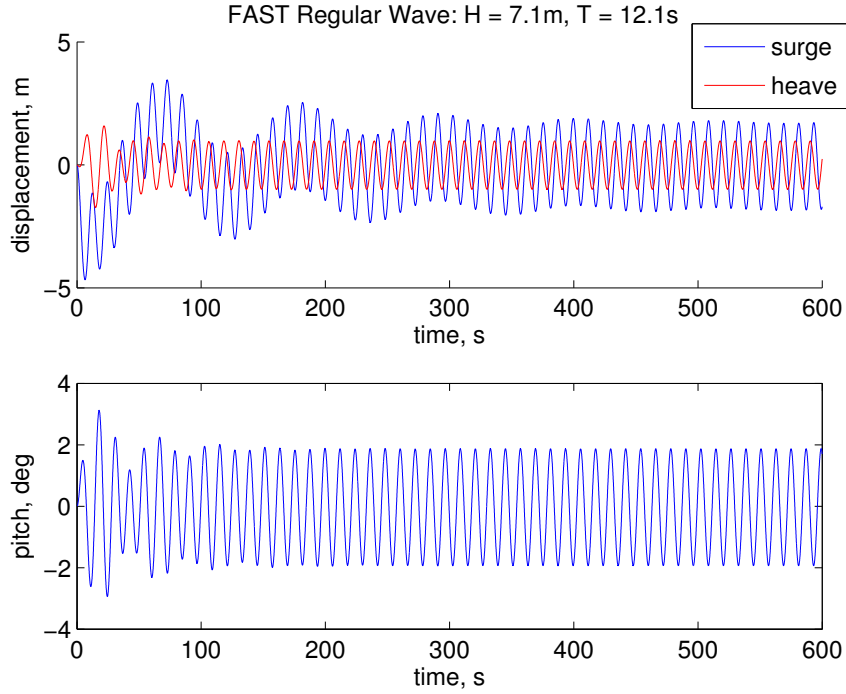
Figure 10.15. FAST results for the simplified semisubmersible geometry in regular waves with H = 7.1 m and T = 12.1 s. A large amount of start up transients is observed in the results, most notably for the surge DoF.

at model scale, which is 1/50th of the prototype scale. All values are scaled with Froude scaling. The three DoFs of the simulated semi-submersible include the pitch, heave and surge. It was expected that limiting the number of degrees of freedom would provide greater numerical stability.

Predicted surge, heave and pitch motions of the semisubmersible are presented in Figure 10.16 as predicted by navalFoam. The results are compared against predictions from FAST for the simplified semisubmersible geometry. The agreement between navalFoam and FAST predictions is good in terms of the frequency content, as well as the magnitude of motions. However, the position about which the semisubmersible is oscillating is not in good agreement. The discrepancy between navalFoam and FAST is most pronounced for the heave DOF where the CFD solution has a a vertical offset, which is incorrect. The offsets between results for the surge DOF can be partially
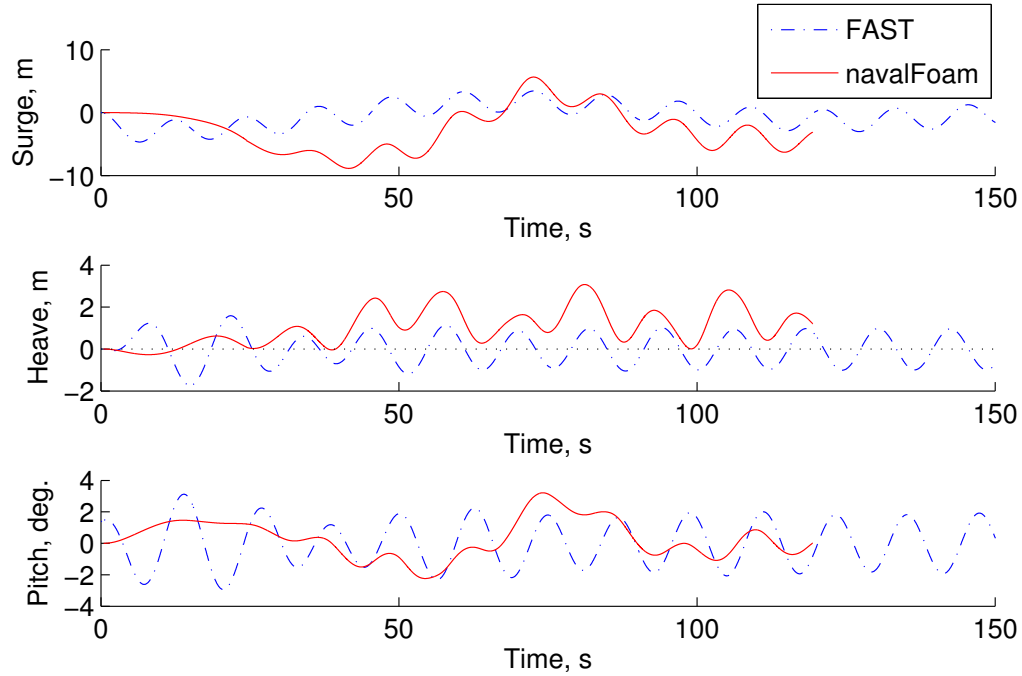
Figure 10.16. Motion of the semisubmersible in regular waves with 7.1 m height and period of 12.1 s (values presented at prototype scale), as predicted by FAST and navalFoam, in blue and red, respectively.

attributed to start-up transients in both the CFD and FAST simulations. In general, the poor agreement between simulations and experiments for the semisubmersible moving in waves is due to the loose coupling of the fluid and structure solution in the navalFoam solver.

The start-up transients inherent to simulating the semisubmersible in waves means that very long simulation times are required to reach the quasi-steady state behavior. Unfortunately, due to the issues with the parallelism of the moving mesh code in the extend branch of OpenFOAM, long run times cannot be guaranteed because of degenerate cells occurring at processor boundaries.

Additionally, the mesh size limitation, due to the moving mesh parallelism issues, prevents refinement necessary to capture larger waves, because of the wide fluid-interface (from wave trough to crest). Instantaneous snapshots from the simulations
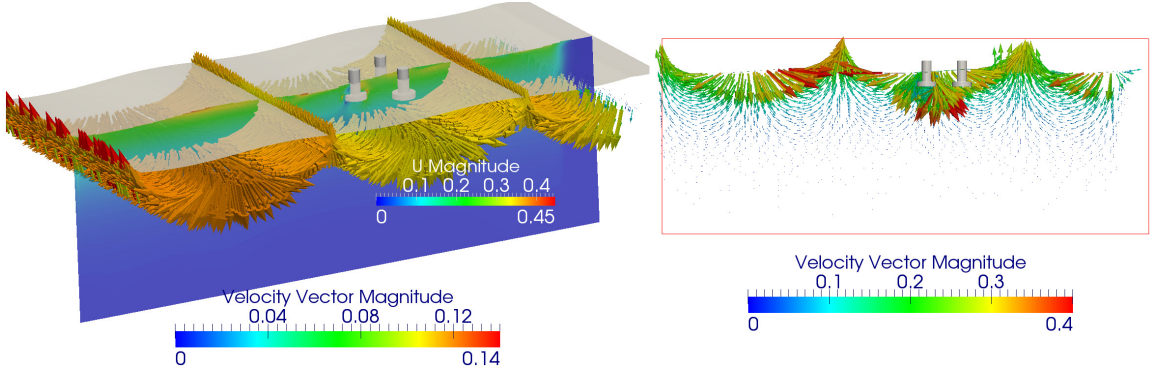
Figure 10.17. Flow field visualizations from navalFoam simulations. On the left, the wave surface is shown in opaque gray, and a vertical slice through the domain shows the variation in velocity magnitude with depth. Velocity vectors are mapped on to a horizontal slice through the domain just below the semisubmersible. On the right, velocity vectors located on a vertical slice through the domain.

of regular waves are shown in Figure 10.17. For irregular wave simulations, even more refinement around the fluid interface is necessary to capture the waves of small amplitude and frequency, as well as the larger sampled waves with bigger frequencies.

10.5.3 CFD Results: Tightly Coupled Solver

Next, simulations of the semisubmersible in regular waves with height 7.1 m and 12.1 s periods were performed with the tightly-coupled solver linked with the wave library, named relaxWaveFoam. The body was allowed to move freely in all 6 DoFs. A wave was generated at the inlet, with a relaxation zone placed at the outlet to prevent spurious wave reflections. Mooring lines were not included in these simulations, due to the code instabilities seen in the surge decay tests discussed earlier.

First, a simplified semisubmersible geometry was simulated, including only the three offset columns and none of the cross-bracing or main column. The body motion predictions from relaxWaveFoam are shown in Figure 10.18, in red, alongside motion predictions from FAST in dotted black lines. Here, the FAST simulations were performed with a simplified WAMIT model which contained only the three offset

columns. The surge, heave and pitch displacements are shown, from top to bottom. All results are presented at prototype scale. The displacements grow in magnitude over time, as the initial waves are generated at the inlet and must travel towards the semisubmersible.
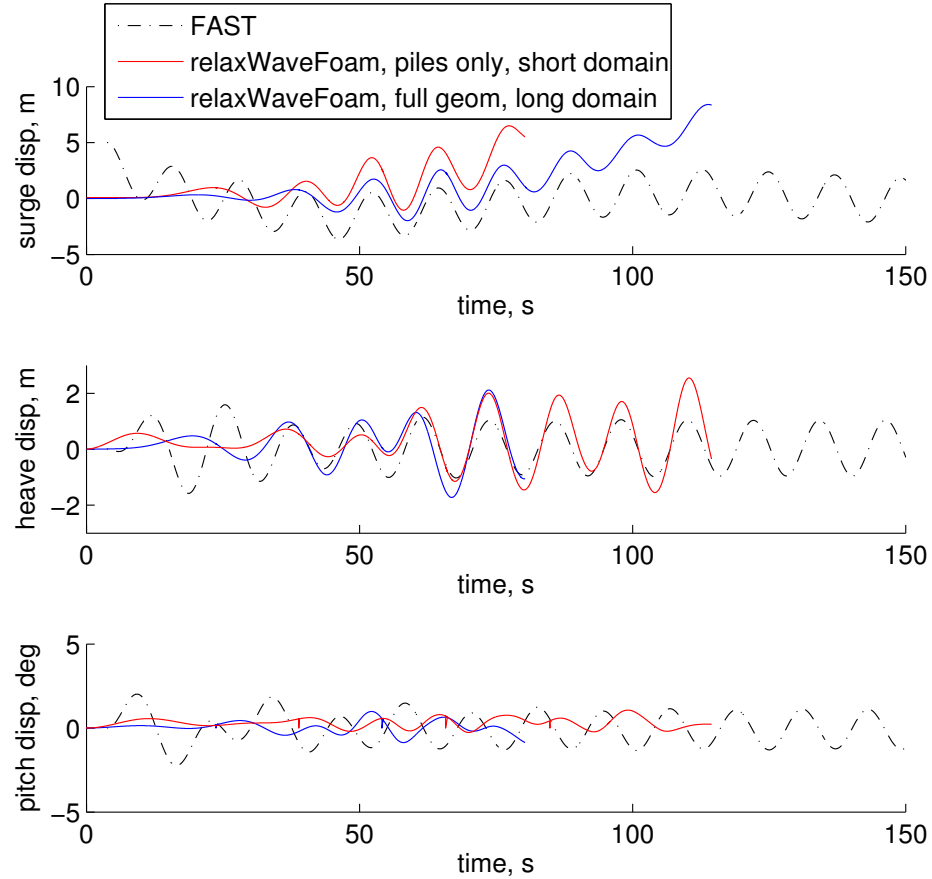
Figure 10.18. Motion predictions for the semisubmersible in a 7.1 m regular wave with 12.1 s period. Results shown for a shorter domain containing a geometry with only the three piles, and a longer domain with the full semisubmersible geometry, including crossbraces.

The surge motion prediction shows the semisubmersible moving in the positive x-direction. Due to concerns about waves reflecting off of the domain outlet and causing poor motion predictions in the surge direction, a simulation with a longer mesh was carried out. The simplified geometry simulations were performed with a

mesh of length 600 m at prototype scale. The longer mesh, which included the full geometry of the semisubmersible, was 50 m longer than the first mesh.

The results from the simulation with the longer mesh are shown in blue lines in Figure 10.18. Again, the same positive bias was found in the surge motion predictions. In each of these cases, the positive bias in the surge motion led to the simulations crashing due to large mesh deformations. Because both cases showed this bias, there is reason to believe the bias is due to the system itself and not simulation errors. This was further corroborated by visualizations of the wave field, and the lack of noticeable wave reflection off the outlet.

Furthermore, the predicted motion of the semisubmersible from FAST simulations shows a large degree of start of transients. This effect is illustrated in Figure 10.15. The positive bias of the surge prediction found in OpenFOAM simulations may well be due to start up transients of the system, just as is found in FAST.

Despite the positive bias in the surge motion, the frequency and cycle amplitudes of the displacements are in good agreement with those found by FAST. The heave motion predictions from relaxWaveFoam show good agreement in terms of frequency, but predict larger displacements than FAST. This discrepancy is likely due to the lack of a mooring line model in the OpenFOAM simulations. Nonetheless, this is an improvement upon the previous wave-body motion results from the navalFoam simulations, discussed in the previous subsection. The navalFoam results gave incorrect predictions for the hydrostatic equilibrium position of the semisubmersible, which is not an issue when simulating the motion with relaxWaveFoam.

Next, force predictions from relaxWaveFoam are provided. The DeepCWind experiments did not take direct load measurements, which the CFD can provide supplementally. In FAST, loads due to waves and body-motion can only be provided after proper tuning of the experimental data and determination of the appropriate hydrodynamic coefficients. The surge, heave and sway force predictions are shown
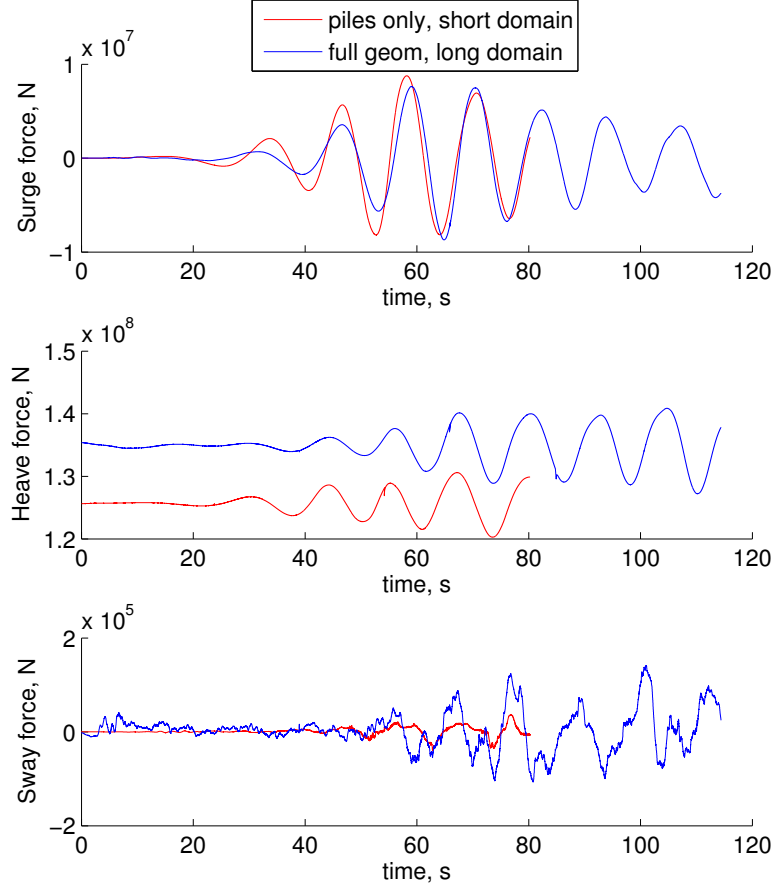
Figure 10.19. Force predictions for the semisubmersible in a 7.1 m regular wave with 12.1 s period. Results shown for a shorter domain containing a geometry with only the three piles, and a longer domain with the full semisubmersible geometry, including crossbraces. Results computed using relaxWaveFoam solver.

in Figure 10.19 from top to bottom, respectively, for both the simplified and full geometry meshes.

Visualizations of the regular waves propagating through the numerical domain and interacting with the full semisubmersible geometry are shown in Figures 10.20 and 10.21. The uniform periodicity of the regular wave is demonstrated in Figures 10.20, where the semisubmersible is located in a trough at the given time shown
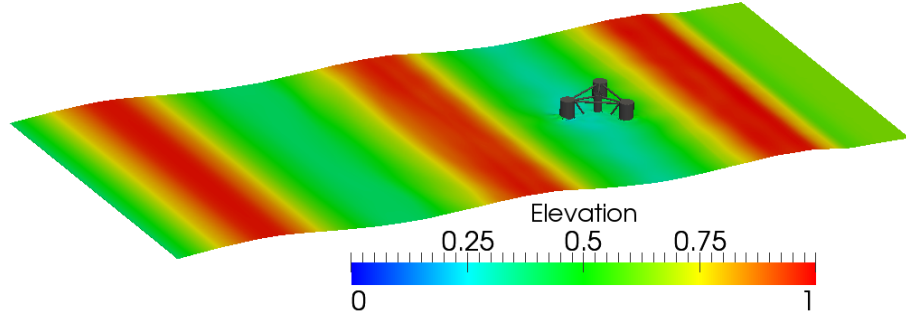
Figure 10.20. Wave elevation, normalized by maximum height, for the regular wave propagating through the domain with the full semisubmersible geometry.
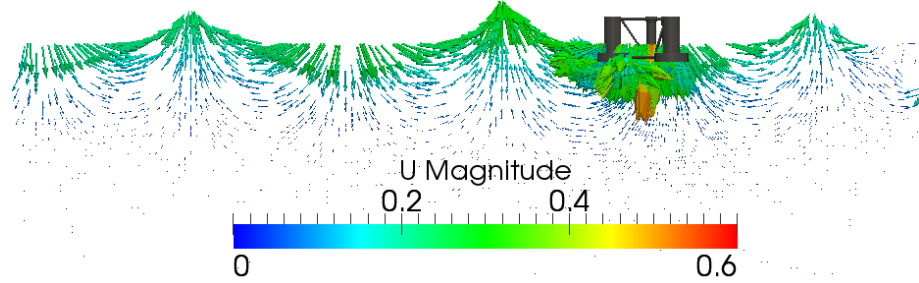
Figure 10.21. Velocity vectors from regular waves on the vertical plane through the semisubmersible.

($114.2\ s$). The velocity vectors shown in Figure 10.21 are taken at the same time, and illustrate the direction of the velocity vectors as a function of space.

10.6   Motion in Irregular Waves: Results and Discussion

Next, the semisubmersible was simulated interacting with irregular waves using the relaxWaveFoam solver. Simulations were not performed with navalFoam, as the regular wave results demonstrated errors with the hydrostatic equilibrium. As a demonstration case, the full geometry with the $650\ m$ domain length was used. The waves had a significant wave height (H_s) of $7.1\ m$ and peak spectral period of $12.1\ s$, and the wave heights and periods were sampled from the JONSWAP spectrum.
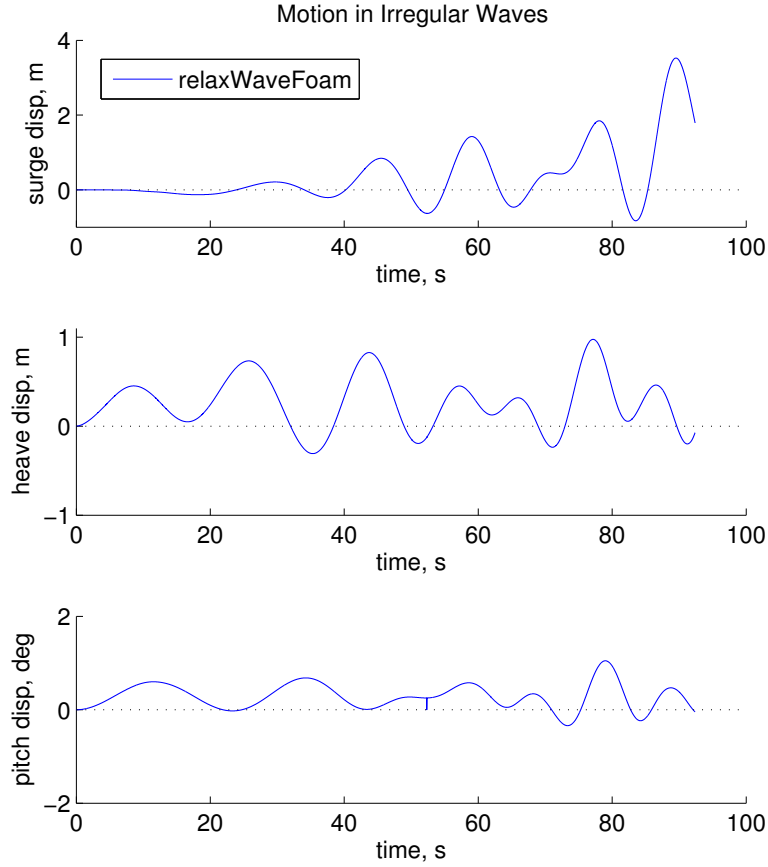
Figure 10.22. Motion predictions for the semisubmersible in an irregular wave with $H_s = 7.1\ m\ T_p = 12.1\ s$.

Motion predictions are given in Figure 10.22, where the surge, heave and pitch displacements are shown from top to bottom, respectively. Again, motions are small at early times when the waves are first generated at the inlet and begin to propagate towards the semisubmersible.

Force predictions due to the semisubmersible interacting with the waves are presented in Figure 10.23. Again, the forces from waves, including regular and irregular, were not measured directly in the DeepCWind experiments. This leaves a gap in the
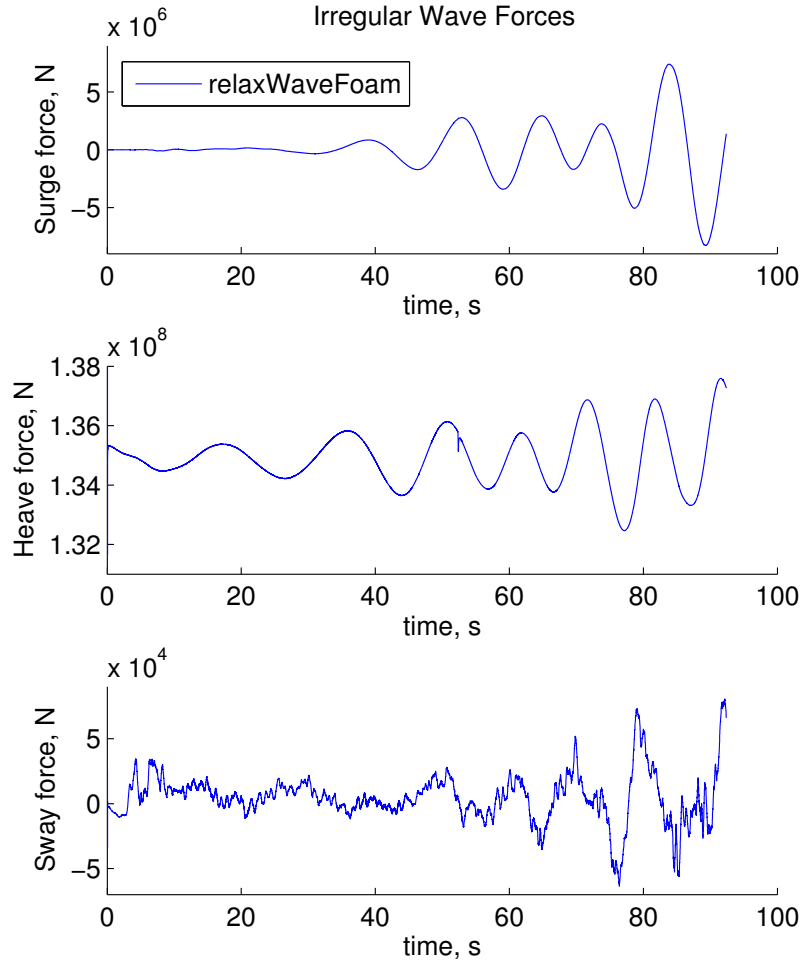
Figure 10.23. Force predictions for the semisubmersible in an irregular wave with $H_s = 7.1 \ m \ T_p = 12.1 \ s$.

data where CFD simulations can provide supplemental knowledge about loads in the three coordinate directions.

The experimental waves were generated for a long period of time, nearly three hours. Long simulation times are necessary because of the stochastic nature of irregular waves. To achieve statistically significant results, long numerical time series are necessary as well. Because such long simulations have not yet been achieved, these results are presented without comparison to experimental nor FAST results, which
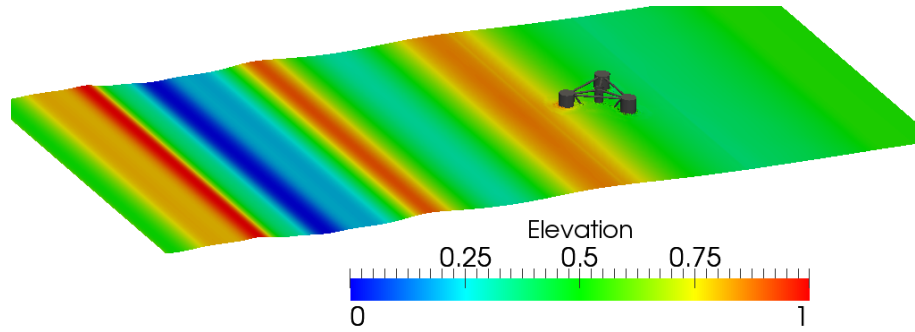
Figure 10.24. Wave elevation, normalized by maximum height, for the irregular wave propagating through the domain with the full semisubmersible geometry.

would require comparing statistical measures taken over a long time history. Instead, the results are presented as a demonstration that irregular waves can be simulated interacting with the semisubmersible using OpenFOAM.

The elevation of the waves at 52.3 s of simulated time are shown in Figure 10.24. While it is more difficult to see the irregularity of the waves from the motion and force results, the visualization of the elevation better demonstrates the variation in frequencies and wave heights. In this image, the waves are just beginning to reach the semisubmersible.
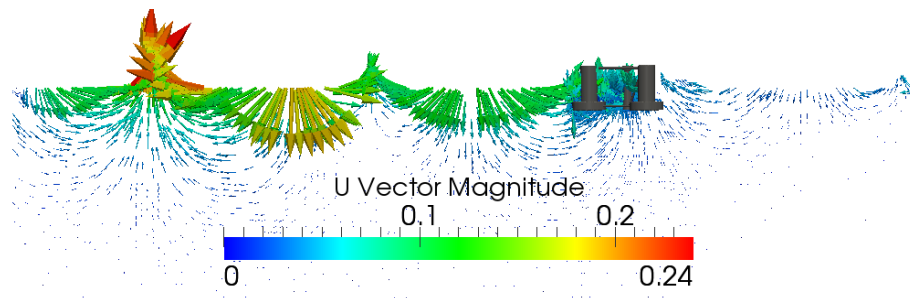
Figure 10.25. Velocity vectors from regular waves on the vertical plane through the semisubmersible.

The irregular waves are also illustrated by the velocity vectors along a vertical plane taken through the center of the semisubmersible, shown in Figure 10.25. Again,

the variations in frequency and wave height can be seen, especially when compared against Figure 10.21 which displays the velocity vectors from regular waves.

Finally, to illustrate the mesh deformation due to the semisubmersible interacting with irregular waves, Figure 10.26 shows the cell displacement field on a vertical plane taken through the center of the semisubmersible. The red indicates where a large degree of mesh deformation occurred, while the dark blue shows where the mesh did not change. The image illustrates how the cell deformation is greatest near the body, and decreases with distance from the surface, following the diffusivity-based algorithm of the dynamic mesh implementation.
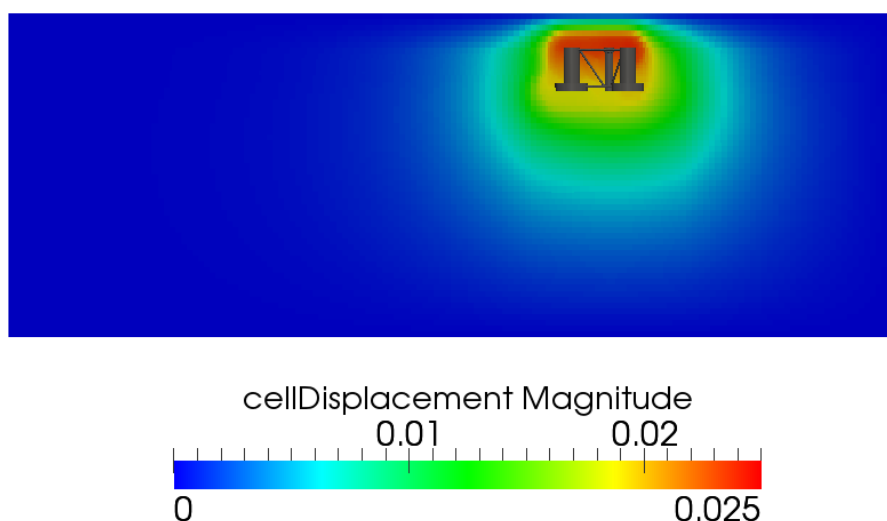
Figure 10.26. Cell displacements on a vertical slice through the center of the semisubmersible, illustrating the degree of mesh deformation resulting from the motion of the semisubmersible interacting with irregular waves.

10.7 Sources of Discrepancy

There are numerous sources of discrepancy between numerical predictions and experimental measurements, which have been discussed throughout this chapter and are

briefly summarized here. The sources of discrepancy fall broadly into three categories; physical, numerical and experimental.

From the physical perspective, it is more difficult to simulate the physics of a free decay test than it is to capture motion in waves. Free decay tests rely on capturing the proper physics of the natural frequency of the system, mooring lines, and the fluid. In waves, the frequency and magnitude of motion are dominated the motion of the fluid, such that capturing the physical parameters of the body is less important, but non-negligible. In wave tests, the dynamics are driven by waves, which are prescribed.

Furthermore, physically the systems that were simulated and measured experimentally did not match perfectly. The geometry used in the experiments included a main column, cross-braces and pontoons. Not only does this alter the complexity of the flow interacting with the body, but it also alters the mass and moments of inertia as compared to the simplified geometry used in the numerical simulations.

Numerically, in terms of the CFD model, the sources of discrepancy are manifold. These include the domain size, level of mesh refinement, boundary conditions and the size of relaxation zones. Additionally, the mooring line model used in the numerical simulations was based on a simple spring model, instead of fully modeling the catenary behavior of the true moorings. When using the ESI branch of OpenFOAM, stability issues were found when implementing more than one mooring line at a time. In wave simulations performed with the ESI branch of OpenFOAM, mooring lines were not included in simulations. Most notably, the method for FSI coupling is of crucial importance to accurately predicting the motion of the body.

Finally, sources of discrepancy can be attributed to various components of the experimental tank tests. In the tank tests, the free decay tests were performed by an experimentalist in a boat hitting the floating body with a stick. The presence of the boat produces disturbances in the water that interact with the body. Furthermore, the use of a stick for displacing the structure from its zero-position produces offsets

in multiple DOFs instead of just the DOF of interest. Additionally, the tower of the wind turbine was attached to a cantilevered dock by sensor cables. These sensor cables provide additionally spring stiffness and damping to the system, on top of the installed mooring lines.

10.8 Summary and Conclusions

Here, simulations of pitch and heave free decay tests of the semisubmersible were carried out using the navalFoam solver which employs loose coupling. The CFD predictions showed good agreement with experimental data for the pitch free decay tests. However, the heave free decay simulations did not agree well with experimental measurements, where the CFD showed a reamplification of the heave motion at late times and a lack of overall damping. Some of the disagreement can be attributed to physical, numerical and experimental discrepancies, as discussed in the previous sections. However, the largest impact on the accurate prediction of body motion is the choice of FSI coupling method.

A simplified two-dimensional case of a heaving squared barge was performed, where the refinement, domain length and relaxation zones were each augmented. In each of these simulations the barge came to rest above the theoretical position of equilibrium. It was found that despite the numerical stability of navalFoam, through its implicit nature and under-relaxation, the predictions for motion can be incorrect. This is due to the loose coupling of the fluid and structure solutions. The same case was simulated with a tightly coupled solver, relaxationDyMFoam, where the barge was seen to oscillate symmetrically about the theoretical equilibrium position with increased damping over time.

A simulation of the semisubmersible in regular waves was also carried out with navalFoam, and while the frequency and magnitude of oscillation matched well with predictions from FAST, the position about which the body oscillated was incorrect.

The heave DoF oscillated about a position above its true point of hydrostatic equilibrium, just as was observed in the two-dimensional barge heave decay simulations. Next, regular waves were simulated with relaxWaveFoam, the tightly-coupled solver linked with the wave library, and the hydrostatic equilibrium issues seen with navalFoam were not present. The magnitude and frequency of the motions matched well with predictions from FAST, however, a positive bias in the surge motion was found. The results from FAST, shown in Figure 10.15, exhibit a slow frequency motion where the surge displacement increases during the roughly the first 75 s of the simulated time. It may be that the predictions from relaxWaveFoam are also capturing this initial increase in surge displacement, due to start up transients, resulting in what appears to be a positive bias.

Finally, an irregular wave was simulated interacting with the semisubmersible, and motion and load predictions were presented. Irregular wave simulations require very long run times due to the stochastic nature of the waves. Predictions from CFD were not compared to FAST for these cases because long run times have not yet been achieved, which would be necessary to determine the statistical properties for comparison. Nonetheless, this work demonstrates the capability of relaxWaveFoam in simulating irregular waves interacting with a floating body with 6 DoFs.

The work presented here shows that the method of FSI coupling is of utmost importance. To accurately capture the free decay motion of the semisubmersible a tightly coupled solver is necessary. The future work will continue to simulate the free decay motion of the semisubmersible, as well as motion in waves, with the tightly coupled solver.

CHAPTER 11

CONCLUSIONS AND FUTURE WORK

This dissertation presents investigations of hydrodynamic loads on structures with various geometric complexities in a variety of environmental conditions, following a thorough validation of the CFD methodologies. The high-fidelity CFD results provide detailed insight about flow interacting with complex geometries on top of what can be attained through experimental and field measurements, and which may be neglected by the assumptions and approximations of reduced order models. The predictions generated in this dissertation describe the underlying physics of flow around complex surface-piercing geometries of limit draft. The effects of geometric factors and environmental conditions were explored through investigations of surface-piercing finite cylinders in uniform flow, and the semisubmersible platform for offshore floating wind turbines in steady current and waves. The CFD results provide suggestions for improving the accuracy of reduced order modeling tools, and supplement experimental measurements by supplying detailed hydrodynamic load predictions. The contributions of this thesis are summarized here, followed by a brief description of the future direction of this work.

11.1   Contributions to Knowledge

1. Surface-piercing cylinders with free ends

CFD simulations of uniform flow past vertical, surface-piercing, truncated cylinders of varying lengths were performed. The numerical load predictions were com-

pared against experimental measurements from the FSI lab at UMass. The work found a sharp drop in the drag coefficient for cylinders with aspect ratio equal to 2. Additionally, the Strouhal number was found to decrease with the aspect ratio, such that below an aspect ratio of 3 vortices were not observed. Finally, sectional loads from CFD simulations were presented, describing the variation in vortex shedding along the cylinder length, with dependency on proximity to the free-surface and to the free-end.

This is the first time this wide of a range of aspect ratios has been studied for cylinders which both pierce a free-surface and have a free-end. Furthermore, this work uniquely provides both experimental measurements and numerical simulations at exactly the same flow conditions and cylinder depths. The work demonstrates that the aspect ratio and free surface had large effects of the magnitude and frequency of loads on the cylinder. Due to the findings of this thesis, it is suggested that these factors be considered when designing floating offshore structures with similar geometric factors, specifically when selecting drag coefficients for input to CAE tools.

2. Stationary semisubmersible in steady current

A stationary semisubmersible platform for offshore floating wind turbines was simulated in steady current conditions. CFD load predictions were compared against results from HydroDyn, and code-to-code discrepancies were examined with high-fidelity CFD flow field visualizations. The effects of geometric factors, including limited draft, multimember arrangements, and surface piercing members, were investigated through member-level load predictions from CFD. CFD predictions found drag coefficients for the semisubmersible far below the values for infinitely long, fully-submerged cylinders at the same Re. Furthermore, it was found that the loads varied in terms of draft, and between upstream and downstream members.

Before now, standard practice in the offshore wind design community was to select drag coefficients from look-up tables for infinitely long, fully submerged cylinders. This work demonstrates that more careful selection of coefficients is necessary and prudent. The effects of geometric complexities on the loading of the semisubmersible had not been previously investigated, nor explained through visualizations of the flow physics. The findings of this part of the thesis suggests that CFD simulations be performed to provide more accurate drag coefficients for input to CAE tools. Furthermore, it is suggested that drag coefficients be assigned on a member level basis, to properly capture shadowing effects, as well as depth-dependent loads.

3. Stationary semisubmersible in regular waves

Next, the stationary semisubmersible platform was simulated in regular waves. Whereas the steady current simulations provided an opportunity to assess load predictions based on Morison's equation, these cases introduce diffraction which in CAE tools is often modeled with potential flow theory. Load predictions from CFD simulations were compared against results from FAST, and must better agreement was found than had been seen in the steady current simulations. In these regular wave cases the contribution to loads from Morison's equation is nearly negligible, such that the excellent code-to-code agreement indicated that the potential flow theory of HydroDyn performs well for regular waves.

While FAST has been thoroughly verified and validated for land-based wind turbines, this work provided new verification for the hydrodynamics of floating offshore wind turbines. The work demonstrates that regular wave loads are well predicted by the existing model equations in HydroDyn.

4. Loads on slanted cylinders

CFD simulations of loads on slanted cylinders of varying angles of orientation in uniform were carried out. This work was performed to assess the way in which HydroDyn calculates loads only in the normal direction to members. The dimensions and orientations of the slanted cylinders were selected such that they matched those of the cross braces of the semisubmersible platform. Four yaw orientations of the slanted cylinder with a pitch angle matching the cross braces were studied. The drag coefficient was found to vary depending on the yaw orientation, as well as length along the cylinder.

This is the first time slanted cylinders of differing yaw orientations have been studied with CFD. The results show that orientation of the cylinder relative to the flow direction does have an impact on the loading. Furthermore, the conditions at either end of the cylinders were found to affect the loads. The results of this portion of the thesis suggest that variable drag coefficients be assigned along the length of a cylinder, and to consider the orientation of the body relative to the flow.

5. Motion of the semisubmersible

Finally, motion of the semisubmersible platform was simulated with 6 DoF solvers in both free decay tests and waves. A loosely-coupled fluid-structure interaction (FSI) solver predicted motions of the semisubmersible in pitch free decay tests which agreed well with experimental measurements. However, poor agreement was found for the case of heave decay motion of the semisubmersible when the loosely-coupled solver was employed. Further testing revealed that while the loosely-coupled solver could provide stable simulations due to its implicit nature for the fluid solution, it returned poor predictions for motion, whereas a tightly-coupled solver produced accurate motion predictions. The loosely-coupled FSI solver was also used to simulate the semisubmersible in regular waves, and again, the motion predictions came out poorly. Wave simulations carried out with the tightly-coupled solver gave better

motion predictions, which did not include issues with the hydrostatic equilibrium position. Additionally, this work demonstrated the capability of simulating irregular waves interacting with the semisubmersible. This work demonstrates that a stable FSI solver is a necessary but not sufficient requirement for achieving accurate motion predictions of a floating body.

Before now, the open-source CFD toolbox OpenFOAM has not been used to simulate free decay tests of the semisubmersible which include a mooring line model, nor have the CFD predictions been compared against experimental data. The work presented in this thesis provides the first steps towards providing the supplemental force data which is missing from DeepCWind tank tests. Further FSI simulations of the semisubmersible in free decay tests and waves will be performed to further supplement the test data, and provide the missing component to a three-way comparison between CFD, CAE tools and experimental measurements.

11.2 Future Work

Future work will continue to simulate the semisubmersible in free decay tests using the tightly-coupled FSI method. Additionally, simulations of the semisubmersible in regular and irregular waves will be performed to reach longer simulated times, also with the tightly-coupled solver. These CFD methods can continue to better inform experimental measurements, provide higher fidelity results than reduced-order engineering tools and recommend improvements to these models which contain various assumptions and approximations. Moreover, high-fidelity CFD simulations can substantially improve the accuracy of breaking wave load predictions on offshore structures, including breaking wave limit criteria and slamming coefficient formulations. CFD can also generate results beyond what has been measured experimentally in wave tanks or the ocean, including investigation of loads and motion in extreme conditions and also simulations at full scale. The CFD toolboxes that were gathered and

thoroughly validated in this work can be extended to address other novel applications beyond offshore wind energy, such as wave and tidal energy technologies, as well as an assortment of other offshore engineering applications.

BIBLIOGRAPHY

[1] *National Meteorological Library and Archive Fact sheet 6.* Met Office, 2010.

[2] Achenbach, E. Distribution of local pressure and skin friction around a circular cylinder in cross-flow up to Re 5e6. *J. Fluid Mechanics 34* (1968), 625–639.

[3] Achenbach, E., and Heinecke, E. On vortex shedding from smooth and rough cylinders in the range of reynolds numbers $6x10^3$ to $5x10^6$. *Journal of Fluid Mechanics 109* (1981), 239–251.

[4] Adalsteinsson D., Sethian J.A. A fast level set method for propagating interfaces. *Journal of Comp. Phys. 118* (1995), 269–277.

[5] Adaramola, M.S., Akinlade, O.J., Sumner, D., Bergstrom, D.J., and Schenstead, A.J. Turbulent wake of a finite circular cylinder of small aspect ratio. *Journal of Fluids and Structures 22* (2006), 919–928.

[6] Afgan, I., Moulinec, C., and Laurence, D. Large eddy simulation of flow over a vertically mounted finite cylinder on a flat plate. In *The 13th International Conference on Fluid Flow Technologies, Conference on Modelling Fluid Flow (CMFF06)* (Budapest, Hungary, 2006).

[7] Agarwal, P., and Manuel, L. On the Modeling of Nonlinear Waves for Prediction of Long-Term Offshore Wind Turbine Loads. *Journal of Offshore Mechanics and Arctic Engineering 131* (2009).

[8] Agarwal, P., and Manuel, L. Incorporating irregular nonlinear waves in coupled simulation and reliability studies of offshorewindturbines. *Applied Ocean Research 33* (2011), 215–227.

[9] Ahn, Hyung Taek, and Shashkov, Mikhail. Adaptive moment-of-fluid method. *Journal of Computational Physics 228* (2009), 2792–2821.

[10] Akilli, H., and Rockwell, D. Vortex formation from a cylinder in shallow water. *Physics of Fluids 14* (2000), 2957–2967.

[11] Apel, John R. *Principles of Ocean Physics.* Academic Press, New York, 1987.

[12] Beyer, F., Arnold, M., and Cheng, P.W. Analysis of Floating Offshore Wind Turbine Hydrodynamics Using coupled CFD and Multibody Methods . In *Proceedings of the Twenty-third (2013) International Offshore and Polar Engineering* (Anchorage, Alaska, 2013).

[13] Blevins, R.D. *Flow-Induced Vibration.* Van Nostrand Reinhold, 1990.

[14] Blom, F.J. Considerations on the spring analogy. *International Journal for Numerical Methods in Fluids 32* (2000), 647–668.

[15] Bourlioux, A. A coupled level-set volume-of-fluid algorithm for tracking material interfaces. In *Sixth International Symposium on Computational Fluid Dynamics* (Lake Tahoe, CA, 1995).

[16] Bredmose, H., and Jacobsen, N.G. Breaking Wave Impacts on Offshore Wind Turbine Foundations: Focused Wave Groups and CFD. In *ASME 2010 29th International Conference on Ocean, Offshore and Arctic Engineering* (Shanghai, China, 2010).

[17] Bredmose, H., and Jacobsen, N.G. Vertical Wave Impacts on Offshore Wind Turbine Inspection Platforms. In *Proceedings of the ASME 2011 30th International Conference on Ocean, Offshore and Arctic Engineering* (Rotterdam, the Netherlands, 2011).

[18] Bredmose, H., Skourup, J., Hansen, E.A., Christensen, E.D., Pedersen, L.M., and Mitzlaff, A. Numerical Reproduction of Extreme Wave Loads on a Gravity Wind Turbine Foundation. In *25th International Conference on Offshore Mechanics and Arctic Engineering* (Hamburg, Germany, 2006).

[19] Breuer, M. A challenging test case for large eddy simulation: high Reynolds number circular cylinder flow. *International Journal of Heat and Fluid Flow 21* (2000), 648–654.

[20] Brewer, M., Diachin, L.F., Knupp, P., Leurent, T., and Melander, D. The Mesquite Mesh Quality Improvement Toolkit. Tech. rep., Technical Report, Sandia National Laboratories, 2003.

[21] Bunnik, Tim, and Huijsmans, René. Identification of Quadratic Responses of Floating Structures in Waves. In *ISOPE Conference* (San Francisco, 2006), pp. 1–8.

[22] Castiglione, T., Stern, F., Bova, S., and Kandasamy, M. Numerical investigation of the seakeeping behavior of a catamaran advancing in regular head waves. *Ocean Engineering 38* (2011), 1806–1822.

[23] Catalano, P., Wang, M., Iaccarin, G., and Moin, P. Numerical simulation of the flow around a circular cylinder at high Reynolds numbers. *International Journal of Heat and Flow 24* (2003), 463–469.

[24] Causin, P., Gerbeau J.F. Nobile F. Added-mass effect in the design of partitioned algorithms for fluidstructure problems. *Computer Methods in Applied Mechanics and Engineering 194* (2005), 4506–4527.

255

[25] Cermelli, Christian, Roddier, Dominique, and Aubault, Alexia. Windfloat: A floating foundation for offshore wind turbines, Part II: Hydrodynamics Analysis. In *Proceedings of the ASME 28th International Conference on Ocean, Offshore and Artic Engineering* (Honolulu, Hawaii, 2009).

[26] Chakrabarti, Subrata K. *Handbook of Offshore Engineering.* Elsevier, Boston, 2005.

[27] Chaplin, J.R., and Teigen, P. Steady flow past a vertical surface-piercing circular cylinder. *Journal of Fluids and Structures 18* (2003), 271 – 285.

[28] Cheng, P.W. *A Reliability Based Design Methodology for Extreme Responses of Offshore Wind Turbines.* Dissertation, University of Technology, Delft, 2002.

[29] Christensen, E.D., Bredmose, H., and E.A., Hansen. Extreme wave forces and wave run-up on offshore wind turbine foundations. In *Proceedings of Copenhagen Offshore Wind* (Copenhagen, 2005).

[30] Christensen, E.D., Lohmann, I.P., Hansen, H.F., Haerens, P., Merclis, P., and Demuynck, A. Irregular Wave Loads on a Gravity Based Foundation in Shallow Water. In *ASME 2011 30th International Conference on Ocean, Offshore and Arctic Engineering* (Rotterdam, the Netherlands, 2011).

[31] Cordle, A., and Jonkman, J. State of the Art in Floating Wind Turbine Design Tools. In *Proceedings of the Twenty-first (2011) International Offshore and Polar Engineering Conference* (Maui, Hawaii, 2011).

[32] Coward, Adrian V., Renardy, Yuriko Y., Renardy, Michael, and Richards, John R. Temporal Evolution of Periodic Disturbances in Two-Layer Couette Flow. *Journal of Computational Physics 132* (1997), 346–361.

[33] Crapper, G.D. *Introduction to Water Waves.* Ellis Horwood Limited, New York, 1984.

[34] de Ridder, E.J., Koop, A.H., and van Doeveren, A.G. DeepCWind Floating Wind Turbine Model Tests. *Report No. 24602-1-OB* (2011).

[35] de Sousa, F.S., Mangiavacchi, N., Nonato, L.G., Castelo, A., Tom, M.F., Ferreira, V.G., Cuminato, J.A., and McKee, S. A front-tracking/front-capturing method for the simulation of 3d multi-fluid flows with free surfaces. *Journal of Computational Physics 198*, 2 (2004), 469–499.

[36] Dean, Robert G., and Dalrymple, Robert A. *Water Wave Mechanics for Engineers and Scientists.* WIT Press, Englewood Cliffs, NJ, 1984.

[37] DeBar, R. Fundamentals of the KRAKEN code. *Technical Report, Lawrence Livermore National Lab UCIR-760* (1974).

[38] Delany, K., and Sorenson, E. Low-speed drag of cylinders of various shapes. *Nat. Adv. Comm. Aero. 3038* (1953).

[39] Demirdzic, I., and Peric, M. Space Conservation law in Finite Volume Calculations of Fluid Flow. *International Journal for Numerical Methods in Fluids 8* (1988), 1037 – 1050.

[40] Detter, W., and Peric, D. A computational framework for fluidstructure interaction: finite element formulation and application. *Comput. Methods Appl. Mech. Engrg. 195* (2006), 5754–5779.

[41] Detter, W., and Peric, D. A fully implicit computational strategy for strongly coupled fluid solid interaction. *Arch. Comput. Methods Engrg. 14* (2007), 205–247.

[42] Dunbar, A.J., Craven, B.A., and Paterson, E.G. Development and validation of a tightly coupled CFD/6-DOF solver for simulating floating offshore wind turbine platforms. *Ocean Engineering 110* (2015), 98–105.

[43] Dyadechoko, V., and Shashkov, M. Moment-of-fluid interface reconstruction. *Tech. Rep. Los Alamos National Laboratory* (October 2003).

[44] Eecen, P.J. *Wind Waves: Forces Due to Waves on Offshore Wind Turbines.* Springer, The Netherlands: Energy Research Centre of The Netherlands, 2003.

[45] Enright, D., Fedkiw, R., Ferziger, J., and Mitchell, I. A hybrid particle level set method for improved interface captuing. *Journal of Computational Physics 183* (2002).

[46] Esmaeeli, A., and Tryggvason, G. An inverse energy cascade in two-dimensional low Reynolds number bubbly flows. *Journal of Fluid Mechanics Digital Archive 314*, 1 (1996), 315–330.

[47] Esmaeeli, A., and Tryggvason, G. Direct numerical simulations of bubbly flows. Part 1. Low Reynolds number arrays. *Journal of Fluid Mechanics 377* (1998), 313–345.

[48] Faizal, Mohammed, Ahmed, M. Rafiuddin, and Lee, Young-Ho. On utilizing the orbital motion in water waves to drive a savonius rotor. *Renewable Energy 35*, 1 (2010), 164 – 169.

[49] Faltinsen, O.M., Kjaerland, O., Nø ttveit, O., and Vinje, T. Water impact loads and dynamics response of horizontal circular cylinders in offshore structures. In *Proceedings of the Offshore Technology Conference, OTC 2741* (Houston, TX, 1977).

[50] Farhat, C., Lesoinne, M., and LeTallec, P. Load and motion transfer algorithms for fluid/structure interaction problems with non-matching discrete interfaces. *Comp. Meth. App. Mech. and Eng. 157* (1998), 95–114.

[51] Farivar, D.J. The near-wake structure of a cantilevered cylinder in a cross-flow. *Z Flugwiss 24* (1981), 77–82.

[52] Fekken, G., Veldman, A.E.P., and Buchner, B. Simulation of Green Water Flow Using the Navier-Stokes Equations. In *Seventh International Conference on Numerical Ship Hydromechanics* (Nantes, 1999).

[53] Ferziger, J.H., and Peric, M. *Computational Methods for Fluid Dynamics.* Springer, 1999.

[54] Förster, Christiane, Wall, Wolfgang, and Ramm, Ekkehard. Added mass instabilities in sequential staggered coupling of nonlinear structures and incompressible viscous flows. *Computers Methods in Applied Mechanics and Engineering 196* (2007), 1278–1293.

[55] Fox, T.A., and West, G.S. Fluid-induced loading of cantilevered circular cylinders in a low-turbulence uniform flow. Part 1: Mean loading with aspect ratios in the range of 4 to 30. *Journal of Fluids and Structures 7* (1993), 1–14.

[56] Frohlich, J., and Rodi, W. LES of the flow around a circular cylinder of finite height. *J. Heat and Fluid Flow 25* (2004), 537–548.

[57] Fulton, G.R., Malcolm, D.J., and Moroz, E. Design of a Semi-Submersible Platform for a 5MW Wind Turbine. In *44th AIAA Aerospace Sciences Meeting and Exhibit* (Reston, VA, 2006).

[58] Fung, Y.C. Fluctuating Lift and Drag Acting on a Cylinder in a Flow at Supercritical Reynolds Numbers. *Journal of the Aerospace Sciences 27* (1960).

[59] Gee, M.W., Küttler, U., and Wall, W.A. Truly monolithic algebraic multigrid for fluid structure interaction. *Int. J. Numer. Meth. Eng. 85* (2011), 987–1016.

[60] Gerrits, J., and Veldman, A.E.P. Dynamics of liquid-filled spacecraft. *Journal of Engineering Mechanics 45* (2003), 21–38.

[61] Gilmanov, A., and Sotiropoulos, F. A hybrid Cartesian/immersed boundary method for simulating flows with 3D, geometrically complex, moving bodies. *Journal of Computational Physics 207* (2005), 457–492.

[62] Glimm, J., Graham, M.J., Grove, J., Li, X.L., Smith, T.M., Tan, D., Tangerman, F., and Zhang, Q. Front tracking in two and three dimensions. *Computers and Mathematics with Applications 35*, 7 (1998), 1–11.

[63] Glimm, J., McBryan, O., Menikoff, R., and Sharp, D.H. Front tracking applied to Rayleigh-Taylor Instability. *SIAM Journal on Scientific and Statistical Computing 7*, 1 (1986), 230–251.

[64] Goncalves, R.T., Franzini, G.R., Rosetti, G.F., Meneghini, J.R, and Fujarra, A.L.C. Flow around circular cylinders with very low aspect ratio. *Journal of Fluids and Structures* (2014).

[65] Greenshields, C.J., and Weller, H.G. A unified formulation for continuum mechanics applied to fluid-structure interaction in flexible tubes. *Int. J. Numer. Meth. Eng. 64* (2005), 1575–1593.

[66] Grigoriadis, D.G.E., Sarris, I.E., and Kassinos, S.C. MHD flow past a circular cylinder using the immersed boundary method. *Computers and Fluids 39* (2010), 345–358.

[67] Gueydon, S., and Weller, S. Study of a floating foundation for wind turbines. In *OMAE ASME 31st International Conference on Ocean, Offshore and Arctic Engineering* (Rio de Janeiro, Brazil, 2012).

[68] Habchi, C., Russeil, S., Bougeard, B., Harion, J., Lemenand, T., Ghanem, A., Della Valle, D., and Peerhossaini, H. Partitioned solver for strongly coupled fluidstructure interaction. *Computers and Fluids 71* (2013), 306–319.

[69] Hadzic, I., Hennig, J., Peric, M., and Xing-Kaeding, Y. Computation of flow-induced motion of floating bodies. *Applied Mathematical Modelling 29* (2005), 1196–1210.

[70] Harlow, F.H., and Welch, J.E. Numerical calculation of time-dependent viscous incompressible flow of fluid with free surface. *Physics of Fluids 8*, 12 (1965), 2182–2189.

[71] Hasselman, K. Measurement of wind-wave growth and sweel decay during the Joint North Sea Wave Project (JONSWAP). *Dtsch. Hydrogr. Inst, Hamburg* (1973).

[72] Hay, A.D. Flow about semi-submerged cylinders of finite length, 1947.

[73] Heil, M. An efficient solver for the fully coupled solution of large-displacement fluidstructure interaction problems. *Computers and Fluids 193* (2004), 1–23.

[74] Hogben, N., and Standing, R.G. Experience in computing wave loads on large bodies. *Offshore Tech. Conf., Houston* (1975), 2189.

[75] Hu, C., and Kashiwagi, M. Two-dimensional numerical simulation and experiment on strongly nonlinear wave-body interactions. *Journal of Marine Science and Technology 14* (2009), 200–213.

[76] Hübner, B., Walhorn, E., and D., Dinkler. A monolithic approach to fluidstructure interaction using space time finite elements. *Comput. Methods Appl. 193* (2004), 2087–2104.

[77] Ilinca, F., and Hetu, J.F. A finite element immersed boundary method for fluid flow around rigid objects. *International Journal for Numerical Methods in Fluids* (2010).

[78] Inoue, M., Baba, N., and Himeno, Y. Experimental and Numerical Study of Viscous Flow Field Around an Advancing Vertical Circular Cylinder Piercing Free-Surface. *J Kansai Soc Naval Arch 220* (1993), 57–65.

[79] Iungo, G.V., Pii, L.M., and Buresti, G. Experimental investigation on the aerodynamic loads and wake flow features of a low aspect-ratio circular cylinder. *Fluids Struct. 28* (2003), 279–291.

[80] Jacobsen, Niels G., Fuhrman, David R., and Fredsøe, Jørgen. A wave generation toolbox for the open-source CFD library : OpenFoam. *International Journal for Numerical Methods in Fluids* (2011).

[81] James, W.D., Paris, S.W., and Malcolm, G.V. Study of viscous cross flow effects on circular cylinders at high Reynolds numbers. *AIAA Journal 18* (1980), 1066–72.

[82] Jaouen, F., Koop, A., and Vaz, G. Predicting Roll Added Mass and Damping of a Ship Hull Section Using CFD. In *ASME 2011 30th International Conference on Ocean, Offshore and Arctic Engineering* (Rotterdamn, the Netherlands, 2011).

[83] Jasak, H. Dynamic Mesh Handling in OpenFOAM. In *47th AIAA Aerospace Sciences Meeting* (Orlando, Florida, 2009).

[84] Jasak, H., Rusche, H., and Christ, D. The Naval Hydro Pack and its Application in the Simulation of Ship Hydrodynamics.

[85] Jasak, H., and Tukovic, Z. Automatic mesh motion for the unstructured finite volume method. *Journal of Computational Physics 42* (2004), 1 – 30.

[86] Jasak, H., and Tukovic, Z. Dynamic mesh handling in OpenFOAM applied to fluid-structure interaction simulations.

[87] Jeffreys, H. On The Formation of Waves by Wind. *Proc. Roy. Soc. London Ser. A 107* (1924), 189–206.

[88] Jeffreys, H. On The Formation of Waves by Wind II. *Proc. Roy. Soc. London Ser. A 110* (1925), 341–347.

[89] Johannessen, T.B., Haver, S., Bunnik, T., and Buchner, B. Extreme Wave Effects on Deep Water TLPs : Lessons Learned from the Snorre A Model Tests. In *DOT Conference* (Houston, 2006).

[90] Jonkman, J. Dynamics of offshore floating wind turbines - model development and verification. *Wind Energy 12* (2009), 459–492.

[91] Jonkman, J., and Buhl, M. L. FAST User's Guide, 2006.

[92] Jonkman, J., and Jonkman, B. NWTC Computer-Aided Engineering Tools (FAST (Modularization Framework), Last modified 25-October-2013; accessed 30-January-2014.

[93] Jonkman, J., Larsen, T., Hansen, A., Nygaard, T., Maus, K., Karimirad, M., Gao, Z., Moan, T., Fylling, I., Nichols, J., Kohlmeier, M., Pascual Vergara, J., Merino, D., Shi, W., and Park, H. Offshore Code Comparison Collaboration with IEA Wind Tank 23: Phase IV Results Regarding Floating Wind Turbine Modeling. In *European Wind Energy Conference (EWEC)* (Warsaw, Poland, 2010).

[94] Jonkman, J., and Matha, D. Dynamics of offshore floating wind turbines analysis of three concepts. *Wind Energy 14* (2011), 557–569.

[95] Jonkman, J.M. *Dynamics Modeling and Loads Analysis of an Offshore Floating Wind Turbine* . Dissertation, University of Colorado, 2007.

[96] Jordan, S.A. Transition to turbulence in the separated shear layers of yawed circular cylinders. *Journal of Heat and Fluid Flow 31* (2010), 489–498.

[97] Jung, Kwang Hyo, Chang, Kuang-an, and Jo, Hyo Jae. Viscous Effect on the Roll Motion of a Rectangular Structure. *Journal of Engineering Mechanics*, February (2006).

[98] Juric, D., and Tryggvason, G. Computation of boiling flows. *International Journal of Multiphase Flow 24*, 3 (1998), 387–410.

[99] Kallinderis, Y., and Ahn, H.T. Incompressible Navier-Stokes method with general hybrid meshes. *Journal of Computational Physics 210* (2005), 75–108.

[100] Kamath, A., Bihs, H., and Artsen, A. Calculation of Wave Forces on Cylindrical Piles Using a 3D Numerical Wave Tank. In *ASME 2013 32nd International Conference on Ocean, Offshore and Arctic Engineering* (Nantes, France, 2013).

[101] Karimirad, M., Meissonnier, Q., Gao, Z., and Moan, T. Hydroelastic code-to-code comparison for a tension leg spar-type floating wind turbine. *Marine Structures 24* (2011), 412.

[102] Karimirad, Madjid, and Moan, Torgeir. Wave- and Wind-Induced Dynamic Response of a Spar-Type Offshore Wind Turbine. *Journal of Waterway, Port, Coastal and Ocean Engineering 138* (2011), 9–20.

[103] Kassiotis, C., Ibrahimbegovic, A., Niekamp, R., and Matthies, H.G. Nonlinear fluidstructure interaction problem. Part I: Implicit partitioned algorithm, nonlinear stability proof and validation examples. *Comput. Mech. 47* (2011), 305–323.

[104] Kawamura, T., Hiwada, M., Hibino, T., Mabuchi, I., and Kumada, M. Flow around a Finite Circular Cylinder on a Flat Plate. *Bulletin of JSME 27* (1984), 2142–2151.

[105] Kawamura, T., Mayer, S., Garapon, A., and Srensen, L. Large eddy simulation of a flow past free surface piercing circular cylinder. *ASME Journal of Fluids Engineering 124* (2002), 91 –101.

[106] Kim, J.W., Magee, A., and Guan, K.Y.H. CFD Simulation of Flow-Induced Motions of a Multi-Column Floating Platform. In *ASME 2011 30th International Conference on Ocean, Offshore and Arctic Engineering* (Rotterdam, the Netherlands, 2011).

[107] Kim, K.J., and Durbin, P.A. Observations of the frequencies in a sphere wake and drag increase by acoustic excitation. *Physics of Fluids 31* (1988), 3260–3265.

[108] King, S. Vortex excited oscillations of yawed circular cylinders. *ASME Journal of Fluids Engineering 99* (1977), 495–502.

[109] Kleefsman, K.M.T., Fekken, G., Veldman, A.E.P., Iwanowski, B., and Buchner, B. A Volume-of-Fluid based simulation method for wave impact problems. *Journal of Computational Physics 206*, 1 (June 2005), 363–393.

[110] Kleinman, Ralph E. On The Mathematical Theory of the Motion of Floating Bodies - An Update. *Ship Performance Department, Research and Development Report* (1982).

[111] Koop, A., and Bereznitski, A. Model-Scale And Full-Scale CFD Calculations For Current Loads On Semi-Submersible. In *30th International Conference on Ocean, Offshore and Arctic Engineering (OMAE)* (Rotterdamn, the Netherlands, 2011).

[112] Korteweg, D.J., and de Vries, G. On the Change of Form of Long Waves Advancing in a Rectangular Canal, and on a New Type of Long Stationary Waves. *Philosophical Magazine 240* (1895), 422–443.

[113] Kothe, Douglas B., and Rider, William J. Practical Considerations for Interface Tracking Methods. In *6th ISCFD* (1995).

[114] Kovasznay, L.S.G. Hot-Wire Investigation of the Wake Behind Cylinders at Low Reynolds Numbers. *Proc. Roy. Roc. 198* (1949), 174.

[115] Krajnovic, S. Flow around a tall finite cylinder explored by large eddy simulation. *J. Fluid Mech. 676* (2011), 294–317.

[116] Küttler, U., and Wall, W.A. Fixed-point fluid-structure interaction solvers with dynamic relaxation. *Comput. Mech. 43* (2008), 61–72.

[117] Lam, K., Lin, Y.F., Zou, L., and Liu, Y. Investigation of turbulent flow past a yawed wavy cylinder. *Journal of Fluids and Structures 26* (2010), 1078–1097.

[118] Lamb, Horace. *Hydrodynamics.* CJ Clay and Sons, Cambridge, 1895.

[119] Lara, J., Higuera, P., Guanche, R., and Losada, I.J. Wave Interaction With Piled Structures: Application With IH-FOAM. In *ASME 2013 32nd International Conference on Ocean, Offshore and Arctic Engineering* (Nantes, France, 2013).

[120] Le Méhauté, B. *An Introduction to Hydrodynamics and Water Waves.* Springer-Verlag, 1976.

[121] Lee, C.H. *WAMIT Theory Manual*, 95-2 ed. Dept. of Ocean Eng. MIT, 1995.

[122] Lee, T., Lin, C.L., and Friehe, C.A. Large-eddy simulation of air flow around a wall-mounted circular cylinder and a tripod tower. *J. Turbul. 29* (2007), 1–28.

[123] Lefevre, C., Constantinides, Y., Kim, H.W., Henneke, M, Gordon, R., Jang, H., and Wu, G. Guidelines for CFD Simulations of Spar VIM. In *ASME 2013 32nd International Conference on Ocean, Offshore and Arctic Engineering* (Nantes, France, 2013).

[124] Levi Civita, T. Determination regoureuse des ondes permanentes d'ampleur finie. *Math. Ann. 93* (1925), 264–314.

[125] Liang, C., and Papadakis, G. Large eddy simulation of pulsating flow over a circular cylinder at subcritical Reynolds number. *Computers and Fluids 36* (2007), 299–312.

[126] Longuet-Higgins, M.S. On wave breaking and equilibrium spectrum of wind-generated waves. *Proc. Roy. Soc. London Ser. A 310* (1969), 151–159.

[127] Luo, S.C., Gan, T.L., and Chew, Y.T. Flow around a Finite Circular Cylinder on a Flat Plate. *J. Wind. Eng. Ind. Aerodyn 59* (1996), 69–93.

[128] Lysenko, D.A., Ertesvag, I.S., and Rian, K.E. Modeling of turbulent separated flows using OpenFOAM. *Computers and Fluids 80* (2013), 408–422.

[129] Majumdar, S., and Rodi, W. Three-dimensional computation of flow past cylindrical structures and model cooling towers. *Build. Environ. 24* (1989), 3–22.

[130] Maki, Kevin. Ship Resistance Simulations with OpenFOAM. In *6th OpenFOAM Workshop* (State College, June 2011), pp. 1–22.

[131] Malan, A.G., and Oxtoby, O.F. A matrix-free, implicit, incompressible fractional-step algorithm for fluidstructure interaction applications. *J. Comput. Phys. 231* (2012), 5389–5405.

[132] Malan, A.G., and Oxtoby, O.F. An accelerated, fully-coupled, parallel 3D hybrid finite-volume fluidstructure interaction scheme. *Computer Methods in Applied Mechanics and Engineering 253* (2013), 426–438.

[133] Marella, S., Krishnan, S., Liu, H., and Udaykumar, H.S. Sharp Interface Cartesian Grid Method I: An easily implemented technique for 3D moving boundary computations. *Journal of Computational Physics 210* (2005), 1–31.

[134] Matthies, H., Niekamp, R., and Steindorf, J. Algorithms for strong coupling procedures. *Computer Methods in Applied Mechanics and Engineering 195* (2006), 2028–2049.

[135] Matthies, H.G., and Steindorf, J. Partitioned but strongly coupled iteration schemes for nonlinear fluidstructure interaction. *Comput. Struct 80* (2002), 1991–1999.

[136] Mei, C.C. Numerical Methods in Water-Wave Diffraction and Radiation. *Annual Review of Fluid Mechanics 10*, 1 (Jan. 1978), 393–416.

[137] Mei, Chiang. *The Applied Dynamics of Ocean Surface Waves*. John Wiley and Sons, New York, 1982.

[138] Mercier, J.A. *Large Amplitude Oscillations of a Circular Cylinder in a Low-Speed Stream*. Dissertation, Stevens Institute of Technology, 1973.

[139] Michel, J.H. The highest waves in water. *Philosophical Magazine 36* (1893), 430–437.

[140] Miles, J.W. On the Generation of Surface Waves by Shear Flows. *Journal of Fluid Mechanics 3* (1957), 185–204.

[141] Miles, J.W. On the Generation of Surface Waves by Shear Flows Part 2. *Journal of Fluid Mechanics 6* (1959), 568–582.

[142] Miles, J.W. On the Generation of Surface Waves by Shear Flows Part 3. *Journal of Fluid Mechanics 6* (1959), 583–598.

[143] Miles, J.W. On the Generation of Surface Waves by Shear Flows Part 4. *Journal of Fluid Mechanics 13* (1962), 433–448.

[144] Miles, J.W. Solitary Waves. *Annual Review of Fluid Mechanics 12*, 1 (Jan. 1980), 11–43.

[145] Miller, A., Chang, B., Issa, R., and Chen, G. Review of computer-aided numerical simulation in wind energy. *Renewable and Sustainable Energy Reviews 25* (2013), 122–134.

[146] Miller, B.L. The hydrodynamic drag of roughened circular cylinders. *J. R. Inst. Nav. Arch. 119* (1977), 55–70.

[147] Minkenberg, H.L., and Gie, Tan Seng. Will the "Regular Wave Concept" Yield Meaningful Motion Predictions for Offshore structures ? In *Offshore Technology Conference* (Dallas, 1974).

[148] Mittal, R., and Iaccarino, G. Immersed Boundary Methods. *Annual Review of Fluid Mechanics 37* (2005), 239–261.

[149] Mok, D.P., and Wall, W.A. Partitioned analysis schemes for the transient interaction of incompressible flows and nonlinear flexible structures. In *Trends in Computational Structural Mechanics* (Barcelona, 2011).

[150] Munk, Walter H. Origin and generation of waves. In *Proceedings 1st International Conference on Coast Engineering, ASCE* (Long Beach, CA, 1950).

[151] Musial, W. Offshore Wind Electricity: A Viable Energy Source for the Coastal United States. *Mar. Technol. Soc. J.* (2007), 32–43.

[152] Musial, W., and Ram, B. Large-scale offshore wind power in the united states: Assessment of opportunities and barriers. *Technical Report NREL/TP-500-40745, U.S. Department of Energy* (2010), 1–221.

[153] Newren, E.P. *Enhancing the immersed boundary method: stability, volume conservation and implict solvers.* Dissertation, University of Utah, 2007.

[154] Nicholls-Lee, R., Turbock, S., and Boyd, S. A Method of Analysing Fluid Structure Interactions on a Horizontal Axis Tidal Turbine. In *Proc. 9th European Wave and Tidal Energy Conference EWTEC* (2011).

[155] Nichols, B.D., and Hirt, C.W. Methods for calculating multi-dimensional transient free-surface flows past bodies. *Technical Report, Los Alamos National Lab* (1975).

[156] Niedzwecki, J., and Duggal, A. Drag of Cylinders of Simple Shapes. *Report No. 619* (1923).

[157] Niedzwecki, J., and Duggal, A. Wave Runup and Forces on a Circular Cylinder in Regular and Random Waves. *Journal of Waterway, Port, Coastal and Ocean Engineering 118* (1992), 615–620.

[158] Nielsen, G.N., Hanson, T.D., and Skaare, B. Integrated Dynamic Analysis of Floating Offshore Wind Turbines. In *Volume 1: Offshore Technology; Offshore Wind Energy; Ocean Research Technology; LNG Specialty Symposium / Offshore Wind Energy* (Hamburg, Germany, 2006).

[159] Noh, P., and Woodward, P. SLIC (Simple Line Interface Calculation). *5th International Conference on Fluid Dynamics 59* (1976).

[160] Ochi, Michel K. *Ocean Waves: The Stochastic Approach.* Cambridge University Press, New York, 1998.

265

[161] Ochi, M.K., and Tsai, C.H. Prediction of cocurrence of breaking waves in deep water. *Journal of Physical Oceanography 13*, 11 (1983), 2008–2019.

[162] Okamoto, S., and Sunabashiri, Y. Vortex shedding from a circular cylinder of nite length placed on a ground plane. *J Fluid EngT ASME 144* (1992), 512–521.

[163] Okamoto, S., and Yagita, M. The experimental investigation on the flow past a circular cylinder of nite length placed normal to the plane surface in a uniform stream. *Bull JSME 16* (1973), 805–814.

[164] Palau-Salvador, G., Stoesser, T., Frohlich, J., Kappler, M., and Rodi, W. Large eddy simulations and experiments of flow around finite-height cylinders. *Flow Turbul. Combust. 84* (2010), 239–275.

[165] Panahi, R., Jahanbakhsh, E., and Seif, M.S. Development of a VoF-fractional step solver for floating body motion simulation. *Applied Ocean Research 28* (2006), 171–181.

[166] Panahi, R., Jahanbakhsh, E., and Seif, M.S. Towards simulation of 3D nonlinear high-speed vessels motion. *Ocean Engineering 36* (2009), 256–265.

[167] Park, C.W., and Lee, S.J. Flow structure around a finite circular cylinder embedded in various atmospheric boundary layers. *Fluid Dynamics Research 30* (2002), 197–215.

[168] Passon, P., and Kühn, M. State-of-the-art and Development Needs of Simulation Codes for Offshore Wind Turbines. *Copenhagen Offshore Conference* (2005).

[169] Patankar, S.V. *Numerical heat transfer and fluid flow.* Taylor & Francis, 1980.

[170] Pattenden, R.J., Bressloff, N.W., Turnock, S.R., and Zhang, X. Unsteady simulations of the flow around a short surface-mounted cylinder. *Intl J. Numer. Meth. Fluids 53* (2007), 895–914.

[171] Pattenden, R.J., Turnock, S.R., and Zhang, X. Measurements of the flow over a low-aspect-ratio cylinder mounted on a ground plane. *Experiments in Fluids 39* (2005), 10–21.

[172] Peng, A., Wellens, P., and Raaijmakers, T. 3-D Numerical Modeling of Wave Run-Up on Monopiles. In *ASME 2012 31st International Conference on Ocean, Offshore and Arctic Engineering* (Rio de Janeiro, Brazil, 2012).

[173] Peng, D., Merriman, B., Osher, S., Zhao, H., and Kang, M. A PDE-based fast local level set method. *Journal of Computational Physics 155*, 2 (1999), 410–438.

[174] Perkovic, L., Silva, P., Ban, M., and Kranjcevic, N. Harvesting high altitude wind energy for power production: The concept based on Magnus effect. *Applied Energy 101* (2013), 151–160.

[175] Peskin, C.S. *Flow patterns around heartvalves: a digital computer method for solving the equations of motion.* Dissertation, Albert Einstein College of Medicine, 1972.

[176] Peskin, C.S. The immersed boundary method. *Acta Numerica* (2002), 479–517.

[177] Phillips, O.M. The equilibrium range in the spectrum of wind-generated waves. *Journal of Fluid Mechanics 4* (1958), 785–790.

[178] Phillips, O.M. *The Dynamics of the Upper Ocean.* Cambridge University Press, Cambridge, 1977.

[179] Phuc, V.P., and Ishihara, T. A study on the dynamic response of a semi-submersible floating offshore wind turbine Part 2: numerical simulation. In *ICWE12* (Cairns, 2012).

[180] Pierson, W., and Moskowitz, L. A proposed spectral form for fully developed wind seas based on the similarity theory of S. A. Kitaigorodskii. *Journal of Geophysical Research 69*, 24 (1964), 5181.

[181] Pilliod, J.E., and Puckett, E.G. Second-order accurate volume-of-fluid algorithms for tracking material interfaces. *Journal of Computational Physics 199*, 2 (2004), 465–502.

[182] Pinkster, J.A., and Huijsmans, R.H.M. The Low Frequency Motions of a Semi-submersible in Waves. In *BOSS Conference* (Cambridge, Massachusetts, 1982).

[183] Piro, D., and Maki, K.J. Hydroelastic analysis of bodies that enter and exit water. *Journal of Fluids and Stuctures 37* (2013), 134–150.

[184] Quallen, S., Xing, T., Carrica, P., Li, Y., and Xu, J. CFD Simulation of a Floating Offshore Wind Turbine System Using a Quasi-Static Crowfoot Mooring-Line Model. In *Proceedings of the Twenty-third (2013) International Offshore and Polar Engineering* (Anchorage, Alaska, 2013).

[185] Quan, S., and Schmidt, D.P. An interface tracking method with moving mesh for simulation of three-dimensional two-phase flows. In *18th Annual Conference on Liquid Atomization and Spray Systems* (Irvine, CA, 2005).

[186] Relf, E.F., and Simmons, F.G. The frequency of eddies generated by the motion of circular cylinders through a fluid. *Aero. Res. Counc. 917* (1924).

[187] Robertson, A., Jonkman, J., Masciola, M., Song, H., Goupee, A., Coulling, A., and Luan, C. Definition of the semisubmersible floating system for phase II of OC4, 2014.

[188] Robertson, A., Jonkman, J., Wendt, F., Goupee, A., and Dagher, H. Definition of the OC5 semisubmersible floating system, 2015.

[189] Roesetti, G.F., Vaz, G., Hoekstra, M., Goncalves, R.T., and Fujarra, A.L.C. CFD calculations for free-surface-piercing low aspect ratio circular cylinder with solution verification and comparison with experiments. In *32nd International Conference on Ocean, Offshore and Arctic Engineering* (Nantes, France, 2013).

[190] Roh, S.C., and Park, S.O. Vortical flow over the free end surface of a finite circular cylinder mounted on a flat plate. *Experiments in Fluids 34* (2003), 63–67.

[191] Roshko, A. Experiments of the flow past a circular cylinder at very high Reynolds number. *Journal of Fluid Mechanics 10* (1961), 345–356.

[192] Rostamy, N., Sumner, D., Bergstrom, D.J., and Bugg, J.D. Local flow field of a surface-mounted finite circular cylinder. *Journal of Fluids and Structures 34* (2012), 105–122.

[193] Ruprecht, A., Ruopp, A., and Lippold, F. Fluid Structure Simulations on Distributed High Performance Computer Resources. *Proc. MpCCI UserForum* (2009).

[194] Rusche, Henrik. *Computational Fluid Dynamics of Dispersed Two-Phase Flows at High Phase Fractions*. Dissertation, Imperial College of Science, Technology and Medicine, 2002.

[195] Sabersky, R., Acosta, A., and Hauptmann, E. *luid Flow: A First Course in Fluid Mechanics*. MacMillian Publishers, New York, 1998.

[196] Sakamoto, H., and Arie, M. Vortex shedding from a rectangular prism and a circular cylinder placed vertically in a turbulence boundary layer. *Journal of Fluid Mechanics 126* (1983), 147–165.

[197] Sakamoto, H., and Oiwake, S. Fluctuating forces on a rectangular prism and a circular cylinder placed vertically in a turbulent boundary layer. *J Fluid EngT ASME 106* (1984), 160–166.

[198] Sanderse, B., vanDerPijl, S.P., and Koren, B. Review of computational fluid dynamics for wind turbine wake aerodynamics. *Wind Energy 14* (2011), 799–819.

[199] Sarpkaya, T. Transverse Oscillations of a Cylinder in Uniform Flow. *Rep. Monterey: Department of the Navy* (1977).

[200] Sarpkaya, T. Water impact laods and dynamics response of horizontal circular cylinders in offshore structures. In *Proceedings of the Offshore Technology Conference, OTC 3065* (Houston, TX, 1978).

[201] Sarpkaya, Turgut. *Wave Forces on Offshore Structures*. Cambridge University Press, Cambridge, 2010.

[202] Sarpkaya, Turgut, and Isaacson, Michael. *Mechanics of Wave Forces on Offshore Structures*. Van Nostrand Reinhold Company, New York, 1981.

[203] Sato, Y., Miyata, H., and Sato, T. CFD simulation of 3-dimensional motion of a ship in waves: application to an advancing ship in regular heading waves. *Journal of Marine Science and Technology 4* (1999), 108–116.

[204] Scardovelli, Ruben, and Zaleski, Stéphane. Direct Numerical Simulation of Free-Surface and Interfacial Flow. *Annual Review of Fluid Mechanics 31*, 1 (Jan. 1999), 567–603.

[205] Schewe, G. On the force fluctuations acting on a circular cylinder in cross flow from subcritical up to transcritical Reynolds numbers. *J Fluid Mechanics 133* (1983), 265–85.

[206] Sclavounos, P.D. Nonlinear Impulse of Ocean Waves on Floating Bodies. *Journal of Fluid Mechanics 697* (2012), 316–335.

[207] Scott, A., McLaughlin, J., , and Chu, F. The soliton: a new concept in applied science. *Proc. IEEE 61* (1973), 240–243.

[208] Scott Russell, J. Report on Waves. *Fourteenth meeting of the British Association for the Advancement of Science* (1844).

[209] Sethian, J.A., and Smereka, P. Level Set Methods for Fluid Interfaces. *Annual Review of Fluid Mechanics 35* (2003), 341–372.

[210] Shao, W., Zhang, Y., Zhu, D., and Zhang, T. Drag force on a free surface-piercing yawed circular cylinder in steady flow. *Journal of Fluids and Structures 43* (2013), 145–163.

[211] Shi, X., and Lim, S.P. A LBM-DLM/FD method for 3D fluid-structure interactions. *Journal of Computational Physics 226* (2007), 2028–2043.

[212] Singh, S.P., and S., Mittal. Flow past a cylinder: shear layer instability and drag crisis. *Int J Numer Meth Fluids 47* (2005), 75–98.

[213] Sommerfeld, A. *Partial Differential Equations in Physics*. Academic Press, New York, 1949.

[214] Song, C, and Yuan, M. Simulation of Vortex-Shedding Flow About a Circular Cylinder at High Reynolds Numbers. *Journal of Fluids Engineering 112* (1990), 155–163.

[215] Sorenson, N.N., Bechmann, A., and Zahle, F. 3D CFD computations of transitional flows using DES and a correlation based transition model. *Wind Energy 14* (2011), 77–90.

[216] Soyoz, Serder, and Aydin, Can. Effects of higher wave harmonics on the response of monopile type offshore wind turbines. *Wind Energy* (2012).

[217] Spalart, P.R., and Allmaras, S.R. A One-Equation Turbulence Model for Aerodynamic Flows. In *American Institute of Aeronautics and Astronautics (AIAA) Paper 92-0439* (Reston, VA., 1992).

[218] Spalding, D.B. A Single Formula for the Law of the Wall. *Trans. ASME., J. Appl. Mech. 28* (1961), 444 – 458.

[219] Stoker, J.J. *Water Waves: The Mathematical Theory with Applications.* Interscience Publishers, Inc, New York, 1957.

[220] Stokes, G.G. *Mathematical and Physical Papers. Volume I.* Cambridge University Press, 1880.

[221] Suh, J.S., Yang, J.M., and Stern, F. The effect of airwater interface on the vortex shedding from a vertical circular cylinder. *ASME Journal of Fluids Engineering 27* (2011), 1 – 22.

[222] Sumner, D. Two circular cylinders in cross-flow: A review. *Journal of Fluids and Structures 26* (2010), 849–899.

[223] Sumner, D. Flow above the free end of a surface-mounted finite-height circular cylinder: A review. *Journal of Fluids and Structures* (2013).

[224] Sumner, D., Heseltine, J.L., and Dansereau, O.J.P. Wake structure of a finite circular cylinder of small aspect ratio. *Experiments in Fluids 37* (2004), 720 – 730.

[225] Sun, H., and Faltinsen, O.M. Prediction of cocurrence of breaking waves in deep water. *Appl. Ocean Res. 28*, 5 (2006), 299–311.

[226] Sun, S.M. Non-existence of truly solitary waves in water with small surface tension. *Proceedings: Mathematical, Physical and Engineering Sciences 455*, 1986 (1999), 2191–2228.

[227] Sussman, M., and Fatemi, E. An efficient, interface-preserving level set redistancing algorithm and its application to interfacial incompressible fluid flow. *J. Sci. Comput. 20*, 4 (1999), 1165–1191.

[228] Sussman, M., and Puckett, E.G. A coupled level set and volume-of-fluid method for computing 3D and axisymmetric incompressible two-phase flows. *Journal of Computational Physics 162* (2000), 301–337.

[229] Sverdrup, H.U., and Munk, W.H. Wind, sea and swell. Theory of relations for forecasting. *U.S. Hydrogr. Office, Washington 601* (1947).

[230] Tan, J.H.C., Magee, A., Kim, J.W., Teng, Y.J., and Zukni, N.A. CFD Simulation for Vortex Induced Motions of a Multi-Column Floating Platform. In *ASME 2013 32nd International Conference on Ocean, Offshore and Arctic Engineering* (Nantes, France, 2013).

[231] Taniguchi, S., Sakamoto, H., and Arie, M. Flow around circular cylinders of nite height placed vertically in turbulent boundary layers. *Bull JSME 24* (1981), 37–44.

[232] Taubin, G. A signal processing approach to fair surface design. *Proceedings of SIGGRAPH 95* (1995), 351–358.

[233] Taylor, G.I. Generation of Ripples by Wind Blowing Over a Viscous Fluid. In *The Scientific Papers of G.I. Taylor*, G K Batchelor, Ed. Cambridge, London, 1963, ch. 25, pp. 244–254.

[234] Teixeira, A., Mooney, K.G., Kruger, J.S., Williams, C.L., Suszynski, W.J., Schmidt, L.D., Schmidt, D.P., and Dauenhauer, P.J. Aerosol generation by reactive boiling ejection of molten cellulose. *Energy and Environmental Science* (2011), 1–17.

[235] Tezduyar, T.E., Sathe, S., Keedy, R., and Stein, K. Space time finite element techniques for computation of fluid structure interactions. *Int. J. Numer. Methods Fluids 195* (2006), 2022–2027.

[236] Tezduyar, T.E., Sathe, S., and Stein, K. Solution techniques for the fully discretized equations in computation of fluid structure interactions with the space-time formulations. *Comput. Methods Appl. Mech. Engrg. 195* (2006), 5743–5753.

[237] Thiagarajan, K. P., and Dagher, H. J. State-of-the-Art Review of Floating Platform Concepts for Offshore Wind Energy Generation. *Journal of Offshore Mechanics and Arctic Engineering 7* (2012), 489–495.

[238] Travin, A., Shur, M., Strelets, M., and Spalart, P. Detached Eddy Simulations Past a Circular Cylinder. *Flow, Turbulence and Combustion 63* (1999), 293–313.

[239] Triton, D.J. Experiments on the flow past a circular cylinder at low Reynolds number. *Journal of Fluid Mechanics 547* (1959).

[240] Tryggvason, G., Bunner, B., Esmaeli, A., Juric, D., Al-Rawahi, N., Tauber, W., Han, J., Nas, S., and Y.J., Jan. A front-tracking method for the computations of multiphase flow. *Journal of Computational Physics 169*, 2 (2001), 708–759.

[241] Tryggvason, G., Esmaeeli, A., and Al-Rawahi. Direct numerical simulations of flows with phase change. *Computers and Structures 83*, 6-7 (2005), 445–453.

[242] Ubbink, O., and Issa, R.I. A method for capturing sharp fluid interfaces on arbitary meshes. *Journal of Computational Physics 153*, 1 (1999), 26–30.

[243] Unverdi, S.O., and Tryggvason, G. A front-tracking method for viscous, incompressible, multi-fluid flows. *Journal of Computational Physics 100*, 1 (1992), 25–37.

[244] van der Pijl, S.P., Segal, A., Viuk, C., and Wesseling, P. A mass-conserving level-set method for modelling of multi-phase flows. *International Journal for Numerical Methods in Fluids 47*, 4 (2005), 339–361.

[245] VanDaalen, E.F.G., Kleefsman, K.M.T., Gerrits, J., Luth, H.R., Veldman, A.E.P., Box, P.O., and Wageningen, A.A. Experimental validation of anti-roll tank simulations with a volume of fluid based Navier-Stokes solver. In *Symposium on Naval Hydrodynamics* (Val de Reuil, 2000), vol. 2.

[246] Veldkamp, H.F., and van der Tempel, J. Influence of Wave Modeling on the Prediction of Fatigue for Offshore Wind Turbines. *Wind Energy 8* (2005), 49–65.

[247] von Scheven, M., and Ramm, E. Strong coupling schemes for interaction of thin-walled structures and incompressible flows. *Int. J. Numer. Methods Engrg. 87* (2011), 214–231.

[248] Wall, W.A., Genkinger, S., and Ramm, E. A strong coupling partitioned approach for fluid-structure interaction with free surfaces. *Comput. Fluids 36* (2007), 169–183.

[249] Wayman, E.N., Sclavounos, P.D., Butterfield, S., Jonkman, J., and Musial, W. Coupled Dynamic Modeling of Floating Wind Turbine Systems. In *Offshore Technology Conference (OTC)* (Houston, TX, 2006).

[250] Wemmenhove, Rik, Loots, Erwin, Luppes, Roel, and Veldman, Arthur. Modeling of Two-Phase Flow with Offshore Applications. In *OMAE Conference* (Halkidiki, 2005), pp. 1–9.

[251] Weymouth, G.D., Wilson, R.V., and Stern, F. RANS CFD predictions of pitch and heave ship motions in head seas. *Journal of Ship Research 49* (2005), 80–97.

[252] Whitham, G.B. *Linear and Nonlinear Waves*. John Wiley and Sons, New York, 1974.

[253] Wieselsberger, C., Betz, A., and Prandtl, L. Versuche über den Widerstand gerundeter und kantiger Körper. *Ergebnisse AVA Göttingen* (1923), 22–32.

[254] Withee, J.E. *Fully Coupled Dynamic Analysis of a Floating Wind Turbine System*. Dissertation, Department of Ocean Engineering, Massachusetts Institute of Technology, 2004.

[255] W.J., Pierson. Wind generated gravity waves. *Advances in Geophysics* (1955), 93–178.

[256] Wu, C.S., and Young, D.L. Simulations of free-surface flows with an embedded object by a coupling partitioned approach. *Computers and Fluids 89* (2014), 66–77.

[257] Yabe, T., Xiao, F., and Utsumi, T. The constrained interpolation profile method for multiphase analysis. *Journal of Computational Physics 169* (2001), 556–593.

[258] Yang, C., Lohner, R., and Lu, H. An Unstructured-Grid Based Volume-of-Fluid Method for Extreme wave and Freely-Floating Structure Interactions. In *Conference of Global Chinese Scholars on Hydrodynamics* (2006), pp. 415–422.

[259] Yang, J., Peidikman, S., and Balaras, E. A strongly coupled, embedded-boundary method for fluid-structure interactions of elastically mounted rigid bodies . *Journal of Fluids and Structures 24* (2008), 5167–5182.

[260] Yang, J., Sakamoto, N., Wang, Z., Carrica, P., and Stern, F. Two Phase Level-Set/Immersed-Boundary Cartesian Grid Method for Ship Hydrodynamics. In *9th International Conference on Numerical Ship Hydrodynamics* (Ann Arbor, Michigan, 2007).

[261] Yang, Jianming, and Stern, Frederick. A simple and efficient direct forcing immersed boundary framework for fluid-structure interactions. *Journal of Computational Physics 231* (2012), 5029–5061.

[262] Youngs, D.L. An interface tracking method for 3D Eulerian hydrodynamics code. *Tech. Rep, AWRE*, 44/92/35 (1984).

[263] Yu, G., Avital, E.J., and Williams, J.J.R. Large eddy simulation of flow past free surface piercing circular cylinders. *ASME Journal of Fluids Engineering 130* (2008).

[264] Yu, Z., and Shao, X. A three-dimensional fictitious domain method for the simulation of fluid-structure interactions. *Journal of Hydrodynamics 22* (2010), 178–183.

[265] Zabusky, N.J., and Kruskal, M.D. Interaction of "Solitons" in a Collisionless Plasma and the Recurrence of Initial States. *Phys. Rev. Lett. 15* (1965), 240–243.

[266] Zambrano, T., MacCready, T., Kiceniuk, T., D.G., Roddier, and Cermelli, C.A. Dynamic Modeling of Deepwater Offshore Wind Turbine Structures in Gulf of Mexico Storm Conditions. *Journal of Fluid Mechanics 697* (2006), 316–335.

[267] Zdrakovich, M.M. *Oxford University Press* (1997).

[268] Zhao, M., Cheng, L., and Zhou, T.M. Direct numerical simulation of three-dimensional flow past a yawed circular cylinder of infinite length. *Journal of Fluids and Structures 25* (2009), 831–847.

[269] Zhou, H., Cao, H., and Wan, D. Numerical Predictions of Wave Impacts on the Supporting Structures of Shanghai Donghai-Bridge Offshore Wind Turbines. In *Proceedings of the Twenty-third (2013) International Offshore and Polar Engineering* (Anchorage, Alaska, 2013).